Title

Leveraging Electrostatic Interactions in Engineering Advanced Semiconducting Polymers

Author

Le, My Linh

Publication Date

2023

Peer reviewed|Thesis/dissertation

UNIVERSITY OF CALIFORNIA

Santa Barbara

Leveraging Electrostatic Interactions in Engineering Advanced Semiconducting Polymers

A dissertation submitted in partial satisfaction of the

requirements for the degree Doctor of Philosophy

in Materials

by

My Linh Le

Committee in charge:

Professor Michael Chabinyc, Co-Chair

Professor Rachel Segalman, Co-Chair

Professor Glenn Fredrickson

Professor Craig Hawker

Professor Thuc-Quyen Nguyen

June 2023

The Dissertation of My Linh Le is approved.

Professor Glenn Fredrickson

Professor Craig Hawker

Professor Thuc-Quyen Nguyen

Professor Michael Chabinyc, Committee Co-Chair

Professor Rachel Segalman, Committee Co-Chair

June 2023

Leveraging Electrostatic Interactions in Engineering Advanced Semiconducting Polymers

ACKNOWLEDGEMENTS

The past 4 years at UCSB have been one of the most difficult times in my life – navigating through a PhD program and facing some unexpected life turbulences. I owe everything to the people listed below – without them, their guidance, their patience, their empathy, and their support, I would have never come this far.

First and foremost, I need to thank my advisors, Rachel and Michael. Rachel is the female scientist role model that I always admire. She constantly reminds me that she is here to help me grow instead of being a manager. The Segalman group, under Rachel's leadership, is a welcoming and supporting community where I feel a strong sense of belonging. I was once a summer undergraduate intern in the Segalman group, and I loved the group culture so much that I came back for my PhD. Rachel has also given me so much freedom in exploring the research directions that I found interesting, and always provided great feedback on experiment ideas and how to effectively communicate them. Her skills in presenting a scientific idea, especially, always amaze me – I have learned so much on that from working with her. Last but certainly not the least, Rachel, thank you so much for telling me that I am doing just fine, for urging me to go home when things got rough, and for being a great resource in almost everything: science, career, and life.

I have worked with Michael for 4 years, but to this day I am still amazed by his attention to details, his deep insights and breadth of knowledge in almost every topic that I have questions on, and his ability to pull out a paper from the 80s – 90s in just 1 minute to support our research discussions. Michael always encourages me to think critically about a problem, and teaches me how to come up with a hypothesis and to go through estimations of how it might work. These are invaluable skills that I will continue working on improving and

hope to make the best use of regardless of what I do in next in life. Michael, I appreciate how you, being a PI and a department chair, still took your valuable time to go into the lab with me and showed me your tricks on experiments. Lastly, thank you so much for the kind reminder that there is only one of me.

I also want to express my appreciation to 3 other members in my thesis committee, Craig, Glenn, and Quyen, for their valuable inputs during my qualifying exam and annual committee meeting, many of which turned into parts of Chapter 3 and Chapter 5 in this Dissertation. Craig shows me how much fun science can be, and teaches me a lot on how to be confident and to take ownership of my work. Glenn inspires me with his brilliant mind and tremendous insights on fundamental polymer physics. Quyen, thank you for being a great inspiration not only for me but also for many young girls in Vietnam who want to pursue a career in science. On top of that, thank you so much for your carrier advice and support in connecting me with research collaborators and relevant people in the industry.

I am thankful for current and past members in the Segalman and Chabinyc groups who have helped me tremendously throughout my time at UCSB. Nicole, you were such a big inspiration, a great mentor, a role model, and a caring friend. Scott, who I only met briefly during my summer internship and left UCSB by the time I joined as a graduate student – I wish we had more overlapping time. Thank you so much for all the great insights to my project, and for kindly answering all the emails from a clueless first year trying to understand what a coacervate is and how to make a pretty phase diagram on PowerPoint. Dakota, who has always gone above and beyond to support me. Audra, for all the hugs, the encouragement, the weekend rides to the Bay Area, and all the cute sticky notes you left on my desk. Zoey, for sharing with me that “depressing student office corner” and making the best out of it.

Gordon, Phong, and Saejin, for all the great science discussions and random rants in the lab, and for always helping me with a smile. Seamus, for his encouragement and support even way back when I was an undergraduate intern. Elayne, Manny, Eunhee, and Naveen, for their career advice and life-after-school insights. Last but not least, everyone else in the Segalman and Chabinyc groups, for being the best (late night/weekend) labmates/boba-mates/movie-mates/almost-Taylor-Swift-concert-mates (hey Jerrick!!) that I could ask for.

I am also grateful to have the opportunity to collaborate with and learn from many brilliant researchers at UCSB. I want to thank PK, for having taught me so much about polymer mechanics, for his authentic home-made Pad Thai, and for tolerating my constant whining. To Doug, Shuyi, Amy, Rhys, Kaitlin, Jacob, Alex, and Oscar, for being such great collaborators, for inspiring me with your work ethics, and for helping me tremendously throughout our collaborations.

I want to thank instrument and beamline scientists, particularly Amanda Strom, Dmitriy Uchenik, Ruipeng Li, Rachel Schoeppner, Rachel Behrens, Tom Mates, Shamon Walker, Youli Li, and Phillip Kohl, for their assistance with instrument training, experiment trouble-shooting, data acquisition, and many great science discussions.

I want to express my appreciation to the PIs that I have worked with during my undergraduate career. Dr. Wei Chen, who introduced me to scientific research, supported me every step along the way, and took care of me as if I was her own daughter – Wei, I am forever grateful to know you and to be your mentee. Dr. Sara Thoi, who gave me the opportunity to work in her lab in summer 2017 – Sara, thank you so much for giving me that experience, for 3 months of exciting learning and great mentorship, and for making me feeling so empowered.

I also want to dedicate this Dissertation to Dr. Thang V. Nguyen, a very dear friend of mine who lost his battle to cancer. While you are no longer with us, your integrity, your dedication to research, and your unconditional kindness have been and will always be the inspiration for not only me but also generations of students in Vietnam. I hope that you are proud of how much I have grown – from calling you in the middle of the night panicking about my first paper, to now submitting this Dissertation for the completion of this degree.

To Minh and our 2 cats, Binz and Soobin – you all are my second family, my mental support, my source of joy, and my safe haven. I cannot count how many times you have saved me from negative thoughts and given me reasons to be strong. People say the sound of a cat purring has healing power, and I can confirm that this is true. Minh, thank you so much for your constant support in the past 7 years, for seeing the best in me even in my worst time. I am glad that I got to share this journey with you.

To my sister, Kieu Anh, I am sorry that I have been absent for most of your teenage and college years. Thank you for always giving me the best time when I go back to Vietnam, and for your support from afar. Thanks for always being there for mom and dad.

I am indebted to my parents, who gave me this life and let me live it the way I wanted to. Mom and dad, thank you for supporting all my decisions, from leaving the house at 14 to attend high school in Hanoi, going to the US for a college degree, to now continuing to be away for this graduate school journey. I know how difficult it has been for you, and I hope that with the completion of this degree, you will finally get to see more of me around.

VITA OF MY LINH LE
May 2023

Education

Sep 2019 – June 2023: Ph.D. in Materials (expected), University of California, Santa Barbara
Co-Advisors: Professor Michael Chabinyc and
Professor Rachel Segalman

Sep 2015 – May 2019: B.A. Chemistry, Mathematics minor, Mount Holyoke College
Summa Cum Laude – Advisor: Professor Wei Chen

Publications

11. *(Alphabetical)* Aspuru-Guzik, A., Choi, D., **Le, M. L.,** Lo, S., Luginbuhl, B., Nguyen, T-Q., Schopp, N., Seifrid, M., Gary, G. Machine Learning on Organic Photovoltaics Data with Device Processing Parameters. *[working title]*, *in preparation.*

10. **Le, M. L.,*** Lapkriengkri, I.,* Albanese, K., Nguyen, H. P., Tran, C., Blankenship, J., Segalman, R. A., Bates, C., and Chabinyc, M. L. Engineering Soft, Elastic, and Conductive Polymers for Stretchable Electronics Using Ionic Compatibilization. *[working title]*, *in preparation.* (*equal contribution)

9. Pace, G. T., **Le, M. L.,** Clément, R. J., Segalman, R. A. A Coacervate-Based Mixed-Conducting Binder for High Power, High Energy Batteries. *ACS Energy Lett.* **2023**. DOI: 10.1021/acsenergylett.3c00829

8. **Le, M. L.,** Warner, C., Chabinyc, M. L., Segalman, R. A. Role of Complexation Strength on the Optoelectronic Properties of Conjugated Polyelectrolyte - Polymeric Ionic Liquid Blends. *Chem. Mater*. **2023**. DOI: 10.1021/acs.chemmater.3c00627

7. Yuan, D., Plunkett, E., Nguyen, P. H., Rawlings, D., **Le, M. L**., Kroon, R., Müller, C., R. A. Segalman, M. L. Chabinyc. Double Doping of Semiconducting Polymers Using Ion-Exchange with a Dianion. *Adv. Funct. Mater*. **2023**. DOI: 10.1002/adfm.202300934

6. **Le, M. L.**, Grzetic, D., Delaney, K. T., Yang, K. C., Xie, S., Fredrickson, G. H., Chabinyc, M. L., Segalman, R. A. Electrostatic Interactions Control the Nanostructure of Conjugated Polyelectrolyte-Polymeric Ionic Liquid Blends. *Macromolecules* **2022**, 55, 8321−8331. DOI: 10.1021/acs.macromol.2c01142

5. Fredrickson, G. H., Xie, S., Edmund, J., **Le, M. L.**, Sun, D., Grzetic, D. J., Vigil, D. L., Delaney, K. T., Chabinyc, M. L., Segalman, R. A. Ionic Compatibilization of Polymers. *ACS Polym. Au* **2022***,* 2, 299−312. DOI: 10.1021/acspolymersau.2c00026

4. **Le, M. L.**, Rawlings, D., Danielsen, S. P. O., Kennard, R., Chabinyc, M. L., Segalman, R. A. Aqueous Formulation of Concentrated Semiconductive Fluid Using Polyelectrolyte Coacervation. *ACS Macro Lett.* **2021**, 10, 8, 1008–1014. DOI: 10.1021/acsmacrolett.1c00354

3. Schauser, N. S., Grzetic, D. J., Tabassum, T., Kliegle, G. A., **Le, M. L.**, Susca, E. M., Antoine, S., Keller, T. J., Delaney, K. T., Han, S., Seshadri, R., Fredrickson, G. H., Segalman,

R. A. The Role of Backbone Polarity on Aggregation and Conduction of Ions in Polymer Electrolytes. *J. Am. Chem. Soc.* **2020**, 142, 15, 7055–7065. DOI:10.1021/jacs.0c00587

2. **Le, M. L.*,** Zhou, Y.*, Byun, J.*, Kolozsvari. K., Xu, S., Chen, W. Using A Spin-Coater to Capture Adhesive Species during Polydopamine Thin-Film Fabrication. *Langmuir* **2019**, 35, 39, 12722–12730. DOI: 10.1021/acs.langmuir.9b02525 (*equal contribution)

1. Han, X., Wang, M., **Le, M. L.**, Bedford, N. M., Woehl, T. J., Thoi, V. S. Effects of Substrate Porosity in Carbon Aerogel Supported Copper for Electrocatalytic Carbon Dioxide Reduction. *Electrochimica Acta* **2019**, 297, 545-552. DOI: 10.1016/j.electacta.2018.11.203

Patent

Pace, G. T., **Le, M. L.**, Clément, R. J., Segalman, R. A. "Electrostatically Driven Polymer Complex Composed of Oppositely Charged Polyelectrolytes as a Multifunctional Battery Binder". UC Case 2023-848

ABSTRACT

Leveraging Electrostatic Interactions in Engineering Advanced Semiconducting Polymers

by

My Linh Le

Semiconducting conjugated polymers (CPs) are an important class of organic electronic materials due to their mechanical flexibility, molecular design versatility, and compatibility with inexpensive and scalable processing methods. However, the limited solubility of CPs in most solvents and their melt intractability remain one of the key challenges in harnessing their optoelectronic performance. In particular, these processing limits hinder the fabrication of CPs into thick films and bulk structures that are required in a wide range of applications, such as actuators, bioelectronic scaffolds, or thermoelectric modules.

Complexation between two oppositely charged polyelectrolytes offers unique opportunities for solvent-lean processing of semiconducting polymers, facilitated by the formation of a polymer-dense fluid phase known as the coacervate. Moreover, the electrostatic interactions in these systems provide additional handles for controlling the material's structure and properties. Despite extensive investigation on coacervate of two insulating polyelectrolytes, studies focusing on the coacervate where at least one of the components is conjugated are sparse. The processability of the conjugated coacervate and the solid-state properties of the resulting polymer complex are still not well understood.

This thesis investigates how electrostatic interactions can be leveraged to design advanced semiconducting polymeric materials by developing fundamental understanding on the

structure – processing – property relationships of charged conjugated polymer complexes. First, we demonstrate how electrostatic attraction between a conjugated polyelectrolyte (CPE) and an oppositely charged insulating polymeric ionic liquid can be utilized to formulate a conjugated coacervate with notably high polymer loading. We show that this coacervate can be easily blade coated to fabricate μm-thick films, a task that is otherwise challenging to achieve with conventional solution casting of semiconducting polymers. We then look into the solid-state structure of charged conjugated polymer complexes and examine how electrostatic interactions can be leveraged to control the self-assembly of this material. We find that manipulation of electrostatic parameters, including polymer charge fraction and counterion concentration, can adjust the morphology of these polymer complexes from a homogeneously mixed state to a weakly structured state in which the local ordering arises from backbone-immiscibility-induced segregation. Subsequently, we elucidate how this structural evolution influences the local order and interconnectivity of the CPE chains within these complexes. Our findings demonstrate that the structural disorders along the CPE backbone is alleviated in strongly mixed complexes. Charge transport on the other hand is improved in all morphologies, indicating the enhancement in the long-range connectivity of the CPE upon complexation. These studies suggest electrostatic interactions as an effective handle for controlling the structure and properties of charged conjugated polymer complexes to obtain targeted optoelectronic performance. Finally, we utilize the attractive electrostatic interactions to effectively combine conjugated and bottlebrush polyelectrolytes. The resulting material is a phase-compatible complex that is soft, stretchable, elastic, and conductive. This study emphasizes ionic complexation as an exciting pathway for engineering multifunctional polymeric materials.

TABLE OF CONTENTS

Chapter 1

Introduction

This chapter is reproduced in part with permission from:

Fredrickson, G. H., Xie, S., Edmund, J., **Le, M. L.**, Sun, D., Grzetic, D. J., Vigil, D. L., Delaney, K. T., Chabinyc, M. L., Segalman, R. A. Ionic Compatibilization of Polymers. *ACS Polym. Au* **2022***,* 2, 299−312. DOI: 10.1021/acspolymersau.2c00026

1.1 Fundamentals of semiconducting polymers

Conjugated polymers, whose backbone is composed of alternating single and double bonds, are an emerging class of organic semiconductor due to their low cost, versatility for molecular modifications, superior flexibility compared to many traditional inorganic semiconductors, and compatibility with large-scale industrial processing protocols. The semiconducting nature of conjugated polymers comes from the sp2-hybridized atoms (commonly C) that make up their backbones.[1] The π-bond in these structure is formed by sharing of an electron pair from the unhybridized p_z orbitals between 2 neighboring atoms. In conjugated small molecules, the p_z atomic orbitals across the entire molecule overlap, forming a delocalized π-molecular orbital that can be described as a linear combination of the participating atomic orbitals. For conjugated polymer, this delocalization of π-molecular orbital can span across several repeat units. This is commonly referred to as the conjugation length of the polymer. As the conjugation length increases, the energy levels become more closely spaced, analogous to increasing the box side in the classical particle-in-a-box argument. This results in the band-like electronic structure in conjugated polymers, where the highest occupied molecular orbital

(HOMO) is comparable to the valence band, and the lowest unoccupied molecular orbital (LUMO) is comparable to the conduction band in inorganic semiconducting materials.[2]

One of the first major breakthroughs in the field of semiconducting polymers is the discovery of the metallic behavior of polyacetylene (structure shown in **Figure 1.1a**) when it is oxidized by halogens and halogenated oxidant.[3] While being an insulator at pristine state, polyacetylene was shown to experience ≈ 7 orders of magnitude increase in conductivity when it is oxidized. While this system is considered responsible for launching of the conductive plastic field, studies have shifted away from polyacetylene due to its poor solution processability and poor stability in ambient conditions. Since then, much progress has been made on improving the solution processability of conjugated polymers, mostly via side-chain engineering. For example, polythiophene's solution processability was imparted by the addition of alkyl side-chains to these backbones, yielding poly(3-alkyl thiophene) (P3AT). Indeed, poly(3-alkyl thiophene) (P3HT) is one of the most studied semiconducting polymers to date. The inclusion polar side chains with oligoether or ionic groups,[4–6] on the other hand, can promote dissolution of these hydrophobic-backbone polymers in polar organic solvents or aqueous media. These design strategies have expand the application of conjugated polymers to more advanced mixed ionic – electronic application such as in electrochemical and bio-interfacing devices.[7–9]

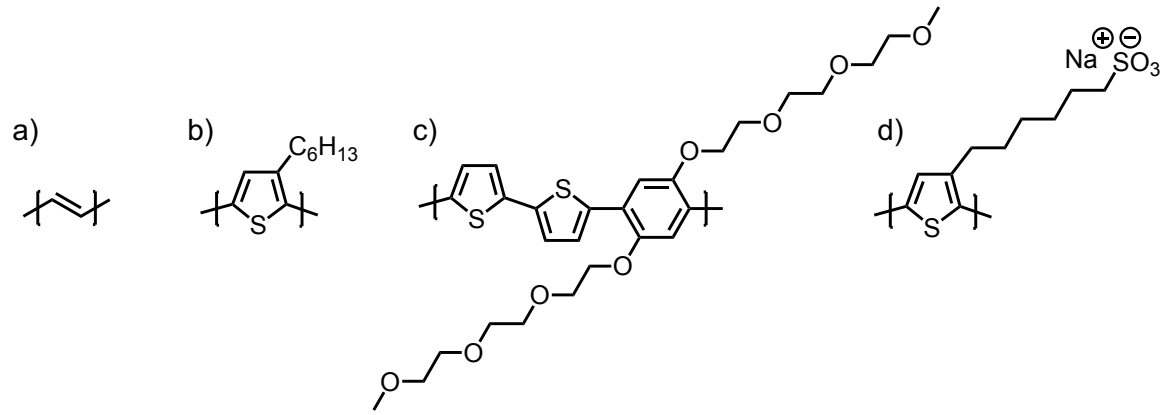

Figure 1.1 Chemical structures of (a) Polyacetylene (b) P3HT (c) poly[2,5-bis(thiophenyl)-1,4-bis(2-(2-(2-methoxyethoxy)ethoxy)ethoxy)benzene] and (d) poly[6-(thiophen-3-yl) hexane-1-sulfonate sodium]

1.2 Electronic structure and charge transport in semiconducting polymers

An important parameter that directly govern the optoelectronic performance of conjugated polymers is their band gap, or transport gap $E_{transport}$, defined as the energy different between the HOMO and LUMO energy levels.[10] Due to its dependence on the intramolecular interactions between molecular orbitals along the conjugated backbone, the band gap is highly tunable via modifications of the molecular architecture and chain conformation of conjugated polymers. Intermolecular interactions in solid-state can also modify single chain energy states, however these interactions are generally much weaker than intramolecular interactions.[11] As a result, band gap engineering has been mostly done via molecular design of the polymer's repeat unit, copolymerization of different conjugated structures, or post-polymerization functionalization.[12]

Another critical parameter of conjugated polymer is their optical gap E_{opt}, defined as the energy of the lowest electronic transition accessible via absorption of a single photon.[10] $E_{opt} \approx E_{transport}$ is most inorganic semiconductors, implying that free charge carriers can be generated with optical excitation. However, for organic semiconductors such as conjugated

polymers, the small dielectric constant ($\varepsilon \approx 2 - 5$) and the localized electron – electron and electron – phonon couplings lead to the formation of a bound electron – hole pair, called an exciton, upon photoexcitation.[13] The energy difference between E_{opt} and $E_{transport}$ is the binding energy E_b of the exciton, which is usually in the order of $\approx 0.5 - 1$ eV.[14] Both the transport gap and the optical gap are determinative factors in the fabrication and performance of many devices where organic semiconductors are employed, such as the photocurrent generation efficiency in organic photovoltaics or the photoluminescence quantum yield in organic light-emitting diodes.

Concentration of mobile charge carriers is very low in pristine conjugated polymers because they are neutral organic compounds. A process called doping is thus required to generate enough charge carriers to induce electrical conduction. It is noted that this process is different from doping in inorganic semiconductor, and indeed is simply a redox reaction between the polymer and the "dopant". Doping can be done by different methods, such as field-effect doping,[15] electrochemical doping,[16] or doping with a molecular dopant, which is the doping method utilized in this Dissertation. During molecular doping, the insulating neutral polymer is reduced (n-type) or oxidized (p-type) by the dopant, generating a free electron (n-type) or hole (p-type) accompanied by an counterion from the oxidized or reduced dopant molecule. Strong acids can also be used to protonate the backbone, which then subsequently reacts with neighboring chain segments to form charge carriers. However, understanding the exact mechanism on how this redox reaction happens between protonated chain and pristine chain remains an ongoing research effort. To ensure efficient doping of conjugated polymer, it is important to choose a polymer – dopant pair with proper energy levels alignment (**Figure**

1.2). p-type doping has been much more commonly studied than n-type doping due to the high HOMO level of most organic semiconductors (typically between 4.8 – 5.3 eV) that is well above the LUMO level of many molecular dopants.[17] Additionally, the high energy LUMO level of conjugated polymers makes the addition of an electron to this orbital highly unstable. Additions of electron-withdrawing functional groups to the repeat unit can lower the LUMO energy, but this strategy introduces significant challenges in the polymerization step.[18] As a result, the design and development of n-type polymeric semiconductor has faced many major limitations.

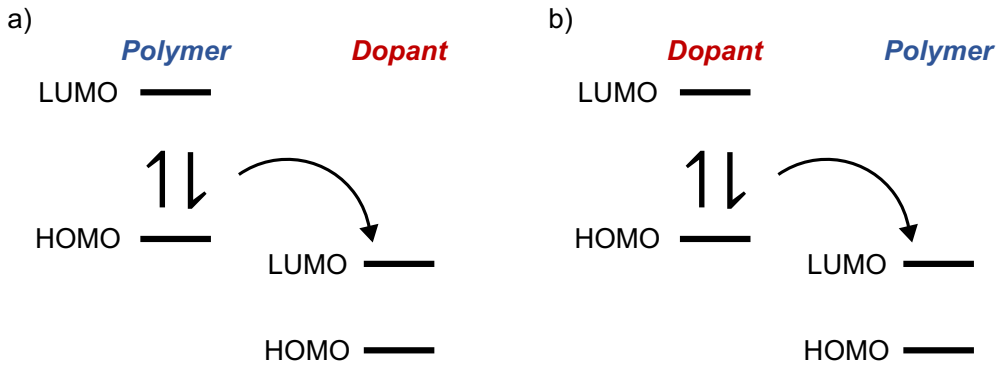

Figure 1.2. (a) p-type and (b) n-type doping of conjugated polymer

Transport of charge carriers (electrons in n-type and holes in p-type) is one of the most important processes when considering the utilization of conjugated polymers for an application. For most organic compounds, the weak intermolecular interactions do not maintain the coherence between adjacent molecules, so band-like transport is not possible. Transport in organic semiconductors is thus dominated by phonon-assisted hopping of charge carriers between adjacent sites. In conjugated polymers, charge carriers can delocalized coherently along the polymer backbone (intrachain transport) or hopping between neighboring chain segments (interchain transport). Intrachain transport is generally orders of magnitude faster than interchain hopping.[19] However, backbone structural defects such as torsions of

twists could break the conjugation of the electronic wavefunction, forming localized trapped states and significantly reducing carrier mobility. Due to the finite molecular weight of a polymer, transport in conjugated polymers is always limited by interchain hopping. On a larger length scale, macroscopic transport is limited by transport in the amorphous regions where interchain stackings are disrupted and charge carriers are more likely to encounter structural traps. As transport is more efficient within crystallites, for a long time improving the crystallinity and long-range order of conjugated polymers has been the main approach for optimizing charge transport in these systems. Many highly crystalline conjugated polymers have been synthesized with charge carrier mobility ranging between 0.01 – 0.1 $cm^2V^{-1}s^{-1}$.[20,21] However, recent reports on a new class of conjugated polymer whose backbone consists of electron donor and acceptor repeat units, commonly referred to as donor – acceptor (D-A) polymer, with high field-effect mobility (up to 10 $cm^2V^{-1}s^{-1}$) without long-range crystallinity have challenged this design rule.[22,23] It then has been shown that improving interconnectivity between intermolecular aggregates (which can be large polymer crystallites or local regions of as few as 2 chains overlapping) is critical in optimizing charge transport in conjugated polymers.[24,25]

1.3 Morphological complexities of conjugated polymers

The solid-state morphology of conjugated polymers is fundamentally complexed, with hierarchical heterogeneities. The electronic interactions between the planar conjugated backbones often results in their co-facial arrangement called π-π stacking. This π-π stacking is more commonly observed in polymers with regioregular (RR) backbones and/or more planar backbone repeat units. While these π-π stacks can persist over several nanometers and

form polymer crystallites, they can also form short-range aggregates that do not have any long-range translational order. Polymer chains can also form lamellar stack that are separated by their sidechains. An example of an idealized conjugated polymer crystalline stacking is shown in **Figure 1.3a** for P3HT. In reality, the side-chains have considerable freedom and are not confined to the backbone plane. Moreover, there is usually not much persistence of order across the π-π stacking direction. Added functionalities on the side-chain and variation in intrachain spacing of these side chains can also induce additional ordering. For example, interdigitated stacking of side chains has been reported for conjugated polymers with sparsely spaced oligoether side chains.[26] Lastly, most conjugated polymers are semicrystalline in nature, with regions of ordered crystallites coexisting with amorphous areas where the polymer chains coil up and do not co-align. At a larger length scale, ordered domains can be connected by tie molecules – the polymer chains that extend across the amorphous region and connect ordered crystallites/aggregates. These molecules are often high molecular weight chains so they can sufficiently span the intervening amorphous area. The ordered crystallites/aggregates can sometimes aligned isotropically or sharing a preferential orientation over a macroscopic distance.

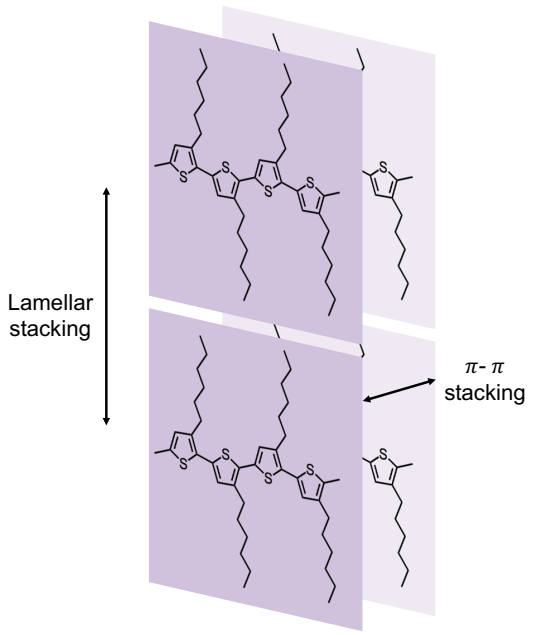

Figure 1.3 Packing of crystallite in semiconducting polymers, example shown for P3HT

Doping introduces charge carriers on the backbone that are compensated by a dopant counterions, ultimately disrupt the pristine state's intrachain ordering and solid-state morphology of semiconducting polymers. In particular, doping can affect chain conformation by introducing electrostatic and steric interactions.[11] Doping can also lead to changes in the crystalline regions of conjugated polymers, even though these effects are highly dependent on the polymer – dopant system. It has been shown that the counterions reside in the amorphous regions of a semicrystalline polymer at low doping level, but infiltrates the crystalline region at higher doping level.[27] Expansion of the side-chain stacks and the contraction of the π-π stacks within the polymer crystallites have been reported for various systems upon dopant infiltration.[27–30] Small and planar molecular dopants, such as 2,3,5,6-Tetrafluoro-7,7,8,8-tetracyanoquinodimethane (F4TCNQ), can co-crystallize with P3HT by intercalating between the π-stacked backbones.[31] Lastly, dopant-induced morphological changes are shown to be dependent on the doping method. Sequential doping, when the dopant is introduced after the

polymer films has been casted, usually results in less disruption to the morphology, especially the crystalline ordering, of the polymer than solution doping, when the polymer and the dopant are dissolved and casted from the same solution.[26,29]

Several characterization methods can be used to probe the structural ordering of semiconducting polymers across several length scales. High-resolution transmission electron microscopy (HR-TEM) has successfully captured down to single-chain resolution the stacking of conjugated polymers in the crystallite.[32] Conventional hard X-ray scattering can be used to probe the degree of crystallinity as well as crystallite size. Resonant soft X-ray scattering can be used to probe the long-range orientational correlation of the polymer crystallites.[33] Spectroscopy is another powerful set of techniques that can probe the local chain conformation, intermolecular aggregates, and the relative amount of crystalline and amorphous region within a sample.[34]

As discussed above, the hierarchical structures of conjugated polymers in the solid state directly govern their optoelectronic and transport performance.[35–42] As a result, significant efforts in improving the performance of conjugated polymers has been made by optimizing their solid-state self-assembly via molecular design or variation of processing conditions.[43–50]

1.4 Limited processability of conjugated polymers hinders their utilizations

Due to their high melting temperature and their tendency to aggregate in solution, conjugated polymers suffer from melt intractability and limited compatibility with most solvents. As previously mentioned, much effort has been made since the discovery of conductive doped

polyacetylene on improving the solubility of semiconducting polymers. However, there exists a trade-off between performance and processability, as the inclusion of the bulky solubilizing side-chains often results in disruption of the π–π interactions and compromise the optoelectronic properties of the backbone.[51] Moreover, most polymers are still processed at low concentration (typically ≈ 1 wt%), thus studies of these materials are mostly limited to thin film configurations. This significantly limits the understanding on other critical properties of conjugated polymers such as their thermal conductivity or mechanical properties since these measurements often require thick films or bulk samples. Additionally, the utilization of conjugated polymers in various applications is strictly hindered. For example, thick films are needed to maintain a large thermal gradients in thermoelectric modules; or the ability to fabricate bulk 3 dimensional structures is also a critical factor in free-form energy harvesting or wearable devices. Therefore, designs to increase or broaden the processability of conjugated polymers in parallel with optimizing their optoelectronic properties have been of longstanding interest.

1.5 Electrostatic assembly as a pathway to engineer advanced semiconducting polymers

Complex coacervation between 2 oppositely charged polyelectrolyte provides a viable strategy to improve the solvent compatibility of semiconducting polymers. Uncharged mixtures of dissimilar polymers are commonly immiscible over a full composition range due to the small entropy of mixing per unit volume, which scales as 1/N where N is the degree of polymerization of a chain, and a positive Flory–Huggins interaction parameter χ. However, intimate mixing between 2 oppositely charged polyelectrolytes is thermodynamically favorable due to the electrostatic attraction of charged groups. When solutions of 2 oppositely

charged polyelectrolytes are mixed at some certain conditions, associative liquid – liquid phase separation emerges, resulting in the formation of a polymer-dense fluid phase called the coacervate (typically 20 – 30 wt%) [52] coexisting in equilibrium with the polymer-depleted supernatant. The high polymer content in the coacervate and its liquid-like properties make it an attractive candidate for enabling solvent-lean processing of conjugated polymers.

The concept of complex coacervation was first introduced in 1929 and is the underlying co-assembly process in various natural and man-made materials. The widespread relevance of this material class has resulted in its utilization in many applications ranging from personal care products, biomedical applications, to the food industry. Remarkable progress has been made in developing fundamental understandings the thermodynamic phase behavior, dynamics and mechanical properties, and self-assembled structure [53] of complex coacervates. However, majority of the literature focuses on coacervation of colloids, proteins, surfactants, and non-conjugated polyelectrolytes.[54–59]

It is important to note that electrostatic assemblies have previously been utilized for conjugated polymers to improve their aqueous processability, such as the widely investigated interpolymer complexes of poly(3,4-ethylenedioxythiophene) with poly(styrenesulfonate) (PEDOT:PSS) or of polyaniline with poly(2-acryl amido-2-methyl-1-propanesulfonic acid) (PANI:PAAMPSA). However, this strategy is fundamentally different from the complex coacervation phenomenon. In particular, the conjugated monomers in this case are polymerized on the polymer acid templates, where the hydrophilic nature of the template forms a shell that stabilizes the hydrophobic conjugated core in water. Such a stabilization

pathway results in the formation of a polymer particle dispersion in water, and the structures of such primary particles are hierarchical, ill-defined, and sensitive to processing conditions. Moreover, the concentration of the electroactive material in these formulations is still similar to typical solutions of conjugated polymer in organic solvent. On the other hand, polyelectrolyte coacervation results in the intimate mixing of the two polymers in an electrostatically stabilized fluid or gel with high viscosity that can be tailored toward specific processing protocols.[60]

Studies on complex coacervate of conjugated polyelectrolytes are still limited and have been reported in a only few studies. In particular, a conjugated polymer coacervate was demonstrated for a blend of a polythiophene-based CPE with PSS.[61] Unlike traditional aqueous coacervate systems, the coacervate region emerged upon the addition of organic solvent. This observation suggests the critical role of solvent quality for the hydrophobic π-conjugated backbone in modulating the phase behavior of a conjugated coacervate, likely due to the strong intermolecular interactions between aromatic repeat units that are not present in nonconjugated systems. Interestingly, planarization of the CPE backbone that yields enhanced emissivity of the coacervate compared to the neat CPE solution was observed, indicating potentials of the complex coacervation process on the optoelectronic performance of the electroactive component. In another study, a gel coacervate phase was obtained by mixing a cationic semiflexible donor–acceptor CPE with PSS in aqueous media.[62] Although the phase behavior in this system more closely resembles that of conventional aqueous polyelectrolyte mixtures, the formation of small, liquid-like spherical coacervate droplets was not observed.

Instead, the polymer-rich coacervate phase had a colloidal gel structure with the gel modulus enhanced with added salt and the particle size diminished.

While some initial insights have been made on conjugated coacervates, early studies only assessed the solvated state of these polyelectrolyte complex systems. On the other hand, conjugated polymers are mostly utilized in solid-state devices. As a result, it is critical to examine the processing pathway for obtaining a solid film from conjugated coacervates. After solvent removal, the conjugated coacervate will transform into an ionically crosslinked polymer complex whose structure and properties remain largely unknown. Properties of conjugated polymers in solutions have been demonstrated to survive the casting process and be carried over to the solid state. Thus, investigating the optoelectronic properties of the solid polymer complex obtained from drying the coacervate will yield insights to how the characteristics of the solvated coacervate can inform the complex's solid state performance.

Lastly, evidence from theories and experiments has presented a breadth of electrostatic complexes of 2 distinct polymers. This suggests opportunities not only to improve the processability and the existing properties of conjugated polymers but also to introduce additional functionalities by leveraging ionic complexation. While investigation on charge-mediated complexation of polymers is dated back to ≈ 30 years ago,[63] it remains a largely unexplored topic in the semiconducting polymer research community. Further investigation of charged conjugated polymer complexes is required to develop a robust understanding on how electrostatic assembly can be leveraged toward the development of next generation semiconducting polymeric materials. This will enable the access to advanced processing

protocols and multifunctional applications where the potentials of semiconducting polymers have not yet been realized.

1.6 Thesis outline

The studies detailed in this dissertation aim to leverage electrostatic interactions to impart solvent-lean processability while controlling and optimizing the structure and properties of semiconducting polymers. Throughout this thesis, charge-mediated complexation between a CPE and an oppositely charged insulating polyelectrolyte was utilized, and the resulting dry polymer complexes were thoroughly investigated. Insights from findings in this Dissertation provide fundamental understanding on the structure – processing – property relations in this novel system of solid-state semiconductor and emphasize the potentials of electrostatic assembly in future developments of advanced semiconducting polymeric materials.

In the next chapter, the processability of a CPE – polymeric ionic liquid (PIL) coacervate is examined, and the solid-state optoelectronic performance of the solid film obtained from casting such coacervate is discussed. Chapter 3 and 4 utilize a model system of CPE – PIL random copolymers where the complexation strength can be controlled by varying the frequency of charged repeat units on the 2 polymers. In chapter 3, the impact of complexation strength on the mesoscopic structure of the CPE – PIL complex is examined. Chapter 4 details how the evolution of the material's structure with complexation strength affects the local structure and interconnectivity of the CPE chains within these complexes. Discussion on how these effect translate to the optoelectronic and transport properties of the material is provided. In chapter 5, realizing the great potential of ionic complexation in compatibilizing 2

chemically distinct polymers, we discuss how this pathway can be leveraged to obtain multifunctional electronic materials. A demonstration of a effectively mixed polymer complex that is soft, elastic, and conductive is provided.

The final chapter provides a short conclusions on what I have learned from the studies detailed in this thesis, and a brief discussion on the future directions that I think are necessary to effectively utilize electrostatic interactions in designing high-performing semiconducting polymers.

1.7 References

(1) Heeger, A. J. Semiconducting Polymers: The Third Generation. Chem. Soc. Rev. 2010, 39 (7), 2354–2371. https://doi.org/10.1039/b914956m.

(2) Clarke, T. M.; Durrant, J. R. Charge Photogeneration in Organic Solar Cells. Chem. Rev. 2010, 110 (11), 6736–6767. https://doi.org/10.1021/CR900271S/ASSET/IMAGES/MEDIUM/CR-2009-00271S_0001.GIF.

(3) Chiang, C. K.; Fincher, C. R.; Park, Y. W.; Heeger, A. J.; Shirakawa, H.; Louis, E. J.; Gau, S. C.; MacDiarmid, A. G. Electrical Conductivity in Doped Polyacetylene. Phys. Rev. Lett. 1977, 39 (17), 1098–1101. https://doi.org/10.1103/PHYSREVLETT.39.1098/FIGURE/1/THUMB.

(4) Dong, B. X.; Nowak, C.; Onorato, J. W.; Strzalka, J.; Escobedo, F. A.; Luscombe, C. K.; Nealey, P. F.; Patel, S. N. Influence of Side-Chain Chemistry on Structure and Ionic Conduction Characteristics of Polythiophene Derivatives: A Computational and Experimental Study. Chem. Mater. 2019, 31 (4), 1418–1429. https://doi.org/10.1021/acs.chemmater.8b05257.

(5) Flagg, L. Q.; Bischak, C. G.; Onorato, J. W.; Rashid, R. B.; Luscombe, C. K.; Ginger, D. S. Polymer Crystallinity Controls Water Uptake in Glycol Side-Chain Polymer Organic Electrochemical Transistors. J. Am. Chem. Soc. 2019, 141 (10), 4345–4354. https://doi.org/10.1021/jacs.8b12640.

(6) Lee, W.; Seo, J. H.; Woo, H. Y. Conjugated Polyelectrolytes: A New Class of Semiconducting Material for Organic Electronic Devices. Polymer (Guildf). 2013, 54 (19), 5104–5121. https://doi.org/10.1016/j.polymer.2013.07.015.

(7) McCuskey, S. R.; Su, Y.; Leifert, D.; Moreland, A. S.; Bazan, G. C. Living Bioelectrochemical Composites. Adv. Mater. 2020, 32 (24), 1908178. https://doi.org/10.1002/ADMA.201908178.

(8) Agee, A.; Pace, G.; Yang, V.; Segalman, R.; Furst, A.; Agee, A.; Yang, V.; Furst, A.;

Pace, G.; Segalman, R. Conductive Polymers to 'Wire' the Microbial Electronics Interface. 2023. https://doi.org/10.26434/CHEMRXIV-2023-DNQPD.

(9) Das, P.; Elizalde-Segovia, R.; Zayat, B.; Salamat, C. Z.; Pace, G.; Zhai, K.; Vincent, R. C.; Dunn, B. S.; Segalman, R. A.; Tolbert, S. H.; Narayan, S. R.; Thompson, B. C. Enhancing the Ionic Conductivity of Poly(3,4-Propylenedioxythiophenes) with Oligoether Side Chains for Use as Conductive Cathode Binders in Lithium-Ion Batteries. Chem. Mater. 2022, 34 (6), 2672–2686. https://doi.org/10.1021/ACS.CHEMMATER.1C03971/ASSET/IMAGES/LARGE/CM1C03971_0011.JPEG.

(10) Bredas, J. L. Mind the Gap! Mater. Horizons 2014, 1 (1), 17–19. https://doi.org/10.1039/c3mh00098b.

(11) Peterson, K. A.; Thomas, E. M.; Chabinyc, M. L. Thermoelectric Properties of Semiconducting Polymers. 2020. https://doi.org/10.1146/annurev-matsci-082219.

(12) Müllen, K.; Pisula, W. Donor-Acceptor Polymers. J. Am. Chem. Soc. 2015, 137 (30), 9503–9505. https://doi.org/10.1021/jacs.5b07015.

(13) Brédas, J. L.; Cornil, J.; Heeger, A. J. The Exciton Binding Energy in Luminescent Conjugated Polymers. Adv. Mater. 1996, 8 (5), 447–452. https://doi.org/10.1002/ADMA.19960080517.

(14) Bässler, H.; Köhler, A. Charge Transport in Organic Semiconductors. Top. Curr. Chem. 2012, 312 (5), 1–65. https://doi.org/10.1007/128_2011_218/FIGURES/25.

(15) Rawlings, D.; Thomas, E. M.; Segalman, R. A.; Chabinyc, M. L. Controlling the Doping Mechanism in Poly(3-Hexylthiophene) Thin-Film Transistors with Polymeric Ionic Liquid Dielectrics. Chem. Mater. 2019. https://doi.org/10.1021/acs.chemmater.9b02803.

(16) Rivnay, J.; Inal, S.; Salleo, A.; Owens, R. M.; Berggren, M.; Malliaras, G. G. Organic Electrochemical Transistors. Nat. Rev. Mater. 2018, 3. https://doi.org/10.1038/natrevmats.2017.86.

(17) Zaumseil, J.; Sirringhaus, H. Electron and Ambipolar Transport in Organic Field-Effect Transistors. Chem. Rev. 2007, 107 (4), 1296–1323. https://doi.org/10.1021/CR0501543/ASSET/IMAGES/LARGE/CR0501543F00024.JPEG.

(18) Jeong, M.-K.; Suh, E. H.; Lee, K.; Jang, J.; Jung, I. H. Acceptor-Acceptor-Type Conjugated Polymer for Use in n-Type Organic Thin-Film Transistors and Thermoelectric Devices. 2020. https://doi.org/10.1016/j.orgel.2020.105921.

(19) Noriega, R.; Salleo, A.; Spakowitz, A. J. Chain Conformations Dictate Multiscale Charge Transport Phenomena in Disordered Semiconducting Polymers. Proc. Natl. Acad. Sci. U. S. A. 2013, 110 (41), 16315–16320. https://doi.org/10.1073/pnas.1307158110.

(20) McCulloch, I.; Heeney, M.; Bailey, C.; Genevicius, K.; MacDonald, I.; Shkunov, M.; Sparrowe, D.; Tierney, S.; Wagner, R.; Zhang, W.; Chabinyc, M. L.; Kline, R. J.; McGehee, M. D.; Toney, M. F. Liquid-Crystalline Semiconducting Polymers with High Charge-Carrier Mobility. Nat. Mater. 2006 54 2006, 5 (4), 328–333. https://doi.org/10.1038/nmat1612.

(21) Bao, Z.; Dodabalapur, A.; Lovinger, A. J. Soluble and Processable Regioregular Poly(3-Hexylthiophene) for Thin Film Field-Effect Transistor Applications with High Mobility. Phys. Lett 1996, 69 (26).

(22) Noriega, R.; Rivnay, J.; Vandewal, K.; Koch, F. P. V.; Stingelin, N.; Smith, P.; Toney, M. F.; Salleo, A. A General Relationship between Disorder, Aggregation and Charge Transport in Conjugated Polymers. Nat. Mater. 2013, 12 (11), 1038–1044. https://doi.org/10.1038/nmat3722.
(23) Zhang, X.; Bronstein, H.; Kronemeijer, A. J.; Smith, J.; Kim, Y.; Kline, R. J.; Richter, L. J.; Anthopoulos, T. D.; Sirringhaus, H.; Song, K.; Heeney, M.; Zhang, W.; McCulloch, I.; Delongchamp, D. M. Molecular Origin of High Field-Effect Mobility in an Indacenodithiophene-Benzothiadiazole Copolymer. Nat. Commun. 2013, 4. https://doi.org/10.1038/NCOMMS3238.
(24) Wang, S.; Fabiano, S.; Himmelberger, S.; Puzinas, S.; Crispin, X.; Salleo, A.; Berggren, M. Experimental Evidence That Short-Range Intermolecular Aggregation Is Sufficient for Efficient Charge Transport in Conjugated Polymers. Proc. Natl. Acad. Sci. U. S. A. 2015, 112 (34), 10599–10604. https://doi.org/10.1073/pnas.1501381112.
(25) Patel, S. N.; Glaudell, A. M.; Peterson, K. A.; Thomas, E. M.; O'Hara, K. A.; Lim, E.; Chabinyc, M. L. Morphology Controls the Thermoelectric Power Factor of a Doped Semiconducting Polymer. Sci. Adv. 2017, 3 (6). https://doi.org/10.1126/sciadv.1700434.
(26) Bischak, C. G.; Flagg, L. Q.; Yan, K.; Rehman, T.; Davies, D. W.; Quezada, R. J.; Onorato, J. W.; Luscombe, C. K.; Diao, Y.; Li, C. Z.; Ginger, D. S. A Reversible Structural Phase Transition by Electrochemically-Driven Ion Injection into a Conjugated Polymer. J. Am. Chem. Soc. 2020, 142 (16), 7434–7442. https://doi.org/10.1021/jacs.9b12769.
(27) Thomas, E. M.; Brady, M. A.; Nakayama, H.; Popere, B. C.; Segalman, R. A.; Chabinyc, M. L. X-Ray Scattering Reveals Ion-Induced Microstructural Changes During Electrochemical Gating of Poly(3-Hexylthiophene). Adv. Funct. Mater. 2018, 28 (44), 1–8. https://doi.org/10.1002/adfm.201803687.
(28) Lim, E.; Peterson, K. A.; Su, G. M.; Chabinyc, M. L. Thermoelectric Properties of Poly(3-Hexylthiophene) (P3HT) Doped with 2,3,5,6-Tetrafluoro-7,7,8,8-Tetracyanoquinodimethane (F4TCNQ) by Vapor-Phase Infiltration. Chem. Mater. 2018, 30 (3), 998–1010. https://doi.org/10.1021/acs.chemmater.7b04849.
(29) Patel, S. N.; Glaudell, A. M.; Kiefer, D.; Chabinyc, M. L. Increasing the Thermoelectric Power Factor of a Semiconducting Polymer by Doping from the Vapor Phase. ACS Macro Lett. 2016, 5 (3), 268–272. https://doi.org/10.1021/acsmacrolett.5b00887.
(30) Tashiro, K.; Kobayashi, M.; Kawai, T.; Yoshino, K. Crystal Structural Change in Poly(3-Alkyl Thiophene)s Induced by Iodine Doping as Studied by an Organized Combination of X-Ray Diffraction, Infrared/Raman Spectroscopy and Computer Simulation Techniques. Polymer (Guildf). 1997, 38 (12), 2867–2879. https://doi.org/10.1016/S0032-3861(96)00876-2.
(31) Méndez, H.; Heimel, G.; Winkler, S.; Frisch, J.; Opitz, A.; Sauer, K.; Wegner, B.; Oehzelt, M.; Röthel, C.; Duhm, S.; Többens, D.; Koch, N.; Salzmann, I. Charge-Transfer Crystallites as Molecular Electrical Dopants. Nat. Commun. 2015, 6. https://doi.org/10.1038/ncomms9560.
(32) Kuei, B.; Gomez, E. D. Pushing the Limits of High-Resolution Polymer Microscopy Using Antioxidants. Nat. Commun. 2021 121 2021, 12 (1), 1–7. https://doi.org/10.1038/s41467-020-20363-1.
(33) Collins, B. A.; Cochran, J. E.; Yan, H.; Gann, E.; Hub, C.; Fink, R.; Wang, C.;

Schuettfort, T.; McNeill, C. R.; Chabinyc, M. L.; Ade, H. Polarized X-Ray Scattering Reveals Non-Crystalline Orientational Ordering in Organic Films. Nat. Mater. 2012, 11 (6), 536–543. https://doi.org/10.1038/nmat3310.

(34) Spano, F. C. Modeling Disorder in Polymer Aggregates: The Optical Spectroscopy of Regioregular Poly(3-Hexylthiophene) Thin Films. J. Chem. Phys. 2005, 122 (23), 234701. https://doi.org/10.1063/1.1914768.

(35) O'Connor, B.; Kline, R. J.; Conrad, B. R.; Richter, L. J.; Gundlach, D.; Toney, M. F.; DeLongchamp, D. M. Anisotropic Structure and Charge Transport in Highly Strain-Aligned Regioregular Poly(3-Hexylthiophene). Adv. Funct. Mater. 2011, 21 (19), 3697–3705. https://doi.org/10.1002/adfm.201100904.

(36) Patel, S. N.; Glaudell, A. M.; Peterson, K. A.; Thomas, E. M.; O'Hara, K. A.; Lim, E.; Chabinyc, M. L. Morphology Controls the Thermoelectric Power Factor of a Doped Semiconducting Polymer. Sci. Adv. 2017, 3 (6). https://doi.org/10.1126/sciadv.1700434.

(37) Panzer, F.; Bässler, H.; Köhler, A. Temperature Induced Order-Disorder Transition in Solutions of Conjugated Polymers Probed by Optical Spectroscopy. J. Phys. Chem. Lett. 2017, 8 (1), 114–125. https://doi.org/10.1021/acs.jpclett.6b01641.

(38) Noriega, R.; Rivnay, J.; Vandewal, K.; Koch, F. P. V.; Stingelin, N.; Smith, P.; Toney, M. F.; Salleo, A. A General Relationship between Disorder, Aggregation and Charge Transport in Conjugated Polymers. Nat. Mater. 2013, 12 (11), 1038–1044. https://doi.org/10.1038/nmat3722.

(39) Persson, N. E.; Chu, P. H.; McBride, M.; Grover, M.; Reichmanis, E. Nucleation, Growth, and Alignment of Poly(3-Hexylthiophene) Nanofibers for High-Performance OFETs. Acc. Chem. Res. 2017, 50 (4), 932–942. https://doi.org/10.1021/acs.accounts.6b00639.

(40) Lim, E.; Glaudell, A. M.; Miller, R.; Chabinyc, M. L. The Role of Ordering on the Thermoelectric Properties of Blends of Regioregular and Regiorandom Poly(3-Hexylthiophene). Adv. Electron. Mater. 2019, 5 (11), 1800915. https://doi.org/10.1002/aelm.201800915.

(41) Botiz, I.; Durbin, M. M.; Stingelin, N. Providing a Window into the Phase Behavior of Semiconducting Polymers. Macromolecules 2021, 54 (12), 5304–5320. https://doi.org/10.1021/acs.macromol.1c00296.

(42) McCulloch, I.; Heeney, M.; Bailey, C.; Genevicius, K.; MacDonald, I.; Shkunov, M.; Sparrowe, D.; Tierney, S.; Wagner, R.; Zhang, W.; Chabinyc, M. L.; Kline, R. J.; McGehee, M. D.; Toney, M. F. Liquid-Crystalline Semiconducting Polymers with High Charge-Carrier Mobility. Nat. Mater. 2006, 5 (4), 328–333. https://doi.org/10.1038/nmat1612.

(43) Paquin, F.; Yamagata, H.; Hestand, N. J.; Sakowicz, M.; Bérubé, N.; Côté, M.; Reynolds, L. X.; Haque, S. A.; Stingelin, N.; Spano, F. C.; Silva, C. Two-Dimensional Spatial Coherence of Excitons in Semicrystalline Polymeric Semiconductors: Effect of Molecular Weight. Phys. Rev. B - Condens. Matter Mater. Phys. 2013, 88 (15), 155202. https://doi.org/10.1103/PhysRevB.88.155202.

(44) Scharsich, C.; Lohwasser, R. H.; Sommer, M.; Asawapirom, U.; Scherf, U.; Thelakkat, M.; Neher, D.; Köhler, A. Control of Aggregate Formation in Poly(3-Hexylthiophene) by Solvent, Molecular Weight, and Synthetic Method. J. Polym. Sci. Part B Polym. Phys. 2012, 50 (6), 442–453. https://doi.org/10.1002/polb.23022.

(45) Kline, R. J.; McGehee, M. D.; Kadnikova, E. N.; Liu, J.; Fréchet, J. M. J.; Toney, M. F. Dependence of Regioregular Poly(3-Hexylthiophene) Film Morphology and Field-Effect Mobility on Molecular Weight. Macromolecules 2005, 38 (8), 3312–3319. https://doi.org/10.1021/ma047415f.
(46) Koch, F. P. V.; Rivnay, J.; Foster, S.; Müller, C.; Downing, J. M.; Buchaca-Domingo, E.; Westacott, P.; Yu, L.; Yuan, M.; Baklar, M.; Fei, Z.; Luscombe, C.; McLachlan, M. A.; Heeney, M.; Rumbles, G.; Silva, C.; Salleo, A.; Nelson, J.; Smith, P.; Stingelin, N. The Impact of Molecular Weight on Microstructure and Charge Transport in Semicrystalline Polymer Semiconductors-Poly(3-Hexylthiophene), a Model Study. Prog. Polym. Sci. 2013, 38 (12), 1978–1989. https://doi.org/10.1016/j.progpolymsci.2013.07.009.
(47) Choi, D.; Chang, M.; Reichmanis, E. Controlled Assembly of Poly(3-Hexylthiophene): Managing the Disorder to Order Transition on the Nano- through Meso-Scales. Adv. Funct. Mater. 2015, 25 (6), 920–927. https://doi.org/10.1002/adfm.201403708.
(48) Diao, Y.; Shaw, L.; Bao, Z.; Mannsfeld, S. C. B. Morphology Control Strategies for Solution-Processed Organic Semiconductor Thin Films. Energy Environ. Sci. 2014, 7 (7), 2145–2159. https://doi.org/10.1039/c4ee00688g.
(49) Sirringhaus, H.; Brown, P. J.; Friend, R. H.; Nielsen, M. M.; Bechgaard, K.; Langeveld-Voss, B. M. W.; Spiering, A. J. H.; Janssen, R. A. J.; Meijer, E. W.; Herwig, P.; De Leeuw, D. M. Two-Dimensional Charge Transport in Self-Organized, High-Mobility Conjugated Polymers. Nature 1999, 401 (6754), 685–688. https://doi.org/10.1038/44359.
(50) Crossland, E. J. W.; Rahimi, K.; Reiter, G.; Steiner, U.; Ludwigs, S. Systematic Control of Nucleation Density in Poly(3-Hexylthiophene) Thin Films. Adv. Funct. Mater. 2011, 21 (3), 518–524. https://doi.org/10.1002/adfm.201001682.
(51) Ponder, J. F.; Gregory, S. A.; Atassi, A.; Menon, A. K.; Lang, A. W.; Savagian, L. R.; Reynolds, J. R.; Yee, S. K. Significant Enhancement of the Electrical Conductivity of Conjugated Polymers by Post-Processing Side Chain Removal. J. Am. Chem. Soc. 2022, 144 (3), 1351–1360. https://doi.org/10.1021/JACS.1C11558/ASSET/IMAGES/LARGE/JA1C11558_0005.JPEG.
(52) Bungenberg de Jong, H. G.; Kruyt, H. R. Coacervation (Partial Miscibility in Colloid Systems). Proc.Acad.Sci Amsterdam 1929, 32 (1927), 849–856.
(53) Sing, C. E.; Perry, S. L. Recent Progress in the Science of Complex Coacervation. Soft Matter 2020, 16 (12), 2885–2914. https://doi.org/10.1039/d0sm00001a.
(54) Laaser, J. E.; McGovern, M.; Jiang, Y.; Lohmann, E.; Reineke, T. M.; Morse, D. C.; Dorfman, K. D.; Lodge, T. P. Equilibration of Micelle-Polyelectrolyte Complexes: Mechanistic Differences between Static and Annealed Charge Distributions. J. Phys. Chem. B 2017, 121 (17), 4631–4641. https://doi.org/10.1021/ACS.JPCB.7B01953/ASSET/IMAGES/LARGE/JP-2017-01953P_0007.JPEG.
(55) Kizilay, E.; Kayitmazer, A. B.; Dubin, P. L. Complexation and Coacervation of Polyelectrolytes with Oppositely Charged Colloids. Adv. Colloid Interface Sci. 2011, 167 (1–2), 24–37. https://doi.org/10.1016/J.CIS.2011.06.006.
(56) De Kruif, C. G.; Weinbreck, F.; De Vries, R. Complex Coacervation of Proteins and Anionic Polysaccharides. Curr. Opin. Colloid Interface Sci. 2004, 9 (5), 340–349.

https://doi.org/10.1016/J.COCIS.2004.09.006.
(57) Cooper, C. L.; Dubin, P. L.; Kayitmazer, A. B.; Turksen, S. Polyelectrolyte–Protein Complexes. Curr. Opin. Colloid Interface Sci. 2005, 10 (1–2), 52–78. https://doi.org/10.1016/J.COCIS.2005.05.007.
(58) Welch, P.; Muthukumar, M. Dendrimer−Polyelectrolyte Complexation: A Model Guest−Host System. Macromolecules 2000, 33 (16), 6159–6167. https://doi.org/10.1021/MA000021D.
(59) Gucht, J. van der; Spruijt, E.; Lemmers, M.; Cohen Stuart, M. A. Polyelectrolyte Complexes: Bulk Phases and Colloidal Systems. J. Colloid Interface Sci. 2011, 361 (2), 407–422. https://doi.org/10.1016/J.JCIS.2011.05.080.
(60) Wang, Q.; Schlenoff, J. B. The Polyelectrolyte Complex/Coacervate Continuum. Macromolecules 2014, 47 (9), 3108–3116. https://doi.org/10.1021/ma500500q.
(61) Danielsen, S. P. O.; Nguyen, T. Q.; Fredrickson, G. H.; Segalman, R. A. Complexation of a Conjugated Polyelectrolyte and Impact on Optoelectronic Properties. ACS Macro Lett. 2019, 8 (1), 88–94. https://doi.org/10.1021/acsmacrolett.8b00924.
(62) Johnston, A. R.; Perry, S. L.; Ayzner, A. L. Associative Phase Separation of Aqueous π-Conjugated Polyelectrolytes Couples Photophysical and Mechanical Properties. Chem. Mater. 2021, 33 (4), 1116–1129. https://doi.org/10.1021/acs.chemmater.0c02424.
(63) Eisenberg, A.; Smith, P.; Zhou, Z. -L. Compatibilization of the Polystyrene/Poly(Ethyl Acrylate) and Polystyrene/Polysoprene Systems through Ionic Interactions. Polym. Eng. Sci. 1982, 22 (17), 1117–1122. https://doi.org/10.1002/PEN.760221711.

Chapter 2

Aqueous Formulation of Concentrated Semiconductive Fluid Using Polyelectrolyte Coacervation

This chapter is reproduced with permission from:

Le, M. L., Rawlings, D., Danielsen, S. P. O., Kennard, R., Chabinyc, M. L., Segalman, R. A. Aqueous Formulation of Concentrated Semiconductive Fluid Using Polyelectrolyte Coacervation. *ACS Macro Lett.* **2021**, 10, 8, 1008–1014. DOI: 10.1021/acsmacrolett.1c00354

2.1 Abstract

Conjugated polyelectrolytes (CPEs), which combine πconjugated backbones with ionic side chains, are intrinsically soluble in polar solvents and have demonstrated tunability with respect to solution processability and optoelectronic performance. However, this class of polymers often suffers from limited solubility in water. Here, we demonstrate how polyelectrolyte coacervation can be utilized for aqueous processing of conjugated polymers at extremely high polymer loading. Sampling various mixing conditions, we identify compositions that enable the formation of complex coacervates of an alkoxysulfonatesubstituted PEDOT (PEDOT-S) with poly(3-methyl-1 propylimidazolylacrylamide) (PA-MPI). The resulting coacervate is a viscous fluid containing 50% w/v polymer and can be readily blade-coated into films of 4 ± 0.5 μm thick. Subsequent acid doping of the film increased the electrical conductivity of the coacervate to twice that of a doped film of neat PEDOT-S. This higher conductivity of the doped coacervate film suggests an enhancement in charge carrier transport along PEDOT-S backbone, in

agreement with spectroscopic data, which shows an enhancement in the conjugation length of PEDOT-S upon coacervation. This study illustrates the utilization of electrostatic interactions in aqueous processing of conjugated polymers, which will be useful in large-scale industrial processing of semiconductive materials using limited solvent and with added enhancements to optoelectronic properties

2.2 Introduction

Aqueous formulation of conjugated polymers enables environmentally benign processing routes, fabrication of multi-layer devices *via* deposition from varying solvents, and bioelectronic applications.[1] Enhanced dissolution of conjugated polymers in water can be achieved by ionic functionalization of side chains that compensate for the hydrophobicity of the π-conjugated backbone. This class of materials, conjugated polyelectrolytes (CPEs),[2] offers orthogonal control of the material's optoelectronic properties and aqueous processability. Nonetheless, the limited solubility of CPEs in water often inhibits the ability to make concentrated solutions that are desirable for many applications.

Complexation with polyelectrolytes offers a promising route to improve the aqueous solubility of CPEs. Mixing two oppositely charged polyelectrolytes can result in formulations with much higher concentrations than simple solutions of polymers and solvents.[3] Intimate mixing of two polyelectrolytes is thermodynamically favorable because of the electrostatic attraction of charged groups, in contrast to the common immiscibility of uncharged polymers that results from a high Flory–Huggins interaction parameter χ. In certain conditions, mixing of two polyelectrolytes results in an associative liquid–liquid phase separation in which a

polymer-depleted phase, the supernatant, is in coexistence with a polymer-dense phase (typically 20-30% *w/v* polymer) called the coacervate.[4] The fluid nature of the coacervate suggests its potential compatibility with industrial processing protocols such as blade coating and gravure printing.[5] Polyelectrolyte coacervation is important to several biological processes including the formation of membraneless organelles [6,7] and underwater adhesives, [8,9] and has been widely proposed for new biotechnologies.[10–12] Since the first observation of coacervation almost a century ago,[4,13] much effort has been devoted to elucidating a general theoretical thermodynamic framework, phase behavior, dynamics and mechanics, and self-assembled structure of polyelectrolyte complex coacervates.[15–27]

Despite this large body of literature on non-conjugated polyelectrolytes, coacervation has only been reported in a few conjugated polymer systems.[3,27] For example, the coacervation between a polythiophene-based CPE and an insulating polyelectrolyte in THF/water solvent mixtures has been shown to increase the CPE's conjugation length and photoluminescence yield.[3] CPE–polyelectrolyte coacervation was also reported to occur in aqueous high-salt media, with the mixture's phase behavior and photophysical properties showing a strong dependence on the identity of the cation salt.[27] Studies on CPE-CPE complexation in salt-free water,[28,29] focusing on dilute regimes and the solid-state complexes, have further elucidated how the inclusion of the conjugated moieties fundamentally affects complexation thermodynamics. Similar to the CPE–polyelectrolyte coacervate, complexation of two CPEs in the dilute regime was shown to induce extension and planarization of the CPE backbone. Lastly, a study on the complexation between a di-block(neutral conjugated polymer-CPE) and DNA in dilute environments points out that the microstructure of the complex and the photophysical

properties of the conjugated components could be tunned via modification of the polycation-polyanion mixing ratio.[30] Together, these studies demonstrate that polyelectrolyte complexation can be utilized as a highly versatile self-assembly motif to formulate dense coacervates of CPEs with beneficial changes in optoelectronic performance.

Prior studies have only focused on conjugated polymer complexes in the solvated state, while many electronic applications require the use of the conjugated material in the form of solvent-free solid. Thus, it is crucial to investigate processing routes for obtaining solid films from the CPE coacervate and the impacts that coacervation might have on the material's solid-state properties. Understanding these formulation—processing–property relationships will not only allow us to evaluate the properties of the solid polymer blend obtained by drying the coacervate, but also assess the practicality of this self-assembly pathway for processing of high concentration conjugated polymer solutions for use in optoelectronic devices.

Herein, we show that the aqueous coacervation between a CPE and an oppositely charged polymerized ionic liquid (PIL), an analogy to polyelectrolytes but with larger and more diffusive ionic sidechains, can be used to obtain a concentrated functional fluid of 50% *w/v* polymer. This viscous fluid was blade coated and dried to form a homogeneous solid film of μm-scale thickness. Spectroscopy and conductivity measurements of the film cast from the coacervate indicate that coacervation enhanced the conjugated length in both solvated and solid states of the CPE and, as a result, increased the charge carrier mobility along the conjugated backbone. This study suggests that polymer–polymer coacervation is a viable route for formulation of a highly concentrated semiconductive fluid phase that can be casted into solid films with enhanced optoelectronic properties.

2.3 Experimental Methods

PEDOT-S synthesis: (2,3-Dihydrothieno[3,4-b][1,4]dioxin-2-yl)methanol (EDOT-OH) was purchased from Sigma-Aldrich. The conversion of EDOT-OH to 4-(2,3-dihydrothieno [3,4-b][1,4]dioxin-2-yl-meth-oxy)-l-butanesulfonic acid, sodium salt (EDOT-S) monomer was carried out using a previously described procedure.[31]

H^1 NMR (600 MHz) in D2O: 6.42 (2H, s); 4.34 (1H, m); 4.20 (1H,m): 4.00 (1H, m); 3.65 (2H, m); 3.52 (2H, m); 2.83 (2H, t); 1.69 (2H, m); 1.61 (2H, m).

MS (ESI) m/z calculated for $C_{11}H_{15}O_6S_2Na$: 330.3; found: 307.0 $(M-Na)^-$

In a dry round bottom flask, EDOT-S (0.7 g, 2.1 mmol) and 3.3 equiv of anhydrous iron(III) chloride were mixed in 50 mL of anhydrous chloroform. The mixture was stirred vigorously under nitrogen atmosphere at room temperature for 24 hours. A few drops of hydrazine solution (35 %wt in H_2O) was added to the mixture at the end of the reaction, and the solution then poured into 250 mL of methanol. This mixture was then centrifuged at 3500 rpm for 5 minutes, and the dark precipitate was stirred in a solution of 50 mL sodium hydroxide in methanol for 1 day to exchange the iron ions for sodium. The solution was centrifuged again, and the collected black polymer powder was dissolved in deionized water. This polymer solution was dialyzed against deionized water for 3 days using a 10 000 g/mol cutoff membrane, and the water was exchanged every 12 hours. The polymer was freeze-dried to obtain 0.5g (71.4 % yield) black powder. Water GPC with PSS standard was used to determine the MW of PEDOT-S: M_n = 16.7 kDa, M_w = 32.6 kDa, PDI = 1.95

PA-MPI synthesis PA-MPI was synthesized according to a previously described procedure in literature.[32] H NMR end-group analysis in deuterated methanol was used to determine the M_n of the polymer, yielding a M_n of 13.0 kDa.

Materials Characterization: 1H NMR spectra were recorded at 600 MHz (Varian VNMRS). Chemical shifts are reported in ppm referenced to residual solvent peaks. Mass spectroscopy was performed using Electrospray ionization (ESI) methods on a Waters LCT Premier ESI TOF mass spectrometer. Gel permeation chromatography (GPC) was performed using a Waters system (Waters Alliance HPLC 2695) with a Tosoh TSKgel G3000PWXL (7um) and a TSKgel G5000PWXL (10um) columns. This system used a refractive index (Waters 2414) and a photodiode array (Waters 2998) detectors. Milli-Q Water with 0.1M $NaNO_3$ (pH 7) at 25°C was used as the mobile phase with a flow rate of 1 mL min^{-1}.

XPS analysis: Experiments were performed using an Escalab Xi+ Spectrometer (ThermoFisher Scientific) with a monochromatic aluminum Kα X-ray source under a vacuum of ~ 5 x 10^{-9} mbar. Charge compensation was carried out using a dual ion-electron low-energy flood source. High-resolution spectra were recorded at 20 eV pass energy at intervals of 0.05 eV. Survey spectra were recorded at 100 eV pass energy at intervals of 0.5 eV. Depth profiling was completed with a monatomic Ar source with a beam energy of 2 kV and a raster size of 1.5 mm.

UV-Vis Absorption spectra: were collected using an Agilent Cary 60 UV-vis Spectrophotometer. Wet samples were sandwiched between 2 quartz slides with a Kapton spacer. Solid-state samples were used as casted.

X-ray Characterization: Grazing Incident Wide Angle X-ray Scattering (GIWAXS) was conducted on beamline 11-BM at the Brookhaven National Laboratory (NSLS-II). Silver behenate was used as a calibration for determination of the beam center and the sample-to-detector distance. An incidence angle of 0.1° with 5-10 s exposure times were used.

Construction of PEDOT-S:PA-MPI phase diagram: Solutions of PEDOT-S and PA-MPI were mixed in charge stoichiometric ratio. Aqueous KBr solutions were used as the solvent, and the dielectric medium was tuned by varying the concentration of salt. To prevent the self-doping of PEDOT-S in the mildly acidic condition of milli-Q water[33] prior to mixing, 3.5 wt% hydrazine was added to all PEDOT-S solutions. Mixing was done on a glass microscope slide using a total volume of 20 μL of solutions. A cover slip was then put over the glass slide, and the mixture was looked under an Olympus BX51 optical microscope in bright-field mode for determination of phases. Images were calibrated with StreamView (Olympus). All mixing experiments were carried out in ambient temperature, which is expected to stay relatively constant at 25°C

Coacervate Film Casting Procedure: 100μL solutions of 100 mM PEDOT-S and PA-MPI in 500 mM KBr were added to a 500 μL Eppendorf tube. The tube was vortexed for 1 minute to ensure even mixing. The mixture was then centrifuged at 7000 rpm for 5 minutes to promote

complete coalescence of the coacervate droplets. The supernatant phase was then decanted, and the coacervate was scooped out of the tube using a plastic spatula. This coacervate was transferred to a flat substrate, and a square frame applicator with a gap height of 635μm was glided at a speed of 10 mm/s across the substrate. Upon drying, the film was immersed in 50 mL of milli-Q water overnight for removal of KBr salt ions. The film was then heated at 50°C in nitrogen atmosphere for 30 minutes, and further dried under high vacuum for 12 hours before being immediately transferred to a glovebox.

Film Characterization: Film thickness was measured using a Bruker DektakXT Stylus profilometer. The morphology of the film was characterized using an FEI Nova Nano FEG scanning electron microscopy operating at 5 kV accelerating voltage with beam currents of 0.40-0.80 nA. Coacervate film was sputter-coated with gold prior to SEM measurement to prevent charging.

Vapor Doping: All doping experiments were carried out inside a glovebox under nitrogen atmosphere. HTFSI crystals were placed inside a clean glass jar, and the pristine polymer film was attached to the jar lid using double sided Kapton tape. The far was closed tightly and heated at 50°C for certain exposure times on a hot plate. For the coacervate film, the film was transferred to another closed clean glass jar and annealed at 60°C over the course of 24 hours to promote efficient diffusion of dopants into the film and to prevent leakage of dopant vapor. Eventually the film was quenched at 25°C for 30 minutes prior to characterization.

Conductivity Measurements: 15 mg/mL solution of PEDOT-S in water was spun cast on gold coated quartz substrate to make neat CPE conductivity samples. Chromium (3 nm) and gold (40 nm) contacts were thermally evaporated on coacervate-coated quartz substrates using a shadow mask to make coacervate conductivity samples. Transmission line measurements were carried out in the in-plane direction using a Keithley 6485 picoammeter. For fully doped coacervate film, impedance measurements were carried out using a Biologic VSP-300 potentiostat.

2.4 Results and Discussion

A CPE:PIL model system was designed to achieve highly tunable ionic interactions between two polymers and to facilitate the doping of the CPE component. An alkyl sulfonate derivative of poly(3,4-ethylenedioxythiophene) with sodium counter-ions (PEDOT-S, **Figure 2.1**) was chosen as the CPE. The dioxane ring has been shown to donate electron density to the thiophene ring and thus lowers the band gap and the oxidation potential of EDOT-based polymers relative to polythiophenes.[34,35] Moreover, the oxygen atoms on the dioxane ring give PEDOT-S the capability to accept hydrogen bonds, enhancing the polymer solubility in water. For the PIL, a polyacrylamide backbone with methyl-imidazolium functionalized side chains and iodine counter-ions was used (PA-MPI, **Figure 2.1**). The wide electrochemical stability window of the imidazolium group [36] allows it to remain stable upon electrical doping of the CPE coacervate. PEDOT-S and PA-MPI polymers were obtained *via* oxidative polymerization and reversible addition-fragmentation chain transfer polymerizations (**Figure S2.1** and **S2.2**). The number-average molecular weights are 16 kDa for PEDOT-S (relative to a Bovine Serum Albumin (BSA) standard in aqueous Gel-Permeation Chromatography) and

13 kDa for PA-MPI (obtained *via* NMR end group analysis). We note that PEDOT-S has a high dispersity (Đ=1.95 relative to PSS standard) due to the nature of oxidative polymerization.

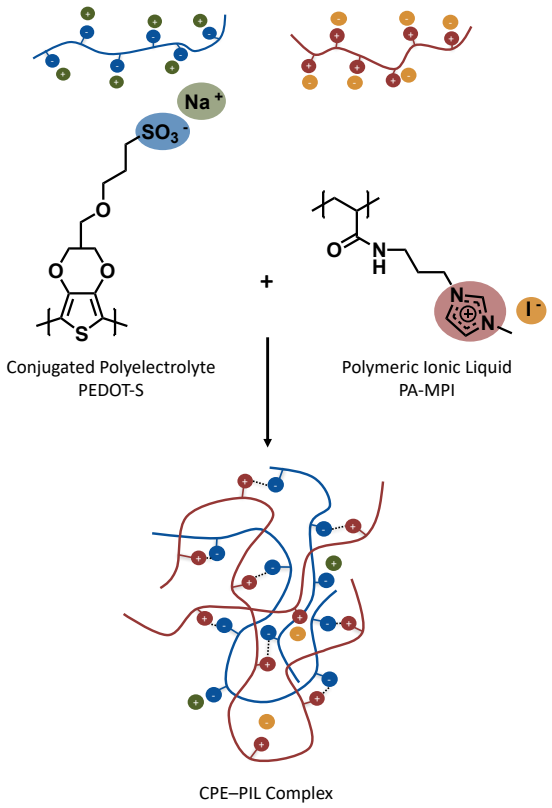

Figure 2.1. Chemical structures of PA-MPI (polycation) and PEDOT-S (polyanion) and their formation of a polyelectrolyte complex upon mixing.

The phase behavior of the CPE:PIL complex, which was examined by varying the concentration aqueous KBr solvent and the concentration of the polymers in the stock solutions, shows a wide coacervate window that stretches across a broad region of the phase diagram (**Figure 2.2**). In particular, the coexistence of the coacervate and the supernatant was absent only in the diagram's top-left and the bottom-right corners. In the high-salt-low-polymer region (top-left), the strong electrostatic screening from the added ionic strength suppresses the charge-mediated complexation between the CPE and the PIL. As a result, only

1-phase solutions form in these conditions. In the low-salt-high-polymer region (bottom-right), the strong electrostatic interactions trap the complex structure to form a dense complex. This phase is commonly referred to as the precipitate.[37] Due to its solid-like nature, the precipitate is much more challenging to process than the coacervate. The CPE:PIL coacervate was observed in the rest of the phase diagram, covering the majority of the mixing conditions where the balance between ionic screening and kinetics was maintained. The PEDOT-S:PA-MPI phase diagram therefore suggests the processability of the complex across a wide range of accessible compositions.

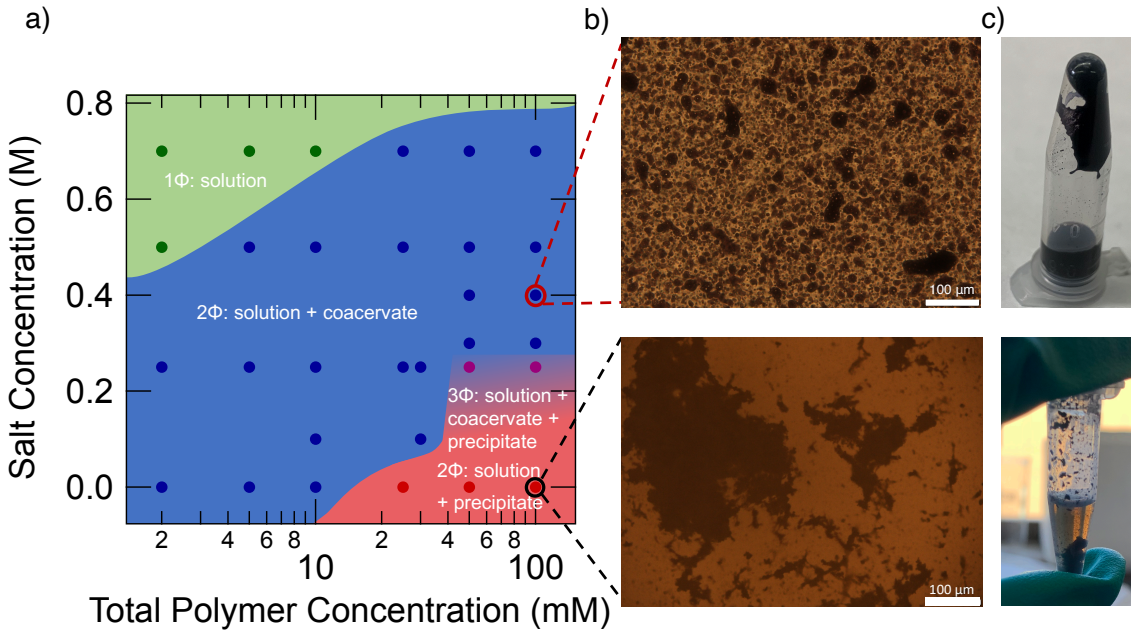

Figure 2.2 (a) Phase diagram of PEDOT-S and PA-MPI as a function of solvent KBr concentration and total polymer concentration. The coacervate–solution coexistence region covers the majority of the accessible phase diagram. At high polymer concentrations and intermediate ionic strength (~0.25M KBr solution), there was a crossover "three phase" region in which both the coacervate and the precipitate were in co-existence with the supernatant (b) Optical microscopy images and (c) color photographs of the coacervate (upper) and the precipitate (lower) phases in coexistence with their supernatant phases. The complexed phases are distinctive by optical microscopy and by their macroscopic behavior. Both the coacervate and precipitate are optically dense due to the high concentration of CPE while the solution is less optically dense. At the macroscopic scale, the precipitate appears as dense solid chunks aggregated at the bottom of the Eppendorf tube, while the coacervate has more liquid-like behavior and sticks to the tube walls upon centrifugation.

For the following studies of thin solid films, the coacervate was used because of its increased processability relative to the precipitate. The 100mM total polymer with 0.5M KBr condition was chosen, as it is well within the coacervate region in the phase diagram. For processing and characterization of the coacervate, the mixture was centrifuged to promote complete coalescence of the coacervate droplets. This coacervate was highly concentrated with 50% *w/v* polymer and was left in contact with the supernatant phase to preserve the equilibrium conditions until ready for use.

Interestingly, the complexation process with the PIL only induces a minimal change in the chain conformation of PEDOT-S possibly due to the stiffer nature of this polymer relative to other CPEs. As shown in **Figure 2.3**, the π–π* electronic transition peaks of the stock CPE solution and the coacervate are both at ≈ 2.2 eV, with the coacervate's absorption peak shifted slightly to lower energies. Red shifts in the absorption peak were previously reported in polymer–small molecule [38] and polymer–polymer [3,27,28] complex systems and were attributed to the reduction in conformational disorder along the conjugated backbone leading to an increase in the conjugation length. A Gaussian fitting procedure was performed on both spectra, deconvoluting this peak into two overlapping peaks (**Figure S2.3** and **S2.4**) whose positions red-shifted minimally (~ 0.02 eV) upon coacervation. This observation is fundamentally different from our previously reported results, where much larger red-shifts (up to 0.25 eV) in the absorption peak of (poly{3-[6′-(N-butylimidazolium)-hexyl]thiophene}bromide (P3BImHT$^+$:Br$^-$) were observed upon the CPE's complexation with sodium poly(styrenesulfonate) (Na$^+$:PSS$^-$).[3] However, in a recent study, the complexation

between poly(fluorene-*alt*-phenylene) (PFPI) and Na^+:PSS^- was reported to lead to red-shifts of only 0.04 – 0.08 eV in the absorption profile of the CPE.[27] Thus, it is likely that the higher rigidity of PEDOT-S and PFPI backbones compared to P3BImHT$^+$:Br^- made these polymers less susceptible to conformational changes upon complexation.

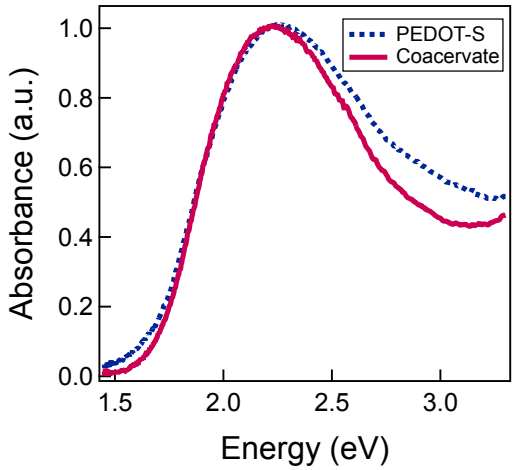

Figure 2.3. UV-Vis spectra of PEDOT-S in stock CPE solution form and in the swollen complex coacervate. The position of the optical absorption peak slightly red-shifted upon coacervation, suggesting a small enhancement in the conjugation length of PEDOT-S upon coacervation.

Due to its high solids loading and viscous nature, the PEDOT-S:PA-MPI coacervate can be easily blade coated to form a solid film with little thickness loss upon drying (~ 4.0 ± 0.5 μm). The preparation of the coacervate in an aqueous KBr solution led to the partition of salt ions into the cast film. Elemental analysis of the solid film cast from the coacervate confirmed the presence of K and Br (Table S1) indicating doping by the salt. Nonetheless, these ions can be removed easily from the coacervate by immersing the resulting film in milli-Q water overnight to promote diffusion of salt ions out of the film.

The lyophilic nature of the coacervate stabilizes the hydrophobic CPE backbone in a gel-like homogeneous network instead of forming collapsed aggregates with hydrophilic outer shell (for example as PEDOT:PSS). The homogeneous distribution of the conjugated material in the coacervate is indicated by the homogeneous intensity of brown of the coacervate droplets in the microscopic image (**Figure 2.2**). Memory of the conformations from the solvated-coacervate appears to be retained in the solid-state, as indicated by the homogeneous morphology of the complex film (scanning electron microscope (SEM) images of the film, **Figure 2.4**).

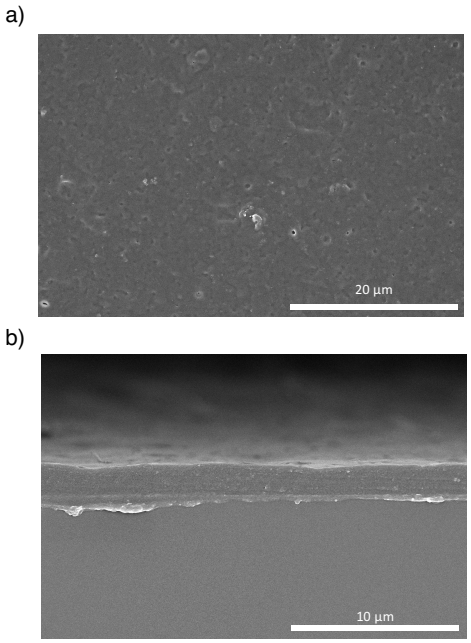

Figure 2.4. (a) Top view and (b) side view SEM images of a dry film cast from the coacervate after salt removal.

Electronic charge carriers could be introduced into the solid formed from the coacervate via doping to form electrically conductive films. In this study, we introduced the dopant from the vapor phase to not disturb the coacervate assembly. Other methods such as doping in solution,[39–41] solution-sequential doping,[42] and immersion doping,[43] which have been

successfully utilized with neat semiconducting polymers, introduced complications in processing. In particular, when doping in solution was attempted, the additional charges along the doped CPE backbone led to preferential formation of the dense precipitate over the weakly complexed coacervate. The use of salt to effectively screen the strong electrostatic interactions within the doped system was counteracted by the poor solubility of doped PEDOT-S in aqueous solution with large levels of added salt. Immersion doping and solution-sequential doping did not interrupt the mixing phase behavior but disrupted the structure of the solid film cast from the coacervate. We attribute this observation to the ionic cross-linking within the polymer–polymer complex breaking up by infiltration of dopant molecules into the film in the presence of a solvent, analogous to the partitioning of salt. As a result, the complex film partially dissolved or detached from the substrate. The infiltration of a dopant from the vapor phase, in contrast, not only ensured the formation of the coacervate phase (prior to doping) but also minimized interruption to the complexed structure during doping. HTFSI was chosen to be the dopant, as this strong acid vapor has been used effectively in doping of other conjugated polymers [44] and the resulting TFSI anion has good thermal and chemical stability. Moreover, the low sublimation temperature of HTFSI allows the doping process to be carried out at relatively low temperature, which is desirable for preserving the coacervate film structure.[45]

Effective electronic doping of the complex film was evidenced by the emergence of the polaronic features (1.2 – 1.5 eV) and the bleaching of the neutral polymer peak at 2.2 eV in the optical absorption spectrum of the film upon doping (**Figure 2.5**). Interestingly, we also observe a shift to lower energy when comparing the polaronic absorption peaks of the doped

coacervate and doped CPE films. This agreement between the optical spectra of doped and pristine samples confirms the enhancement in the conjugation length of the CPE upon coacervation that leads to more delocalized polaron along the CPE backbone.

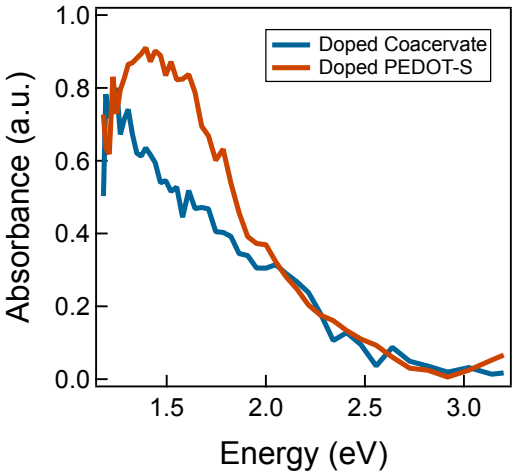

Figure 2.5. UV-Vis spectra of PEDOT-S and complex films doped with HTFSI vapor. The position of the polaron peak was red-shifted upon coacervation, indicating more delocalization of the radical cation along complexed PEDOT-S backbone.

Consistent with the conjugation length enhancement of the CPE observed in the UV-Vis spectra, coacervation appears to have increased the charge carrier mobility of PEDOT-S. In particular, the conductivity of the complex film at the optimal doping level was 2 $x10^{-4}$ S cm^{-1}, twice that of the PEDOT-S film doped by the same method. Since approximately half of the material in the coacervate was insulating, this difference in conductivity suggests a higher charge-carrier mobility in the coacervate than in the PEDOT-S film.

Beyond enhancing the conjugation of the CPE, coacervation may have possibly increased the conductivity of the coacervate by the partitioning of longer chains in the coacervate relative to the stock CPE sample from which it was formed. Higher fractions of long polymer chains have been shown to increase charge carrier mobility due to the enhancement in intrachain

charge transport.[46] There are two possible driving forces for this partitioning of long chains into the coacervate. Firstly, longer chains have smaller reduction of translational entropy upon coacervation. Secondly, longer polymer chains likely have poor solubility in the supernatant phase, as elemental analysis of the film casted from the coacervate indicates the preferential partitioning of KBr into the supernatant and thus making it a high-salt environment (Table S1.) Previous studies on conventional polyelectrolyte coacervate also reported the preferential partitioning of long polymer chains from stock solution into the coacervate phase, as indicated by a higher average radius of gyration (R_g) of the polymer in the coacervate than that in the stock polymer solution.[47] We note that the high polydispersity of our PEDOT-S sample might further amplify the impact of long-chain-partitioning.

It appears that the enhanced charge carrier mobility is unlikely to be a caused by changes in ordering, as both the neat PEDOT-S and the coacervate are amorphous with no evidence of long-range ordering in X-ray scattering (**Figure S2.5**). This lack of crystallinity in both PEDOT-S and the complex films also explains their relatively low conductivities compared to some other conjugated polymers. It is likely that the highly charged nature (charge fraction f = 1) and the uncontrolled regiochemistry of PEDOT-S synthesis have prevented sufficient interchain packing in these materials.

Interestingly, we also observed excellent ion solvation by the CPE:PIL complex film. At the optimal electronic doping level, a room-temperature ionic conductivity of 9×10^{-5} S cm^{-1} was measured. Since the complete removal of KBr was confirmed *via* XPS, this ionic conductivity was contributed solely by HTFSI. XPS elemental analysis of the film supports this

observation: the F/S ratio, which is an indication of the amount of TFSI anion relative to PEDOT-S, in the doped complex film was approximately 2 times higher than in the doped PEDOT-S film (Table S2.1). Etching experiments performed on the complex film show this trend to be consistent through the film's μm-scale depth. These results indicate that upon its infiltration to the complex film, HTFSI not only doped the PEDOT-S backbone but also act as an ionic dopant, possibly by partitioning into the side chain regions (**Figure 2.6**). A major driving force for this process is likely the much lower pKa of HTFSI (pKa ~ -12) [48] compared to that of polymerized sulfonic acid, whose pKa decreases with higher degree of polymerization and plateaus at around 2.9 for poly(styrene sulfonic acid).[49] This significant difference in pKa makes the association of protons with PEDOT-S side chains preferential over TFSI anions. It is not clear whether HTFSI partitions first into the side chain regions or dopes the PEDOT-S backbone. Nonetheless, the relatively high ionic conductivity of the complex at room temperature indicates that this CPE:PIL complex can solvate and facilitate the transport of a significant number of ions in solvent-free conditions, suggesting its great potential as a solid-state ion conductor.

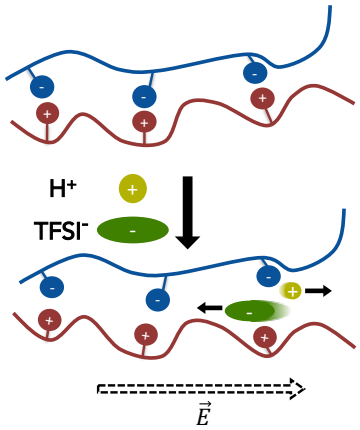

Figure 2.6. Schematic of the partitioning of HTFSI into the coacervate system and the contribution of the dissociated protons and TFSI anions to the observed ionic conductivity.

2.5 Conclusion

We have shown that CPE:PIL coacervation provides a promising route for processing of conjugated polymers in aqueous media at exceptionally higher polymer concentrations (50% *w/v* polymer) than conventional solution processing methods (~ 1% *w/v* polymer). The resulting coacervate fluid is compatible with large-scale processing methods such as blade coating, and the highly concentrated nature of this material enables the fabrication of µm-thick films. Thick films also possess advantages over thin (100s nm) films in some applications such as thermoelectrics [50] and pressure sensors.[51] This approach is highly versatile for use in CPE systems, as the complexation process can be easily tuned by changing mixing conditions such as solvent dielectric strength and polymer concentration. Salt is often needed to achieve the fluidic coacervate phase, yet the salt ions remaining in the coacervate can be removed easily at the end of the film casting process.

Beyond advantages in processing, coacervation also can positively impact the optoelectronic performance of conjugated polymers. In particular, a reduction in conformational disorder along the CPE backbone upon its coacervation with another polyelectrolyte results in enhanced conjugation length and higher charge carrier mobility. Thus, the process of polyelectrolyte coacervation could also be utilized for improved performance of organic optoelectronic devices.

While not investigated in this study, it is expected that tuning of other factors such as the Flory–Huggins parameter and the mixing ratio of the two polyelectrolytes could result in interesting morphological changes of the coacervate from a homogeneous, disordered

complex to microphase-separated structure,[52,53] or even macrophases rich in either the polycation or polyanion.[54–56] These changes in morphology will likely affect the electronic conduction pathway and as a result the transport property of the coacervate drastically. An analogous trend has been observed with PEDOT:PSS, where a significant improvement in the electrical conductivity of this material was achieved by promoting microphase-segregation within the complex to produce PEDOT-rich and PSS-rich domains.[57] Thus, further studies toward the manipulation of the complexation process to access different morphologies are needed to provide a more thorough understanding of the structure—properties relationships in this system.

2.6 Acknowledgement

The authors acknowledge funding support from the Department of Energy Office of Basic Energy Sciences under grant no. DE-SC0016390. The authors acknowledge the use of shared facilities of the UCSB MRSEC (NSF DMR 1720256), a member of the Materials Research Facilities Network (www.mrfn.org) and the use of the Nanostructures Cleanroom Facility within the California NanoSystems Institute, supported by the University of California, Santa Barbara and the University of California, Office of the President. This research used resources of the National Synchrotron Light Source II, a U.S. Department of Energy Office of Science User Facility (DE-SC0012704; beamline 11-BM). The authors thank Dr. Thomas Mates for XPS and Dr. Rachel Behrens for GPC data acquisition and analysis.

2.7 Appendix

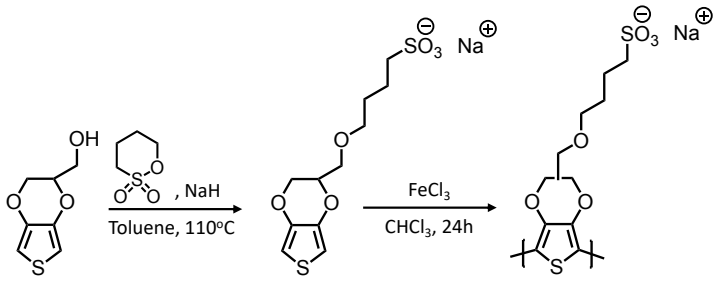

Figure S2.1. Synthesis of PEDOT-S

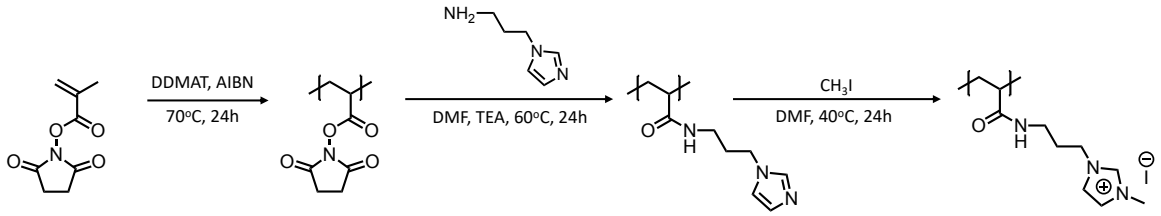

Figure S2.2. Synthesis of PA-MPI

Table S2.1. XPS elemental analysis of solid films processed from neat PEDOT-S and PEDOT-S:PA-MPI coacervate. XPS data indicates that in the film casted from the coacervate, there is 1 KBr molecule for every 3 monomers. As the total concentration of KBr is 5 times higher than the monomer concentration, this indicate that KBr preferentially stays in the supernatant phase.

Film	Chemical Element Atomic %								
	C	O	S	I	Na	Br	N	K	F
Coacervate as-cast	60.65	20.77	5.28	0.18	0.07	1.85	9.0	2.2	0
Coacervate salt-free	64.47	18.63	4.71	0	0	0.15	12.0	0	0
Doped PEDOT-S	40.59	28.60	11.14	0	0.37	0	6.77	0	12.53
Doped coacervate	33.42	23.09	11.49	0	0	0	11.9	0	20.14

Furthermore, there appears to be a cation-dependent partitioning of ions into the coacervate. In particular, the total concentration of K^+ in the PEDOT-S:PA-MPI mixture is 10 times higher than Na^+. However, the K^+ concentration in the coacervate were roughly 31 times higher than the Na^+ concentration. We postulate that the competition between ion size and the energy cost of the solvation process that the ion experiences when partitioning into the coacervate is what determines the relative concentrations of ions in the complex film.

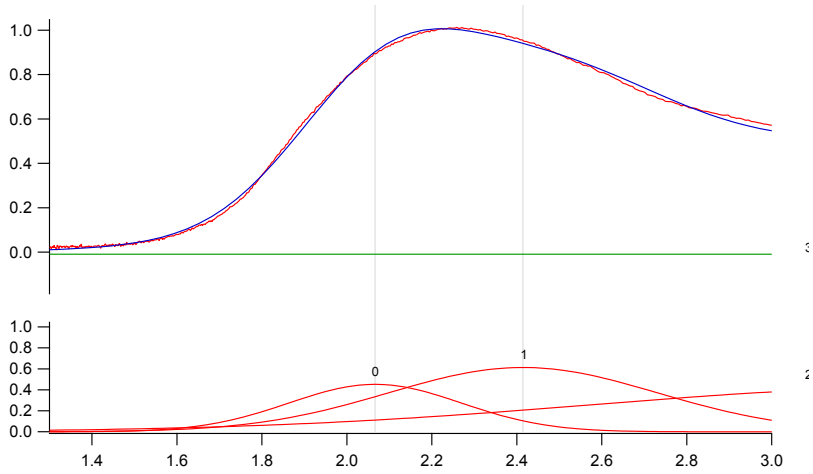

Figure S2.3. Peak fitting results for UV-Vis data of PEDOT-S film. Peak 0: 2.07 eV, peak 1: 2.41eV

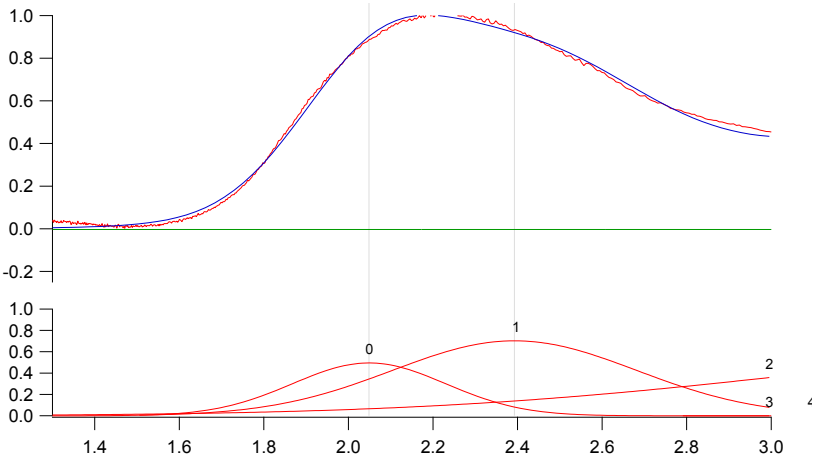

Figure S2.4. Peak fitting results for UV-Vis data of coacervate film. Peak 0: 2.05 eV, peak 1: 2.39eV

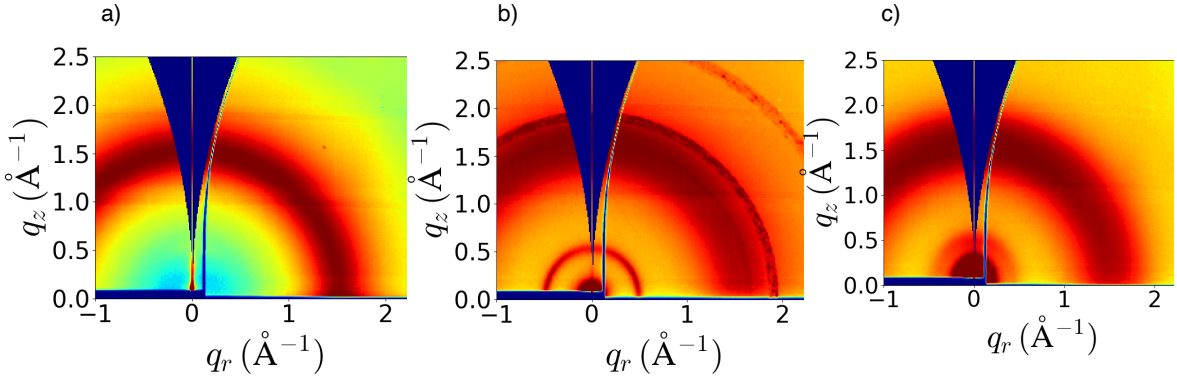

Figure S2.5. GIWAXS pattern for (a) neat PEDOT-S film, (b) coacervate film, and (c) coacervate film after salt removal. Upon salt removal, the high-q features, which we attribute to the scattering from salt crystals, disappeared. This data confirms the complete removal of ions from the coacervate after the water immersion process. We also note the scattering ring at q = 0.4 $Å^{-1}$, which is commonly assigned to side-chain lamellar stacking, was broadened after salt removal. This is likely a result of the disruption to the stacking caused by water infiltration and the movement of ions out of the polymer complex film during the salt removal process.

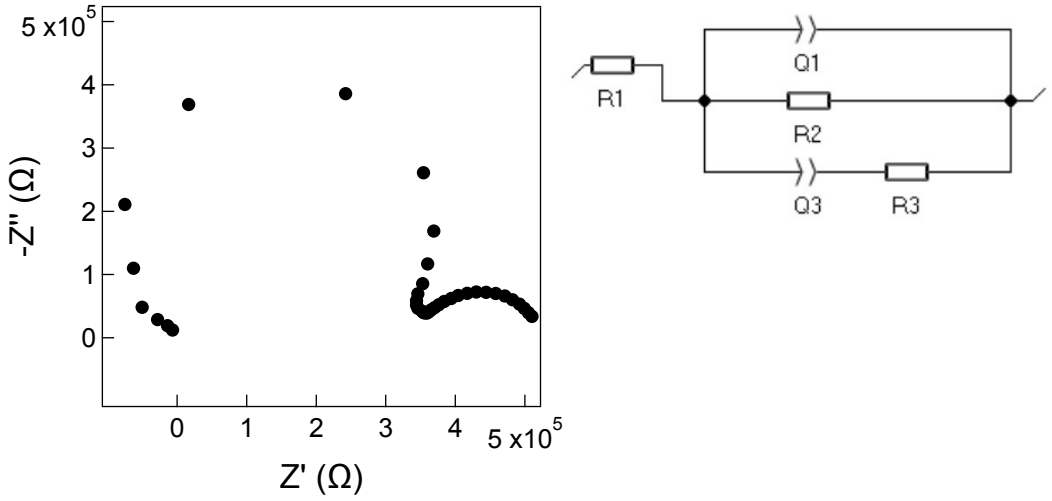

Figure S2.6. Nyquist plot of optimally doped coacervate film and the circuit model used for fitting of electrochemical impedance data. The ionic conductivity determined from this circuit model is 9 x 10^{-5} S/cm, and the electronic conductivity is 2 x 10^{-4} S/cm – consistent with the electronic conductivity obtained from transmission line method.

2.8 References

(1) Savagian, L. R.; Österholm, A. M.; Ponder, J. F.; Barth, K. J.; Rivnay, J.; Reynolds, J. R. Balancing Charge Storage and Mobility in an Oligo(Ether) Functionalized Dioxythiophene Copolymer for Organic- and Aqueous- Based Electrochemical Devices and Transistors. Adv. Mater. 2018, 30 (50), 1804647. https://doi.org/10.1002/adma.201804647.

(2) Pinto, M. R.; Scinanze, K. S. Conjugated Polyelectrolytes: Synthesis and Applications. 2002.

(3) Danielsen, S. P. O.; Nguyen, T. Q.; Fredrickson, G. H.; Segalman, R. A. Complexation of a Conjugated Polyelectrolyte and Impact on Optoelectronic Properties. ACS Macro Lett. 2019, 8 (1), 88–94. https://doi.org/10.1021/acsmacrolett.8b00924.

(4) Imamura, K. Studies on the Energy for Sperm Motility (Japanese); 1975; Vol. 20.

(5) Søndergaard, R. R.; Hösel, M.; Krebs, F. C. Roll-to-Roll Fabrication of Large Area Functional Organic Materials. Journal of Polymer Science, Part B: Polymer Physics. Wiley Periodicals, Inc January 1, 2013, pp 16–34. https://doi.org/10.1002/polb.23192.

(6) Hyman, A. A.; Weber, C. A.; Jülicher, F. Liquid-Liquid Phase Separation in Biology. Annu. Rev. Cell Dev. Biol. 2014, 30, 39–58. https://doi.org/10.1146/annurev-cellbio-100913-013325.
(7) Banani, S. F.; Lee, H. O.; Hyman, A. A.; Rosen, M. K. Biomolecular Condensates: Organizers of Cellular Biochemistry. Nature Reviews Molecular Cell Biology. Nature Publishing Group May 1, 2017, pp 285–298. https://doi.org/10.1038/nrm.2017.7.
(8) Wei, W.; Tan, Y.; Martinez Rodriguez, N. R.; Yu, J.; Israelachvili, J. N.; Waite, J. H. A Mussel-Derived One Component Adhesive Coacervate. Acta Biomater. 2014, 10 (4), 1663–1670. https://doi.org/10.1016/j.actbio.2013.09.007.
(9) Hwang, D. S.; Zeng, H.; Srivastava, A.; Krogstad, D. V.; Tirrell, M.; Israelachvili, J. N.; Waite, J. H. Viscosity and Interfacial Properties in a Mussel-Inspired Adhesive Coacervate. Soft Matter 2010, 6 (14), 3232–3236. https://doi.org/10.1039/c002632h.
(10) Sing, C. E.; Perry, S. L. Recent Progress in the Science of Complex Coacervation. Soft Matter 2020, 16 (12), 2885–2914. https://doi.org/10.1039/d0sm00001a.
(11) Macleod, G. S.; Collett, J. H.; Fell, J. T. The Potential Use of Mixed Films of Pectin, Chitosan and HPMC for Bimodal Drug Release. J. Control. Release 1999, 58 (3), 303–310. https://doi.org/10.1016/S0168-3659(98)00168-0.
(12) Genta, I.; Perugini, P.; Modena, T.; Pavanetto, F.; Castelli, F.; Muzzarelli, R. A. A.; Muzzarelli, C.; Conti, B. Miconazole-Loaded 6-Oxychitin-Chitosan Microcapsules. Carbohydr. Polym. 2003, 52 (1), 11–18. https://doi.org/10.1016/S0144-8617(02)00257-6.
(13) OVERBEEK, J. T.; VOORN, M. J. Phase Separation in Polyelectrolyte Solutions; Theory of Complex Coacervation. J. Cell. Physiol. Suppl. 1957, 49 (Suppl 1), 7–26. https://doi.org/10.1002/jcp.1030490404.
(14) Manoj Lalwani, S.; Eneh, C. I.; Lutkenhaus, J. L. Emerging Trends in the Dynamics of Polyelectrolyte Complexes. Physical Chemistry Chemical Physics. Royal Society of Chemistry November 14, 2020, pp 24157–24177. https://doi.org/10.1039/d0cp03696j.
(15) Lytle, T. K.; Sing, C. E. Tuning Chain Interaction Entropy in Complex Coacervation Using Polymer Stiffness, Architecture, and Salt Valency. Mol. Syst. Des. Eng. 2018, 3 (1), 183–196. https://doi.org/10.1039/c7me00108h.
(16) Salehi, A.; Larson, R. G. A Molecular Thermodynamic Model of Complexation in Mixtures of Oppositely Charged Polyelectrolytes with Explicit Account of Charge Association/Dissociation. Macromolecules 2016, 49 (24), 9706–9719. https://doi.org/10.1021/acs.macromol.6b01464.
(17) Hamad, F. G.; Chen, Q.; Colby, R. H. Linear Viscoelasticity and Swelling of Polyelectrolyte Complex Coacervates. Macromolecules 2018, 51 (15), 5547–5555. https://doi.org/10.1021/acs.macromol.8b00401.
(18) Larson, R. G.; Liu, Y.; Li, H. Linear Viscoelasticity and Time-Temperature-Salt and Other Superpositions in Polyelectrolyte Coacervates. J. Rheol. (N. Y. N. Y). 2021, 65 (1), 77–102. https://doi.org/10.1122/8.0000156.
(19) Danielsen, S. P. O.; Panyukov, S.; Rubinstein, M. Ion Pairing and the Structure of Gel Coacervates. Macromolecules 2020, 53 (21), 9420–9442. https://doi.org/10.1021/acs.macromol.0c01360.

(20) Rubinstein, M.; Liao, Q.; Panyukov, S. Structure of Liquid Coacervates Formed by Oppositely Charged Polyelectrolytes. Macromolecules 2018, 51 (23), 9572–9588. https://doi.org/10.1021/acs.macromol.8b02059.
(21) Delaney, K. T.; Fredrickson, G. H. Theory of Polyelectrolyte Complexation - Complex Coacervates Are Self-Coacervates. J. Chem. Phys. 2017, 146 (22), 224902. https://doi.org/10.1063/1.4985568.
(22) Danielsen, S. P. O.; McCarty, J.; Shea, J. E.; Delaney, K. T.; Fredrickson, G. H. Small Ion Effects on Self-Coacervation Phenomena in Block Polyampholytes. J. Chem. Phys. 2019, 151 (3), 34904. https://doi.org/10.1063/1.5109045.
(23) Yang, M.; Shi, J.; Schlenoff, J. B. Control of Dynamics in Polyelectrolyte Complexes by Temperature and Salt. Macromolecules 2019, 52 (5), 1930–1941. https://doi.org/10.1021/acs.macromol.8b02577.
(24) Fares, H. M.; Ghoussoub, Y. E.; Delgado, J. D.; Fu, J.; Urban, V. S.; Schlenoff, J. B. Scattering Neutrons along the Polyelectrolyte Complex/Coacervate Continuum. Macromolecules 2018, 51 (13), 4945–4955. https://doi.org/10.1021/acs.macromol.8b00699.
(25) Blocher McTigue, W. C.; Perry, S. L. Protein Encapsulation Using Complex Coacervates: What Nature Has to Teach Us. Small. Wiley-VCH Verlag July 1, 2020, p 1907671. https://doi.org/10.1002/smll.201907671.
(26) Friedowitz, S.; Salehi, A.; Larson, R. G.; Qin, J. Role of Electrostatic Correlations in Polyelectrolyte Charge Association. J. Chem. Phys. 2018, 149 (16), 163335. https://doi.org/10.1063/1.5034454.
(27) Johnston, A. R.; Perry, S. L.; Ayzner, A. L. Associative Phase Separation of Aqueous π-Conjugated Polyelectrolytes Couples Photophysical and Mechanical Properties. Chem. Mater. 2021, 33 (4), 1116–1129. https://doi.org/10.1021/acs.chemmater.0c02424.
(28) Hollingsworth, W. R.; Segura, C.; Balderrama, J.; Lopez, N.; Schleissner, P.; Ayzner, A. L. Exciton Transfer and Emergent Excitonic States in Oppositely-Charged Conjugated Polyelectrolyte Complexes. J. Phys. Chem. B 2016, 120 (31), 7767–7774. https://doi.org/10.1021/acs.jpcb.6b06533.
(29) Hollingsworth, W. R.; Williams, V.; Ayzner, A. L. Semiconducting Eggs and Ladders: Understanding Exciton Landscape Formation in Aqueous π-Conjugated Inter-Polyelectrolyte Complexes. Macromolecules 2020, 53 (7), 2724–2734. https://doi.org/10.1021/acs.macromol.0c00029.
(30) Knaapila, M.; Costa, T.; Garamus, V. M.; Kraft, M.; Drechsler, M.; Scherf, U.; Burrows, H. D. Polyelectrolyte Complexes of a Cationic All Conjugated Fluorene-Thiophene Diblock Copolymer with Aqueous DNA. J. Phys. Chem. B 2015, 119 (7), 3231–3241. https://doi.org/10.1021/jp5110032.
(31) Stéphan, O.; Schottland, P.; Le Gall, P. Y.; Chevrot, C.; Mariet, C.; Carrier, M. Electrochemical Behaviour of 3,4-Ethylenedioxythiophene Functionalized by a Sulphonate Group. Application to the Preparation of Poly(3,4-Ethylenedioxythiophene) Having Permanent Cation-Exchange Properties. J. Electroanal. Chem. 1998, 443 (2), 217–226. https://doi.org/10.1016/S0022-0728(97)00548-2.
(32) Evans, C. M.; Sanoja, G. E.; Popere, B. C.; Segalman, R. A. Anhydrous Proton Transport in Polymerized Ionic Liquid Block Copolymers: Roles of Block Length,

Ionic Content, and Confinement. Macromolecules 2016, 49 (1), 395–404. https://doi.org/10.1021/acs.macromol.5b02202.
(33) Cutler, C. A.; Bouguettaya, M.; Kang, T. S.; Reynolds, J. R. Alkoxysulfonate-Functionalized PEDOT Polyelectrolyte Multilayer Films: Electrochromic and Hole Transport Materials. Macromolecules 2005, 38 (8), 3068–3074. https://doi.org/10.1021/ma047396+.
(34) Ponder, J. F.; Österholm, A. M.; Reynolds, J. R. Designing a Soluble PEDOT Analogue without Surfactants or Dispersants. Macromolecules 2016, 49 (6), 2106–2111. https://doi.org/10.1021/acs.macromol.5b02638.
(35) Reeves, B. D.; Grenier, C. R. G.; Argun, A. A.; Cirpan, A.; McCarley, T. D.; Reynolds, J. R. Spray Coatable Electrochromic Dioxythiophene Polymers with High Coloration Efficiencies. Macromolecules 2004, 37 (20), 7559–7569. https://doi.org/10.1021/ma049222y.
(36) Kazemiabnavi, S.; Zhang, Z.; Thornton, K.; Banerjee, S. Electrochemical Stability Window of Imidazolium-Based Ionic Liquids as Electrolytes for Lithium Batteries. J. Phys. Chem. B 2016, 120 (25), 5691–5702. https://doi.org/10.1021/acs.jpcb.6b03433.
(37) Kulkarni, A. D.; Vanjari, Y. H.; Sancheti, K. H.; Patel, H. M.; Belgamwar, V. S.; Surana, S. J.; Pardeshi, C. V. Polyelectrolyte Complexes: Mechanisms, Critical Experimental Aspects, and Applications. Artif. Cells, Nanomedicine Biotechnol. 2016, 44 (7), 1615–1625. https://doi.org/10.3109/21691401.2015.1129624.
(38) Evans, R. C.; Knaapila, M.; Willis-Fox, N.; Kraft, M.; Terry, A.; Burrows, H. D.; Scherf, U. Cationic Polythiophene-Surfactant Self-Assembly Complexes: Phase Transitions, Optical Response, and Sensing. Langmuir 2012, 28 (33), 12348–12356. https://doi.org/10.1021/la302166a.
(39) Pingel, P.; Neher, D. Comprehensive Picture of P-Type Doping of P3HT with the Molecular Acceptor F4TCNQ. Phys. Rev. B - Condens. Matter Mater. Phys. 2013, 87 (11), 115209. https://doi.org/10.1103/PhysRevB.87.115209.
(40) Duong, D. T.; Wang, C.; Antono, E.; Toney, M. F.; Salleo, A. The Chemical and Structural Origin of Efficient P-Type Doping in P3HT. Org. Electron. 2013, 14 (5), 1330–1336. https://doi.org/10.1016/j.orgel.2013.02.028.
(41) Wang, C.; Duong, D. T.; Vandewal, K.; Rivnay, J.; Salleo, A. Optical Measurement of Doping Efficiency in Poly(3-Hexylthiophene) Solutions and Thin Films. Phys. Rev. B - Condens. Matter Mater. Phys. 2015, 91 (8), 085205. https://doi.org/10.1103/PhysRevB.91.085205.
(42) Scholes, D. T.; Hawks, S. A.; Yee, P. Y.; Wu, H.; Lindemuth, J. R.; Tolbert, S. H.; Schwartz, B. J. Overcoming Film Quality Issues for Conjugated Polymers Doped with F4TCNQ by Solution Sequential Processing: Hall Effect, Structural, and Optical Measurements. J. Phys. Chem. Lett. 2015, 6 (23), 4786–4793. https://doi.org/10.1021/acs.jpclett.5b02332.
(43) Kolesov, V. A.; Fuentes-Hernandez, C.; Chou, W. F.; Aizawa, N.; Larrain, F. A.; Wang, M.; Perrotta, A.; Choi, S.; Graham, S.; Bazan, G. C.; Nguyen, T. Q.; Marder, S. R.; Kippelen, B. Solution-Based Electrical Doping of Semiconducting Polymer Films over a Limited Depth. Nat. Mater. 2017, 16 (4), 474–481. https://doi.org/10.1038/NMAT4818.

(44) Hofmann, A. I.; Kroon, R.; Yu, L.; Müller, C. Highly Stable Doping of a Polar Polythiophene through Co-Processing with Sulfonic Acids and Bistriflimide. J. Mater. Chem. C 2018, 6 (26), 6905–6910. https://doi.org/10.1039/C8TC01593G.
(45) Evans, C. M.; Bridges, C. R.; Sanoja, G. E.; Bartels, J.; Segalman, R. A. Role of Tethered Ion Placement on Polymerized Ionic Liquid Structure and Conductivity: Pendant versus Backbone Charge Placement. ACS Macro Lett. 2016, 5 (8), 925–930. https://doi.org/10.1021/acsmacrolett.6b00534.
(46) Gu, K.; Snyder, C. R.; Onorato, J.; Luscombe, C. K.; Bosse, A. W.; Loo, Y. L. Assessing the Huang-Brown Description of Tie Chains for Charge Transport in Conjugated Polymers. ACS Macro Lett. 2018, 7 (11), 1333–1338. https://doi.org/10.1021/acsmacrolett.8b00626.
(47) Spruijt, E.; Leermakers, F. A. M.; Fokkink, R.; Schweins, R.; Van Well, A. A.; Cohen Stuart, M. A.; Van Der Gucht, J. Structure and Dynamics of Polyelectrolyte Complex Coacervates Studied by Scattering of Neutrons, X-Rays, and Light. Macromolecules 2013, 46 (11), 4596–4605. https://doi.org/10.1021/ma400132s.
(48) Patel, S. N.; Glaudell, A. M.; Peterson, K. A.; Thomas, E. M.; O'Hara, K. A.; Lim, E.; Chabinyc, M. L. Morphology Controls the Thermoelectric Power Factor of a Doped Semiconducting Polymer. Sci. Adv. 2017, 3 (6), e1700434. https://doi.org/10.1126/sciadv.1700434.
(49) Dong, H.; Du, H.; Wickramasinghe, S. R.; Qian, X. The Effects of Chemical Substitution and Polymerization on the PK a Values of Sulfonic Acids. J. Phys. Chem. B 2009, 113 (43), 14094–14101. https://doi.org/10.1021/jp906087c.
(50) Russ, B.; Glaudell, A.; Urban, J. J.; Chabinyc, M. L.; Segalman, R. A. Organic Thermoelectric Materials for Energy Harvesting and Temperature Control. Nature Reviews Materials. Nature Publishing Group August 2, 2016, p 16050. https://doi.org/10.1038/natrevmats.2016.50.
(51) Harsányi, G.; Hahn, E. Thick-Film Pressure Sensors. Mechatronics 1993, 3 (2), 167–171.
(52) Rumyantsev, A. M.; Kramarenko, E. Y.; Borisov, O. V. Microphase Separation in Complex Coacervate Due to Incompatibility between Polyanion and Polycation. Macromolecules 2018, 51 (17), 6587–6601. https://doi.org/10.1021/acs.macromol.8b00721.
(53) Rumyantsev, A. M.; Kramarenko, E. Y. Two Regions of Microphase Separation in Ion-Containing Polymer Solutions. Soft Matter 2017, 13 (38), 6831–6844. https://doi.org/10.1039/c7sm01340j.
(54) Zhang, P.; Alsaifi, N. M.; Wu, J.; Wang, Z. G. Polyelectrolyte Complex Coacervation: Effects of Concentration Asymmetry. J. Chem. Phys. 2018, 149 (16), 163303. https://doi.org/10.1063/1.5028524.
(55) Oskolkov, N. N.; Potemkin, I. I. Complexation in Asymmetric Solutions of Oppositely Charged Polyelectrolytes: Phase Diagram. Macromolecules 2007, 40 (23), 8423–8429. https://doi.org/10.1021/ma0709304.
(56) Zhang, R.; Shklovskii, B. I. Phase Diagram of Solution of Oppositely Charged Polyelectrolytes. Phys. A Stat. Mech. its Appl. 2005, 352 (1), 216–238. https://doi.org/10.1016/j.physa.2004.12.037.

(57) Shi, H.; Liu, C.; Jiang, Q.; Xu, J. Effective Approaches to Improve the Electrical Conductivity of PEDOT:PSS: A Review. Adv. Electron. Mater. 2015, 1 (4), 1500017. https://doi.org/10.1002/aelm.201500017.

Chapter 3

Electrostatic interactions control the nanostructure of conjugated polyelectrolyte – polymeric ionic liquid blends

This chapter is reproduced with permission from:

Le, M. L., Grzetic, D., Delaney, K. T., Yang, K. C., Xie, S., Fredrickson, G. H., Chabinyc, M. L., Segalman, R. A. Electrostatic interactions control the nanostructure of conjugated polyelectrolyte-polymeric ionic liquid blends. *Macromolecules* **2022**, 55, 8321−8331. DOI: 10.1021/acs.macromol.2c01142. Copyright 2022 American Chemical Society.

Field-theoretic simulations and RPA calculations were done by Dr. Douglas Grzetic.

3.1 Abstract

Polyelectrolyte complexation offers unique opportunities to compatibilize polymers with very different backbone chemistries and to control the morphology of the resulting blend via electrostatic manipulation. In this study, we demonstrate the ability to formulate homogeneous complexes of a conjugated polyelectrolyte with a polymeric ionic liquid utilizing the electrostatic attraction among their oppositely charged sidechains. Variation of electrostatic parameters, such as counterion concentration or polymer charge fraction, tunes the morphology of these polymer complexes from homogeneously disordered blend to weakly structured microemulsion where the local ordering arises from backbone-immiscibility-induced microphase segregation. Our experimental observations are in qualitative agreement with both field theoretic simulation and random phase approximation calculations. Simulated morphology snapshots suggest and experimental evidence also indicates that the microphase segregated complex likely takes on a co-continuous microemulsion structure. Our findings

show that ionic interactions are an effective pathway to compatibilize polymers at macroscopic length scales while achieving controlled nanostructures in these ionic blends. Such systems have great potential for engineering the nanostructure of polymers to tailor applications such as nanofiltration, catalysis, and energy storage, where local ordering can enhance the physical properties of an otherwise macroscopically homogeneous structure.

3.2 Introduction

Multicomponent polymeric systems have been utilized widely in polymer science to achieve functional requirements that cannot be fulfilled by using single-component materials. There are many examples where multicomponent systems were successfully leveraged to simultaneously combine orthogonal properties such as toughness and elasticity,[1] ionic conductivity and mechanical strength,[2] or ionic and electronic conductivity [3–5] into the final material. Additionally, these systems could be engineered to tune the material's final properties, such as electronic density of states [6–8] or luminous efficiency.[9] In some cases, the use of multicomponent systems can also impart processability [10] and/or environmental stability [11,12] to the final material.

Controlling the morphology of the material is critical in all of these applications. However, simple blends of neutral polymers are prone to macrophase separation due to the unfavorable enthalpic interactions between dissimilar polymer chains. To promote mixing and to control the morphology of the resulting material, it is essential to push the blend out of the miscibility gap. This usually requires extreme dilution of one of the components, and in many cases the dilution can detrimentally affect the material's performance. Another commonly used

approach is to covalently link the individual components together to form copolymers. In copolymers, macrophase separation is prohibited by the presence of the covalent linkages, so the material possesses either a homogeneous disordered or a microphase-segregated ordered morphology. Dissimilar monomers can be combined in copolymers in random, alternating, graft, or block architectures. Among these architectures, block and graft copolymers have received significant investigation due to their ability to self-assemble into ordered structures down to nanoscale that can be tuned precisely via various parameters such as chemical composition, chain length, and chain conformation.[13,14] Non-covalent or *supramolecular* linkages, in the form of e.g. hydrogen bonds [15] or metal-ligand interactions,[16] can also be used as an alternative to covalent linkages in order to compatibilize dissimilar polymers. For example, hydrogen bonding has been utilized widely in many miscible blends of poly(vinyl alcohol), poly(acrylic acid), or poly(4-vinyl phenol) with polyesters, polyacrylates, or polyethers.[17] Dipole-dipole interactions have been used to achieve mixing of polyacrylates with poly(vinylidene fluoride).[18] Donor-acceptor interactions were used to compatibilize poly[w-(3,5- dinitrobenzoyl)-hydroxy-alkylmethacrylate] with poly[2-(N-carbazolyl)ethyl methacrylate].[19] In addition to the compatibilization effect, the reversibility of these supramolecular bonds can improve the processability of the resulting material and may also be leveraged to achieve desirable stimuli-response or self-healing properties.[20,21]

In addition to these approaches, polyelectrolyte complexation, mediated by the electrostatic attraction among side chains of oppositely charged polymers, offers very unique opportunities to promote mixing between polymers of different backbone chemistries. In this case, electrostatic interactions are leveraged to overcome repulsive interactions that would render a

conventional polymer blend immiscible. In the context of such *polyelectrolyte complexes* (PECs) the electrostatic interactions play an analogous role to the covalent bond in a block copolymer, i.e. by prohibiting macrophase separation and stabilizing the disordered phase. For example, taking a pair of A and B polymers, each of length N, and covalently bonding them together into an AB diblock copolymer can expand the window of stability of the homogeneous (mixed) phase from $\chi N < 2$ to $\chi N < 5.248$, where χ is the Flory interaction parameter between A and B segments.[22] Above this value, ordered microphases occur since the covalent bond prohibits macroscale phase separation. In the case of the PEC, no covalent bond is needed and the expansion of the stability window for the mixed phase, compared to an equivalent uncharged blend, can be far greater. Moreover, PEC assembly is controllable by tuning the electrostatic parameters (Bjerrum length, charge density, counterion/salt concentration, etc.).[23–27] In fact, in most cases for a PEC of immiscible backbones, the window of stability for the mixed phase is so expanded that its stability limit is inaccessible for all practical purposes, unless the polyelectrolytes' charge densities are very low. This makes charge complexation an extremely powerful tool to facilitate the mixing of polymers with very different dielectric, mechanical, or conducting properties without the need to resort to block architectures.

Similar to the block copolymer, if the Flory parameter χ between the backbones of the oppositely charged polymers is large enough, the mixed phase of the PEC is expected to give way to ordered *microphases*. In the absence of salt or counterions, macrophase separation of the polyanion and polycation is not possible because it involves charge separation on macroscopic scales and thus costs a prohibitive electrostatic energy. However, in the presence

of any added salt or residual counterions, localization of the small ions could charge-neutralize the A and B-rich domains, opening up the possibility of macrophase separation. In this scenario, the length scale of phase separation is determined by a competition between the entropy of the small ions and the strength of electrostatic interactions that localize those ions so as to locally charge-neutralize the PEC. Indeed, the PEC in principle exhibits a mean-field Lifshitz point, a tricritical point at which tendencies for macrophase and microphase separation are exactly balanced.[28–30] The Lifshitz point in PEC systems can be accessed by adding salt where the critical salt concentration at the Lifshitz point is sensitive to the other electrostatic parameters (Bjerrum length, charge density).[25] Thus, from a theoretical perspective, PECs containing immiscible backbones should exhibit a rich variety of phase behavior, but this has largely been unexplored experimentally.

In this study, we demonstrate the ability to utilize electrostatic interactions to achieve intimate mixing of a conjugated polyelectrolyte (CPE) and a polymeric ionic liquid (PIL). We also show that while the CPE-PIL complex (CPC) stays homogeneously mixed at the macroscopic scale, microphase separation occurs as the attractive interactions among polymer chains are weakened. This leads to the formation of microemulsion structure that stays globally disordered yet locally ordered with a length scale of correlation around 4 nm to 5 nm. Such nanostructure resembles that of a block copolymer melt above, but near, the order-disorder transition temperature (T_{ODT}), but is stabilized by electrostatic interactions in the PEC case rather than by block connectivity. Two electrostatic parameters, the polymer charge density and the concentration of counterions, were both shown to have significant impacts on the local structure of the CPCs. Our results suggest an opportunity to engineer the nanostructure of

polymer blends to tailor specific applications. Lastly, we leverage a field-theoretic model that was recently used to investigate the ordered microphase morphology of PECs [25] and random phase approximation calculations to better understand the nanoscale composition fluctuations at equilibrium in the disordered regime and aid the interpretation of our experimental findings. Our study illustrates an alternate route to compatibilize polymers and to obtain controlled nanostructure of the resulting polymer complex in the disordered regime, with additional tunability and without the need to synthesize block copolymers.

3.3 Experimental and Theoretical Methods

Sample Preparation

All precursors, monomers, and polymers were synthesized according to previously reported literature procedures, which are described in details in the supporting information. Stock solutions of CPE and PIL are prepared by dissolving the polymer in a 40% THF in water mixture, resulting in a final polymer concentration of 1M. Solutions of CPE and PIL with equal charge density were added in stoichiometric ratio to an Eppendorf tube. The tube was vortexed for 1 minute to ensure even mixing. The coacervate droplets that formed during the complexation process (**Figure S3.1**) were collected by centrifugation of the tube at 7000 rpm for 10 minutes. The coacervate phase, which then accumulated at the bottom of the tube, was collected by decanting the supernatant. The residual counterions that partitioned into the coacervate were washed away using dialysis against the THF/water solvent mixture for 3 days, with the solvent being exchanged once every 12 hours. To verify the completion of the dialysis process, AgNO3 was added to the decanted solvent to check for the presence of trace Cl counterions. Since AgCl is poorly soluble, any remaining Cl- in solution rapidly form the

easily detected AgCl aggregates upon AgNO3 addition. If no white AgCl precipitate, then the dialysis process was confirmed to be completed. The dialyzed coacervate was then dried at 50^{o}C under high vacuum (2x10^{-8} Torr) overnight to obtain the dry counterion-free CPCs.

Materials Characterization

1H NMR spectra were recorded at 600 MHz (Varian VNMRS). Gel permeation chromatography (GPC) was performed using a Waters Alliance HPLC system with an Agilent PLgel 5 μm MiniMIX-D column using THF as the eluent. Refractive index traces from a Waters 2414 detector were used for molecular weight determination using polystyrene calibration standards (Agilent Technologies).

Small Angle X-ray Scattering (SAXS)

Samples were loaded into aluminum washers, heated at 50^{o}C overnight under vacuum to remove residual solvent, and cooled slowly to room temperature inside a nitrogen glovebox. These samples were then sealed with Kapton tape. X-ray scattering measurements were performed at the National Synchrotron Light Source II (NSLS-II, beamline 11-BM, Brookhaven National Laboratory), with an X-ray energy of 13.5 keV. Data processing, including detector distance calibration using a silver behenate standard, reduction of 2D raw SAXS images into 1D intensity versus q curves, and corrections for empty cell scattering were performed using the Nika package for Igor Pro for data taken at the ALS, and using the SciAnalysis software for NSLS-II data. Non-linear least-squares fits of scattering profiles to the Teubner-Strey equation were performed using Python SciPy library.

X-ray Photoelectron Spectroscopy (XPS)

Same samples used in X-ray scattering experiments were used for XPS. Experiments were performed using an Escalab Xi+ Spectrometer (ThermoFisher Scientific) with a

monochromatic aluminum Kα X-ray source under a vacuum of ~ 5 x 10^{-9} mbar. Charge compensation was carried out using a dual ion-electron low-energy flood source. High-resolution spectra were recorded at 20 eV pass energy at intervals of 0.05 eV.

Theoretical Model

Our theoretical model is similar to one presented in a recent publication by some of us.[25] We consider a weakly compressible system containing $n_A = n_B = \frac{n_P}{2}$ polycations (A) and polyanions (B), which we model as continuous Gaussian chains having equal degrees of polymerization N, and equal statistical segment lengths b for simplicity. Each polycation/polyanion possesses Q charges that are uniformly smeared along its backbone, giving equal and opposite charge densities $\sigma = \pm\frac{Q}{N}$. In addition, the system contains $n_+ = n_- = \frac{n_{CI}}{2}$ small-molecule monovalent counterions, and is solvent-free. The non-bonded interaction energies in the model include the Flory-Huggins interaction between the polyions:

$$\beta U_1 = \frac{\chi_{AB}}{\rho_0}\int d\boldsymbol{r}\, \check{\rho}_A(\boldsymbol{r})\check{\rho}_B(\boldsymbol{r}) \quad (1)$$

the Coulomb interaction

$$\beta U_c = \frac{l_B}{2}\int d\boldsymbol{r}\int d\boldsymbol{r}'\frac{\check{\rho}_c(\boldsymbol{r})\check{\rho}_c(\boldsymbol{r}')}{|\boldsymbol{r}-\boldsymbol{r}'|} \quad (2)$$

and the Helfand compressibility term

$$\beta U_2 = \frac{\zeta}{2\rho_0}\int d\boldsymbol{r}\,(\check{\rho}(\boldsymbol{r})-\rho_0)^2 \quad (3)$$

Here, $\check{\rho}_i(\boldsymbol{r})$ is the microscopic number density operator for monomers of species i (where $i \in \{A, B, +, -\}$ is the species label, and the labels $i = \pm$ refer to the counterions), $\check{\rho}(\boldsymbol{r}) =$

$\check{\rho}_A(\boldsymbol{r}) + \check{\rho}_B(\boldsymbol{r}) + \check{\rho}_+(\boldsymbol{r}) + \check{\rho}_-(\boldsymbol{r})$ is the total microscopic density operator, $\check{\rho}_c(r) = \sigma\check{\rho}_A(\boldsymbol{r}) - \sigma\check{\rho}_B(\boldsymbol{r}) + \check{\rho}_+(\boldsymbol{r}) - \check{\rho}_-(\boldsymbol{r})$ is the microscopic charge density, and $\rho_0 = \frac{n_A N + n_B N + n_+ + n_-}{V}$ is the bulk density of the system. Note that all microscopic density operators are smeared, having the usual delta function particle density distributions (corresponding to point particles) replaced by normalized Gaussians $\Gamma(\boldsymbol{r}) = (2\pi a^2)^{-\frac{3}{2}} e^{-\frac{r^2}{2a^2}}$,[31] where the smearing range is fixed in this work to be $a = \frac{2}{\sqrt{6}} b \approx 0.8b$; the usage of smeared densities is a regularization strategy that renders the resulting field theory ultraviolet convergent and has become commonplace in polymer field theories in recent years.[32–34] The Flory-Huggins parameter χ_{AB} characterizes the repulsion between unlike backbones, the parameter $l_B = \frac{\beta e^2}{4\pi\epsilon\epsilon_0}$ is the Bjerrum length (where $\beta = \frac{1}{k_B T}$, ϵ_0 is the vacuum permittivity of free space, ϵ is the bulk dielectric constant and e is the elementary charge) and ζ is a parameter that sets the compressibility of the system, which is fixed here to $\zeta = 1$ as in similar recent work.[33]

Using standard techniques, the canonical partition function for the above model in the field-theoretic representation takes the form of a functional integral over field configurations [35]

$$Z = Z_0 \int \mathcal{D}w_1 \int \mathcal{D}w_2 \int \mathcal{D}w_3 \int \mathcal{D}\varphi \; e^{-H[w_1, w_2, w_3, \varphi]} \quad (4)$$

where the fields $w_i(\boldsymbol{r})$ are exchange-mapped chemical potential fields responsible for mediating the Flory-Huggins interaction and Helfand compressibility, and $\varphi(\boldsymbol{r})$ is the electrostatic potential field. Here the pre-factor Z_0 contains the ideal gas terms as well as normalization factors from the Hubbard-Stratonovich transforms. The Hamiltonian

$H[w_1, w_2, w_3, \varphi]$ and related details are presented in the Supporting Information. In order to examine the structure of the fluctuating disordered phase of this model, we will employ field-theoretic simulations with complex Langevin sampling (CL-FTS), which allows us to sample the above statistical field theory model without approximation.[36–43] This approach has been previously used to study polyelectrolyte complexes in various contexts.[44–49] In CL-FTS, the auxiliary fields are promoted to be complex variables and are sampled according to the following Langevin equations of motion:

$$\frac{\partial w_i(\boldsymbol{r},t)}{\partial t} = -\lambda_{w_i}\frac{\delta H[\{w\},\varphi]}{\delta w_i(\boldsymbol{r},t)} + \eta_{w_i}(\boldsymbol{r},t) \quad (5)$$

$$\frac{\partial \varphi(\boldsymbol{r},t)}{\partial t} = -\lambda_{\varphi}\frac{\delta H[\{w\},\varphi]}{\delta \varphi(\boldsymbol{r},t)} + \eta_{\varphi}(\boldsymbol{r},t) \quad (6)$$

where the $\eta_j(\boldsymbol{r},t)$ are real-valued and Gaussian-distributed white noise variables with zero mean ($\langle \eta_j(\boldsymbol{r},t) \rangle = 0$) and which satisfy the fluctuation-dissipation theorem ($\langle \eta_i(\boldsymbol{r},t)\eta_j(\boldsymbol{r}',t') \rangle = 2\lambda_j\delta_{ij}\delta(\boldsymbol{r}-\boldsymbol{r}')\delta(t-t')$). In order to compute a given observable (such as the structure factors presented below), the field-theoretic operator corresponding to that observable is computed as a time average on the complex Langevin trajectory, leveraging the ergodic principle.

In addition to sampling the exact field theory in this work via CL-FTS, we will also consider the particle-center structure factor predictions of the random-phase approximation (RPA) for the same model. In the RPA calculation, the fields are assumed to fluctuate weakly about the

homogeneous saddle point, and the structure factor calculation involves an expansion of the Hamiltonian up to quadratic order in the fields. The RPA calculation for the model above was carried out in a previous work, [25] which we refer the reader to for more details. For the *counterion-free* symmetric system ($N_A = N_B = N$, $b_A = b_B = b$, $\sigma_A = -\sigma_B = \sigma$), the RPA result for the particle-center structure factor $\frac{S_{AA}(k)}{N} = \frac{\langle \hat{\rho}_A(\boldsymbol{k})\hat{\rho}_A(-\boldsymbol{k})\rangle}{N\hat{\Gamma}^2(k)}$ is given by

$$\frac{S_{AA}(k)}{N} = \frac{\Omega(k)}{(\Omega^2(k) - \Lambda^2(k))\hat{\Gamma}^2(k)} \quad (7)$$

where the wavevector-dependent correlation functions Ω and Λ are given by

$$\Omega(k) = \zeta N + \frac{\gamma(\sigma N)^2}{k^2 R_g^2} + \frac{2}{\hat{g}_D(k)\hat{\Gamma}^2(k)} \quad (8)$$

$$\Lambda(k) = \zeta N + \chi_{AB} N - \frac{\gamma(\sigma N)^2}{k^2 R_g^2} \quad (9)$$

Note here that $\hat{g}_D(k) = \frac{2}{k^4 R_g^4}\left(e^{-k^2 R_g^2} - 1 + k^2 R_g^2\right)$ is the Debye function, $R_g = \sqrt{\frac{N}{6}}b$ is the ideal chain radius of gyration, $\hat{\Gamma}(k) = e^{-\frac{a^2 k^2}{2}}$ is the Fourier transform of the Gaussian smearing function, and $\gamma = \frac{4\pi}{6} l_B \rho_0 b^2$ is a dimensionless parameter that characterizes the strength of the electrostatic interactions in the PEC. Note that for the purposes of comparison with CL-FTS simulations, in which the chain backbone contour is discretized, we use Debye functions in our RPA expressions that are computed with the same chain contour discretization as the simulations – these have a slightly different behavior at large-k than the

continuum Debye function given above, but give the same large-k behavior as the CL-FTS results.

3.4 Results and Discussion

The goal of this study is to investigate ionic compatibilization of a CPE and a PIL, and how electrostatic interactions can be utilized to tune the morphology of the resulting blend. A series of copolymers with charged repeat units randomly distributed along the polymer backbone was used as the model system. 4 different charge fractions, 50%, 60%, 75% and 100%, were used (**Figure 3.1**) to vary the strength of electrostatic attraction between polymers in each CPE-PIL pair. Because thiophene-based polymers have been studied extensively both in solution and solid state, and the information on chain conformation and solid state packing is readily available, we used a thiophene-based CPE, poly[6-(thiophen-3-yl)hexane-1-sulfonate-co-3-(hexylthiophene)] copolymers, with tetramethyl ammonium (TMA) counterion for this model system. Acrylamide-based imidazolium-functionalized PIL, poly[(3-methyl-1-propylimidazolylacrylamide)-co-3-methyl-1-(propyl acrylamide)], with chloride counterions was chosen to pair with the CPE. This is because the imidazolium group has been shown to have a wide electrochemical stability window,[50] thus the incorporation of such electrochemically stable PIL enables further investigation of this CPC in electrochemical applications.

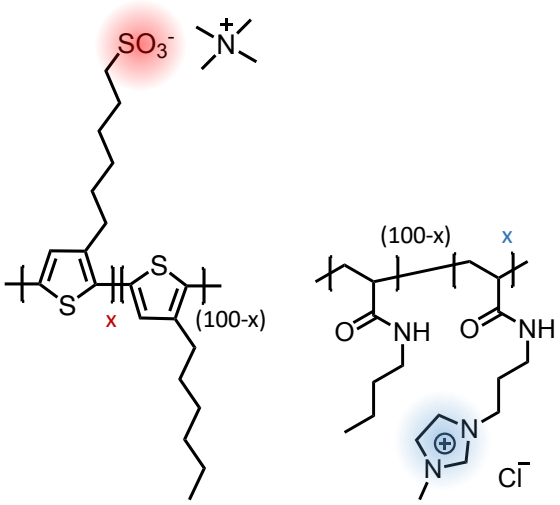

Figure 3.1. Chemical structures of CPE (left) and PIL (right) copolymers utilized in this study. x indicates the mole fraction of charged repeat units, which were spaced out randomly along the polymer chains. We chose 4 different x values: 50%, 60%, 75% and 100% (fully charged polymer).

To isolate charge fraction as the primary variable controlling complexation strength, the same mixing conditions were used to obtain the CPCs. Stock solutions of CPE and PIL were prepared by dissolving the polymer in a 40% THF in water mixture, resulting in a final polymer concentration of 1M. Due to the poor solubility of CPE with < 50% charged repeat units in the employed solvent mixture, in this study we only investigated concentrations above 50% charge fraction. In order to achieve the stable/meta-stable blend, we first obtained the coacervate of the CPE and PIL, and then remove solvent from the coacervate to get the dry CPCs. Unlike more traditional systems used to study coacervation in which coacervation occurs in an added salt environment, in these conjugated systems, the addition of THF promoted the formation of the CPE-PIL coacervate with a broad coacervation window. Similar observations of coacervation between a CPE and a non-conjugated polyelectrolyte upon the addition of THF were the subject of earlier studies.[51] When a CPE-PIL coacervate was formulated in purely aqueous media, the coacervation window was quite narrow and the

system required very high added salt concentration to transition from the kinetically trapped precipitate phase to the coacervate phase.[10] As the presence of the conjugated backbone in these systems introduces additional intermolecular forces, such as π–π stacking, hydrophobic interactions, and cation−π interactions, these systems have a complex mixing thermodynamics that can be very different from non-conjugated systems. For example, prior studies demonstrate that solvent quality plays a critical role in the complexation behavior of systems with conjugated polymers due to the strong hydrophobic interactions within the system.[51] Potential changes to the CPE chain conformation were proposed to result in a significant enthalpic driving force to the complexation process.[52] These studies have illustrated the intriguing physics of conjugated polymer complex systems, highlighting the need of further investigation to fully understand their complexation thermodynamics.

Electrostatic interactions prove to be a powerful pathway for compatibilizing CPEs and PILs, with the microstructure of the resulting complex controlled by polymer charge fraction. In particular, CPE-PIL coacervation occurred across all charge fractions with no macrophase separation observed, indicating the effective mixing of all polymer pairs in this study. However, as illustrated in **Figure 3.2a**, CPCs with partially charged polymers show evidence of local structure formation except for CPC100 whose featureless scattering profile suggests a homogeneously disordered morphology. Particularly, a single broad peak located at $q \approx 0.12 - 0.15$ $Å^{-1}$,corresponding to a length scale of around 5 nm, shows up in SAXS traces of CPC75, 60 and 50. This scattering peak likely corresponds to the length scale of concentration fluctuation caused by the formation of CPE-rich and PIL-rich nanodomains. The emergence of these nanophases is likely induced by the short-range repulsion among the polymers'

immiscible backbones. At lower polymer charge density, these repulsive interactions can compete more effectively with complexation forces, giving rise to microphase segregation. This scattering peak shifts to lower q and gets sharper with decreasing polymer charge density, suggesting an increase in the length scale of segregation and the formation of more well-defined interfaces among nanodomains. Our experimental observation is consistent with prior theoretical studies, where it has been shown that weakening the strength of Coulombic interactions in charged polymer blends enlarges the domain size of their microphase segregated structures.[23,25–27] However, the breadth of the scattering peak and the lack of higher order peaks in the scattering traces of partially charged CPCs indicate that they still maintain a globally well-mixed morphology, with some local nanostructure. The sharpening of the scattering peak at low polymer charge density likely suggests the shift of the CPC's morphology from mean-field disordered to fluctuating disordered nanostructure that resembles a block copolymer melt when heated above the T_{ODT}. Such structures have been shown to possess some topological similarities to a bi-continuous microemulsion, [53] which could be useful in various applications such as filtration membranes or battery electrolytes.

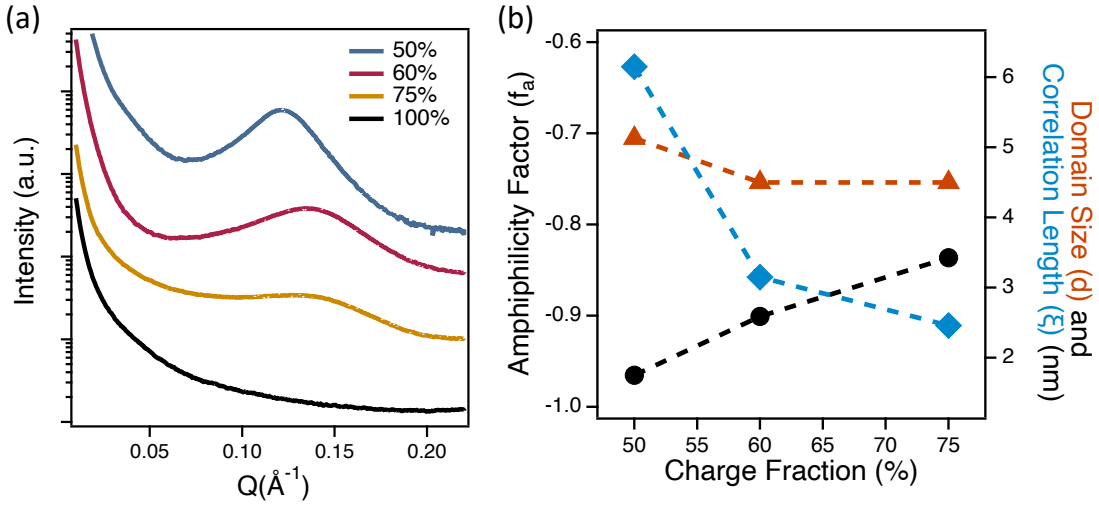

Figure 3.2. (a) Background-subtracted SAXS profiles of CPCs show dependence of peak position, width, and intensity on polymer charge fraction. As the complexation strength decreases, the CPC remains macrophase-mixed, but with more nanoscale texturing. Traces have been shifted vertically for clarity (b) Amphiphilicity factor, domain size and correlation length of CPCs obtained from fitting their scattering traces to the Teubner-Strey equation. The dependence of these 3 parameters on polymer charge fraction is in agreement with the evolution of the scattering peak with complexation strength observed in SAXS.

To quantitatively investigate the morphology of the CPCs in the aforementioned locally structured states, we fit their scattering traces to the Teubner−Strey (TS) model,[54] which is based on a Laudau expansion of a blend free energy. Besides the Berk model,[55] which utilizes the generalized theory of spinodal decomposition to account for microemulsion scattering, the TS model is commonly used for systems that take on a microemulsion-like structure.[53,56,57] Geometric approaches that consider the emulsion to be a distorted lamellar structure [58] also result in a functional form of the correlation function similar to that derived by Teubner and Strey. The TS equation takes in the following form:

$$I(q) = \frac{1}{a_2 + c_1 q^2 + c_2 q^4} \quad (10)$$

Where a_2, c_1 and c_2 are the fitting parameters. From this model, 3 important factors can be extracted:

$$d = 2\pi \left[\frac{1}{2} \left(\frac{a_2}{c_2} \right)^{\frac{1}{2}} - \frac{1}{4} \left(\frac{c_1}{c_2} \right) \right]^{\frac{-1}{2}} \quad (11)$$

$$\xi = \left[\frac{1}{2} \left(\frac{a_2}{c_2} \right)^{\frac{1}{2}} + \frac{1}{4} \left(\frac{c_1}{c_2} \right) \right]^{\frac{-1}{2}} \quad (12)$$

$$f_a = \frac{c_1}{\sqrt{4a_2c_2}} \quad (13)$$

Where d represents the domain size, ξ is the correlation length that indicates the distance over which structural correlations persist,[56,59] and f_a is the amphiphilicity factor that takes on a value between 0 and -1 for microemulsion structures (f_a = -1 corresponds to the lamellar phase, and f_a = 0 is where the system crosses over the Lifshitz line).[60]

Even though TS equation was motivated by the scattering behavior of oil/water/surfactant microemulsions, we found the model to fit relatively well to the scattering data (**Figure S3.2**), suggesting that the partially-charged CPCs form good microemulsions. For CPC50 especially, the peak position and the q^{-4} decay at large q match the experimental data reasonably well. The q^{-4} decay fit becomes slightly worse for CPCs with stronger electrostatic interactions, indicating the lack of sharp interfaces in these complexes. For all CPCs, the TS fit fails to capture the scattering upturn at low q which we attribute to the inaccuracy in background subtraction and some concentration fluctuation that happens at larger length scale. We hypothesize that the microemulsion morphology of these CPCs is likely co-continuous, rather than droplet or multilayers vesicle, due to the compositional symmetry of the blends and as suggested by simulation snapshots (**Figure S3.6**). An analogous morphology was predicted for polymer blends compatibilized by hydrogen bonding in a recent study,[57] where simulations predict a bi-continuous microemulsion structure for systems with intermediate hydrogen bonding strength regardless of the placement of hydrogen bonding sites along the polymer backbones.

The 3 aforementioned physical parameters calculated from the TS fit provide further quantitative insights on how the local ordering of CPCs is enhanced with decreasing polymer charge fraction. As shown in **Figure 3.2b**, all CPCs have their amphiphilicity factor f_a values in the range of 0 and -1, suggesting the microemulsion characteristic of these CPCs. As the CPC's charge fraction becomes smaller, f_a becomes more negative and approaches − 0.96 for x = 50%. Since $f_a = -1$ corresponds to lamellar structure, this suggests that CPC50 locally resembles a lamellar morphology, with distortion of the lamellar stacks happening at larger length scales. While CPC60 and CPC75 have less negative f_a, their values are still well below 0 and thus suggest a significant concentration of interfaces presence in these complexes. We postulate that such interfaces are caused by the tendency of CPE chains to be in proximity due to their attractive intermolecular forces, such as π-π stacking and hydrophobic interaction. In agreement with the trend in f_a values, ξ increases with decreasing charge density. Since ξ reflects how far a certain structural correlation persists, a larger value of ξ indicates higher level of ordering in the system. Given the sharp increase of ξ going from CPC60 to CPC50, it is likely that the CPC transitions from a mean-field-like to a co-continuous fluctuating disordered state between these 2 charge fractions. The dependence of domain spacing, *d,* on the polymer charge fraction *x*, however, is rather modest. In particular, *d* only increases from 4.6 nm to 5.1 nm when *x* was decreased from 75% to x = 50%. The variations in how f_a, ξ and *d* change with respect to *x* underscores the significant impact of electrostatic interactions on the segregation-induced morphology of CPCs within the range of polymer charge density chosen in this study, while the length scale of the segregation only shows a minimal change.

In agreement with our experimental observation of effective CPE-PIL mixing across all charge fractions used in this study, our RPA calculation suggests that charged polymer complexes stay well-mixed down to extremely low polymer charge density before crossing the order-disorder transition (ODT) threshold. **Figure 3.3** shows this universal RPA prediction for the ODT value of χN, as a function of $\gamma(\sigma N)^2$ where σ is the density of charge per polymer chain. The RPA expression for the structure factor indicates that in the special case of a symmetric CPC without counterions, the ODT should collapse to a universal curve that depends on the electrostatic interactions only through the dimensionless group $\gamma(\sigma N)^2$. Determining the precise value of γ for RPA calculations of our experimental system is challenging because it requires the exact values of the statistical segment length and the conformation of polymer chains inside the complex, as well as the bulk dielectric constant of the CPC environment. However, rough estimations can be made assuming a dielectric constant of 2-3, which are typical values for polymer melts, a number-density of 1 repeat unit for every nm^3, and a polymer statistical segment length between 2 and 6 nm (corresponding to roughly 2 to 6 repeat units per segment). It should be noted that prior studies on conjugated coacervate have raised some speculations on the extension of CPE chains upon complexation, yet more concrete observations of such extension are still lacking.[10,51] As a result, the aforementioned estimation of statistical segment length likely underestimates the actual value of γ for this system due to potential extension of polymer chains in the CPC. Nonetheless, the estimation yields γ values within the range of 150-250, implying that we should at least assume that γ is of order 10^2. Assuming that polymer length N is also in the order of 10^2, the parameter $\gamma(\sigma N)^2$ is of order 10^4 for fully charged polymer complexes. As shown in **Figure 3.3**, crossing the ODT of such system requires $\chi N \approx 700$, corresponding to χ value of 7 which

is rarely seen in any polymer backbone pair. Our calculation indicates that prohibitively large values of χN are required to drive the system to phase separate *unless the polymer charge density is very low* ($\sigma N \sim 1$), meaning one or a few charges per polymer chain. This low charge-density requirement is quite stringent if one wishes to obtain the ordered microphases, but it also underscores the power of electrostatic interactions to compatibilize polymer blends comprising completely different backbones that would not normally be miscible.

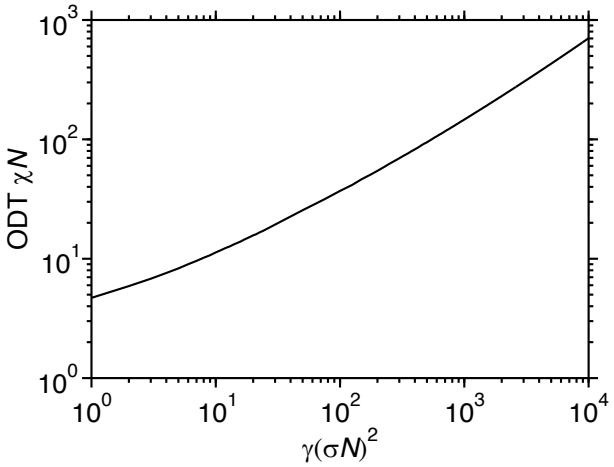

Figure 3.3. Value of $\chi_{AB}N$ needed to cross the ODT, as a function of dimensionless group $\gamma(\sigma N)^2$, according to RPA, for a symmetric CPC without counterions.

An examination of the density correlations using RPA also suggests qualitative agreement with X-ray scattering with respect to the dependence of CPC morphology on polymer charge fraction. As shown in **Figure 3.4a**, the polycation-polycation structure factor ($S_{AA}(k)$) at $\gamma = 20$ is a function of charge fraction: the structure factor peak shifts to larger wavevector and diminishes in intensity when the polymer charge density increases. For large charge densities, a shoulder in the structure factor becomes apparent (this can be seen most clearly for $\sigma = 1.0$). This underlying feature appears to be caused by the particle smearing in the model, as it is independent of the electrostatic parameters but changes with the smearing range (**Figure**

S3.7), and thus is not a feature that we are interested in here. As highlighted earlier, the value of γ in our system could be as high as 250. However, due to challenges associated with conducting FTS simulations at such high electrostatic strength, as well as difficulties in interpreting RPA at such large γ due to the above-mentioned smearing-related feature, we will consider more moderate values of γ in our theoretical comparisons. Most importantly, we note that while the specific value of γ does affect the overall structure factor peak intensity and wavevector, it does *not* appear to have a qualitative effect on the complexation strength *dependence* of the structure factors. This can be seen more clearly in **Figure 3.4b**, which shows the dependence of the domain size (given by $L = \frac{2\pi}{k_m}$, where k_m is the electrostatic correlation peak wavevector from the structure factor) on the polymer charge fraction for different values of gamma ranging from small ($\gamma = 1$) to relatively large ($\gamma = 50$). The domain size decreases monotonically as charge density is increased, and diverges as $\sigma \to 0$ where the conventional (uncharged) binary blend limit (with peak wavevector $k_m = 0$) is recovered. Though not investigated in this study, a prior study of on charged polymer blends with low charge fraction also reported a transition of the blend from a homogeneous single-phase to a macrophase separated mixture as charge fraction was decreased from 5% to 2%.[61] This observation is in line with the how quickly the domain size increases at low polymer charge fraction σ as shown in **Figure 3.4b**. Increasing γ reduces the length scale associated with the concentration fluctuations overall, but does not change the trend with charge density. For a given fixed value of gamma, the change in this length scale with charge density is rather modest (provided that the charge density is not close to zero), in agreement with the trend observed for domain size d shown in **Figure 3.2b**. Note that our theoretical model assumes linear and uniformly charged polymer chains and thus ignores the side-chain architecture and

consequent monomer aspect ratio of the experimental system. However, qualitative agreement between RPA calculations and experimental SAXS data was still achieved, suggesting that the observed trends are primarily governed by electrostatic parameters such as the overall charge density of the chains, rather than the specific backbone architecture

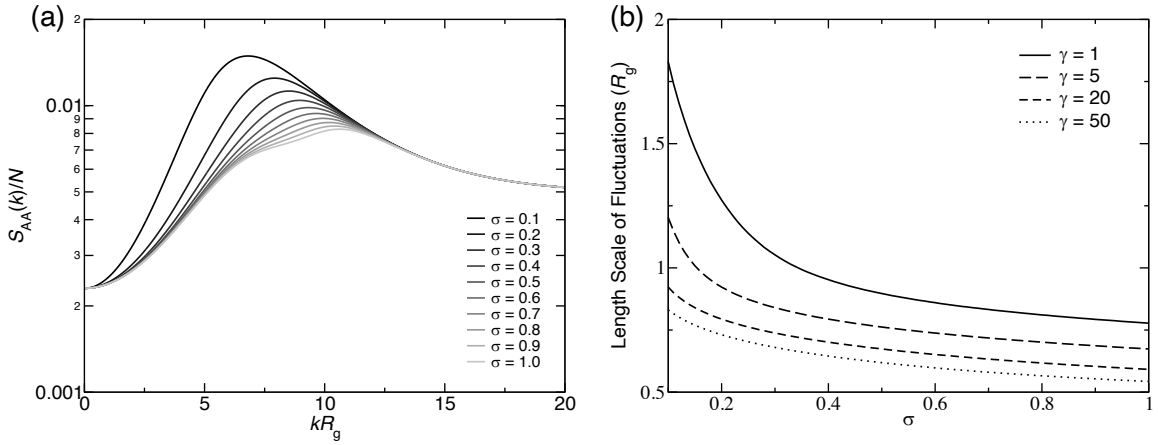

Figure 3.4. a) RPA structure factor dependence on polymer charge fraction σ, for $\gamma = 20$. b) Length scale of concentration fluctuations (obtained from the peak positions k_m) as a function of σ for several values of γ. All results use $N = 100$, $\chi_{AB} = 0.15$ and correspond to counterion-free systems.

Besides polymer charge fraction, an important parameter that is also frequently examined in theoretical studies is the concentration of counterions in the polymer complex.[23,62] In this study, we probed the impact of counterion concentration on CPCs structure by comparing CPCs with and without the dialysis step. Prior to dialysis, dry CPCs contain residual counterions that partition into the polymer complex during the coacervation process. The presence of these residual counterions is confirmed by the strong Cl peaks in high-resolution XPS scans of all CPC samples before dialysis (**Figure S3.3**). These peaks disappeared in XPS traces of all CPCs after dialysis, confirming that dialysis effectively yielded counterion-free CPCs. To understand the dependence of CPCs structure on the inclusion/removal of

counterions, SAXS profiles of CPCs before dialysis were also collected and compared to that of counterion-free CPCs. Because TMACl (the salt of the 2 counterions) does not show any scattering peak in the SAXS region (**Figure S3.4**), any difference in the SAXS traces of CPC samples with and without counterions was not caused by salt scattering and thus is attributed to the ion-induced structural perturbations.

Similar to polymer charge density, the concentration of counterions also influences the structure of CPCs, but likely via a combination of ionic screening and excluded volume effects. As shown in **Figure 3.5a**, except for CPC100 which stays homogeneously disordered regardless of the counterion concentration, the scattering peaks of all partially charged CPCs with counterions are at lower q values and are broader compared to those of counterion-free CPCs. This trend suggests that the presence of counterions leads to larger domain size and less ordered local structure in microphase-segregated charged polymer complexes. The amphiphilicity factors extracted from TS fit for CI-containing CPCs are also closer to 0 than those of the CI-free CPCs (**Figure S3.5**), implying that the inclusion of counterions in the systems leads to more disordered structure with less well-defined interfaces. These impacts are likely driven by 2 factors. Firstly, the added ionic strength from counterions can effectively screen the electrostatic attraction among polymer side chains, leading to stronger segregation between CPE and PIL. This effect is analogous to lowering polymer charge fraction, which also increases domain size and improves local ordering, thus enhancing the intensity of the scattering peaks, in CPCs. Another factor is the excluded volume of counterions, which can swell the polymer complex and dilute the structure. Such dilution effect can also result in increasing domain size and swelling of the interfaces among the domains. Given the shift in

the scattering peak is rather modest, it is not clear which of these effects is the primary cause for the counterion-dependence of CPC structure.

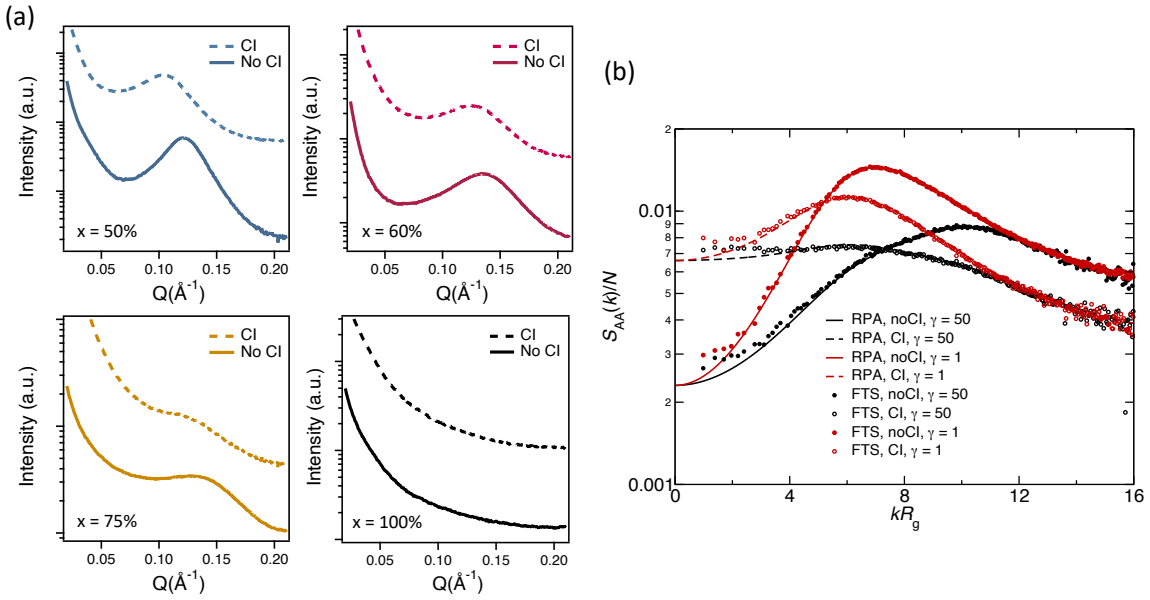

Figure 3.5. (a) SAXS traces of CPCs before (dashed line) and after (solid line) dialysis. For CPCs with microphase segregation, the presence of residual counterions (CI) shifts the scattering peak to lower q and broadens the peak relative to CI-free CPCs. Data has been shifted vertically for clarity (b) Effect of counterions on the structure factor peak intensity and position in RPA and CL-FTS simulations for the $x = 50\%$ CPC. Solid lines/filled symbols correspond to the counterion-free system, and dashed lines/hollow symbols correspond to the system with charge-neutralizing counterions. $\gamma = 1$ is shown in red, $\gamma = 50$ in black, and in both cases $\chi_{AB}N = 15$.

Results from FTS and RPA, as shown in **Figure 3.5b**, show that the presence of counterions weakens CPC scattering peak and shifts the peak to lower q values, in qualitative agreement with SAXS data. In our model, the size of the counterion is assumed to be similar to that of a polymer repeat unit. Values of $\gamma = 1$ and $\gamma = 50$ are shown, for a charge fraction of $\sigma = 0.5$. Despite a factor of 50 difference in the 2 chosen γ values, a same trend was observed on how the structure factor changes with respect to counterion presence for both γ values. This qualitative agreement between the two scenarios again confirms that the precise value of γ is not so critical to describe qualitatively the features of the disordered CPC structure.

Furthermore, the RPA (lines) and CL-FTS (points) results are in excellent agreement, indicating that RPA provides a very accurate approximation for this system. To visualize the weaker segregation strength and less ordered local structure in CPCs with retained counterions, we conducted a line scan of the concentration fluctuations through the system (**Figure 3.6**) in simulation. The change in the interface sharpness, or the local ordering, of CPCs with and without counterions can be seen from the clear difference in concentration fluctuation within CPCs with and without counterions. However, the rather modest change in the length scale of the fluctuations (which is quantified by the shift in peak position in the structure factors of **Figure 3.5**) is more difficult to see visually.

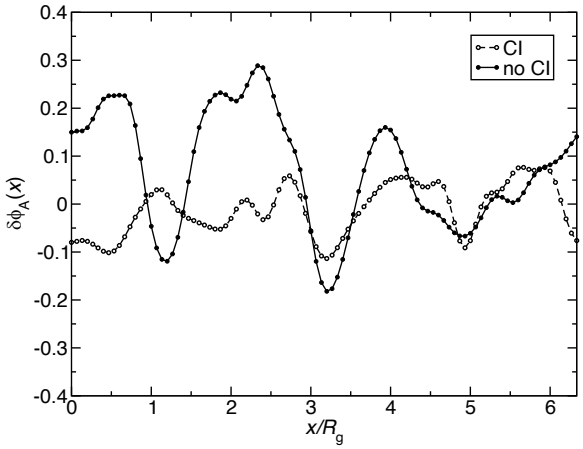

Figure 3.6. Example line scan of concentration fluctuations of the polycation ($\delta\phi_A(x) = \phi_A(x) - \phi_A$) through the simulation box in CL-FTS, for the 50% CPC with $\gamma = 50$ and $\chi_{AB}N = 15$. Filled symbols (solid lines) are without counterions, hollow symbols (dashed lines) are with counterions.

3.5 Conclusions

This study illustrates that ionic interactions can be a powerful pathway to compatibilize two polymers with very different backbone chemistries (CPE and PIL), and to control the morphology of the resulting polymer complexes. Effective mixing of the CPE and the PIL was observed across all polymer charge fractions used in this study. While the ability to

compatibilize polymers by ionic interactions is not new, prior experimental studies only focused on the weak complexation regime where the blend resembles a supramolecular block copolymer and self-assembles to form ordered morphology.[63–65] This was achieved by adding only a few, or even just 1, charged repeat unit per polymer chain. This study demonstrates that in the intermediate complexation regime when the blend appears to be homogeneously mixed, some short-range local ordering with domain size of a few nm can emerge. In particular, when the complexation strength was decreased via lowering of the polymer charge fractions, microphase separation happened, leading to the formation of CPE-rich and PIL-rich domains ranging between 4 nm to 5 nm in size while the complexes still maintained globally disordered structures. The morphology of these microphase-segregated CPCs is microemulsion-like and likely co-continuous, resembling that of a block copolymer heated above the T_{ODT}. Lastly, manipulation of electrostatic parameters, such as polymer charge fraction and counterion concentration, enable effective control of the local nanostructure such as the domain size and the interface width.

Our observations imply that ionic interactions have great potential in engineering the nanostructure of globally disordered polymer complexes. Prior studies done on disordered block copolymers quenched right above the T_{ODT} have suggested that the presences of the nanoscopic and percolating domains can be beneficial in separation, catalysis, and energy applications.[9,53,56,66] However, achieving such morphology in block copolymers is challenging because the structure only exists right above the ODT temperature and often requires kinetic trapping, chemical crosslinks, or swelling the interface with the addition of a homopolymer. As a result, investigation on stabilized local structures within disordered block copolymers is

still limited compared to the breadth of studies on ordered block copolymers with thermodynamically equilibrated microstructures. This electrostatic assembly pathway offers an exciting opportunity to stabilize this unique structure with great versatility and without introducing any synthetic, kinetic or thermal limitations. In broader contexts, charged polymer complexes also offer much easier structural control compared to the traditional block copolymers. For example, structure variations in charged polymer complexes can simply be achieved by changing the concentration of added salt, or mixing the two polymers in different compositions. In contrast, utilizing the block architecture would require synthesizing an entirely new polymer to achieve similar results. Lastly, we have shown that ionic compatibilization enables the macroscopically homogeneous mixing of a conjugated polymer with a non-conjugated counterpart. This study thus opens up exciting directions in formulation of multifunctional electronic materials via ionic complexation of CPEs with another functional polymer. The morphology of such polymer complexes can be controllably tuned via electrostatic manipulations, enabling fundamental studies on structure-property relationships or for optimization of optoelectronic and other properties.

3.6 Acknowledgement

This work was primarily funded by the Department of Energy Office of Basic Energy Sciences under Grant No. DE-SC0016390. DG and GHF would like to acknowledge funding from DE-SC0019001 for support of the theory and computational work included. The authors acknowledge the use of shared facilities of the UCSB MRSEC (NSF DMR 1720256), a member of the Materials Research Facilities Network (www. mrfn.org). This research used

resources of the National Synchrotron Light Source II, a U.S. Department of Energy Office of Science User Facility (DE-SC0012704; beamline 11-BM).

3.7 Appendix

Synthesis of Poly(3-(6'-bromohexyl)thiophene-co-3-hexylthiophene) (P3BrHT:P3HT)

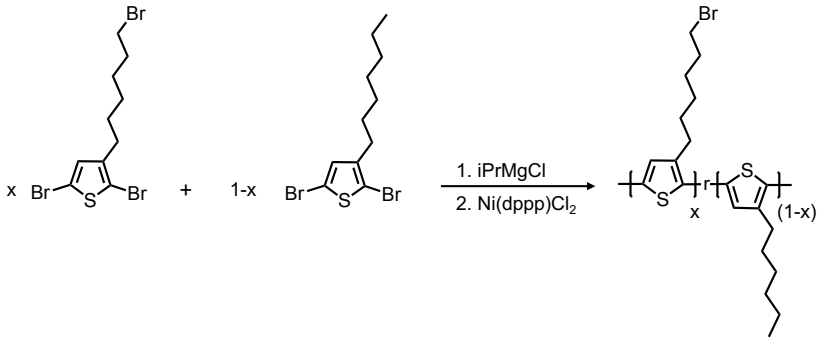

Synthesis of P3BrHT:P3HT random copolymers was carried out following a previously reported protocol.[67] 2,5-dibromo-3-(6-bromohexyl)thiophene and 2,5-dibromo-3-hexylthiophene were mixed in 9:1 molar ratio in an oven-dried round bottom flask equipped with a magnetic stir bar. The reaction flask was sealed with rubber septa and was dried overnight under active vacuum. Anhydrous THF was added to the flask to dissolve the dry monomer mixture, and the flask was purged with dry nitrogen for 20 minutes. Isopropylmagnesium chloride was added dropwise to the reaction flask, and the mixture was stirred at ambient temperature under nitrogen. Care was taken to prevent contact of isopropylmagnesium with air during the transferring process. After 2 hours, Ni(dppp)Cl2 suspended in dry THF was added to the reaction. Immediate color change from pale yellow to vibrant red was observed, indicating the polymerization taking place. After 12 hours, the polymerization was quenched by rapid addition of 1M HCl solution, and was precipitated into cold methanol. The obtained polymer was purified by washing in a Soxhlet apparatus with

methanol, acetone, and ethyl acetate before extraction with THF. The product was concentrated under vacuum, yielding a red-purple solid. The isolated product was then dried overnight under vacuum to remove any remaining solvent.

Synthesis of Poly[6-(thiophen-3-yl)hexane-1-sulfonate-co-3-(hexylthiophene)]

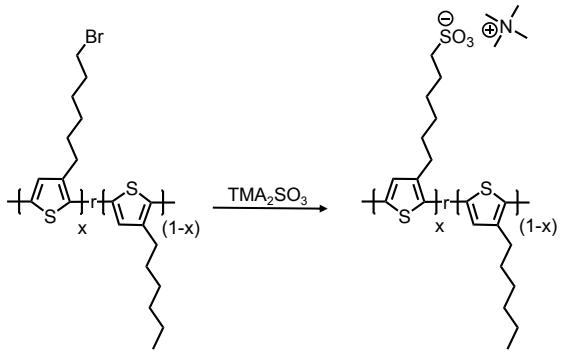

P3BrHT-P3HT was dissolved in THF in a round bottom flask equipped with a magnetic stir bar. The flask was sealed with a rubber septa, and the solution was purged with dry nitrogen gas for 30 minutes. 1M bis(tetramethylammonium)sulfite (TMA2SO3) salt solution in methanol was prepared following a previously reported protocol.[68] 10-fold excess of TMA2SO3 was added to the reaction flask, and the mixture was heated to 70°C and refluxed for 1 hour. After that, more methanol was added to the reaction mixture to help dissolve the ionic-functionalized polymer and drive the reaction to completion. The reaction mixture was left to react overnight. The polymer was purified by dialyzing using 10 kDa cutoff dialysis membranes against deionized water for 3 days, with the dialysate replaced every 12 h. The isolated product was dried with lyophilizer, yielding the CPE as a red-purple solid.

Synthesis of Poly(N-hydroxysuccinimidyl acrylate) (PNHSA)

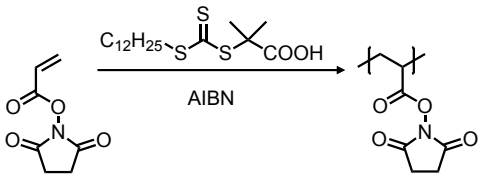

Synthesis of PNHSA was carried out following a previously reported protocol.[69] In a Schlenk flask equipped with a magnetic stir bar, N-acryloxysuccinimide, DDMAT, and AIBN were dissolved in anhydrous DMF. The solution was degassed using five freeze-pump-thaw cycles. After the fifth cycle, the flask was filled with dry nitrogen and heated to 70˚C in an oil bath. The reaction was kept at that temperature for 24 h, and during the process the mixture was stirred vigorously. After cooling to 25˚C, the polymer was precipitated from methanol, filtered and dried in ambient, dissolved in DMF and reprecipitated from methanol, twice. The polymer was filtered and dried under a vacuum at 60˚C for 24 h to yield a pale yellow powder.

Synthesis of Poly[(1-propylimidazolacrylamide)-co-3-methyl-1-(propyl acrylamide)]

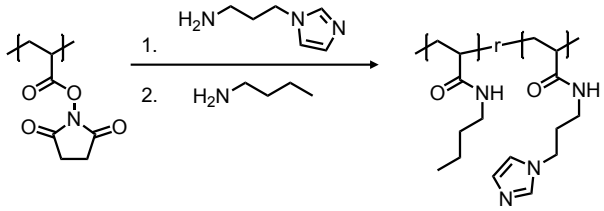

PNHSA repeat units were randomly functionalized with imidazole-amine and butylamine following a previously reported protocol.[70] The polymer was first dissolved in anhydrous DMF in a round bottom flask. The flask was sealed with rubber septa and degassed with dry nitrogen for 30 minutes. After that, appropriate molar equivalent (50%, 60%, 75% and 100%) of 1-(3- aminopropyl)imidazole solution in anhydrous DMF was added dropwise to the vigorously stirring polymer solution. The reaction was left running for 12 hours at 25˚C using a water bath. The resulting polymer was precipitated from ethyl acetate, dissolved in methanol, and re-precipitated from diethyl ether twice. The polymer was collected by centrifugation and dried under a vacuum at 60˚C for 12 h to obtain a pale yellow brittle solid. It was then dissolved in anhydrous DMF and the NHSA groups were reacted with 5-fold

excess of butylamine for 12 h at 25˚C f to yield the neutral random copolymers. NMR end-group analysis indicate an average DP of 60 for the PIL.

Synthesis of Poly[(3-methyl-1-propylimidazolylacrylamide)-co-3-methyl-1-(propyl acrylamide)]

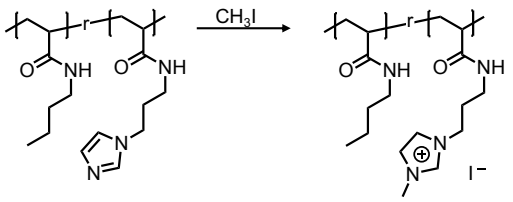

In a round bottom flask, the neutral copolymer was dissolved in anhydrous DMF. The flask was sealed with a rubber septa, and the solution mixture was purged for 30 minutes using dry nitrogen. 3-fold excess of iodomethane (with respect the imidazole) was added to the flask, and the reaction mixture was heated slightly and kept at 40^{o}C for 12 hours. The polymer was then precipitated from diethyl ether and dried under vacuum overnight. The iodine anion was exchanged to chloride by co-dissolving the polymer in methanol with 10-fold excess of NaCl. This mixture was stirred vigorously at 45^{o}C overnight. After that, the solution mixture was dialyzed using a 10 kDa cutoff dialysis membranes against methanol for 4 days, with the dialysate replaced every 12 h. The isolated product was dried under vacuum at 90˚C for 24 h, yielding an off-white solid.

Table S3.1. Mn, Mw and PDI of CPBr precursors

Sample	Mn	Mw	PDI
CPBr100	12.2	22.9	1.88
CPBr75	8.70	11.9	1.37
CPBr60	8.34	11.2	1.34
CPBr50	8.95	12.9	1.44

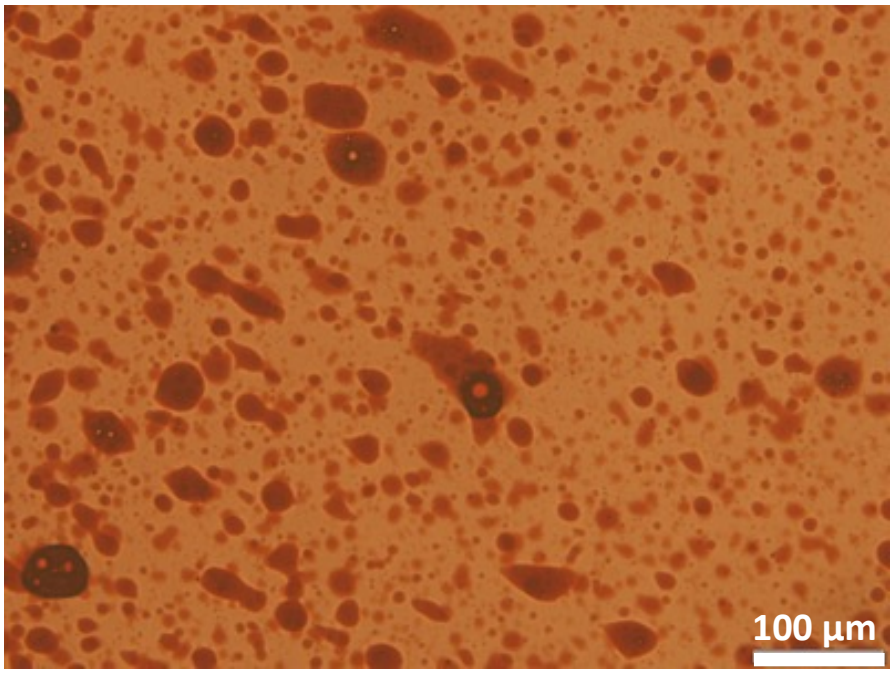

Figure S3.1. Formation of CPE-PIL coacervate (red) droplets upon mixing, in co-existence with the dilute supernatant (orange background). Example shown for x = 50%

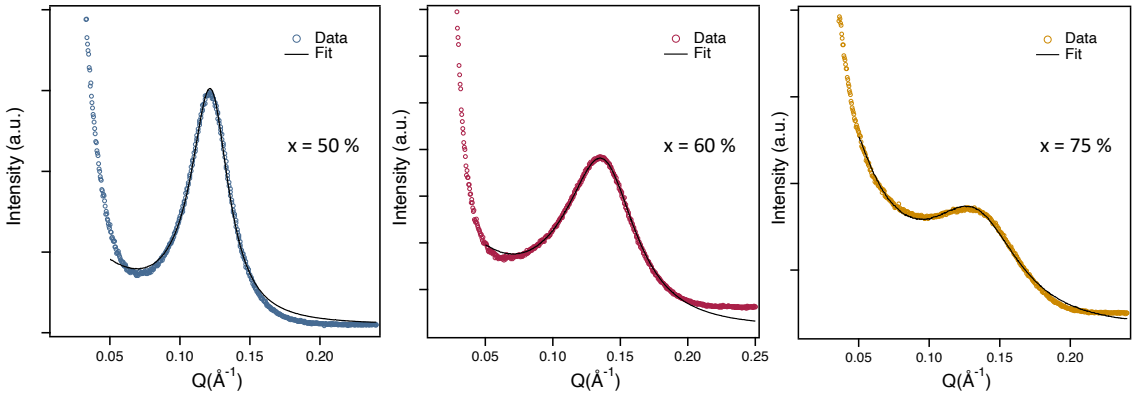

Figure S3.2. Fit results of TS model to the scattering profiles of CPCs with microphase segregation

Table S3.2. Fit parameters of TS model

Sample	a_2	c_1	c_2
CPC75	0.137565	-11.37747	336.182266
CPC60	0.149365	-13.239675	361.532134
CPC50	0.257333	-32.514904	1102.08773

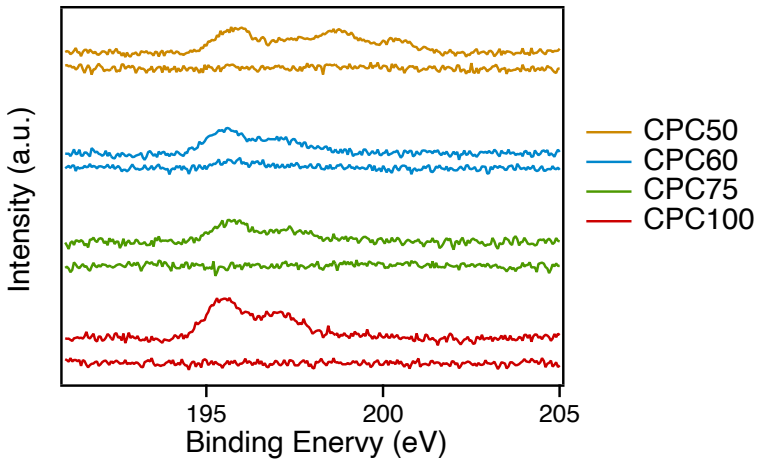

Figure S3.3. High-resolution XPS scans of CPC with (bottom) and without (top) dialysis. Disappearance of Cl signal upon dialysis indicates that Cl ions have been effectively removed from the complex. Data has been shifted vertically for clarity. Elemental analysis from XPS survey scans gives a rough estimation of 1 Cl ion per 3, 5, 6, and 5 charged monomers for CPC50, 60, 75, and 100 respectively.

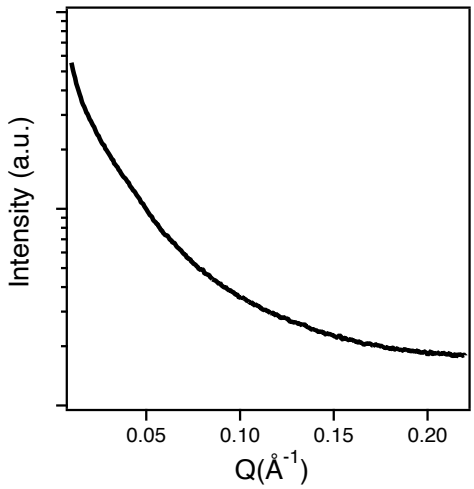

Figure S3.4. SAXS profile of TMACl salt shows no peak, confirming that scattering peaks in CI-containing CPCs are due to the domains segregation

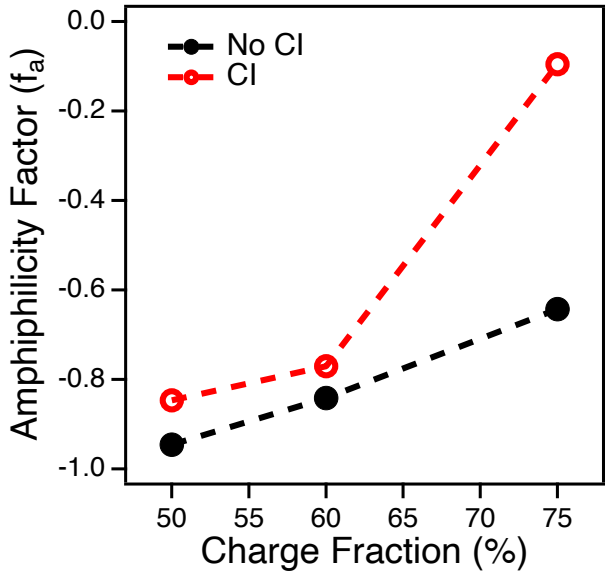

Figure S3.5. The amphiphilicity factors extracted from TS fit for CI-containing CPCs compared to CI-free CPCs showing less ordered nanostructure of ion-containing complexes

Field Theory and Simulation Details

The field-theoretic Hamiltonian is given by

$$H[w_1, w_2, w_3, \varphi]$$

$$= \frac{\rho_0}{2}\sum_{i=1}^{3}\frac{1}{|\mu_i|}\int d\boldsymbol{r}\, w_i^2(\boldsymbol{r}) + \zeta\rho_0\sum_{i=1}^{3}\frac{\xi_i}{\mu_i}\sum_{j=A,B,+,-}\Phi_{ij}\int d\boldsymbol{r}\, w_i(\boldsymbol{r})$$

$$+\frac{1}{8\pi l_B}\int d\boldsymbol{r}\,|\nabla\varphi|^2 - n_A \ln Q_A[\Omega_A] - n_B \ln Q_B[\Omega_B] - n_+ \ln Q_+[\Omega_+]$$

$$- n_- \ln Q_-[\Omega_-].$$

Here the number of w_i fields (in this case three) is determined by the number of non-zero eigenvalues of the contact interaction matrix, the parameters μ_i and Φ_{ij} are the respective eigenvalues and eigenvectors of that matrix, and the parameter ξ_i takes the value 1 if $\mu_i < 0$ and the value i if $\mu_i > 0$. Q_l is the single-molecule partition function for molecular species l,

and Ω_m is the local chemical potential field for bead species m. The single-chain partition functions $Q_{A/B}$ take the form

$$Q_{A/B}[\Omega_{A/B}] = \frac{1}{V}\int d\boldsymbol{r}\, q_{A/B}(\boldsymbol{r}, N; [\Omega_{A/B}]),$$

where the chain propagator $q_{A/B}(\boldsymbol{r}, s; [\Omega_{A/B}])$ satisfies the modified diffusion equation for a linear polymer chain

$$\frac{\partial}{\partial s} q_{A/B}(\boldsymbol{r}, s) = \left[\frac{b^2}{6}\nabla^2 - \Omega_{A/B}(\boldsymbol{r}, s)\right] q_{A/B}(\boldsymbol{r}, s)$$

subject to the initial condition $q_{A/B}(\boldsymbol{r}, 0) = 1$. The counterion partition functions take a simpler form:

$$Q_{\pm}[\Omega_{\pm}] = \frac{1}{V}\int d\boldsymbol{r}\, e^{-\Omega_{\pm}(\boldsymbol{r})}.$$

The species chemical potential fields Ω_m are related to the auxiliary fields according to

$$\Omega_m(\boldsymbol{r}) = \sum_{i=1}^{3} \xi_i \Phi_{im} \overline{w}_i(\boldsymbol{r}) + i\sigma_m \bar{\varphi}(\boldsymbol{r}),$$

where σ_m is the linear charge density ($\pm\sigma$) for polymeric species ($m = A, B$), and $\sigma_{\pm} = \pm 1$ for the counterion species (we assume monovalent counterions). The overbar on the auxiliary fields that appear in the species fields Ω_m indicate that those fields have been smeared via convolution with the smearing function; that is,

$$\overline{w}_i(\boldsymbol{r}) = \int d\boldsymbol{r}' \Gamma(\boldsymbol{r} - \boldsymbol{r}') w_i(\boldsymbol{r}'),$$

and a similar expression for $\bar{\varphi}(\boldsymbol{r})$.

In complex Langevin field-theoretic simulations (FTS), the average of a given thermodynamic operator $\mathcal{O}$, which is formally defined as

$$\langle \mathcal{O}[\{w\},\varphi]\rangle = \frac{\int \mathcal{D}w_1\mathcal{D}w_2\mathcal{D}w_3\mathcal{D}\varphi\, \mathcal{O}[\{w\},\varphi]\exp(-H[\{w\},\varphi])}{\int \mathcal{D}w_1\mathcal{D}w_2\mathcal{D}w_3\mathcal{D}\varphi\, \exp(-H[\{w\},\varphi])}$$

is obtained by sampling the complex Langevin trajectories of the auxiliary fields, and computing the (fictitious) time average of $\mathcal{O}$, leveraging the ergodic principle. In this work, we make use of operators for the density $\rho_i(\boldsymbol{r})$ and the species A (polycation) structure factor $S_{AA}(k)/N$; definitions of these operators can be found in prior publications from some of us.[34,42,71]

All simulations were conducted in a cubic box with dimensions $\left(6.4R_g\right)^3$ subject to periodic boundary conditions, with a spatial collocation mesh spacing equal to the smearing range; that is, $\Delta x = a$ in all cases and all directions, except in the density linescan presented in **Figure 3.6**, for which the mesh spacing in the x-direction (the direction of the linescan) is reduced to $\Delta x = a/3$ in order to provide a higher resolution. The modified diffusion equations are solved using a pseudospectral operator-splitting scheme with a chain contour resolution of $\Delta s = 0.01N$, and the CL equations are evolved using an exponential time differencing (ETD) algorithm with a time step $\Delta t = 0.05$, following our recent work.[33] For all simulations, the system is initialized in a random disordered configuration that has been equilibrated via a warmup simulation on the order of 10^6 timesteps. The structure factor results of **Figure 3.5** in the main manuscript are also the result of an average over 10^6 timesteps, and the $\gamma = 50$ data involve an additional average over 10 independent simulations, the additional averaging being necessary due to the strong electrostatic fluctuations in that case. All simulations were performed on Intel Xeon E5-2650 or E5-2670 CPUs, or NVIDIA Tesla M2075 graphics processing units (GPUs).

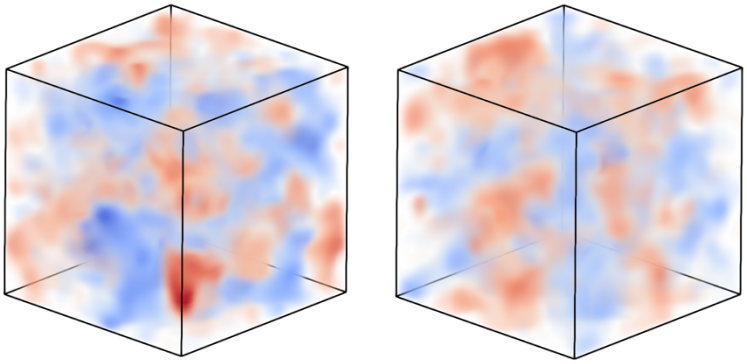

Figure S3.6. Simulated snapshots ($\rho_A(\boldsymbol{r}) - \rho_B(\boldsymbol{r})$) of the 50% CPC from CL-FTS, $\gamma = 50$ suggesting the CPE-PIL microemulsion take on a bi-continuous rather than a droplet morphology. Left snapshot is CPC without counterions, and right snapshot is CPC with counterions.

Random Phase Approximation

The RPA result for $S_{AA}(k)/N$ in the case with counterions is given by

$$\left(\frac{S_{AA}(k)}{N}\right)^{-1} = \Omega_{AA} - \frac{\Omega_{A-}^2}{\Omega_{--}} - \frac{\left(\Omega_{A+} - \frac{\Omega_{A-}\Omega_{+-}}{\Omega_{--}}\right)^2}{\Omega_{++} - \frac{\Omega_{+-}^2}{\Omega_{--}}}$$

$$- \frac{\left[\Omega_{AB} - \frac{\Omega_{A-}\Omega_{B-}}{\Omega_{--}} - \frac{\left(\Omega_{A+} - \frac{\Omega_{A-}\Omega_{+-}}{\Omega_{--}}\right)\left(\Omega_{B+} - \frac{\Omega_{+-}^2}{\Omega_{--}}\right)}{\Omega_{++} - \frac{\Omega_{+-}^2}{\Omega_{--}}}\right]^2}{\Omega_{BB} - \frac{\Omega_{B-}^2}{\Omega_{--}} - \frac{\left(\Omega_{B+} - \frac{\Omega_{B-}\Omega_{+-}}{\Omega_{--}}\right)^2}{\Omega_{++} - \frac{\Omega_{+-}^2}{\Omega_{--}}}}$$

where the correlation functions Ω_{ij} are given by

$$\Omega_{AA}(k) = \zeta N + \frac{\gamma(\sigma N)^2}{k^2 R_g^2} + \frac{1}{\phi_A \hat{g}_D(k)\hat{\Gamma}^2(k)},$$

$$\Omega_{AB}(k) = \zeta N + \chi_{AB} N - \frac{\gamma(\sigma N)^2}{k^2 R_g^2},$$

$$\Omega_{A+}(k) = \zeta N + \frac{\gamma\sigma N^2}{k^2 R_g^2},$$

$$\Omega_{A-}(k) = \zeta N - \frac{\gamma\sigma N^2}{k^2 R_g^2},$$

$$\Omega_{BB}(k) = \zeta N + \frac{\gamma(\sigma N)^2}{k^2 R_g^2} + \frac{1}{\phi_B \hat{g}_D(k)\hat{\Gamma}^2(k)},$$

$$\Omega_{B+}(k) = \zeta N - \frac{\gamma\sigma N^2}{k^2 R_g^2},$$

$$\Omega_{B-}(k) = \zeta N + \frac{\gamma\sigma N^2}{k^2 R_g^2},$$

$$\Omega_{++}(k) = \zeta N + \frac{\gamma N^2}{k^2 R_g^2} + \frac{N}{\phi_+ \hat{\Gamma}^2(k)},$$

$$\Omega_{+-}(k) = \zeta N - \frac{\gamma N^2}{k^2 R_g^2},$$

$$\Omega_{--}(k) = \zeta N + \frac{\gamma N^2}{k^2 R_g^2} + \frac{N}{\phi_- \hat{\Gamma}^2(k)}.$$

The shoulder feature that appears at large γ in the RPA and FTS structure factors is a γ-independent feature that can be isolated by taking the $\gamma \to \infty$ limit. In the $\gamma \to \infty$ limit, the RPA structure factor for the counterion-free system takes the form

$$\frac{S_{AA}(k)}{N} = \frac{1}{2N\left(2\zeta\hat{\Gamma}^2(k) + \frac{2}{N\hat{g}_D(k)} + \chi_{AB}\hat{\Gamma}^2(k)\right)}$$

which exposes this γ-independent peak. In **Figure S3.5a**, we plot the full RPA result for increasing values of γ, compared with the $\gamma \to \infty$ result, demonstrating the presence of this

residual peak in addition to the peak of interest, which shifts to larger k and reduces in intensity as γ is increased. We note that for high values of γ, the presence of the γ-independent peak obfuscates the peak of interest and complicates the interpretation of our theoretical model, which is another motivation for restricting ourselves to lower values of γ in this work. **Figure S3.5b** shows how this gamma-independent peak depends on the smearing range a; note from the expression above that there is also an N-dependence.

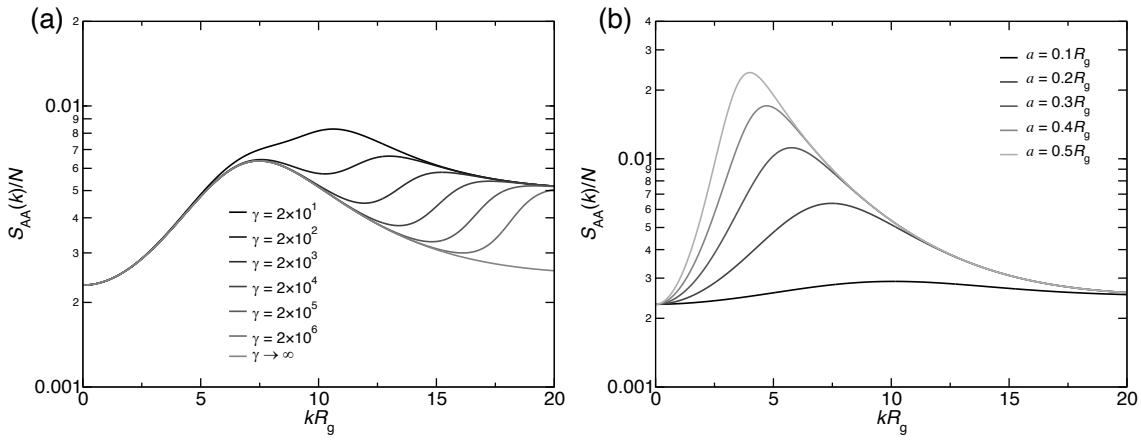

Figure S3.7. a) RPA structure factors for $\sigma = 1$, in the counterion-free system, for increasing values of γ, as well as the $\gamma \to \infty$ limit, reveals a γ-independent feature. b) RPA structure factors in the $\gamma \to \infty$ limit, for different values of the smearing range a, show that this feature is strongly dependent on a.

3.8 References

(1) Spruijt, E.; Westphal, A. H.; Borst, J. W.; Cohen Stuart, M. A.; Van Der Gucht, J. Binodal Compositions of Polyelectrolyte Complexes. Macromolecules 2010, 43 (15), 6476–6484. https://doi.org/10.1021/ma101031t.

(2) Niitani, T.; Shimada, M.; Kawamura, K.; Dokko, K.; Rho, Y. H.; Kanamura, K. Synthesis of Li+ Ion Conductive PEO-PSt Block Copolymer Electrolyte with Microphase Separation Structure. Electrochem. Solid-State Lett. 2005, 8 (8). https://doi.org/10.1149/1.1940491.

(3) Elschner, A.; Kirchmeyer, S.; Lövenich, W.; Merker, U.; Reuter, K. PEDOT: Principles and Applications of an Intrinsically Conductive Polyme. PEDOT Princ. Appl. an Intrinsically Conduct. Polym. 2010, 1–380. https://doi.org/10.1201/b10318.

(4) Cao, Y.; Yu, G.; Heeger, A. J.; Yang, C. Y. Efficient, Fast Response Light-Emitting Electrochemical Cells: Electroluminescent and Solid Electrolyte Polymers with Interpenetrating Network Morphology. Appl. Phys. Lett. 1996, 68 (23), 3218–3220. https://doi.org/10.1063/1.116442.

(5) Stavrinidou, E.; Winther-Jensen, O.; Shekibi, B. S.; Armel, V.; Rivnay, J.; Ismailova, E.; Sanaur, S.; Malliaras, G. G.; Winther-Jensen, B. Engineering Hydrophilic Conducting Composites with Enhanced Ion Mobility. Phys. Chem. Chem. Phys. 2014, 16 (6), 2275–2279. https://doi.org/10.1039/c3cp54061h.

(6) Zuo, G.; Liu, X.; Fahlman, M.; Kemerink, M. Morphology Determines Conductivity and Seebeck Coefficient in Conjugated Polymer Blends. ACS Appl. Mater. Interfaces 2018, 10 (11), 9638–9644. https://doi.org/10.1021/acsami.8b00122.

(7) Zuo, G.; Abdalla, H.; Kemerink, M. Conjugated Polymer Blends for Organic Thermoelectrics. Adv. Electron. Mater. 2019, 5 (11). https://doi.org/10.1002/aelm.201800821.

(8) Abtahi, A.; Johnson, S.; Park, S. M.; Luo, X.; Liang, Z.; Mei, J.; Graham, K. R. Designing π-Conjugated Polymer Blends with Improved Thermoelectric Power Factors. J. Mater. Chem. A 2019, 7 (34), 19774–19785. https://doi.org/10.1039/c9ta07464c.

(9) Zhang, J.; Kremer, K.; Michels, J. J.; Daoulas, K. C. Exploring Disordered Morphologies of Blends and Block Copolymers for Light-Emitting Diodes with Mesoscopic Simulations. Macromolecules 2020, 53 (2), 523–538. https://doi.org/10.1021/acs.macromol.9b02402.

(10) Le, M. L.; Rawlings, D.; Danielsen, S. P. O.; Kennard, R. M.; Chabinyc, M. L.; Segalman, R. A. Aqueous Formulation of Concentrated Semiconductive Fluid Using Polyelectrolyte Coacervation. ACS Macro Lett. 2021, 10 (8), 1008–1014. https://doi.org/10.1021/acsmacrolett.1c00354.

(11) Arias, A. C.; Endicott, F.; Street, R. A. Surface-Induced Self-Encapsulation of Polymer Thin-Film Transistors. Adv. Mater. 2006, 18 (21), 2900–2904. https://doi.org/10.1002/adma.200600623.

(12) Lu, G.; Blakesley, J.; Himmelberger, S.; Pingel, P.; Frisch, J.; Lieberwirth, I.; Salzmann, I.; Oehzelt, M.; Di Pietro, R.; Salleo, A.; Koch, N.; Neher, D. Moderate Doping Leads to High Performance of Semiconductor/Insulator Polymer Blend Transistors. Nat. Commun. 2013, 4 (1), 1–8. https://doi.org/10.1038/ncomms2587.

(13) Bates, F. S.; Fredrickson, G. H. Block Copolymer Thermodynamics: Theory and Experiment. Annu. Rev. Phys. Chem. 1990, 41 (1), 525–557. https://doi.org/10.1146/annurev.pc.41.100190.002521.

(14) Leibler, L. Theory of Microphase Separation in Block Copolymers. Macromolecules 1980, 13 (6), 1602–1617. https://doi.org/10.1021/ma60078a047.

(15) Cordier, P.; Tournilhac, F.; Soulié-Ziakovic, C.; Leibler, L. Self-Healing and Thermoreversible Rubber from Supramolecular Assembly. Nature 2008, 451 (7181), 977–980. https://doi.org/10.1038/nature06669.

(16) Burnworth, M.; Tang, L.; Kumpfer, J. R.; Duncan, A. J.; Beyer, F. L.; Fiore, G. L.; Rowan, S. J.; Weder, C. Optically Healable Supramolecular Polymers. Nature 2011, 472 (7343), 334–337. https://doi.org/10.1038/nature09963.

(17) He, Y.; Zhu, B.; Inoue, Y. Hydrogen Bonds in Polymer Blends. Prog. Polym. Sci. 2004, 29 (10), 1021–1051. https://doi.org/10.1016/j.progpolymsci.2004.07.002.

(18) Paul, D. R.; Barlow, J. W.; Bernstein, R. E.; Wahrmund, D. C. Polymer Blends Containing Poly(Vinylidene Fluoride). Part IV: Thermodynamic Interpretations. Polym. Eng. Sci. 1978, 18 (16), 1225–1234. https://doi.org/10.1002/pen.760181607.
(19) Rodriguez-Parada, J. M.; Percec, V. Interchain Electron Donor-Acceptor Complexes: A Model To Study Polymer-Polymer Miscibility? Macromolecules 1986, 19 (1), 55–64. https://doi.org/10.1021/ma00155a011.
(20) Takata, T. Supramolecular Polymers. Polymer (Guildf). 2017, 128 (12), 242. https://doi.org/10.1016/j.polymer.2017.09.030.
(21) Aida, T.; Meijer, E. W.; Stupp, S. I. Functional Supramolecular Polymers. Science (80-.). 2012, 335 (6070), 813–817. https://doi.org/10.1126/science.1205962.
(22) Geschke, D. Physical Properties of Polymers Handbook. Zeitschrift für Phys. Chemie 1997, 199 (Part_1), 128–128. https://doi.org/10.1524/zpch.1997.199.part_1.128.
(23) Rumyantsev, A. M.; Kramarenko, E. Y.; Borisov, O. V. Microphase Separation in Complex Coacervate Due to Incompatibility between Polyanion and Polycation. Macromolecules 2018, 51 (17), 6587–6601. https://doi.org/10.1021/acs.macromol.8b00721.
(24) Brereton, M. G.; Vilgis, T. A. Compatibility and Phase Behavior in Charged Polymer Systems and Ionomers. Macromolecules 1990, 23 (7), 2044–2049. https://doi.org/10.1021/ma00209a028.
(25) Grzetic, D. J.; Delaney, K. T.; Fredrickson, G. H. Electrostatic Manipulation of Phase Behavior in Immiscible Charged Polymer Blends. Macromolecules 2021, 54 (6), 2604–2616. https://doi.org/10.1021/acs.macromol.1c00095.
(26) Rumyantsev, A. M.; De Pablo, J. J. Microphase Separation in Polyelectrolyte Blends: Weak Segregation Theory and Relation to Nuclear "Pasta." Macromolecules 2020, 53 (4), 1281–1292. https://doi.org/10.1021/acs.macromol.9b02466.
(27) Rumyantsev, A. M.; Gavrilov, A. A.; Kramarenko, E. Y. Electrostatically Stabilized Microphase Separation in Blends of Oppositely Charged Polyelectrolytes. Macromolecules 2019, 52 (19), 7167–7174. https://doi.org/10.1021/acs.macromol.9b00883.
(28) Broseta, D.; Fredrickson, G. H. Phase Equilibria in Copolymer/Homopolymer Ternary Blends: Molecular Weight Effects. J. Chem. Phys. 1990, 93 (4), 2927–2938. https://doi.org/10.1063/1.458877.
(29) Bates, F. S.; Maurer, W.; Lodge, T. P.; Schulz, M. F.; Matsen, M. W.; Almdal, K.; Mortensen, K. Isotropic Lifshitz Behavior in Block Copolymer-Homopolymer Blends. Phys. Rev. Lett. 1995, 75 (24), 4429–4432. https://doi.org/10.1103/PhysRevLett.75.4429.
(30) Bates, F. S.; Maurer, W. W.; Lipic, P. M.; Hillmyer, M. A.; Almdal, K.; Mortensen, K.; Fredrickson, G. H.; Lodge, T. P. Polymeric Bicontinuous Microemulsions. Phys. Rev. Lett. 1997, 79 (5), 849–852. https://doi.org/10.1103/PhysRevLett.79.849.
(31) Wang, Z. G. Fluctuation in Electrolyte Solutions: The Self Energy. Phys. Rev. E - Stat. Nonlinear, Soft Matter Phys. 2010, 81 (2). https://doi.org/10.1103/PhysRevE.81.021501.
(32) Delaney, K. T.; Fredrickson, G. H. Theory of Polyelectrolyte Complexation - Complex Coacervates Are Self-Coacervates. J. Chem. Phys. 2017, 146 (22), 224902. https://doi.org/10.1063/1.4985568.

(33) Grzetic, D. J.; Delaney, K. T.; Fredrickson, G. H. Field-Theoretic Study of Salt-Induced Order and Disorder in a Polarizable Diblock Copolymer. ACS Macro Lett. 2019, 8 (8), 962–967. https://doi.org/10.1021/acsmacrolett.9b00316.
(34) Delaney, K. T.; Fredrickson, G. H. Recent Developments in Fully Fluctuating Field-Theoretic Simulations of Polymer Melts and Solutions. J. Phys. Chem. B 2016, 120 (31), 7615–7634. https://doi.org/10.1021/acs.jpcb.6b05704.
(35) Fredrickson, G. The Equilibrium Theory of Inhomogeneous Polymers. Equilib. Theory Inhomogeneous Polym. 2007, 9780198567, 1–456. https://doi.org/10.1093/acprof:oso/9780198567295.001.0001.
(36) Parisi, G. On Complex Probabilities. Phys. Lett. B 1983, 131 (4–6), 393–395. https://doi.org/10.1016/0370-2693(83)90525-7.
(37) Klauder, J. R.; Lee, S. Improved Complex Langevin Method for (2+1)-Dimensional Lattices. Phys. Rev. D 1992, 45 (6), 2101–2104. https://doi.org/10.1103/PhysRevD.45.2101.
(38) Ganesan, V.; Fredrickson, G. H. Field-Theoretic Polymer Simulations. Europhys. Lett. 2001, 55 (6), 814–820. https://doi.org/10.1209/epl/i2001-00353-8.
(39) Tzeremes, G.; Rasmussen, K.; Lookman, T.; Saxena, A. Efficient Computation of the Structural Phase Behavior of Block Copolymers. Phys. Rev. E - Stat. Physics, Plasmas, Fluids, Relat. Interdiscip. Top. 2002, 65 (4), 5. https://doi.org/10.1103/PhysRevE.65.041806.
(40) Rasmussen, K.; Kalosakas, G. Improved Numerical Algorithm for Exploring Block Copolymer Mesophases. J. Polym. Sci. Part B Polym. Phys. 2002, 40 (16), 1777–1783. https://doi.org/10.1002/polb.10238.
(41) Düchs, D.; Ganesan, V.; Fredrickson, G. H.; Schmid, F. Fluctuation Effects in Ternary AB + A + B Polymeric Emulsions. Macromolecules 2003, 36 (24), 9237–9248. https://doi.org/10.1021/ma030201y.
(42) Düchs, D.; Delaney, K. T.; Fredrickson, G. H. A Multi-Species Exchange Model for Fully Fluctuating Polymer Field Theory Simulations. J. Chem. Phys. 2014, 141 (17), 174103. https://doi.org/10.1063/1.4900574.
(43) Villet, M. C.; Fredrickson, G. H. Efficient Field-Theoretic Simulation of Polymer Solutions. J. Chem. Phys. 2014, 141 (22), 224115. https://doi.org/10.1063/1.4902886.
(44) Lee, J.; Popov, Y. O.; Fredrickson, G. H. Complex Coacervation: A Field Theoretic Simulation Study of Polyelectrolyte Complexation. J. Chem. Phys. 2008, 128 (22), 224908. https://doi.org/10.1063/1.2936834.
(45) Delaney, K. T.; Fredrickson, G. H. Theory of Polyelectrolyte Complexation - Complex Coacervates Are Self-Coacervates. J. Chem. Phys. 2017, 146 (22). https://doi.org/10.1063/1.4985568.
(46) McCarty, J.; Delaney, K. T.; Danielsen, S. P. O.; Fredrickson, G. H.; Shea, J. E. Complete Phase Diagram for Liquid-Liquid Phase Separation of Intrinsically Disordered Proteins. J. Phys. Chem. Lett. 2019, 10 (8), 1644–1652. https://doi.org/10.1021/acs.jpclett.9b00099.
(47) Danielsen, S. P. O.; McCarty, J.; Shea, J. E.; Delaney, K. T.; Fredrickson, G. H. Small Ion Effects on Self-Coacervation Phenomena in Block Polyampholytes. J. Chem. Phys. 2019, 151 (3), 034904. https://doi.org/10.1063/1.5109045.
(48) Danielsen, S. P. O.; McCarty, J.; Shea, J. E.; Delaney, K. T.; Fredrickson, G. H. Molecular Design of Self-Coacervation Phenomena in Block Polyampholytes. Proc.

Natl. Acad. Sci. U. S. A. 2019, 116 (17), 8224–8232. https://doi.org/10.1073/pnas.1900435116.
(49) Najafi, S.; Lin, Y.; Longhini, A. P.; Zhang, X.; Delaney, K. T.; Kosik, K. S.; Fredrickson, G. H.; Shea, J. E.; Han, S. Liquid–Liquid Phase Separation of Tau by Self and Complex Coacervation. Protein Sci. 2021, 30 (7), 1393–1407. https://doi.org/10.1002/pro.4101.
(50) Kazemiabnavi, S.; Zhang, Z.; Thornton, K.; Banerjee, S. Electrochemical Stability Window of Imidazolium-Based Ionic Liquids as Electrolytes for Lithium Batteries. J. Phys. Chem. B 2016, 120 (25), 5691–5702. https://doi.org/10.1021/acs.jpcb.6b03433.
(51) Danielsen, S. P. O.; Nguyen, T. Q.; Fredrickson, G. H.; Segalman, R. A. Complexation of a Conjugated Polyelectrolyte and Impact on Optoelectronic Properties. ACS Macro Lett. 2019, 8 (1), 88–94. https://doi.org/10.1021/acsmacrolett.8b00924.
(52) Hollingsworth, W. R.; Williams, V.; Ayzner, A. L. Semiconducting Eggs and Ladders: Understanding Exciton Landscape Formation in Aqueous π-Conjugated Inter-Polyelectrolyte Complexes. Macromolecules 2020, 53 (7), 2724–2734. https://doi.org/10.1021/acs.macromol.0c00029.
(53) Hampu, N.; Hillmyer, M. A. Molecular Engineering of Nanostructures in Disordered Block Polymers. ACS Macro Lett. 2020, 9 (3), 382–388. https://doi.org/10.1021/acsmacrolett.0c00036.
(54) Teubner, M.; Strey, R. Origin of the Scattering Peak in Microemulsions. J. Chem. Phys. 1987, 87 (5), 3195–3200. https://doi.org/10.1063/1.453006.
(55) Berk, N. F. Scattering Properties of a Model Bicontinuous Structure with a Well Defined Length Scale. Phys. Rev. Lett. 1987, 58 (25), 2718–2721. https://doi.org/10.1103/PhysRevLett.58.2718.
(56) Xie, S.; Meyer, D. J.; Wang, E.; Bates, F. S.; Lodge, T. P. Structure and Properties of Bicontinuous Microemulsions from Salt-Doped Ternary Polymer Blends. Macromolecules 2019, 52 (24), 9693–9702. https://doi.org/10.1021/acs.macromol.9b01963.
(57) Kulshreshtha, A.; Hayward, R. C.; Jayaraman, A. Impact of Composition and Placement of Hydrogen-Bonding Groups along Polymer Chains on Blend Phase Behavior: Coarse-Grained Molecular Dynamics Simulation Study. Macromolecules 2022, 55 (7), 2675–2690. https://doi.org/10.1021/acs.macromol.2c00055.
(58) Vonk, C. G.; Billman, J. F.; Kaler, E. W. Small Angle Scattering of Bicontinuous Structures in Microemulsions. J. Chem. Phys. 1988, 88 (6), 3970–3975. https://doi.org/10.1063/1.453846.
(59) Vonk, C. G.; Billman, J. F.; Kaler, E. W. Small Angle Scattering of Bicontinuous Structures in Microemulsions. J. Chem. Phys. 1988, 88 (6), 3970–3975. https://doi.org/10.1063/1.453846.
(60) Schubert, K. V.; Strey, R.; Kline, S. R.; Kaler, E. W. Small Angle Neutron Scattering near Lifshitz Lines: Transition from Weakly Structured Mixtures to Microemulsions. J. Chem. Phys. 1994, 101 (6), 5343–5355. https://doi.org/10.1063/1.467387.
(61) Douglas, E. P.; Sakurai, K.; MacKnight, W. J. Thermal Analysis and Optical Microscopy of Modified Polystyrene/Poly(Ethyl Acrylate) Blends Containing Specific Interactions. Macromolecules 1991, 24 (25), 6776–6781. https://doi.org/10.1021/ma00025a034.

(62) Grzetic, D. J.; Delaney, K. T.; Fredrickson, G. H. Electrostatic Manipulation of Phase Behavior in Immiscible Charged Polymer Blends. Macromolecules 2021, 54 (6), 2604–2616. https://doi.org/10.1021/acs.macromol.1c00095.
(63) Noro, A.; Tamura, A.; Wakao, S.; Takano, A.; Matsushita, Y. Stoichiometric Effects on Nanostructures of Block- and Graft-Type Supramacromolecules via Acid-Base Complexation. Macromolecules 2008, 41 (23), 9277–9283. https://doi.org/10.1021/ma801661c.
(64) Huh, J.; Park, H. J.; Kim, K. H.; Kim, K. H.; Park, C.; Jo, W. H. Giant Thermal Tunability of the Lamellar Spacing in Block-Copolymer-like Supramolecules Formed from Binary-End-Functionalized Polymer Blends. Adv. Mater. 2006, 18 (5), 624–629. https://doi.org/10.1002/adma.200500963.
(65) Pispas, S.; Floudas, G.; Pakula, T.; Lieser, G.; Sakellariou, S.; Hadjichristidis, N. Miktoarm Block Copolymer Formation via Ionic Interactions. Macromolecules 2003, 36 (3), 759–763. https://doi.org/10.1021/ma0256993.
(66) Vidil, T.; Hampu, N.; Hillmyer, M. A. Nanoporous Thermosets with Percolating Pores from Block Polymers Chemically Fixed above the Order-Disorder Transition. ACS Cent. Sci. 2017, 3 (10), 1114–1120. https://doi.org/10.1021/acscentsci.7b00358.
(67) Danielsen, S. P. O.; Davidson, E. C.; Fredrickson, G. H.; Segalman, R. A. Absence of Electrostatic Rigidity in Conjugated Polyelectrolytes with Pendant Charges. ACS Macro Lett. 2019, 8 (9), 1147–1152. https://doi.org/10.1021/acsmacrolett.9b00551.
(68) Schmode, P.; Ohayon, D.; Reichstein, P. M.; Savva, A.; Inal, S.; Thelakkat, M. High-Performance Organic Electrochemical Transistors Based on Conjugated Polyelectrolyte Copolymers. Chem. Mater. 2019, 31 (14), 5286–5295. https://doi.org/10.1021/acs.chemmater.9b01722.
(69) Evans, C. M.; Sanoja, G. E.; Popere, B. C.; Segalman, R. A. Anhydrous Proton Transport in Polymerized Ionic Liquid Block Copolymers: Roles of Block Length, Ionic Content, and Confinement. Macromolecules 2016, 49 (1), 395–404. https://doi.org/10.1021/acs.macromol.5b02202.
(70) Thomas, E. M.; Popere, B. C.; Fang, H.; Chabinyc, M. L.; Segalman, R. A. Role of Disorder Induced by Doping on the Thermoelectric Properties of Semiconducting Polymers. Chem. Mater. 2018, 30 (9), 2965–2972. https://doi.org/10.1021/acs.chemmater.8b00394.
(71) Grzetic, D. J.; Delaney, K. T.; Fredrickson, G. H. The Effective χ Parameter in Polarizable Polymeric Systems: One-Loop Perturbation Theory and Field-Theoretic Simulations. J. Chem. Phys. 2018, 148 (20), 204903. https://doi.org/10.1063/1.5025720.

Chapter 4

Role of complexation strength on the photophysical and transport properties of semiconducting charged polymer complexes

This chapter is reproduced with permission from:

Le, M. L.; Warner, C.; Segalman, R. A.; Chabinyc, M. L. Role of Complexation Strength on the Photophysical and Transport Properties of Semiconducting Charged Polymer Complexes. *Chem. Mater.* **2023**, DOI: 10.1021/acs.chemmater.3c00627.

4.1 Abstract

The high polymer fraction in complexes of conjugated and insulating polyelectrolytes offers unique opportunities for fabrication of conductive thick films and bulk structures. The electrostatic interactions in these systems further provide a handle for controlling their structure and properties. The impact of charge-mediated complexation strength on the photophysical and electronic transport properties in blends of conjugated polyelectrolytes (CPEs) with oppositely charged polymeric ionic liquids (PILs) was examined. Complexes were formed with varying frequency of charged repeat units, from 50% to 100%, on an anionic polythiophene-based CPE and a complimentary cationic PIL. In highly charged complexes, the intimate mixing between the CPE and the PIL reduced the structural disorder along the CPE backbone, enhancing its intrachain conjugation and interchain stacking. In weakly charged complexes (<90%), these chain planarization effects were absent and microphase separation occurred. At all charge fractions examined, the electrical conductivity of an acid-

doped complex was higher than that of the unblended constituent CPE. The highest electrical conductivity, near 1 S cm-1, was found for a charge fraction of 100%. These results demonstrate the potential for designing effective polymeric conductors using electrostatic complexation.

4.2 Introduction

Conjugated polymers are an important class of organic electronic materials because of their mechanical properties, versatile molecular design, and compatibility with inexpensive and scalable processing methods.[1–4] The hierarchical structures of conjugated polymers in the solid state, including the degree of crystallinity, the size and texture of ordered aggregates, and the long range orientational correlation between backbones, have direct and profound impacts on their optoelectronic and transport properties.[5–12] Significant efforts to optimize the optoelectronic performance of conjugated polymers have been made by controlling and manipulating their solid-state self-assembly. Critical factors have been identified, including molecular weight,[13–16] chain conformations,[17,18] solution and casting conditions,[19,20] interactions with substrates,[21] and the nucleation conditions.[22] In general, the limited solubility of conjugated polymers has also played a strong role in their optoelectronic properties that can be impacted by processing. Therefore, molecular designs to increase or broaden the processability of conjugated polymers have been of longstanding interest.

Conjugated polyelectrolytes (CPEs) are π-conjugated polymers with pendant ionic side chains, making them highly compatible with water and other high dielectric solvents for improved solution processability.[23–25] The CPE side chains, accompanied by counterions, not

only impart potential solubility in polar solvents and ionic conductivity but also present new handles to electrostatically manipulate their self-assembly processes. In particular, the charged side chains impart strong electrostatic interactions within and between chains.[26–28] Thus, the structure of CPEs is controlled by a combination of aromatic interactions as well as electrostatics and hydrophobic forces. Leveraging these added ionic degrees of freedom, it has been demonstrated that the structure and electronic properties of CPE chains in both solution and solid films can be controlled by varying the charge-compensating counterion, ionic strength of solvent, frequency and placement of ionic moieties, and added ionic additives.[29–39]

These same electrostatic interactions, moreover, can be used to induce electrostatic complexation of the CPE with an oppositely charged polyelectrolyte. When solutions of two polyelectrolytes are mixed, the electrostatic attraction of the polymers combined with the entropy gain of exclusion of counterions overcomes the unfavorable enthalpic interactions between the immiscible polymers.[40,41] As a result, associative phase separation emerges, resulting in polymer complex phase with extremely high solid loading in coexistence with the polymer-deficient supernatant.[42,43] Initial studies on complexes of CPEs have suggested changes in the photophysical properties of the CPE upon charged-induced complexation.[33,42–46] Red shifts in optical transitions of the CPE chains upon complexation have been reported, suggesting the more planar conformation of CPE chains in the polymeric complex phases.[42,45] These observations have been attributed to the reduction in torsions and kinks along the CPE backbones in the polymer complex. In complexes where both polyelectrolytes are conjugated polymers with differing backbone rigidity, extension of the more flexible CPE has been

observed.[47] These initial findings underscore the potential of ionic interactions in modulating the photophysical properties of CPEs in charged complexes.

The high polymer loading in charge conjugated complexes suggests potential for the fabrication of solid-state conductive thick films and bulk structures for applications such as thermoelectric and bioelectronics which have been previously illusive due to the limited solubility of most conjugated polymers.[1,48,49] A fundamental understanding of behavior of CPEs within solvent-free complexes is critical to the development of high-performing solid materials. While the coacervate phase is ~50% solvent and gel-like, upon drying, it transforms into an ionically cross-linked polymer network. Because of the high solids loading in the coacervate, thick films (4 – 5 μm) can be obtained from casting the material. Surprisingly, the solid film of ethylenedioxythiophene-based CPE complexed with another insulating polyelectrolyte, once doped with a strong acid, was found to have higher electronic conductivity than the unblended CPE.[43] This suggests that understanding the roles of electrostatic strength and molecular design on both the local order and interconnectivity of the CPE chains in the complex could yield significant improvements on the final optoelectronic properties of the complex materials.

Here, we investigate how the charge-mediated complexation process affects the photophysical and electronic transport properties of CPEs in blends of CPE with an oppositely charged polymeric ionic liquid (PIL) as a function of charge fraction. By varying the frequency of charged repeat units on an anionic polythiophene CPE and a complimentary insulating cationic PIL we developed a model system with controlled complexation strength. We found

that the relative strength of intrachain and interchain excitonic coupling in the CPE aggregates stayed relatively constant between unblended and blended CPE regardless of charge fraction. For densely charged complexes, strong complexation with the PIL reduced structural disorder along the CPE backbones, leading to increased intrachain conjugation and interchain electronic couplings of the CPE. Due to the short-range repulsion between the dissimilar CPE and PIL chains, weakly charged complexes nanophase segregated whereas densely charged complexes were more homogeneous. In both cases, the long-range percolation necessary for electronic transport was improved, resulting in all complexes exhibiting superior electrical conductivity (2-3 orders of magnitude higher) compared to the constituent CPEs when doped with a strong acid. Our findings provide a fundamental basis to understanding the role of complexation on the structural ordering and the optoelectronic properties of CPE chains within electrostatic complexes.

4.3 Experimental Methods

Materials

All chemicals, unless otherwise noted, were commercially available and used as received from Sigma-Aldrich. Deionized water (> 19 MΩ·cm at 25 °C) was used for the synthesis and preparation of samples. Deuterated solvents were obtained from Cambridge Isotope Laboratories.

Molecular Characterization

^{1}H NMR spectra were recorded at using 600 MHz (Varian VNMRS) in CDCl3, DMSO-d6 or d-Methanol. Gel permeation chromatography (GPC) was conducted using a Waters e2695

instrument using THF as the mobile phase with a flow rate of 1 mL/min. Reported molecular weight and polydispersity (Đ) values are relative to a polystyrene (PS) standard.

Sample Preparation

Stock polymer solution was prepared by dissolving the polymer in a 40% THF : 60% water solvent mixture to achieve a final molar concentration of 1M. In an Eppendorf tube, solutions of CPE and PIL of similar charge fraction were mixed in a stoichiometric ratio and the tube was mixed for one minute using a vortex mixer. Subsequently, the mixture was centrifuged at 7000 rpm for 10 minutes to drive the accumulation of coacervate droplets to the bottom of the Eppendorf tube while the polymer-deficient supernatant phase floated to the top. The coacervate was then collected by decanting the supernatant and was blade-coated onto quartz substrates for subsequent spectroscopy and conductivity measurements. CPE solutions were spin cast onto quartz substrate. CPE films are 250 to 300 nm thick, while complex film thickness ranges from 1 μm to 4 μm going from Complex50 to Complex100 due to the difference in polymer loading in the coacervate phase. Film thickness was measured with a Bruker DektakXT Stylus profilometer. Except for UV-Vis experiments where films were spun cast from solutions in Methanol, CPE films used in all other experiments were prepared by spin casting from 40% THF:60% water solutions. All samples were heated at 50°C under vacuum for 30 min to remove excess solvent and were further dried under high vacuum (10^{-8} Torr) overnight.

Vapor Doping

Doping was performed inside a nitrogen glovebox. Polymer film was attached upside down in the lid of a glass jar and HTFSI crystals were placed inside the jar. The jar was closed tightly and heated at 50°C on a hot plate for 13 minutes (CPEs) or 45 minutes (complexes). For the complex films, the films were transferred to another closed clean glass jar and heated at 55°C for an additional 48 hours to promote efficient diffusion of dopants into the film and to prevent leakage of dopant vapor.

Optical Spectroscopy

Films of CPEs and Complexes were casted onto 0.5 mm-thick quartz substrates. UV-Vis absorption spectra were taken using an Agilent Cary 60 UV-Vis spectrophotometer. All measurements were done at ambient temperature (≈ 25°C). Emission spectra were taken using a Horiba FluoroMax® 4 spectrometer at 450 nm excitation wavelength. The sample is illuminated by a 150 W xenon, continuous output, ozone-free lamp. Emission spectrum of each film was averaged over 3 scans.

Electronic Conductivity Measurement

Gold electrical contacts (≈ 60 nm thick) were deposited at ~ 1 Å s^{-1} rate onto casted polymer film on quartz via controlled thermal evaporation through a shadow mask. Transmission line measurements were carried out to determine in-plane electronic conductivity of the polymer film using a Keithley 6485 picoammeter. Electrical measurements were carried out inside a nitrogen glovebox at room temperature. To obtain the activation energy and high-temperature conductivity limit of the samples, temperature-dependent conductivity measurements were performed under vacuum (≈10−4 Torr) in a Lakeshore cryogenic probe station at temperatures

from 300 K down to 180 K; elevated temperature measurements were not carried out to prevent any potential de-doping of the polymer films.

X-ray Scattering

Samples were loaded into aluminum washers, soft-baked at 50 °C under vacuum to remove the excess solvent, and further dried under high vacuum (≈ 10^{-8} Torr) overnight. These samples were then sealed with Kapton tape. X-ray scattering measurements were performed at the National Synchrotron Light Source II (NSLS-II, beamline 11-BM, Brookhaven National Laboratory), with an X-ray energy of 13.5 keV. Data processing, including the detector distance calibration using a silver behenate standard, the reduction of two-dimensional (2D) raw SAXS images into one-dimensional (1D) intensity versus q curves, and corrections for empty cell scattering, was performed using the SciAnalysis software for NSLS-II data.

4.4 Results and Discussion

We sought to investigate the role of electrostatic complexation strength and the resulting nanostructure on the photophysical and electronic transport properties of a series of CPE-PIL complexes. The fraction of charged repeat units on the polymer backbones can be varied to control the strength of electrostatic attraction between CPE and PIL chains. We chose poly[6-(thiophen-3-yl)hexane-1-sulfonate-*co*-3-(hexylthiophene)] copolymers with tetramethyl ammonium (TMA) counterion as the CPE because thiophene-based polymers have well-understood optoelectronic behavior. These CPEs were paired with a PIL, poly[(3-methyl-1-propylimidazolylacrylamide)-*co*-3-methyl-1-(propyl acrylamide)], with chloride counterions as the complimentary polycation. The wide electrochemical stability window of the

imidazolium group makes this PIL an ideal candidate here [50] as it is important that the insulating polymer remains stable upon electrical doping of the CPE within the complex. The chemical structure of the CPEs and PILs are shown in **Figure 4.1a**.

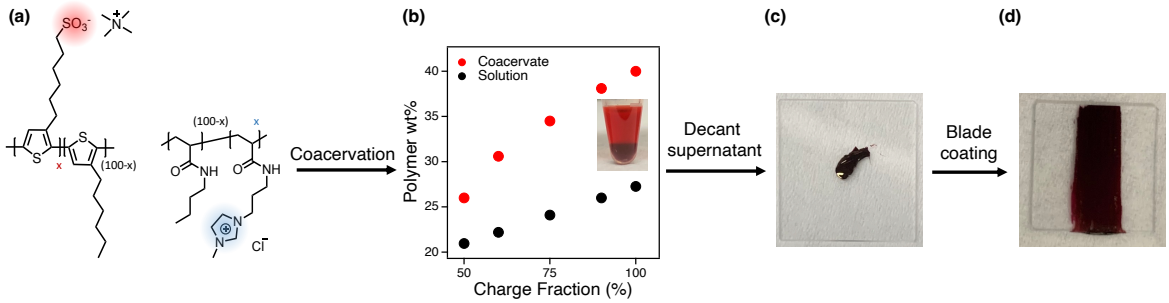

Figure 4.1. Schematic showing the process of obtaining solid-state CPE – PIL charged complex films for further characterizations. **(a)** Chemical structures of the CPE and the PIL used in this study, with x being the percentage of charged units **(b)** Concentration of polymers in the coacervate phase (red markers) in comparison to that in the stock solutions (black markers). Inset showing a photograph of CPE-PIL (x = 75%) coacervate in coexistence with its supernatant **(c)** The coacervate obtained from decanting the supernatant, and drop-casted onto a quartz substrate **(d)** Solid film (≈ 1 μm – 4 μm thick) obtained from blade coating the CPE – PIL coacervate and drying under high vacuum overnight

The solid-state polymer complexes investigated in this study were obtained by drying the coacervate phase that formed upon mixing the solutions of the CPE and the PIL with matching charge fractions. Both polymers were synthesized with charge fraction x of 50%, 60%, 75%, 90%, and 100% to cover a range of complexation strength while maintaining sufficient electrostatic interactions to ensure the formation of the coacervate phase upon mixing. Details of the mixing protocol are included in the Experimental Section. As shown in **Figure 4.1b**, the concentration of polymer in the coacervate phase — both in absolute value and relative to the concentration of the stock solutions — increases with polymer charge fraction, indicating the more favorable partition of polymer chains into the complex coacervate phase. This trend confirms that the polymer charge fraction provides an effective and direct handle to tune the

complexation strength between the CPE and the PIL. Once formed, the coacervate phase was collected by decanting the supernatant (**Figure 4.1c**) and was blade-coated onto quartz substrates and dried under high vacuum (≈ 10^{-8} Torr) (**Figure 4.1d**). Due to the differences in the polymer concentration of the coacervate at different charge fractions *x*, the resulting solid films' thicknesses varied from 1 μm to 4 μm going from Complex50 to Complex100.

Motivated from our prior work demonstrating that the polymer charge fraction effectively controls the nanostructure of conjugated polymer complexes,[51] we aimed to elucidate the impacts of such structural evolution on the hierarchical ordering of CPE chains in the complex and on the optoelectronic properties of these complexes. In particular, we have observed from our prior study that the small angle X-ray scattering (SAXS) profile of the complex transitions from being featureless (x = 100%) to having a single broad peak as the charge fraction is reduced to 50%. These results indicate that at x = 100%, the strong complexation between the CPE and the PIL chains leads to the formation of a homogeneously disordered structure where the polymers are intimately mixed. At lower x values, short-range repulsive forces can compete more effectively with the weaker electrostatic interactions, giving rise to nanoscale phase segregation. As a result, weakly charged complexes have globally homogeneous but locally-ordered structure with a correlation length of 4 – 5 nm. The weaker the electrostatic attractions, the larger the domain size and the sharper the interfaces becomes. Nonetheless, the consequences of this morphological change on the hierarchical ordering and the optoelectronic properties of the CPE component remained unknown.

Absorption and emission spectroscopy measurements provide a means to understand the short-range ordering of the CPE chains within the CPE-PIL complex. It is worth noting that the thick complex films (> 1μm, with ≈ 50% conjugated material) were essentially opaque due to the high absorption coefficient of polythiophenes (≈ 10^5 cm^{-1}).[52] However, we were still able to collect absorption spectra of all the materials (**Figure 4.2b**) and attributed the spectra to transmission through thin spots in the large area of illumination or the edges of the sample. Due to the unknown thickness of the transmitting regions, the UV-Vis spectra of the complexes were not amenable to quantitative fitting as transmission UV-Vis measurements were shown to be very sensitive to the reflection behavior of the sample which varies with sample thickness and surface homogeneity.[53]

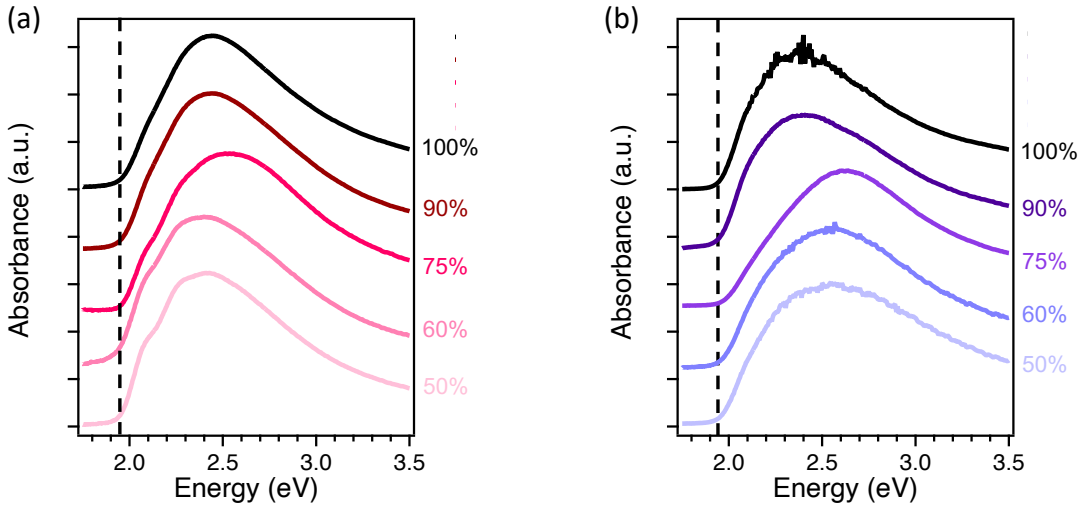

Figure 4.2. Optical absorption spectra of **(a)** thin films (spun-cast) of CPEs and **(b)** thick films (blade-coated) of complexes as a function of charge fraction. The dashed lines show the absorption onset.

Optical absorption spectra of CPE films suggest that these polymers form films with both aggregated and disordered regions. As shown in **Figure 4.2a**, the spectra of the CPEs have a low-energy absorption edge (≈ 1.95 eV), followed by a vibronic shoulder and a broad

absorption peak at higher energy. These general spectral features are similar to those of poly(3-hexylthiophene) P3HT,[54–59] suggesting similar excitonic behavior between charged and neutral polythiophenes. The dipoles from charged side chains and their counterions in CPE films can be considered static within the lifetime of an exciton (within ns), and thus have minimal impact on the excitons. The absorption onset here is slightly blue-shifted compared to the one reported for CPE100 (with the same TMA counterion) in literature (≈ 1.91 eV).[60] The presence of the vibronic progressions from 2.0 – 2.4 eV in the spectra is indicative of polymer aggregates with strong coupling between the electronic transition and the vibrational levels of the conjugated backbone.[57,61] These aggregates of two or more chromophores form due to their favorable electronic interactions between and along the conjugated backbones.[61] Depending on how the transition dipoles of the chromophores are oriented relative to each other, the aggregates can be classified as H-type (cofacial orientation) or J-type (collinear orientation) aggregates.[62] The former leads to optical properties that are dominated by interchain electronic coupling, whereas the latter is dominated by intrachain coupling.[63,64] The molecular weights of the CPEs used in this study are below the chain folding threshold [63] so the possibility of a CPE chain folding back on itself and causing intrachain interaction can be ruled out. The polymer aggregates in these CPE films are likely HJ-type aggregates with predominant interchain aggregates (H-type) characteristic. Interestingly, the absorption peak and shape do not appear to change monotonically with polymer charge fraction (**Figure 4.2a)**, likely because of the variation in the MW and the dispersity index $Đ$ of these CPEs **(Table S4.1**). As no sign of $\pi - \pi$ stacking was observed in wide angle X-ray scattering (WAXS) data of the CPEs (**Figure S4.2**), it is likely that these CPEs only form short-range aggregates but do not maintain any longer range order. Similar observations have been reported for a few

other conjugated polymer systems, where X-ray scattering indicates no crystallite formation, but optical spectroscopy was able to detect short-range ordered domains.[65,66]

The low-energy edge of the absorption spectra of the complexes is similar to that in the spectra of unblended CPE films, suggesting the presence of CPE aggregates in all complexes. As shown in **Figure 4.2b**, the onset of optical absorption showed up at 1.95 eV for all complexes, followed by a vibronic shoulder at ~ 2.15 eV. While these features likely indicate that the dilution from the PIL component in the complexes does not inhibit the aggregation of CPE chains, they can also correspond to the absorption from isolated chains that are stretched out. Thus, further quantitative analysis is needed to determine whether interchain CPE aggregates, isolated and strongly extended CPE chains, or a combination of both give rise to the low energy absorption of complex films. However, as noted above, the application of such analysis to the absorption of the complex could be misleading due to experimental limitations. Given the difficulties in quantitative comparison of the CPEs and complex's absorption spectra, we turned to photoluminescence (PL) spectroscopy, which is only marginally affected by reflectance,[53] to further probe the nature of CPE chromophores in each. The comparison between UV-Vis and PL data was made under the assumption that both techniques probe representative aggregate population within the films.

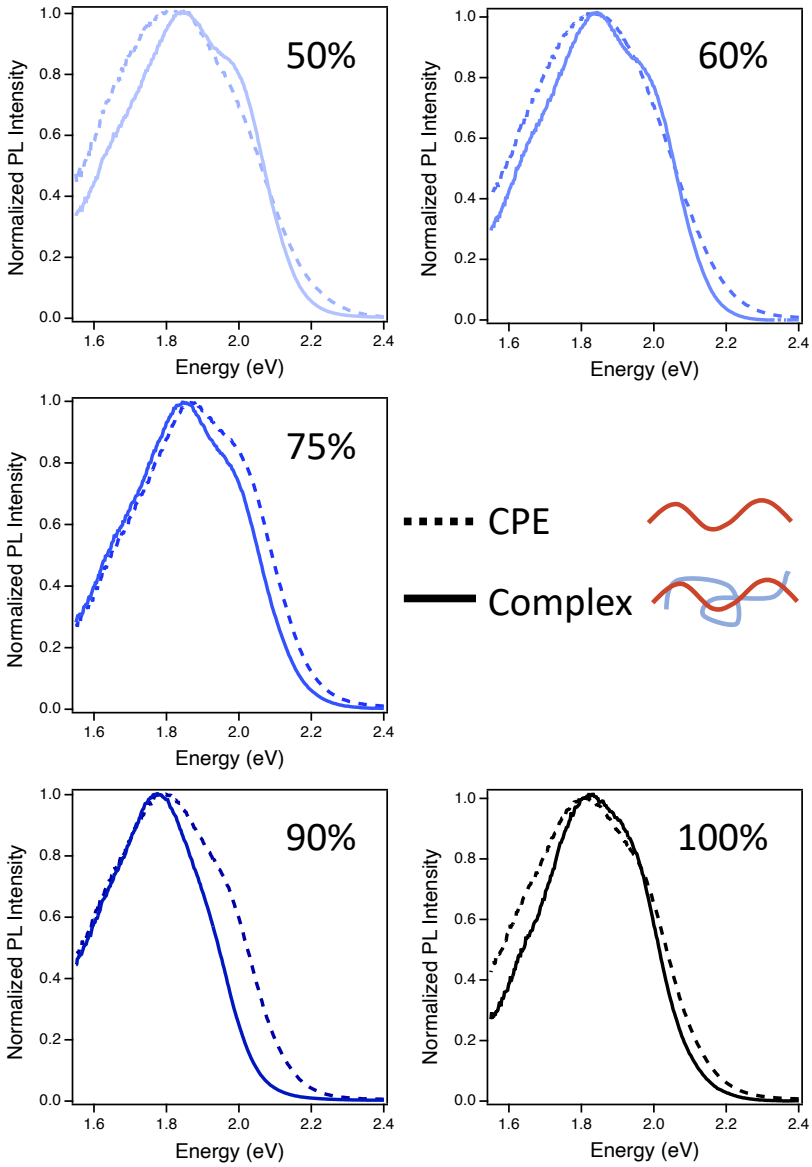

Figure 4.3. Normalized PL spectra of CPEs (dashed traces) and complexes (solid traces) for varying charge fractions. A vibronic progression is present for both CPEs and complexes.

The PL spectra show that blending the CPE with the insulating PIL does not hinder the possibility of two CPE segments being in close proximity, and that the CPE aggregates have comparable emission in neat and complexed form. As shown in **Figure 4.3**, CPEs and complexes both emit at ≈ 2.2 eV and below, and the emission spectra of these samples all have a high-energy shoulder at ≈ 1.9 – 2.0 eV. This shoulder is assigned to the 0-0 emission,

which is forbidden in interchain H-type aggregates; in contrast in a J-type aggregate, the 0-0 emission would have a higher intensity than the 0-1 emission. As a result, the presence of the high-energy shoulder confirms the HJ-aggregate characteristic of CPE aggregates in both neat and complexed films. This observation confirms that while extended isolated CPE chains (J aggregates) can contribute to the absorption onset, appreciable interchain coupling is present in the complex giving rise to the H-J characteristic absorption. Lastly, the emission spectra of the complexes are relatively narrower compared to those of the CPEs, especially for more strongly charged complexes (x = 75%, 90%, and 100%). Commonly, optical transitions are broadened due to the structural disorder along polymer chains.[62] As a result, the narrower and more defined emission profiles of the complexes are consistent with an increase in the conjugation length of the CPEs upon complexation with the PILs.

The PL spectra can be modeled using a framework developed by Spano for conjugated polymers.[54] The emission arises from the aggregated regions of the polymer films and can be described by a summation of S1→S0 emission peaks coupled to vibronic states of the molecules. PL spectra as a function of energy (E) can be fitted to a modified Frank-Condon model (Eq. 1).

$$I(E) = CE^3 \left\{ \alpha \times \exp\left[\frac{(E - E_{0-0})^2}{2\sigma^2}\right] + \sum_{m=1} \frac{S^m}{m!} \times \frac{\exp\left(-\frac{\left(E - E_{0-0} + mE_p\right)^2}{2\sigma^2}\right)}{2\sigma^2} \right\} \quad (1)$$

The model deconvolutes the PL spectrum into a series of Gaussian peaks, each correspond to a S1→S0 transition (coupled to 0-0, 0-1, etc. vibrational states), with a fixed width of σ.[54,62]

In **Eq 1**, E_p is the characteristic C=C phonon stretch of polythiophenes, S is the Huang-Rhys factor, C is a proportionality, σ is the Gaussian width of the transition, $E_{0\text{-}0}$ is the energy of the 0-0 transition, and α is a parameter for exciton coherence. Details of the PL spectra fit are discussed further in the Supporting Information, and the fits are shown in **Figure S4.3**.

The parameters obtained from the modified Frank – Condon fit, in agreement with the PL spectra shapes, support the hypothesis that the CPE chains are more planar in the highly charged complexes. As shown in **Figure 4.4a**, the $E_{0\text{-}0}$ of all samples ranges from 1.9 eV to 2.0 eV. For higher charge fractions, $E_{0\text{-}0}$ is red-shifted from the neat CPE while it is slightly blue-shifted in Complex50 and Complex60. Red-shift in the 0-0 emission peak can be due to enhanced chromophore interactions from the more planar backbone.[62,67] However, this effect can also arise from polarity differences and can be explained by the strongly charged complexes having higher dielectric constants than their corresponding CPEs.

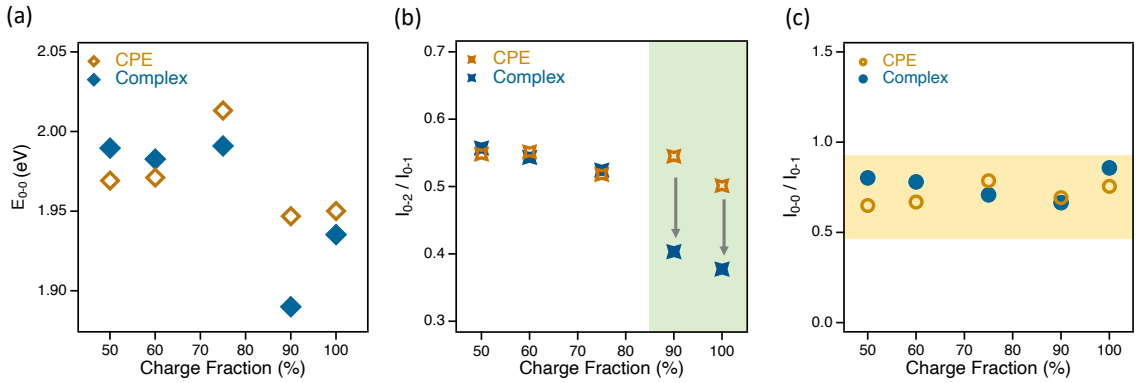

Figure 4.4. (a) Position of the 0-0 emission peak (b) Ratio between 0-2 and 0-1 and (c) 0-0 and 0-1 emission peak intensities of CPE and complex films across charge fractions. Results obtained from fitting PL spectra to equation 1.

The ratio between the 0-2 and 0-1 emission intensities also indicates planarization of the CPE backbone in strongly charged complexes. In particular, $I_{0\text{-}2}/I_{0\text{-}1}$ has been shown to be primarily

governed by the disorder along the polymer backbone and thus is indicative of intrachain excitonic coupling.[68] As illustrated in **Figure 4.4b**, the value of $I_{0\text{-}2}/I_{0\text{-}1}$ remains relatively constant at ≈ 0.55 for all CPEs and the weakly charged complexes. However, for Complex90 and Complex100, this ratio decreased significantly to ≈ 0.4. We hypothesize that the strong mixing with the PIL planarizes the CPE chains, effectively reducing torsions and conformational kinks along the CPE backbone. Such a backbone planarization effect is in agreement with numerous previous studies.[42,43,45] However, in all these complexes, the two polymers are fully charged, and we expect the two polymers are intimately mixed. For the more weakly charged complexes, local phase separation emerged. As a result, the CPE chain is now locally surrounded by neighboring CPE chains, diminishing the complexation-induced backbone planarization effects.

Quantification of the ratio between 0-0 and 0-1 emission can be used to determine the relative H-type to J-type characteristic of CPE aggregates. It appears that the characteristics of CPE aggregates are unperturbed upon complexation. The $I_{0\text{-}0}$ (J-type only) to $I_{0\text{-}1}$ (both H-type and J-type) ratio reflects the relative strength between intra- and interchain coupling and $I_{0\text{-}0}/I_{0\text{-}1}$ is < 1 for all complexes and CPE films, confirming the H-J nature of CPE aggregates in all samples (**Figure 4.4c)**. Interestingly, this value stays relatively consistent (≈ 0.55 eV – 0.75 eV) among all films, suggesting that complexation with the PIL does not perturb the nature of CPE aggregates in both locally-segregated complexes and strongly mixed complexes. This is intuitive for the more weakly charged complexes, as the CPE domains (≈ 4 – 5 nm in size from SAXS)[51] could theoretically accommodate up to ten CPE chains if we assume the length scale is set by π - π stacking. However, it is important to note that it only takes as few as two

chain segments overlapping to form H-type aggregates.[13,66] We postulate that in strongly mixed complexes, where no characteristic length scale is observed in SAXS, the interchain CPE aggregates form from at least two CPE chains in proximity to each other. This length scale is within the sub-nanometer range thus will not appear in small angle X-ray scattering. Spectroscopy, on the other hand, was able to confirm the presence of CPE – CPE overlap, providing information on local ordering of the complex that would otherwise not appear in mesoscopic techniques.

Our observations of minimal disturbance to the CPE aggregates in weakly segregated conjugated polymer charged complexes are fundamentally different from what has been previously reported for blends of neutral conjugated polymers with an insulating and polar polymer. In particular, P3HT aggregates in phase-separated blends of P3HT with poly(ethylene oxide), PEO, and with poly(methyl methacrylate), PMMA, have been reported to significantly shifted from H-J type to predominantly J-type.[69,70] These studies suggested that the change in the nature of P3HT aggregates was induced by the formation of confined P3HT domains within a polar matrix. Due to the strong repulsive forces between dissimilar neutral polymers, the P3HT domains in these studies are within sub-micrometer in size, in contrast to the more intimate mixing that occurs in the complexes studied here (domain size is only $\approx$ 5 nm). Here, the simultaneous presence of electrostatic attractive forces of the side chains and the short-range repulsion of dissimilar polymer backbone results does not result in significant changes in the nature of CPE aggregates in the weakly charged complexes.

The as-cast film of CPEs and conjugated polymer complex films had very low charge carrier concentrations as indicated by the absence of the polaronic peak in their absorption spectra (**Figure 4.2**), suggesting that they did not behave as self-doped polymers.[71–74] To investigate the electrical conductivity, the films were doped with the strong acid bistriflimidic acid (HTFSI) to introduce charge carriers. Films of CPE and conjugated complexes were doped by exposure to a vapor of HTFSI at 50°C. The films of the complexes were further heated at 55°C overnight to promote complete diffusion of dopants throughout the thick film. We defined saturation as the point at which further exposure of the film the HTFSI vapor did not induce additional changes to the absorption spectrum and the electrical conductivity. Evidence of electronic doping can be seen from the bleaching of the neutral polymer absorption in the 2.0 – 3.0 eV region, and the emergence of an absorption peak at ≈ 1.55 eV indicates charge carrier formation (**Figure S4.4**).

All CPE films have relatively low electronic conductivity, which is consistent with their disordered structure indicated by WAXS (**Figure S4.2**) and their low MWs (**Table S4.1**). As shown in **Figure 4.5a**, the electronic conductivity of the CPE films lies between 5×10^{-4} to 5×10^{-3} S/cm and does not vary monotonically with charge fraction. These values are within the same order of magnitude to the previously reported conductivity of other chemically doped CPE systems.[43,75] From the bleaching of the neutral backbone peak in UV-Vis data (**Figure S4.4**), we estimate the charge carrier concentration in these films to be ≈ 6×10^{20} cm^{-3}, corresponding to 1 polaron per 5 – 6 repeat units. The conductivity suggests a charge carrier mobility ~5×10^{-6} to 5×10^{-5} cm^2 V^{-1} s^{-1} for the unblended CPEs, within the same order of magnitude to those reported for other hexylthiophene-based CPE.[76] Low carrier mobility has

also been observed for low MW[77] or regiorandom P3HT.[78] Much higher mobilities of 10^{-3} – 10^{-2} cm^2 V^{-1} s^{-1} have been reported for a series of poly(3-alkylsulfonate thiophene) CPEs with the same tetramethylammonium (TMA) counterion.[79] These values were determined using measurements of organic electrochemical transistors (OECT) where the CPE layer was crosslinked and swollen in aqueous electrolyte making the direct comparison less straightforward.

Interestingly, the conductivities of complex films at each charge fraction are much higher than that of the unblended CPEs despite the dilution with the insulating PIL. As shown in **Figure 4.5a** and **4.5b**, Complex50, Complex60 and Complex 75 have conductivities that are two orders of magnitude greater than the unblended CPEs. For highly charged complexes, the increase was around 1000 times, resulting in an electrical conductivity of ≈ 1 S/cm. The conductivities of Complex90 and Complex100 are comparable to that of the unoptimized commercial-grade PEDOT:PSS [80] and polyaniline–polyacid complexes.[81,82] Assuming that complexes have around half of the charge carrier concentration of unblended CPEs (3×10^{20} cm^{-3}), these conductivity values suggest that the charge carrier mobility is ~10^{-3} cm^2 V^{-1} s^{-1} for weakly charged complexes and ~10^{-2} cm^2 V^{-1} s^{-1} for highly charged complexes.

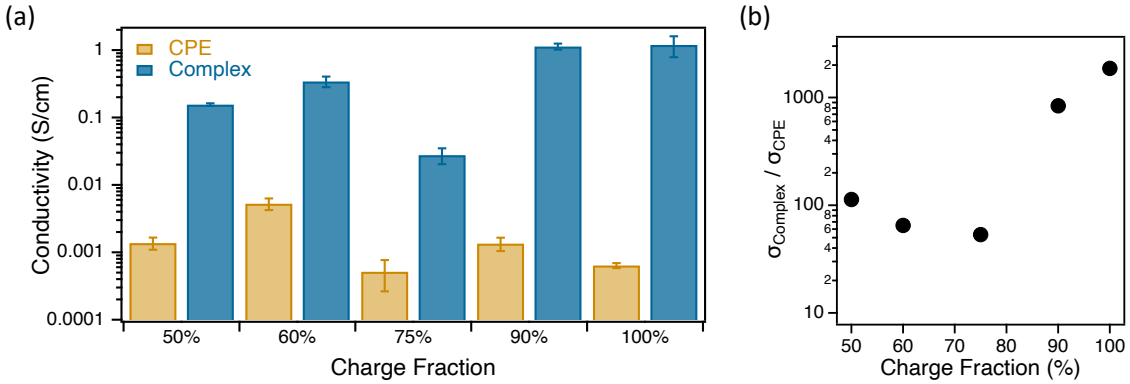

Figure 4.5. (a) Electrical conductivity of CPEs and complexes at varying charge fraction (b) The relative increase in electronic conductivity upon complexation at each charge fraction.

To further elucidate the differences in electronic transport between CPE and conjugated polymer complexes, temperature-dependent conductivity measurements of these samples were performed. As shown in **Figure 4.6**, the temperature-dependent conductivities for both the CPEs and complexes have an Arrhenius-type form (Equation 2)

$$\sigma = \sigma_0 \, exp\left[\frac{-E_a}{k_B T}\right] (2)$$

where the pre-exponential factor σ_0 is the high temperature limit of the conductivity assuming no phase change, E_a is the transport activation energy, k_B is the Boltzmann constant, and T is temperature. The linear relationship between the logarithm of conductivity and T^{-1} indicates thermally activated nearest neighbor hopping transport in these samples between 300 K and 180 K. For comparison, temperature-dependent conductivities of all samples were also fitted with variable-range hopping models, and the results are given in the Supporting Information (**Figures S4.5, S4.6** and **S4.7**). The nearest neighbor hopping model gives the best fit in all cases, as frequently observed for semiconducting polymers having electrical conductivities of 1 S cm^{-1} and below.

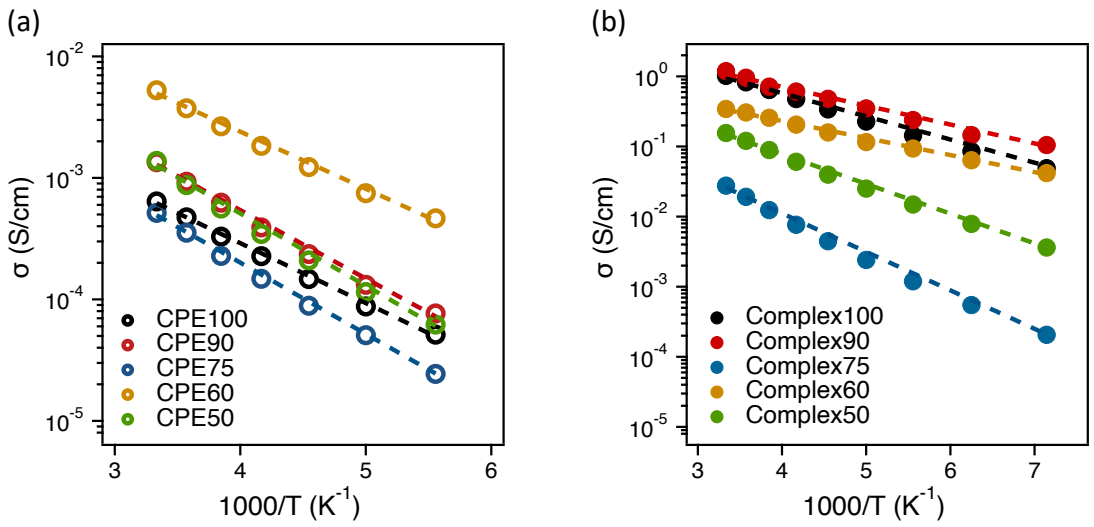

Figure 4.6. Semi-log plot of conductivity of **(a)** CPEs and **(b)** complexes with different charge fractions as a function of inverse temperature, showing nearest neighbor hopping mechanism. Dashed lines are fits to a thermally activated hopping model for transport (Eq. 2).

Values of the two transport parameters E_a and σ_0 obtained from fitting the temperature-dependent conductivity of the samples to Equation (2) suggest more facile electrical transport in complex films, consistent with their higher room-temperature conductivities compared to unblended CPEs. As shown in **Figure 4.7a**, all complexes have lower E_a than their corresponding CPEs across all charge fractions, indicating a lower energy barrier for the hopping of charge carriers. Particularly, the activation energy in CPEs range 90 – 120 meV, within the same range that was reported for vapor-doped P3HT with comparable electrical conductivity.[83] For complexes, that energy barrier is much lower (55 – 100 meV). While there is no clear correlation between activation energy and polymer charge fraction, it is consistent that E_a is larger in CPE films than in complex films for the same charge fraction. Similarly, the values of the pre-factor σ_0 of the complex are consistently higher than those of the CPEs for the same charge fraction (**Figure 4.7b**). Interestingly, the pre-factors σ_0 of the highly charged, homogeneous complexes (x = 90% and 100%) appear to be higher than that of the

locally ordered ones (x = 60% and 50%), even though they all have relatively similar activation energies. Lastly, at x =75%, the complex has the highest E_a as well as the lowest σ_0 and room-temperature conductivity compared to other charge fractions, indicating that electronic transport is the least efficient in this complex.

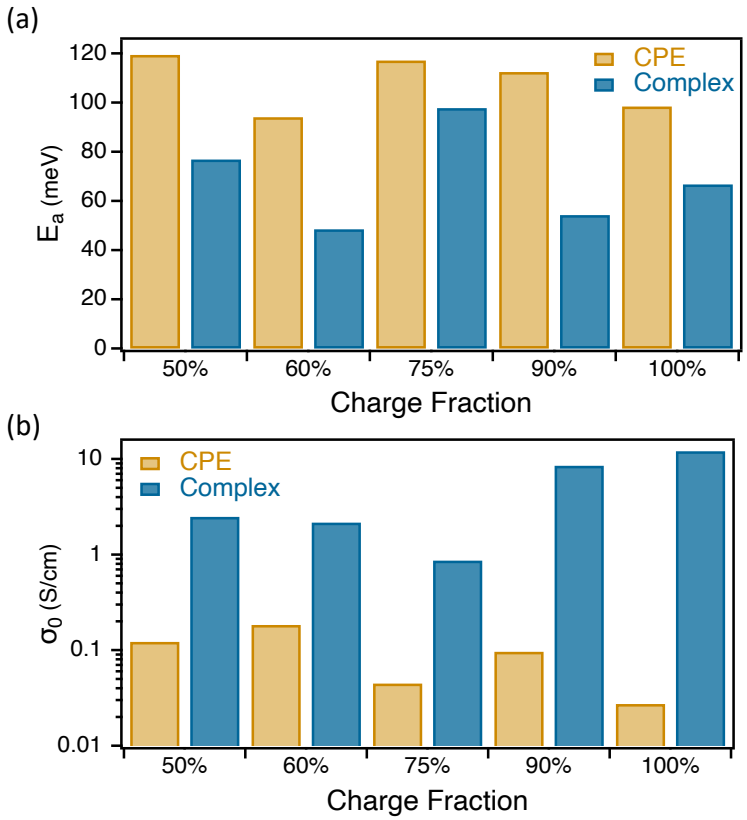

Figure 4.7. (a) Activation energy and (b) high-temperature conductivity limit of CPEs and conjugated polymer complexes

Our data indicates that the complexation process induces morphologies with better connectivity between CPE chains across mesoscopic distances, leading to the enhanced electronic transport properties of the complexes compared to the CPEs. In particular, the increase in electrical conductivity could arise from changes in the breadth of the electronic density of states or changes in the connectivity of the transport pathways in the solid. The interactions of the CPE chains in the complex should impact the density of states and the

hopping barrier between sites impacting E_a, while the percolation of carriers through the solid is mainly associated with the pre-factor σ_0. As shown in **Figure 4.7**, while for all complexes the E_a is smaller than that for the corresponding CPE, the pre-factor the σ_0 is substantially higher. As a result, the overall increase in the conductivity upon complexation is dominated by the pre-factor, σ_0, that is indicative of the long-range connectivity among conductive sites. Our observations support conclusions from prior studies that long-range connectivity is more important than local ordering.[65,84,85]

The mechanism for the improvement in long-range percolation, however, likely varies between different complexes. It is important to note that no improvement in the local ordering of the CPE was observed for phase-segregated complexes, yet a significant increase in conductivity was still observed. Despite the local phase segregation occurring in these weakly charged complexes, their higher pre-factor compared to the corresponding CPEs suggests that the CPE domains still form a continuous pathways that can support efficient electron transport. In strongly mixed complexes, the pre-factor is even higher indicating that the reduction in structural disorder of the CPE backbone in these complexes can improve both the interchain hopping and bridge aggregated regions to improve the transport pathways.[86–88] Lastly, there is a crossover point between strongly mixed and locally segregated morphologies, which is at $x = 75\%$. Among all complexes, Complex75 appears to have the lowest electrical conductivity. We hypothesize that this sample has a combination of both locally segregated and strongly mixed structures, resulting in mesoscopic heterogeneity that disrupts the continuity of transport pathway evidenced by its higher E_a and lower σ_0, relative to the other complexes.

Thus, a morphology that is heterogeneous between strongly mixed and locally ordered is likely detrimental in optimizing electronic transport in charged polymer complexes.

4.5 Conclusion

We have demonstrated that the complexation between a CPE and an oppositely charged PIL results in polymer complexes whose morphology leads to higher electrical conductivity than unblended CPEs. We utilized a model system of CPE and PIL with varying frequency of charged repeat units and found that for complexes of highly charged polymers, the intimate mixing with the PIL reduces structural disorder of the CPE backbone, leading to improvements in the intrachain conjugation. The electrical conductivity is three orders of magnitude higher than in unblended CPEs suggesting that the planarization of CPE chains in the complex improves the π-orbital overlap between adjacent chains for efficient interchain hopping and increases the connectivity between CPE aggregates. For complexes of more weakly charged polymers, the local repulsion between dissimilar chains lead to the formation of nanoscale domains enriched in either the CPE or the PIL. Such phase segregation did not result in major differences in the local structure of the CPE chains as determined by optical spectroscopy compared to its unblended state. However, these complexes still show a two order of magnitude increase in conductivity compared to their corresponding neat CPEs. This suggests that the CPE domains formed via local phase segregation are continuous and thus can support efficient long-range electronic transport.

Our study has elucidated the role of complexation on the structural ordering and the optoelectronic properties of CPE chains within conjugated polymer complexes and provided

fundamental design rules for improving transport performance of CPEs via morphological control. Currently, manipulation of electronic properties of conjugated polymers is limited to variation in synthesis (for new repeat units, changing MW, copolymerization) [15,89,90] or in processing conditions,[56,91,92] or blending with additives.[56,93,94] Our results emphasize the potential of electrostatic interactions in blends as an effective handle for controlling the morphology and electronic structure of conjugated polymers, with added advantages for processing. Charged conjugated polymer complexes offer a versatile design space not only for controlling existing optoelectronic properties, but also for incorporating other desirable properties for soft electronics, such as mechanical behavior, that are difficult to achieve with a single material.

4.6 Acknowledgement

The authors acknowledge funding support from the Department of Energy Office of Basic Energy Sciences under Grant No. DE-SC0016390. The authors acknowledge the use of shared facilities of the UCSB MRSEC (NSF DMR 1720256), a member of the Materials Research Facilities Network (www.mrfn.org) and the use of the Nanostructures Cleanroom Facility within the California NanoSystems Institute, supported by the University of California, Santa Barbara, and the University of California, Office of the President. This research used resources of the National Synchrotron Light Source II, a U.S. Department of Energy Office of Science User Facility (DE-SC0012704; beamline 11-BM).

4.7 Appendix

Synthesis of Poly(3-(6'-bromohexyl)thiophene-co-3-hexylthiophene) (P3BrHT:P3HT)

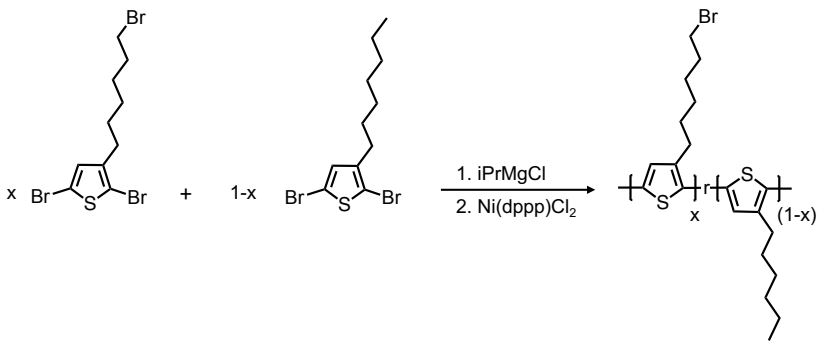

P3BrHT:P3HT random copolymers was synthesized following a previously reported protocol.[95] In an oven-dried round bottom flask equipped with a magnetic stir bar, 2,5-dibromo-3-(6-bromohexyl)thiophene (purchased from eNovation Chemicals LLC) and 2,5-dibromo-3-hexylthiophene monomers were mixed in targeted molar ratios (50:50, 60:40, 75:25, 90:10, and 100:0). The flask was sealed with rubber septa and dried under active vacuum overnight. Distilled THF was added to the flask, and the mixture was stirred and purged with dry nitrogen for 20 minutes. Isopropylmagnesium chloride was then added dropwise to the flask under rigorous stirring, and the mixture was stirred at ambient temperature for two hours under nitrogen. After 2 hours, a suspension of $Ni(dppp)Cl_2$ in distilled THF was added quickly to the reaction. Immediately, the mixture turned from pale yellow to vibrant red, indicating that the polymerization process was taking place. The polymerization was run for 12 hours and was then quenched by rapid addition of 1M HCl solution. The mixture was precipitated in cold methanol, and the obtained polymer was purified by washing in a Soxhlet apparatus with methanol, acetone, and ethyl acetate before extraction with THF. The product was concentrated under vacuum, yielding a red-purple solid. The isolated product was then dried overnight under vacuum to remove any remaining solvent.

Synthesis of Poly[6-(thiophen-3-yl)hexane-1-sulfonate-co-3-(hexylthiophene)]

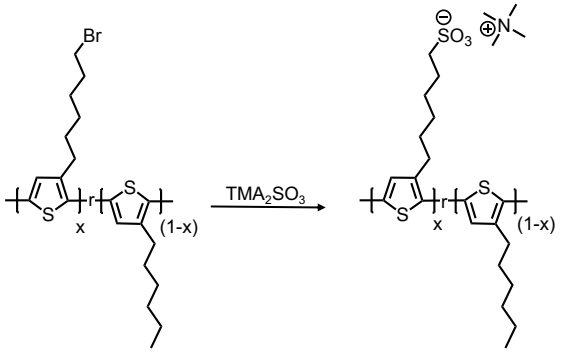

In a round bottom flask equipped with a magnetic stir bar, P3BrHT-P3HT was dissolved in THF and the flask was sealed with a rubber septa. The mixture was stirred and purged with dry nitrogen for 30 minutes. Solution of 1M bis(tetramethylammonium)sulfite (TMA_2SO_3) in methanol was then added in 10-x excess to the reaction flask, and the mixture was refluxed at 70˚C. After 1 hour, more methanol was added to the flask to dissolve the ionic-functionalized polymer and to drive the reaction to completion. The reaction was carried on overnight, and the reaction mixture was then let cool down to room temperature. The polymer was purified by dialyzing with deionized water for 5 days using 10 kDa cutoff membranes for 5 days. The dialysate was replaced every 12 h. The isolated product was dried with lyophilizer, yielding a red-purple solid.

Synthesis of Poly(N-hydroxysuccinimidyl acrylate) (PNHSA)

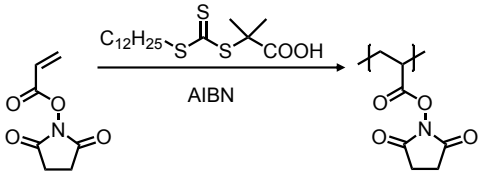

PNHSA was synthesized following a previously reported protocol.[96] In a Schlenk flask equipped with a magnetic stir bar, N-acryloxysuccinimide, DDMAT, and AIBN were dissolved in anhydrous DMF. The solution was degassed using five freeze-pump-thaw cycles. Then, the flask was filled with dry nitrogen and heated to 70˚C in an oil bath. The mixture was stirred vigorously, and the reaction was let run for 24 h. After cooling to 25˚C, the reaction mixture was precipitated from methanol. The mixture was filtered to collect the polymer solid, which was then dried under vacuum, dissolved in DMF, and reprecipitated from methanol, twice. The final product was filtered and dried under a vacuum at 60˚C for 24 h to obtain a pale-yellow polymer powder.

Synthesis of Poly[(1-propylimidazolacrylamide)-co-3-methyl-1-(propyl acrylamide)]

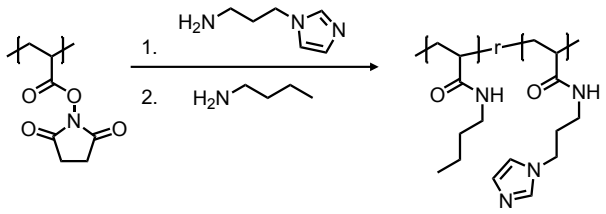

PNHSA was randomly functionalized with imidazole-amine and butylamine according to a previously reported protocol.[97] In a round bottom flask equipped with a magnetic stir bar, the polymer was dissolved in anhydrous DMF. The flask was sealed with rubber septa and was purged with dry nitrogen for 30 minutes. Appropriate amount of 1-(3- aminopropyl)imidazole solution (50%, 60%, 75%, 90%, and 100% molar equivalent) in anhydrous DMF was added dropwise to the polymer solution. The reaction was stirred vigorously and let run at 25˚C. A water bath was used to control the reaction temperature. After 12 hours, the reaction mixture was precipitated from ethyl acetate, the polymer solid was collected and re-dissolve in methanol. The solution was re-precipitated from diethyl ether, and the process was repeated

twice. At the end, the polymer solid was collected and dried under vacuum at 60˚C for 12 h, yielding a pale-yellow brittle solid. This polymer was then dissolved in anhydrous DMF, and 5-fold excess of butylamine was added to the solution. The reaction mixture was stirred for 12 hours at 25˚C to fully react all NHSA groups, yielding the neutral random copolymers.

Synthesis of Poly[(3-methyl-1-propylimidazolylacrylamide)-co-3-methyl-1-(propyl acrylamide)]

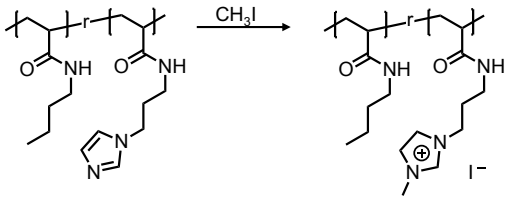

The neutral copolymer was dissolved in anhydrous DMF in a round bottom flask, and the flask was then sealed with a rubber septa. The solution was heated mildly to 40˚C and purged with dry nitrogen for 30 minutes. After that, 3-fold excess of iodomethane was added to the flask with a syringe, and the reaction mixture was stirred continuously for an additional 12 hours. The mixture was then precipitated from diethyl ether, and the solid polymer was collected and dried under vacuum at 60˚C overnight. Exchange of the iodine anion with chloride anion was carried out by dissolving the polymer in a 10-fold excess of NaCl solution in methanol. This mixture was stirred vigorously at 45˚C overnight. The ion-exchanged polymer was purified by dialysis against methanol using a 10 kDa cutoff membrane for 4 days, and the dialysate was replaced every 12 hours. The purified polymer was dried under vacuum at 90˚C for 24 h, yielding a pale yellow solid.

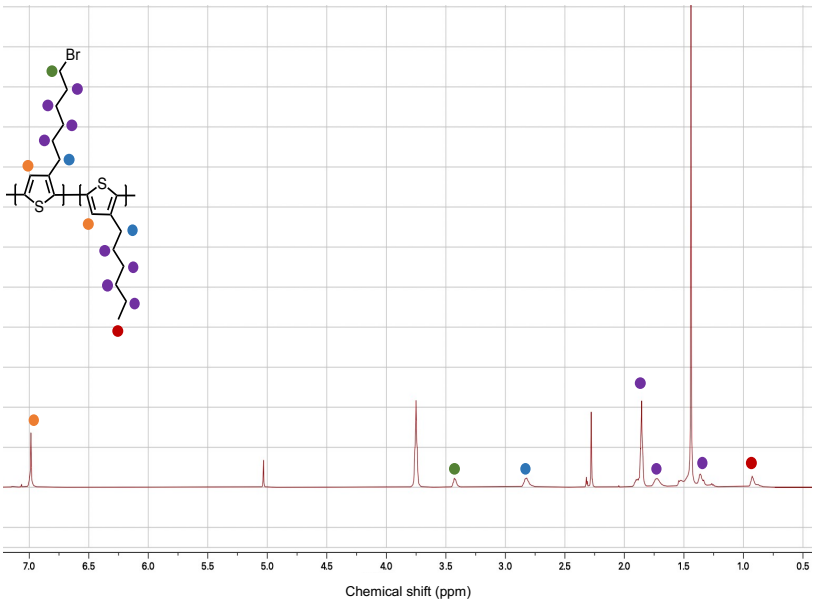

Figure S4.1a. Solution state ^{1}H NMR spectra of Poly(3-(6'-bromohexyl)thiophene-co-3-hexylthiophene)

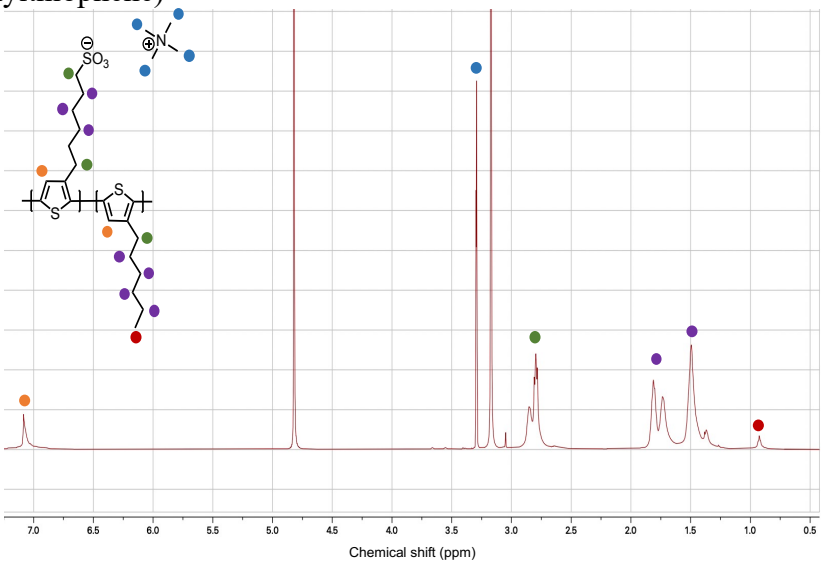

Figure S4.1b. Solution state ^{1}H NMR spectra of Poly[6-(thiophen-3-yl)hexane-1-sulfonate-co-3-(hexylthiophene)] trimethyl amine

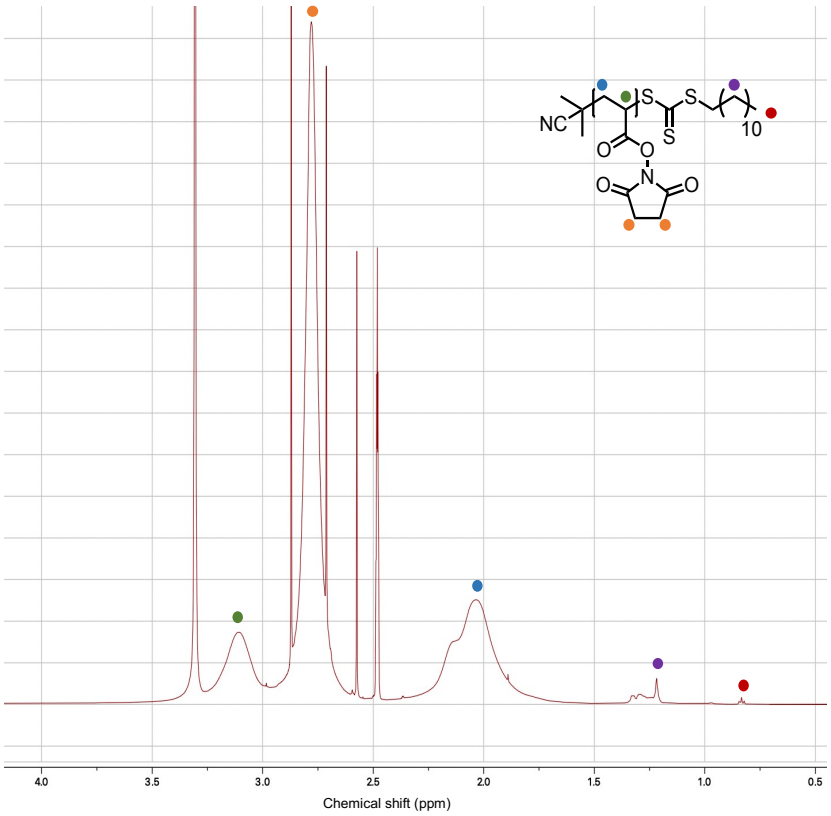

Figure S4.1c. Solution state ^{1}H NMR spectra of Poly(N-hydroxysuccinimidyl acrylate)

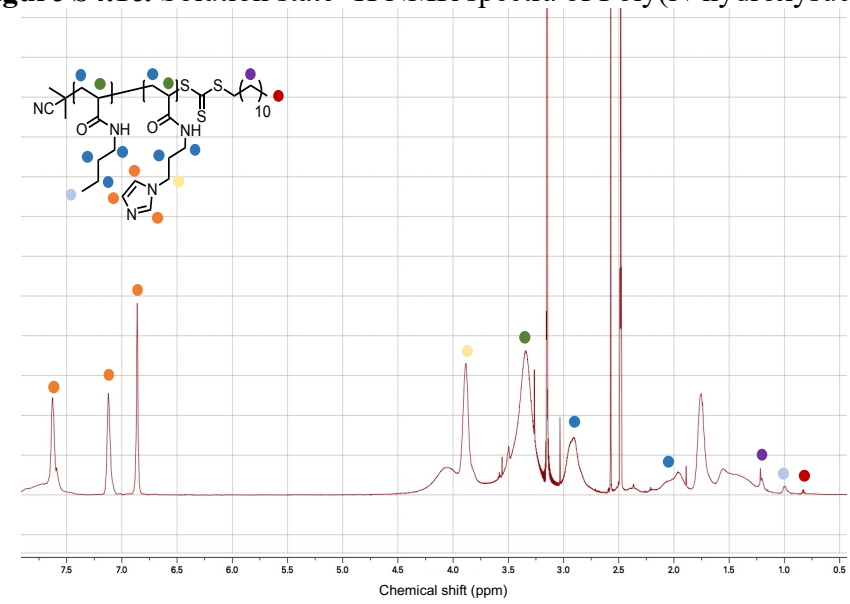

Figure S4.1d. Solution state ^{1}H NMR spectra of Poly[(1-propylimidazolacrylamide)-co-3-methyl-1-(propyl acrylamide)]

Sample Preparation

Stock polymer solution was prepared by dissolving the polymer in a 40% THF : 60% water solvent mixture to achieve a final molar concentration of 1M. Inside an Eppendorf tube, solutions of CPE and PIL of similar charge fraction were mixed in stoichiometric ratio, and the tube was mixed for 1 minute using a vortex mixture. After that, the mixture was centrifuged at 7000 rpm for 10 minutes to drive the accumulation of coacervate droplets to the bottom of the Eppendorf tube, while the polymer-deficient supernatant phase floated to the top due to its lower density.

The coacervate was then collected by decanting the supernatant and was blade-coated onto quartz substrates for subsequent spectroscopy and conductivity measurements. CPE solutions were spin casted onto quartz substrate. CPE films are 250 to 300 nm thick, while CPC film thickness ranges from 1 μm to 4 μm going from CPC50 to CPC100 due to the difference in polymer loading in the coacervate phase and hence variation in the coacervate viscosity. Film thickness was measured with a Bruker DektakXT Stylus profilometer. All samples were soft-baked at 50˚C under vacuum for 30 min to remove excess solvent, and were further dried under high vacuum (10^{-8} Torr) overnight.

Vapor Doping

Doping was done inside a nitrogen glovebox. Polymer film was attached to a lid of a glass jar, and HTFSI crystals were placed inside the jar. The jar was closed tightly and heated at 50˚C on a hot plate for 13 minutes (CPE) or 45 minutes (CPC). For the coacervate film, the film was transferred to another closed clean glass jar and heated at 55ºC for an additional 48 hours to promote efficient diffusion of dopants into the film and to prevent leakage of dopant vapor.

Optical Spectroscopy

UV-Vis absorption spectra of CPE and CPC films were taken using an Agilent Cary 60 UV-Vis spectrophotometer. All measurements were done at ambient temperature (~ 25˚C). Emission spectra were taken using a Horiba FluoroMax® 4 spectrometer at 450 nm excitation wavelength. The sample is illuminated by a 150 W xenon, continuous output, ozone-free lamp. Emission spectrum of each film was averaged over 3 scans.

Electronic Conductivity Measurement

Gold electrical contacts (≈ 60 nm thick) were deposited at 1 Å s^{-1} rate onto casted polymer film on quartz via controlled thermal evaporation through a shadow mask. Transmission line measurements were carried out to determine in-plane electronic conductivity of the polymer film using a Keithley 6485 picoammeter. Measurements were carried out inside a nitrogen glovebox at room temperature. To obtain the activation energy and high-temperature conductivity limit of the samples, temperature-dependent conductivity measurements were performed under vacuum (≈ 10^{-4} Torr) at temperatures from 300K down to 180K to prevent de-doping of the polymer films.

X-ray Scattering

Samples were loaded into aluminum washers, soft-baked at 50 °C under vacuum to remove the excess solvent, and further dried under high vacuum (≈ 10^{-8} Torr) overnight. These samples were then sealed with Kapton tape. X-ray scattering measurements were performed at the National Synchrotron Light Source II (NSLS-II, beamline 11-BM, Brookhaven National

Laboratory), with an X-ray energy of 13.5 keV. Data processings (the detector distance calibration with a silver behenate standard, the reduction of two-dimensional (2D) raw SAXS images into one-dimensional (1D) intensity versus q curves, and corrections for empty cell scattering) were performed using the Nika package for Igor Pro for data taken at the amyotrophic lateral sclerosis (ALS) and using the SciAnalysis software for NSLS-II data.

Table S4.1. MW of CPEs used in this study

Charge fraction	Mn (kDa)	Mw (kDa)	PDI
50	9.01	12.6	1.40
60	8.17	10.7	1.31
75	12.2	15.2	1.24
90	13.6	20.6	1.52
100	13.0	22.9	1.76

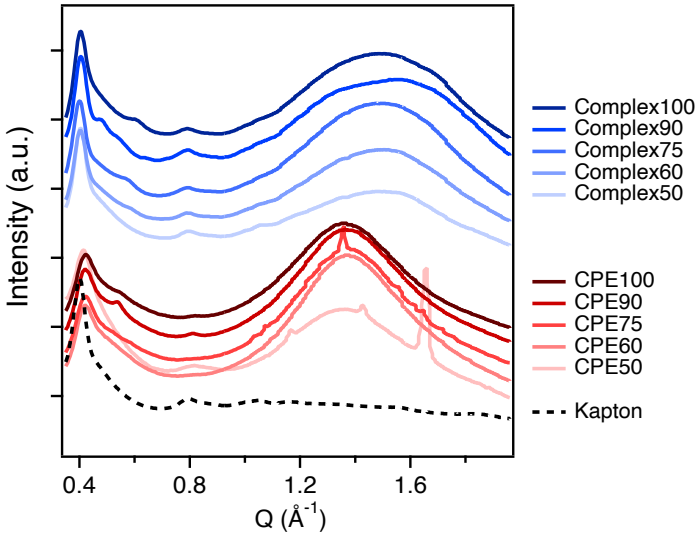

Figure S4.2. WAXS data indicates the lack of crystallinity in both CPEs and CPCs. Some spikes in CPE WAXS traces are likely due to residual salt crystals from CPE solutions. It is possible that there is π-stacked structure, but it appears to be too weak and is completely overwhelmed by the amorphous halo. The shifting of the broad peak at ~ 1.38 $Å^{-1}$ spacing of 4.55 Å in neat CPEs to ~ 1.55 $Å^{-1}$ of 4.0 Å in CPCs could suggest shorter interchain distances.

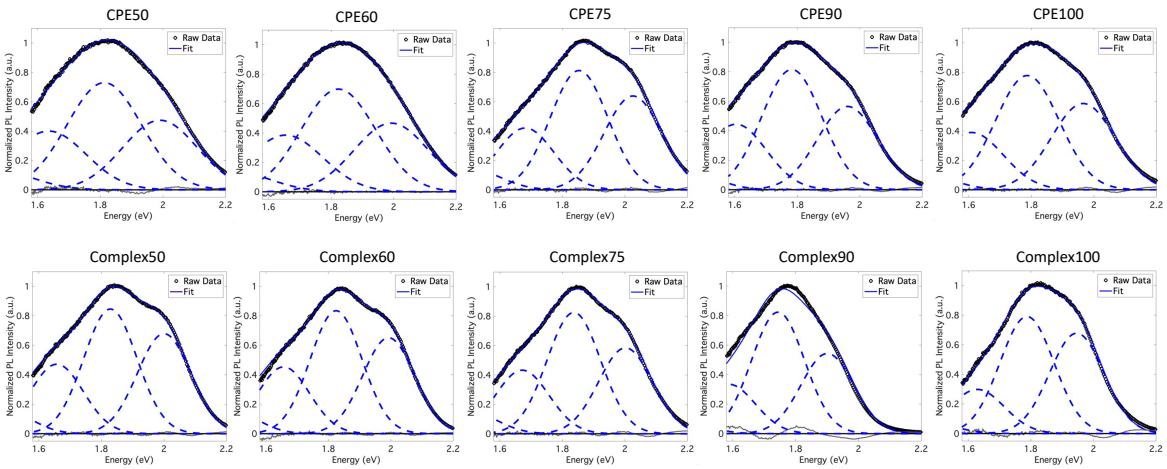

Figure S4.3. PL spectra of CPEs (top row) and CPCs (bottom row) fit to the modified Frank-Condon model according to equation (1) in the main text. Jacobian transformation [98] was used to convert wavelength to energy in all spectra. The refractive index of the film was assumed to be constant across the energy of interest. The Huang – Rhys factor, S, was set to varied within a range of 1.0 – 1.5.

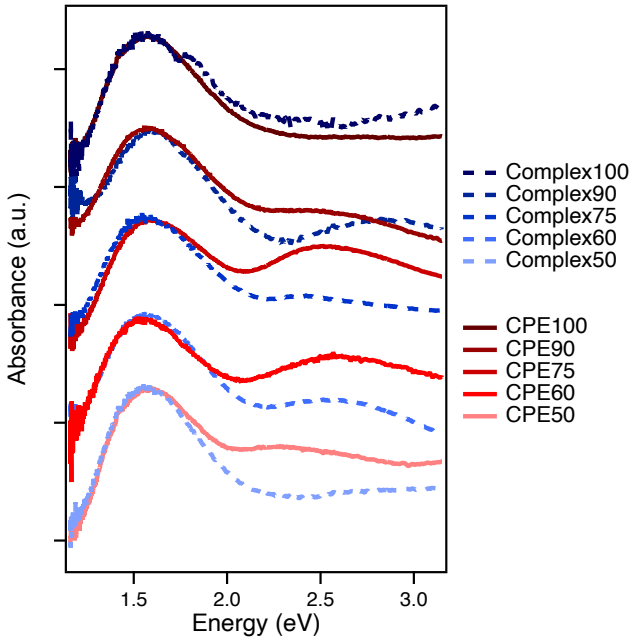

Figure S4.4. UV-Vis spectroscopy confirmed electronic doping of CPE and CPC films upon exposure to acid vapor

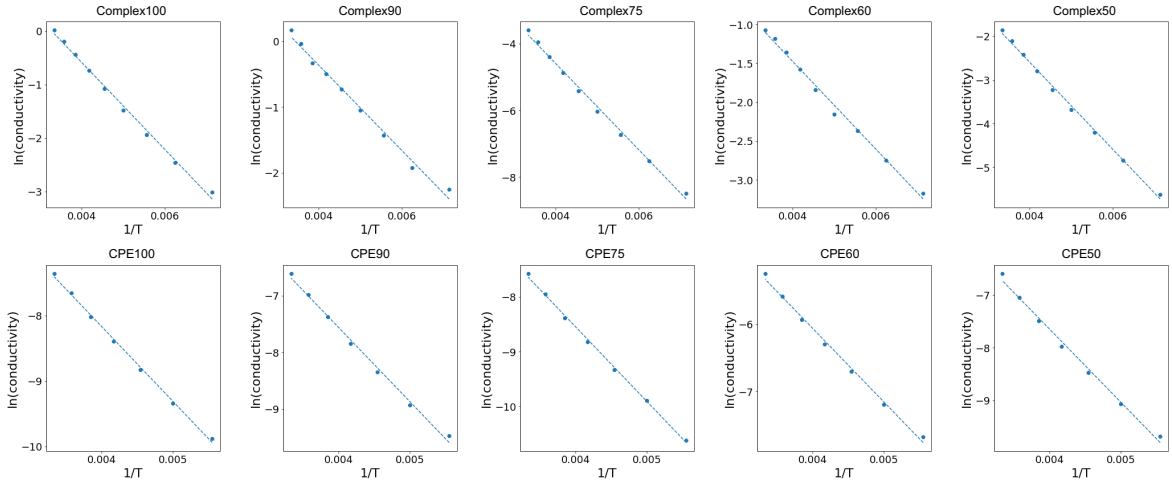

Figure S4.5. Fit of temperature-dependent conductivity data to Arrhenius equation

Variable Range Hopping (VRH) Models

$$\sigma = \sigma_0 \, exp\left[\frac{T_0}{T}^{\beta}\right]$$

Where σ_0 is a pre-factor representing the high temperature limiting conductivity, T_0 is a characteristic temperature, and β = 1/2 for Efros – Shklovskii variable range hopping with a Coulomb gap (or 1-D Mott-type VRH), and β = 1/4 for Mott 3-D VRH.

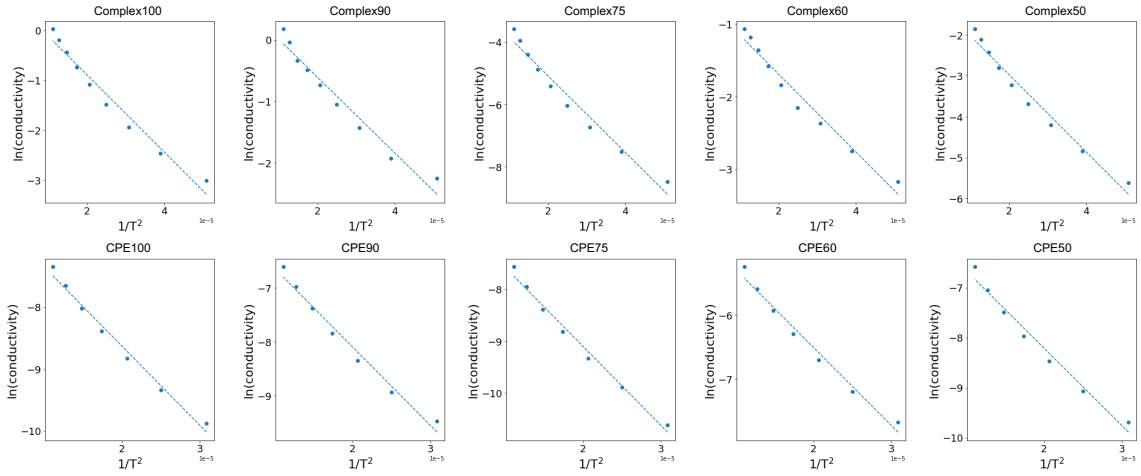

Figure S4.6. Fit of temperature-dependent conductivity data to Efors – Shklovskii VRH model

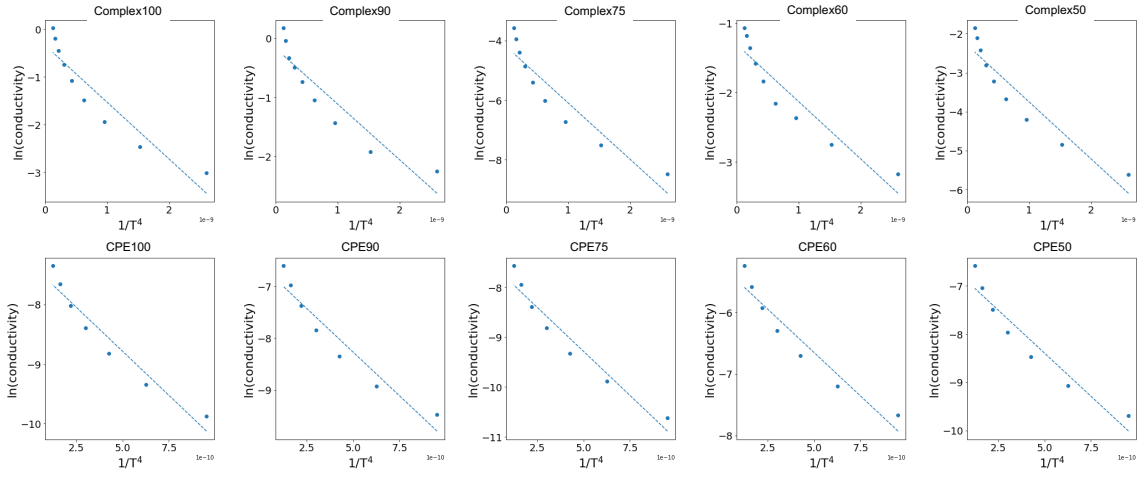

Figure S4.7. Fit of temperature-dependent conductivity data to Mott VRH model

4.8 References

(1) Dimov, I. B.; Moser, M.; Malliaras, G. G.; McCulloch, I. Semiconducting Polymers for Neural Applications. *Chem. Rev.* **2022**, *122* (4), 4356–4396. https://doi.org/10.1021/acs.chemrev.1c00685.

(2) Zheng, Y.; Zhang, S.; Tok, J. B. H.; Bao, Z. Molecular Design of Stretchable Polymer Semiconductors: Current Progress and Future Directions. *J. Am. Chem. Soc.* **2022**, *144* (11), 4699–4715. https://doi.org/10.1021/jacs.2c00072.

(3) Paterson, A. F.; Singh, S.; Fallon, K. J.; Hodsden, T.; Han, Y.; Schroeder, B. C.; Bronstein, H.; Heeney, M.; McCulloch, I.; Anthopoulos, T. D. Recent Progress in High-Mobility Organic Transistors: A Reality Check. *Adv. Mater.* **2018**, *30* (36), 1801079. https://doi.org/10.1002/adma.201801079.

(4) Chen, A. X.; Kleinschmidt, A. T.; Choudhary, K.; Lipomi, D. J. Beyond Stretchability: Strength, Toughness, and Elastic Range in Semiconducting Polymers. *Chem. Mater.* **2020**, *32* (18), 7582–7601. https://doi.org/10.1021/acs.chemmater.0c03019.

(5) O'Connor, B.; Kline, R. J.; Conrad, B. R.; Richter, L. J.; Gundlach, D.; Toney, M. F.; DeLongchamp, D. M. Anisotropic Structure and Charge Transport in Highly Strain-Aligned Regioregular Poly(3-Hexylthiophene). *Adv. Funct. Mater.* **2011**, *21* (19), 3697–3705. https://doi.org/10.1002/adfm.201100904.

(6) Patel, S. N.; Glaudell, A. M.; Peterson, K. A.; Thomas, E. M.; O'Hara, K. A.; Lim, E.; Chabinyc, M. L. Morphology Controls the Thermoelectric Power Factor of a Doped Semiconducting Polymer. *Sci. Adv.* **2017**, *3* (6). https://doi.org/10.1126/sciadv.1700434.

(7) Panzer, F.; Bässler, H.; Köhler, A. Temperature Induced Order-Disorder Transition in Solutions of Conjugated Polymers Probed by Optical Spectroscopy. *J. Phys. Chem. Lett.* **2017**, *8* (1), 114–125. https://doi.org/10.1021/acs.jpclett.6b01641.

(8) Noriega, R.; Rivnay, J.; Vandewal, K.; Koch, F. P. V.; Stingelin, N.; Smith, P.; Toney, M. F.; Salleo, A. A General Relationship between Disorder, Aggregation and Charge

Transport in Conjugated Polymers. *Nat. Mater.* **2013**, *12* (11), 1038–1044. https://doi.org/10.1038/nmat3722.

(9) Persson, N. E.; Chu, P. H.; McBride, M.; Grover, M.; Reichmanis, E. Nucleation, Growth, and Alignment of Poly(3-Hexylthiophene) Nanofibers for High-Performance OFETs. *Acc. Chem. Res.* **2017**, *50* (4), 932–942. https://doi.org/10.1021/acs.accounts.6b00639.

(10) Lim, E.; Glaudell, A. M.; Miller, R.; Chabinyc, M. L. The Role of Ordering on the Thermoelectric Properties of Blends of Regioregular and Regiorandom Poly(3-Hexylthiophene). *Adv. Electron. Mater.* **2019**, *5* (11), 1800915. https://doi.org/10.1002/aelm.201800915.

(11) Botiz, I.; Durbin, M. M.; Stingelin, N. Providing a Window into the Phase Behavior of Semiconducting Polymers. *Macromolecules* **2021**, *54* (12), 5304–5320. https://doi.org/10.1021/acs.macromol.1c00296.

(12) McCulloch, I.; Heeney, M.; Bailey, C.; Genevicius, K.; MacDonald, I.; Shkunov, M.; Sparrowe, D.; Tierney, S.; Wagner, R.; Zhang, W.; Chabinyc, M. L.; Kline, R. J.; McGehee, M. D.; Toney, M. F. Liquid-Crystalline Semiconducting Polymers with High Charge-Carrier Mobility. *Nat. Mater.* **2006**, *5* (4), 328–333. https://doi.org/10.1038/nmat1612.

(13) Paquin, F.; Yamagata, H.; Hestand, N. J.; Sakowicz, M.; Bérubé, N.; Côté, M.; Reynolds, L. X.; Haque, S. A.; Stingelin, N.; Spano, F. C.; Silva, C. Two-Dimensional Spatial Coherence of Excitons in Semicrystalline Polymeric Semiconductors: Effect of Molecular Weight. *Phys. Rev. B - Condens. Matter Mater. Phys.* **2013**, *88* (15), 155202. https://doi.org/10.1103/PhysRevB.88.155202.

(14) Scharsich, C.; Lohwasser, R. H.; Sommer, M.; Asawapirom, U.; Scherf, U.; Thelakkat, M.; Neher, D.; Köhler, A. Control of Aggregate Formation in Poly(3-Hexylthiophene) by Solvent, Molecular Weight, and Synthetic Method. *J. Polym. Sci. Part B Polym. Phys.* **2012**, *50* (6), 442–453. https://doi.org/10.1002/polb.23022.

(15) Kline, R. J.; McGehee, M. D.; Kadnikova, E. N.; Liu, J.; Fréchet, J. M. J.; Toney, M. F. Dependence of Regioregular Poly(3-Hexylthiophene) Film Morphology and Field-Effect Mobility on Molecular Weight. *Macromolecules* **2005**, *38* (8), 3312–3319. https://doi.org/10.1021/ma047415f.

(16) Koch, F. P. V.; Rivnay, J.; Foster, S.; Müller, C.; Downing, J. M.; Buchaca-Domingo, E.; Westacott, P.; Yu, L.; Yuan, M.; Baklar, M.; Fei, Z.; Luscombe, C.; McLachlan, M. A.; Heeney, M.; Rumbles, G.; Silva, C.; Salleo, A.; Nelson, J.; Smith, P.; Stingelin, N. The Impact of Molecular Weight on Microstructure and Charge Transport in Semicrystalline Polymer Semiconductors-Poly(3-Hexylthiophene), a Model Study. *Prog. Polym. Sci.* **2013**, *38* (12), 1978–1989. https://doi.org/10.1016/j.progpolymsci.2013.07.009.

(17) Snyder, C. R.; Henry, J. S.; Delongchamp, D. M. Effect of Regioregularity on the Semicrystalline Structure of Poly(3-Hexylthiophene). *Macromolecules* **2011**, *44* (18), 7088–7091. https://doi.org/10.1021/ma201604n.

(18) Kim, Y.; Cook, S.; Kirkpatrick, J.; Nelson, J.; Durrant, J. R.; Bradley, D. D. C.; Giles, M.; Heeney, M.; Hamilton, R.; McCulloch, I. Effect of the End Group of Regioregular Poly(3-Hexylthiophene) Polymers on the Performance of Polymer/Fullerene Solar Cells. *J. Phys. Chem. C* **2007**, *111* (23), 8137–8141. https://doi.org/10.1021/jp072306z.

(19) Choi, D.; Chang, M.; Reichmanis, E. Controlled Assembly of Poly(3-Hexylthiophene):

Managing the Disorder to Order Transition on the Nano- through Meso-Scales. *Adv. Funct. Mater.* **2015**, *25* (6), 920–927. https://doi.org/10.1002/adfm.201403708.

(20) Diao, Y.; Shaw, L.; Bao, Z.; Mannsfeld, S. C. B. Morphology Control Strategies for Solution-Processed Organic Semiconductor Thin Films. *Energy Environ. Sci.* **2014**, *7* (7), 2145–2159. https://doi.org/10.1039/c4ee00688g.

(21) Sirringhaus, H.; Brown, P. J.; Friend, R. H.; Nielsen, M. M.; Bechgaard, K.; Langeveld-Voss, B. M. W.; Spiering, A. J. H.; Janssen, R. A. J.; Meijer, E. W.; Herwig, P.; De Leeuw, D. M. Two-Dimensional Charge Transport in Self-Organized, High-Mobility Conjugated Polymers. *Nature* **1999**, *401* (6754), 685–688. https://doi.org/10.1038/44359.

(22) Crossland, E. J. W.; Rahimi, K.; Reiter, G.; Steiner, U.; Ludwigs, S. Systematic Control of Nucleation Density in Poly(3-Hexylthiophene) Thin Films. *Adv. Funct. Mater.* **2011**, *21* (3), 518–524. https://doi.org/10.1002/adfm.201001682.

(23) Jiang, H.; Taranekar, P.; Reynolds, J. R.; Schanze, K. S. Conjugated Polyelectrolytes: Synthesis, Photophysics, and Applications. *Angew. Chemie - Int. Ed.* **2009**, *48* (24), 4300–4316. https://doi.org/10.1002/anie.200805456.

(24) Cui, Q.; Bazan, G. C. Narrow Band Gap Conjugated Polyelectrolytes. *Acc. Chem. Res.* **2018**, *51* (1), 202–211. https://doi.org/10.1021/acs.accounts.7b00501.

(25) Jiang, H.; Taranekar, P.; Reynolds, J. R.; Schanze, K. S. Conjugated Polyelectrolytes: Synthesis, Photophysics, and Applications. *Angew. Chemie - Int. Ed.* **2009**, *48* (24), 4300–4316. https://doi.org/10.1002/anie.200805456.

(26) Danielsen, S. P. O.; Sanoja, G. E.; McCuskey, S. R.; Hammouda, B.; Bazan, G. C.; Fredrickson, G. H.; Segalman, R. A. Mixed Conductive Soft Solids by Electrostatically Driven Network Formation of a Conjugated Polyelectrolyte. *Chem. Mater.* **2018**, *30* (4), 1417–1426. https://doi.org/10.1021/acs.chemmater.7b05303.

(27) Yang, R.; Garcia, A.; Korystov, D.; Mikhailovsky, A.; Bazan, G. C.; Nguyen, T. Q. Control of Interchain Contacts, Solid-State Fluorescence Quantum Yield, and Charge Transport of Cationic Conjugated Polyelectrolytes by Choice of Anion. *J. Am. Chem. Soc.* **2006**, *128* (51), 16532–16539. https://doi.org/10.1021/ja0611341.

(28) Wang, D.; Moses, D.; Bazan, G. C.; Heeger, A. J.; Lal, J. Conformation of a Conjugated Polyelectrolyte in Aqueous Solution: Small Angle Neutron Scattering. *J. Macromol. Sci. - Pure Appl. Chem.* **2001**, *38 A* (12), 1175–1189. https://doi.org/10.1081/MA-100108376.

(29) Ang, M. C. Y.; Koh, Q. M.; Tang, C. G.; Seah, Q. J.; Wang, Y.; Callsen, M.; Feng, Y. P.; Png, R. Q.; Chua, L. L. Spectator Cation Size Effect on the Work Function and Stability of Self-Compensated Hole-Doped Polymers. *J. Mater. Chem. C* **2019**, *8* (1), 124–131. https://doi.org/10.1039/c9tc03884a.

(30) Huber, R. C.; Ferreira, A. S.; Thompson, R.; Kilbride, D.; Knutson, N. S.; Devi, L. S.; Toso, D. B.; Challa, J. R.; Zhou, Z. H.; Rubin, Y.; Schwartz, B. J.; Tolbert, S. H. Long-Lived Photoinduced Polaron Formation in Conjugated Polyelectrolyte-Fullerene Assemblies. *Science (80-.).* **2015**, *348* (6241), 1340–1343. https://doi.org/10.1126/science.aaa6850.

(31) Khau, B. V.; Savagian, L. R.; De Keersmaecker, M.; Gonzalez, M. A.; Reichmanis, E. Carboxylic Acid Functionalization Yields Solvent-Resistant Organic Electrochemical Transistors. *ACS Mater. Lett.* **2019**, *1* (6), 599–605. https://doi.org/10.1021/acsmaterialslett.9b00373.

(32) Ponder, J. F.; Österholm, A. M.; Reynolds, J. R. Conjugated Polyelectrolytes as Water Processable Precursors to Aqueous Compatible Redox Active Polymers for Diverse Applications: Electrochromism, Charge Storage, and Biocompatible Organic Electronics. *Chem. Mater.* **2017**, *29* (10), 4385–4392. https://doi.org/10.1021/acs.chemmater.7b00808.
(33) Danielsen, S. P. O.; Thompson, B. J.; Fredrickson, G. H.; Nguyen, T. Q.; Bazan, G. C.; Segalman, R. A. Ionic Tunability of Conjugated Polyelectrolyte Solutions. *Macromolecules* **2022**. https://doi.org/10.1021/acs.macromol.2c00178.
(34) Houston, J. E.; Chevrier, M.; Appavou, M. S.; King, S. M.; Clément, S.; Evans, R. C. A Self-Assembly Toolbox for Thiophene-Based Conjugated Polyelectrolytes: Surfactants, Solvent and Copolymerisation. *Nanoscale* **2017**, *9* (44), 17481–17493. https://doi.org/10.1039/c7nr06169b.
(35) Peterhans, L.; Alloa, E.; Sheima, Y.; Vannay, L.; Leclerc, M.; Corminboeuf, C.; Hayes, S. C.; Banerji, N. Salt-Induced Thermochromism of a Conjugated Polyelectrolyte. *Phys. Chem. Chem. Phys.* **2017**, *19* (42), 28853–28866. https://doi.org/10.1039/c7cp02734f.
(36) Jiang, H.; Zhao, X.; Schanze, K. S. Effects of Polymer Aggregation and Quencher Size on Amplified Fluorescence Quenching of Conjugated Polyelectrolytes. *Langmuir* **2007**, *23* (18), 9481–9486. https://doi.org/10.1021/la701192t.
(37) Mai, C. K.; Schlitz, R. A.; Su, G. M.; Spitzer, D.; Wang, X.; Fronk, S. L.; Cahill, D. G.; Chabinyc, M. L.; Bazan, G. C. Side-Chain Effects on the Conductivity, Morphology, and Thermoelectric Properties of Self-Doped Narrow-Band-Gap Conjugated Polyelectrolytes. *J. Am. Chem. Soc.* **2014**, *136* (39), 13478–13481. https://doi.org/10.1021/ja504284r.
(38) Mai, C. K.; Arai, T.; Liu, X.; Fronk, S. L.; Su, G. M.; Segalman, R. A.; Chabinyc, M. L.; Bazan, G. C. Electrical Properties of Doped Conjugated Polyelectrolytes with Modulated Density of the Ionic Functionalities. *Chem. Commun.* **2015**, *51* (99), 17607–17610. https://doi.org/10.1039/c5cc06690e.
(39) Schmode, P.; Ohayon, D.; Reichstein, P. M.; Savva, A.; Inal, S.; Thelakkat, M. High-Performance Organic Electrochemical Transistors Based on Conjugated Polyelectrolyte Copolymers. *Chem. Mater.* **2019**, *31* (14), 5286–5295. https://doi.org/10.1021/acs.chemmater.9b01722.
(40) OVERBEEK, J. T.; VOORN, M. J. Phase Separation in Polyelectrolyte Solutions; Theory of Complex Coacervation. *J. Cell. Physiol. Suppl.* **1957**, *49* (Suppl 1), 7–26. https://doi.org/10.1002/jcp.1030490404.
(41) Veis, A.; Aranyi, C. Phase Separation in Polyelectrolyte Systems. I. Complex Coacervates of Gelatin. *J. Phys. Chem.* **1960**, *64* (9), 1203–1210. https://doi.org/10.1021/j100838a022.
(42) Danielsen, S. P. O.; Nguyen, T. Q.; Fredrickson, G. H.; Segalman, R. A. Complexation of a Conjugated Polyelectrolyte and Impact on Optoelectronic Properties. *ACS Macro Lett.* **2019**, *8* (1), 88–94. https://doi.org/10.1021/acsmacrolett.8b00924.
(43) Le, M. L.; Rawlings, D.; Danielsen, S. P. O.; Kennard, R. M.; Chabinyc, M. L.; Segalman, R. A. Aqueous Formulation of Concentrated Semiconductive Fluid Using Polyelectrolyte Coacervation. *ACS Macro Lett.* **2021**, *10* (8), 1008–1014. https://doi.org/10.1021/acsmacrolett.1c00354.
(44) Hollingsworth, W. R.; Segura, C.; Balderrama, J.; Lopez, N.; Schleissner, P.; Ayzner,

A. L. Exciton Transfer and Emergent Excitonic States in Oppositely-Charged Conjugated Polyelectrolyte Complexes. *J. Phys. Chem. B* **2016**, *120* (31), 7767–7774. https://doi.org/10.1021/acs.jpcb.6b06533.

(45) Johnston, A. R.; Perry, S. L.; Ayzner, A. L. Associative Phase Separation of Aqueous π-Conjugated Polyelectrolytes Couples Photophysical and Mechanical Properties. *Chem. Mater.* **2021**, *33* (4), 1116–1129. https://doi.org/10.1021/acs.chemmater.0c02424.

(46) Hollingsworth, W. R.; Williams, V.; Ayzner, A. L. Semiconducting Eggs and Ladders: Understanding Exciton Landscape Formation in Aqueous π-Conjugated Inter-Polyelectrolyte Complexes. *Macromolecules* **2020**, *53* (7), 2724–2734. https://doi.org/10.1021/acs.macromol.0c00029.

(47) Hollingsworth, W. R.; Segura, C.; Balderrama, J.; Lopez, N.; Schleissner, P.; Ayzner, A. L. Exciton Transfer and Emergent Excitonic States in Oppositely-Charged Conjugated Polyelectrolyte Complexes. *J. Phys. Chem. B* **2016**, *120* (31), 7767–7774. https://doi.org/10.1021/acs.jpcb.6b06533.

(48) Russ, B.; Glaudell, A.; Urban, J. J.; Chabinyc, M. L.; Segalman, R. A. Organic Thermoelectric Materials for Energy Harvesting and Temperature Control. *Nature Reviews Materials*. Nature Publishing Group August 2, 2016. https://doi.org/10.1038/natrevmats.2016.50.

(49) Fredrickson, G. H.; Xie, S.; Edmund, J.; Le, M. L.; Sun, D.; Grzetic, D. J.; Vigil, D. L.; Delaney, K. T.; Chabinyc, M. L.; Segalman, R. A. Ionic Compatibilization of Polymers. *ACS Polym. Au* **2022**, *2* (5), 299–312. https://doi.org/10.1021/acspolymersau.2c00026.

(50) Kazemiabnavi, S.; Zhang, Z.; Thornton, K.; Banerjee, S. Electrochemical Stability Window of Imidazolium-Based Ionic Liquids as Electrolytes for Lithium Batteries. *J. Phys. Chem. B* **2016**, *120* (25), 5691–5702. https://doi.org/10.1021/acs.jpcb.6b03433.

(51) Le, M. L.; Grzetic, D. J.; Delaney, K. T.; Yang, K. C.; Xie, S.; Fredrickson, G. H.; Chabinyc, M. L.; Segalman, R. A. Electrostatic Interactions Control the Nanostructure of Conjugated Polyelectrolyte-Polymeric Ionic Liquid Blends. *Macromolecules* **2022**, *55* (18), 8321–8331. https://doi.org/10.1021/acs.macromol.2c01142.

(52) Velasco Davoise, L.; Peña Capilla, R.; Díez-Pascual, A. M. Assessment of the Refractive Index and Extinction Coefficient of Graphene-Poly(3-Hexylthiophene) Nanocomposites. *Polymers (Basel).* **2022**, *14* (9). https://doi.org/10.3390/polym14091828.

(53) Ehrenreich, P.; Birkhold, S. T.; Zimmermann, E.; Hu, H.; Kim, K. D.; Weickert, J.; Pfadler, T.; Schmidt-Mende, L. H-Aggregate Analysis of P3HT Thin Films-Capability and Limitation of Photoluminescence and UV/Vis Spectroscopy. *Sci. Rep.* **2016**, *6* (1), 1–8. https://doi.org/10.1038/srep32434.

(54) Spano, F. C.; Clark, J.; Silva, C.; Friend, R. H. Determining Exciton Coherence from the Photoluminescence Spectral Line Shape in Poly(3-Hexylthiophene) Thin Films. *J. Chem. Phys.* **2009**, *130* (7). https://doi.org/10.1063/1.3076079.

(55) Clark, J.; Chang, J. F.; Spano, F. C.; Friend, R. H.; Silva, C. Determining Exciton Bandwidth and Film Microstructure in Polythiophene Films Using Linear Absorption Spectroscopy. *Appl. Phys. Lett.* **2009**, *94* (16), 163306. https://doi.org/10.1063/1.3110904.

(56) Dou, F.; Li, J.; Men, H.; Zhang, X. Controlling Molecule Aggregation and Electronic Spatial Coherence in the H-Aggregate and J-Aggregate Regime at Room Temperature.

Polymers (Basel). **2020**, *12* (4), 786. https://doi.org/10.3390/POLYM12040786.
(57) Brown, P. J.; Thomas, D. S.; Köhler, A.; Wilson, J. S.; Kim, J. S.; Ramsdale, C. M.; Sirringhaus, H.; Friend, R. H. Effect of Interchain Interactions on the Absorption and Emission of Poly(3-Hexylthiophene). *Phys. Rev. B - Condens. Matter Mater. Phys.* **2003**, *67* (6). https://doi.org/10.1103/PhysRevB.67.064203.
(58) Tremel, K.; Ludwigs, S. Morphology of P3HT in Thin Films in Relation to Optical and Electrical Properties. *Adv. Polym. Sci.* **2014**, *265*, 39–82. https://doi.org/10.1007/12_2014_288.
(59) Spano, F. C.; Silva, C. H- and J-Aggregate Behavior in Polymeric Semiconductors. *Annu. Rev. Phys. Chem.* **2014**, *65*, 477–500. https://doi.org/10.1146/annurev-physchem-040513-103639.
(60) Schmidt, M. M.; ElMahmoudy, M.; Malliaras, G. G.; Inal, S.; Thelakkat, M. Smaller Counter Cation for Higher Transconductance in Anionic Conjugated Polyelectrolytes. *Macromol. Chem. Phys.* **2018**, *219* (2). https://doi.org/10.1002/macp.201700374.
(61) Panzer, F.; Bässler, H.; Köhler, A. Temperature Induced Order-Disorder Transition in Solutions of Conjugated Polymers Probed by Optical Spectroscopy. *J. Phys. Chem. Lett.* **2017**, *8* (1), 114–125. https://doi.org/10.1021/acs.jpclett.6b01641.
(62) Köhler, A.; Bässler, H. *Electronic Processes in Organic Semiconductors: An Introduction*; Wiley-VCH Verlag: Weinheim, 2015. https://doi.org/10.1002/9783527685172.
(63) Baghgar, M.; Labastide, J. A.; Bokel, F.; Hayward, R. C.; Barnes, M. D. Effect of Polymer Chain Folding on the Transition from H- to J-Aggregate Behavior in P3HT Nanofibers. *J. Phys. Chem. C* **2014**, *118* (4), 2229–2235. https://doi.org/10.1021/jp411668g.
(64) Spano, F. C. Modeling Disorder in Polymer Aggregates: The Optical Spectroscopy of Regioregular Poly(3-Hexylthiophene) Thin Films. *J. Chem. Phys.* **2005**, *122* (23), 234701. https://doi.org/10.1063/1.1914768.
(65) Wang, S.; Fabiano, S.; Himmelberger, S.; Puzinas, S.; Crispin, X.; Salleo, A.; Berggren, M. Experimental Evidence That Short-Range Intermolecular Aggregation Is Sufficient for Efficient Charge Transport in Conjugated Polymers. *Proc. Natl. Acad. Sci. U. S. A.* **2015**, *112* (34), 10599–10604. https://doi.org/10.1073/pnas.1501381112.
(66) Duong, D. T.; Toney, M. F.; Salleo, A. Role of Confinement and Aggregation in Charge Transport in Semicrystalline Polythiophene Thin Films. *Phys. Rev. B - Condens. Matter Mater. Phys.* **2012**, *86* (20), 205205. https://doi.org/10.1103/PhysRevB.86.205205.
(67) Nguyen, T. Q.; Schwartz, B. J. Ionomeric Control of Interchain Interactions, Morphology, and the Electronic Properties of Conjugated Polymer Solutions and Films. *J. Chem. Phys.* **2002**, *116* (18), 8198–8208. https://doi.org/10.1063/1.1468215.
(68) Paquin, F.; Yamagata, H.; Hestand, N. J.; Sakowicz, M.; Bérubé, N.; Côté, M.; Reynolds, L. X.; Haque, S. A.; Stingelin, N.; Spano, F. C.; Silva, C. Two-Dimensional Spatial Coherence of Excitons in Semicrystalline Polymeric Semiconductors: Effect of Molecular Weight. *Phys. Rev. B - Condens. Matter Mater. Phys.* **2013**, *88* (15), 155202. https://doi.org/10.1103/PhysRevB.88.155202.
(69) Dimitriev, O. P. Effect of Confinement on Photophysical Properties of P3HT Chains in PMMA Matrix. *Nanoscale Res. Lett.* **2017**, *12*. https://doi.org/10.1186/s11671-017-2270-y.
(70) Hellmann, C.; Paquin, F.; Treat, N. D.; Bruno, A.; Reynolds, L. X.; Haque, S. A.;

Stavrinou, P. N.; Silva, C.; Stingelin, N. Controlling the Interaction of Light with Polymer Semiconductors. *Adv. Mater.* **2013**, *25* (35), 4906–4911. https://doi.org/10.1002/adma.201300881.

(71) Patil, A. O.; Ikenoue, Y.; Basescu, N.; Colaneri, N.; Chen, J.; Wudl, F.; Heeger, A. J. Self-Doped Conducting Polymers. *Synth. Met.* **1987**, *20* (2), 151–159. https://doi.org/10.1016/0379-6779(87)90554-6.

(72) Ikenoue, Y.; Chiang, J.; Patil, A. O.; Wudl, F.; Heeger, A. J. Verification of the "Cation-Popping" Doping Mechanism of Self-Doped Polymers. *J. Am. Chem. Soc.* **1988**, *110* (9), 2983–2985. https://doi.org/10.1021/ja00217a055.

(73) Zhang, N.; Wu, R.; Li, Q.; Pakbaz, K.; Yoon, C. O.; Wudl, F. Synthesis and Properties of an N-Self-Doped Conducting Polymer. *Chem. Mater.* **1993**, *5* (11), 1598–1599. https://doi.org/10.1021/cm00035a003.

(74) Wudl, F.; Patil, A. O.; Ikenoue, Y. Recent Advances in Self Doped Conducting Polymers and Arylenevinylenes. *Funct. Polym.* **1989**, 99–105. https://doi.org/10.1007/978-1-4613-0815-7_8.

(75) Rawlings, D.; Lee, D.; Kim, J.; Magdău, I. B.; Pace, G.; Richardson, P. M.; Thomas, E. M.; Danielsen, S. P. O.; Tolbert, S. H.; Miller, T. F.; Seshadri, R.; Segalman, R. A. Li+and Oxidant Addition to Control Ionic and Electronic Conduction in Ionic Liquid-Functionalized Conjugated Polymers. *Chem. Mater.* **2021**, *33* (16), 6464–6474. https://doi.org/10.1021/acs.chemmater.1c01811.

(76) Thalluri, G. K. V. V.; Bolsée, J. C.; Gadisa, A.; Parchine, M.; Boonen, T.; Dhaen, J.; Boyukbayram, A. E.; Vandenbergh, J.; Cleij, T. J.; Lutsen, L.; Vanderzande, D.; Manca, J. Opto-Electrical and Morphological Characterization of Water Soluble Conjugated Polymers for Eco-Friendly Hybrid Solar Cells. *Sol. Energy Mater. Sol. Cells* **2011**, *95* (12), 3262–3268. https://doi.org/10.1016/j.solmat.2011.07.010.

(77) Goh, C.; Kline, R. J.; McGehee, M. D.; Kadnikova, E. N.; Fŕchet, J. M. J. Molecular-Weight-Dependent Mobilities in Regioregular Poly(3-Hexyl- Thiophene) Diodes. *Appl. Phys. Lett.* **2005**, *86* (12), 1–3. https://doi.org/10.1063/1.1891301.

(78) Lim, E.; Glaudell, A. M.; Miller, R.; Chabinyc, M. L. The Role of Ordering on the Thermoelectric Properties of Blends of Regioregular and Regiorandom Poly(3-Hexylthiophene). *Adv. Electron. Mater.* **2019**, *5* (11), 1800915. https://doi.org/10.1002/aelm.201800915.

(79) Schmode, P.; Ohayon, D.; Reichstein, P. M.; Savva, A.; Inal, S.; Thelakkat, M. High-Performance Organic Electrochemical Transistors Based on Conjugated Polyelectrolyte Copolymers. *Chem. Mater.* **2019**, *31* (14), 5286–5295. https://doi.org/10.1021/acs.chemmater.9b01722.

(80) Shi, H.; Liu, C.; Jiang, Q.; Xu, J. Effective Approaches to Improve the Electrical Conductivity of PEDOT:PSS: A Review. *Adv. Electron. Mater.* **2015**, *1* (4), 1500017. https://doi.org/10.1002/aelm.201500017.

(81) Yoo, J. E.; Bucholz, T. L.; Jung, S.; Loo, Y. L. Narrowing the Size Distribution of the Polymer Acid Improves PANI Conductivity. *J. Mater. Chem.* **2008**, *18* (26), 3129–3135. https://doi.org/10.1039/b802829j.

(82) Yoo, J. E.; Lee, K. S.; Garcia, A.; Tarver, J.; Gomez, E. D.; Baldwin, K.; Sun, Y.; Meng, H.; Nguyen, T. Q.; Loo, Y. L. Directly Patternable, Highly Conducting Polymers for Broad Applications in Organic Electronics. *Proc. Natl. Acad. Sci. U. S. A.* **2010**, *107* (13), 5712–5717. https://doi.org/10.1073/pnas.0913879107.

(83) Glaudell, A. M.; Cochran, J. E.; Patel, S. N.; Chabinyc, M. L. Impact of the Doping Method on Conductivity and Thermopower in Semiconducting Polythiophenes. *Adv. Energy Mater.* **2015**, *5* (4). https://doi.org/10.1002/aenm.201401072.

(84) Patel, S. N.; Glaudell, A. M.; Peterson, K. A.; Thomas, E. M.; O'Hara, K. A.; Lim, E.; Chabinyc, M. L. Morphology Controls the Thermoelectric Power Factor of a Doped Semiconducting Polymer. *Sci. Adv.* **2017**, *3* (6). https://doi.org/10.1126/sciadv.1700434.

(85) Lo, C. Y.; Wu, Y.; Awuyah, E.; Meli, D.; Nguyen, D. M.; Wu, R.; Xu, B.; Strzalka, J.; Rivnay, J.; Martin, D. C.; Kayser, L. V. Influence of the Molecular Weight and Size Distribution of PSS on Mixed Ionic-Electronic Transport in PEDOT:PSS. *Polym. Chem.* **2022**, *13* (19), 2764–2775. https://doi.org/10.1039/d2py00271j.

(86) Mollinger, S. A.; Krajina, B. A.; Noriega, R.; Salleo, A.; Spakowitz, A. J. Percolation, Tie-Molecules, and the Microstructural Determinants of Charge Transport in Semicrystalline Conjugated Polymers. *ACS Macro Lett.* **2015**, *4* (7), 708–712. https://doi.org/10.1021/acsmacrolett.5b00314.

(87) Gu, K.; Onorato, J. W.; Luscombe, C. K.; Loo, Y. L. The Role of Tie Chains on the Mechano-Electrical Properties of Semiconducting Polymer Films. *Adv. Electron. Mater.* **2020**, *6* (4), 1–8. https://doi.org/10.1002/aelm.201901070.

(88) Gu, K.; Snyder, C. R.; Onorato, J.; Luscombe, C. K.; Bosse, A. W.; Loo, Y. L. Assessing the Huang-Brown Description of Tie Chains for Charge Transport in Conjugated Polymers. *ACS Macro Lett.* **2018**, *7* (11), 1333–1338. https://doi.org/10.1021/acsmacrolett.8b00626.

(89) Himmelberger, S.; Vandewal, K.; Fei, Z.; Heeney, M.; Salleo, A. Role of Molecular Weight Distribution on Charge Transport in Semiconducting Polymers. *Macromolecules* **2014**, *47* (20), 7151–7157. https://doi.org/10.1021/ma501508j.

(90) Bridges, C. R.; Ford, M. J.; Thomas, E. M.; Gomez, C.; Bazan, G. C.; Segalman, R. A. Effects of Side Chain Branch Point on Self Assembly, Structure, and Electronic Properties of High Mobility Semiconducting Polymers. *Macromolecules* **2018**, *51* (21), 8597–8604. https://doi.org/10.1021/acs.macromol.8b01906.

(91) Reichenberger, M.; Kroh, D.; Matrone, G. M. M.; Schötz, K.; Pröller, S.; Filonik, O.; Thordardottir, M. E.; Herzig, E. M.; Bässler, H.; Stingelin, N.; Köhler, A. Controlling Aggregate Formation in Conjugated Polymers by Spin-Coating below the Critical Temperature of the Disorder–Order Transition. *J. Polym. Sci. Part B Polym. Phys.* **2018**, *56* (6), 532–542. https://doi.org/10.1002/polb.24562.

(92) Hynynen, J.; Kiefer, D.; Müller, C. Influence of Crystallinity on the Thermoelectric Power Factor of P3HT Vapour-Doped with F4TCNQ. *RSC Adv.* **2018**, *8* (3), 1593–1599. https://doi.org/10.1039/c7ra11912g.

(93) Hellmann, C.; Treat, N. D.; Scaccabarozzi, A. D.; Hollis, J. R.; Fleischli, F. D.; Bannock, J. H.; De Mello, J.; Michels, J. J.; Kim, J. S.; Stingelin, N. Solution Processing of Polymer Semiconductor:Insulator Blends - Tailored Optical Properties through Liquid-Liquid Phase Separation Control. *J. Polym. Sci. Part B Polym. Phys.* **2015**, *53* (4), 304–310. https://doi.org/10.1002/polb.23656.

(94) Evans, R. C.; Knaapila, M.; Willis-Fox, N.; Kraft, M.; Terry, A.; Burrows, H. D.; Scherf, U. Cationic Polythiophene-Surfactant Self-Assembly Complexes: Phase Transitions, Optical Response, and Sensing. *Langmuir* **2012**, *28* (33), 12348–12356. https://doi.org/10.1021/la302166a.

(95) Danielsen, S. P. O.; Davidson, E. C.; Fredrickson, G. H.; Segalman, R. A. Absence of Electrostatic Rigidity in Conjugated Polyelectrolytes with Pendant Charges. *ACS Macro Lett.* **2019**, *8* (9), 1147–1152. https://doi.org/10.1021/acsmacrolett.9b00551.
(96) Evans, C. M.; Sanoja, G. E.; Popere, B. C.; Segalman, R. A. Anhydrous Proton Transport in Polymerized Ionic Liquid Block Copolymers: Roles of Block Length, Ionic Content, and Confinement. *Macromolecules* **2016**, *49* (1), 395–404. https://doi.org/10.1021/acs.macromol.5b02202.
(97) Thomas, E. M.; Popere, B. C.; Fang, H.; Chabinyc, M. L.; Segalman, R. A. Role of Disorder Induced by Doping on the Thermoelectric Properties of Semiconducting Polymers. *Chem. Mater.* **2018**, *30* (9), 2965–2972. https://doi.org/10.1021/acs.chemmater.8b00394.
(98) Mooney, J.; Kambhampati, P. Get the Basics Right: Jacobian Conversion of Wavelength and Energy Scales for Quantitative Analysis of Emission Spectra. *J. Phys. Chem. Lett.* **2013**, *4* (19), 3316–3318. https://doi.org/10.1021/jz401508t.

Chapter 5

Engineering soft, elastic, and conductive polymers for stretchable electronics using ionic compatibilization

This chapter is reproduced in part from:

Le, M. L.,* Lapkriengkri, I.,* Albanese, K. R., Nguyen, H. P., Tran, C., Blankenship, J. R., Segalman, R. A., Bates, C. M., and Chabinyc, M. L. Engineering Soft, Elastic, and Conductive Polymers for Stretchable Electronics Using Ionic Compatibilization. *[working title]*, *manuscript in preparation.*

* M. L. L. and I. L. contributed equally to this work.

Bottlebrush polymer synthesis and mechanical characterizations were done by Intanon Lapkriengkri

5.1 Abstract

Designing a material that is soft, elastic, and conductive for bio-interfacing technologies has remained a major challenge due to the high stiffness of conventional conductive materials. The homogeneous mixing of a polymeric elastomer with a conductive material to gain the requisite composite properties has presented a formidable challenge due to the general immiscibility of these two classes of polymers. Herein, we demonstrate that electrostatic interactions provide an effective pathway to compatibilize distinct polymer chemistries and backbone architectures to achieve homogeneous and multifunctional (soft, elastic, and conductive) polymer complexes. In particular, an anionic conjugated polyelectrolyte (CPE) was blended with a cationic bottlebrush polyelectrolyte (BPE). In this design, the CPE provides electrical conductivity, while the BPE offers a super-soft matrix for mechanical flexibility. The strong electrostatic attraction between the oppositely charged pendant side

chains of the CPE and the BPE effectively suppresses phase separation, and the polymers formed a phase-compatible complex despite the stark differences in their chemistries and architecture. Upon drying of the solvent, the ionic complexes act as dynamic crosslinks, and the resulting material behaves like a viscoelastic solid. Moreover, the dynamic nature of the ionic crosslinks and the low glass-transition temperature of the BPE enable room-temperature reprocessing of the complex with simple pressing. Once doped with a strong acid, this polymer complex yields a conductivity up to 0.3 S/cm and maintains a low tensile modulus of 0.2 MPa. Moreover, this CPE – BPE complex shows superior recovery of its electronic conductivity after an applied strain is removed. Our findings emphasize the potential of electrostatic interactions in designing advanced polymer complexes by compatibilizing polymers with different functionalities, demonstrated here for soft and stretchable electronics, with potentially added processing and performance advantages.

5.2 Introduction

Soft robotics and wearable electronics create a need for materials with tailored electrical conductivity and mechanical properties that are challenging to obtain. For example, the significant difference in mechanical modulus between conventional conductive materials ($E \geq 10^8$ Pa) and biological tissues ($E \leq 10^6$ Pa) leads to interfacial mismatches in mechanical behavior.[1,2] Geometric engineering, *i.e.* utilizing special spatial structuring into meshes, kirigamis, or waves,[3–6] has been shown to be effective in imparting stretchability of intrinsically rigid conductive materials, but can be challenging to implement in some applications. The development of materials that are both soft and electrically conductive could help to address these issues.

Conjugated polymers offer the ability to form conductive materials with varying mechanical properties set by molecular design. The backbone of semiconducting polymers can be relatively stiff, but modification of the design of sidechains can modify their mechanical softness. For example, polythiophenes with tetra-ethylene glycol side chains have been shown to have a Young's modulus of only 8 MPa,[7] which is up to 2 orders of magnitude lower than polythiophenes with alkyl sidechains (60 – 900 MPa).[8–10] However, these softer conjugated polymers have been shown to experience significant increase in stiffness (up to 50 times) upon doping to achieve charge carrier concentrations necessary for electrical conduction. Another strategy is adding conjugation-break spacers (CBS) to the backbone of semiconducting polymers for improved softness.[11] However, this strategy possesses major softness-conductivity trade-offs, and the moduli of these polymers still fall within the range of 100 – 1000 MPa.[11–15]

Blends or composites are a common strategy to modify mechanical and electrical properties that are beyond what is achievable with a single material. The development of composites between soft (commonly made of polymeric elastomers such as PDMS based silicone/triblock thermoplastic elastomers [16–18] or hydrogels [19,20]) and conductive materials (such as carbon nanotubes (CNTs),[21–23] metal,[24–27] or conjugated polymers [28–30]) allow tunable electrical and mechanical properties. CNTs have been successfully embedded in elastomer matrixes via solution mixing, melt mixing, and in situ polymerization.[31] A wide range of properties, between 10^{-4} to 10^{0} S/cm for conductivity and 10^{5} to 10^{9} Pa for elastic modulus, have been reported for the resultant polymer nanocomposites, depending heavily on the modification of

the CNTS and the mixing procedure.[31–33] On the other hand, studies that blended conductive polymers with polymeric elastomers have reported conductivity values from 10^0 up to 10^4 S/cm, with moduli ranging from 10^5 to 10^9 Pa.[28–30] Softer composites ($E \leq 10^5$ Pa) have been reported for systems using super-soft bottlebrush elastomer [2,34] and hydrogels [19,20] as the soft matrix, with reported conductivities ranging between 10^{-3} to 10^1 S/cm.[2,34,35]

Despite these reports of promising performance, there are major obstacles in formulating soft and conductive composite systems. Firstly, a tradeoff between mechanical softness and conductivity originates from a requirement that the conductive material (with inherently high stiffness) percolates to provide a transport pathway. This ultimately increases the modulus of the composite and can potentially render it unsuitable for soft electronics. While systems such as hydrogels possess impressively low moduli and can mitigate the stiffening effect from hard fillers, they rely critically on an exact degree of swelling or hydration which is impossible to maintain in many device configurations. Secondly, blending and homogenizing a soft and a conductive materials is extremely difficult. In particular, conductive particles have tendency to agglomerate, making them difficult to disperse homogeneously. The reaggregation of these particles during use results in poor stability and deterioration in performance.[32] Further, these classes of materials are generally immiscible and tend to macrophase separate. This can obstruct the formation of a continuous transport pathway, cause undue brittleness, and present significant processing complications. Lastly, the requirement of chemical crosslinking to impart elasticity in many systems introduces additional challenges such as poor compatibility between the crosslinker and the system, sophisticated curing procedures, and compromise of the blend's stability.

Ionic compatibilization of polymers offers the opportunity to effectively combine distinct polymers into a single homogeneous system. In mixtures of oppositely charged ionic polymers, the strong electrostatic attractions between the two species can limit the domain size of microphase separation. The long range nature of electrostatic attractions can even overcome the enthalpic penalties that lead to macrophase separation entirely. [36–44] Indeed, calculations suggest that the inclusion of just 10 charges per polymer chain can increase the critical segregation strength $(\chi N)_c$ of a blend from 2 to 400 for a typical polymer melt dielectric environment.[45] We have previously investigated the processability, self-assembly, photophysical, and optoelectronic properties of complexes obtained from the blending of linear ionic conjugated polymer and linear polyelectrolytes.[46–48] However the role of molecular architecture of the polymers in these complexes and the ability to leverage ionic compatibilization in formulating multifunctional complexes have not been investigated.

Here, we find that ionic interactions can effectively stabilize a homogeneous blend of two polymers that are different in not only chemistry but also backbone architecture for achieving soft and conductive polymer complex. A complex of a linear conjugated polyelectrolyte (CPE) and a bottlebrush polyelectrolyte (BPE) was formed by coacervation of the 2 polymers. We show that the solid-state CPE – BPE blend forms an ionically crosslinked polymer network with appreciable elasticity without any addition of crosslinkers, and can be reprocessed by simple pressing at room temperature. Moreover, the blend possesses the properties of both components: soft and semiconductive. In particular, due to the brush architecture of the BPE, which suppresses chain entanglements,[49–51] the modulus of the blend

is 0.7 MPa, which is comparable with the modulus of biological soft tissues.[2] The CPE, despite being highly dispersed in the complex, forms a percolating conducting network. As a result, the complex conductivity can go up to 3×10^{-1} S/cm when the material is doped with a strong acid vapor. Doping also decreases the modulus of the complex to 0.2 MPa. The complex (both when pristine and after doping) can be stretched to appreciable strains (450% and 100%, respectively), with great elastic mechanical and electrical conductivity recovery behavior. Our findings emphasize the potential of electrostatic interactions in compatibilizing 2 distinct polymers for multifunctional blends – particularly here for soft electronic – with added processing and performance advantages.

5.3 Experimental Methods

Materials

N-(hydroxyethyl)-*cis*-5-norbornene-*exo*-2,3-dicarboximide was prepared according to the literature.[52] Grubbs' second-generation metathesis catalyst [(H_2IMes)(PCy_3)($Cl)_2$Ru=CHPh] was purchased from Sigma Aldrich. Grubbs' third-generation metathesis catalyst [(H_2IMes)(pyr)$_2$($Cl)_2$Ru=CHPh] (G3) was prepared according to the literature.[53] *N*-(hydroxyethyl)-cis-5-norbornene-exo-2,3-dicarboximide (Nb-OH) was synthesized according to literature.[52] Poly(4-methylcaprolactone) (pMCL) macromonomer and bottlebrushes were prepared using previously reported methods.[54] Tin(II) 2-ethylhexanoate ($Sn(Oct)_2$, Sigma Aldrich, 92.5–100%) was purified according to literature.[55] 2,5-dibromo-3-(6-bromohexyl)thiophene (eNovation Chemicals LLC), 1*H*-Imidazol-1-ylacetic acid (Sigma Aldrich). *N*-(3-Dimethylaminopropyl)-*N*′-ethylcarbodiimide hydrochloride (EDC·HCl, Sigma Aldrich, commercial grade), 4-(Dimethylamino)pyridine (DMAP, Sigma Aldrich),

ethanol amine (Sigma Aldrich, purity ≥ 99%), Chloroform (Sigma Aldrich, anhydrous, contains amylenes as a stabilizer, purity ≥ 99%), acetone (Fisher Scientific, purity ≥ 99.5%), methanol (Fisher Scientific, purity = 99.5%), dichloromethane (Fisher Scientific, purity ≥ 99.5%), ethyl vinyl ether (ACROS Organic, Contains 0.1% KOH as stabilizer, purity = 99%), dimethylformamide (dry over molecular sieve), $CDCl_3$ (Cambridge Isotope Laboratories, purity = 99.8%), and acetone-d_6 (Cambridge Isotope Laboratories, purity = 99.9%) were used as received.

Complex formation

120 mM stock solutions of the BPE and the CPE were prepared by dissolving the polymers in adequate amount of solvent mixtures of 80%THF:20% water and 60%THF:40% water, respectively. BPE and CPE solutions were mixed in stoichiometric ratio in an Eppendorf tube, and the mixture was vortexed for 1 minute to ensure even mixing. The coacervate droplets that formed during the complexation process were collected by centrifugation of the tube at 7000 rpm for 10 min followed by decanting the supernatant.

Film fabrication

The complex film was obtained by drop casting the CPE – BPE coacervate onto a silicon substrate with custom made gold digits, and the substrate was heated at 50°C for 10 minutes to remove most solvent. The substrate with the roughly dried complex was then pressed between 2 metal plates separated by Teflon spacers, resulting in a $\approx 20 - 30\ \mu$m thick film. The film was then fully dried under high vacuum ($\approx 2 \times 10^{-8}$ Torr) at 50°C overnight. CPE films were obtain by spin casting the 120 mM stock solution at 500 rpm for 2 min 30 sec.

Vapor Doping

Doping was done inside a nitrogen glovebox. The complex film on substrate was attached to a lid of a glass jar with HTFSI crystals. The jar was closed tightly and heated at 50˚C on a hot plate for 13 minutes (CPE) or 1 hour (CPC). For the complex film, the film was transferred to another closed clean glass jar and kept at 55^{o}C for an additional 48 hours to promote efficient diffusion of dopants into the film and to prevent leakage of dopant vapor. After this, the film was put under vacuum for 2 days to fully remove all the excess HTFSI molecules. For bulk sample, vapor doping was carried out for 48 hours, as we observed that after this no further mass gain was observed. The sample was then put under vacuum for an additional 72 hours to obtain the doped bulk sample.

Nuclear magnetic resonance (NMR)

All bottlebrush polymer ^{1}H NMR spectra were collected using a Varian Unity Inova AS600 600 MHz equipped with a 5 mm Varian triple resonance ^{1}H/^{13}C/^{15}N inverse detection probe with *z*-axis pulsed field gradient (PFG). Other materials' ^{1}H and ^{13}C NMR spectra were collected using either a Bruker Avance NEO 500 MHz equipped with a CryoProbe Prodigy BBO probe with *z*-axis PFG, or a Varian VNMRS 600 MHz.

Size-exclusion chromatography (SEC)

SEC was performed on a Waters Alliance HPLC System equipped with 2690 Separation Module, or a Waters Alliance HPLC system with an Agilent PLgel 5 μm MiniMIX-D column. The former uses chloroform with 0.25% triethylamine, while the latter uses THF as the eluent.

For the former, refractive index from a Waters 2410 Differential Refractometer detector were used to estimate the molar mass and dispersity relative to linear polystyrene standards. For the latter, refractive index traces from a Waters 2414 detector were used for molecular weight determination using polystyrene calibration standards (Agilent Technologies).

Tensile tests

Uniaxial tensile testing was performed with a TA.XTplusC texture analyzer equipped with A/MTG tensile grips. Samples were clamped without additional adhesive. The pristine complex was prepared by simple pressing into a metal rectangular mold (8 mm wide × 15 mm long × 0.5 mm thick) sandwich between 2 PTFE sheet at room temperature using 1 metric ton of force. The samples were punch into a dog-bone shape (10 mm long × 1.5 mm wide × 0.5 mm thick) using a brass punch. The doped complex was prepared by firstly simple pressing of CPE−BPE into a rectangular shape previously described, then the rectangular-shaped sample was doped with HTFSI as described in the vapor doping section. All measurements were done at a constant strain rate of 1 min^{-1}.

Dynamic mechanical analysis

Cyclic stress-controlled recovery measurements were performed on a Discovery DMA 850 at room temperature. A film clamp was used, and the sample was clamped without additional adhesive. Strain-sweep experiments were performed prior to the recovery experiment to determine the linear-viscoelastic region (LVE) of the materials. In each measurement, the sample were strain with a constant stress (dwell time = 1 min) before letting to relax. The samples were prepared similarly to the uniaxial tensile measurements.

Rheology

A strain-controlled ARES-G2 rheometer equipped with a liquid nitrogen dewar from TA Instruments was used to investigate the shear stress relaxation, and linear viscoelastic properties of the blend. A pair of 8-mm stainless steel parallel plates were used for all measurements. Strain-sweep experiments were performed prior to measurement to determine the linear-viscoelastic region (LVE) of the materials. Stress relaxation data were collected under small amount of axial force to prevent slipping. To generate mastercurves, isothermal frequency sweep between 100 and 0.1 rad/s at a constant 1% strain were collected at different temperatures. A mastercurve was constructed using time-temperature superposition (TTS) under Williams–Landel–Ferry (WLF) relation.

Differential Scanning Calorimetry (DSC)

DSC measurements were performed on a DSC 2500 calorimeter (TA Instruments). Approximately 5 mg of material was sealed in Tzero hermetic pans and cycled between −80 and 200 °C at 10 °C/min. The glass transition temperature (T_g) of the sample was determined on the second heating cycle using the midpoint analysis method.

Optical Spectroscopy

UV-Vis absorption spectra of CPE and the complex films were taken using an Agilent Cary 60 UV-Vis spectrophotometer. All measurements were done at ambient temperature (~ 25˚C). Emission spectra were taken using a Horiba FluoroMax® 4 spectrometer at 450 nm excitation wavelength with a 495 nm long pass filter. The sample is illuminated by a 150 W xenon,

continuous output, ozone-free lamp. Emission spectrum of each film was averaged over 3 scans.

Conductivity Measurement

In-plane electronic conductivity of the samples were measured with transmission line measurements using custom made gold digits on silicon substrates. For the strain-dependent and strain cycling conductivity tests, complex film was casted onto a Kraton substrate. The whole Kraton substrate with casted complex film was subjected to the designated strain. For the cycling test, the sample was first subjected to 20% strain for 15 seconds, and the measurement at 0% strain was done after the sample was let relax for 15 minutes. All measurements done with a Keithley 6485 picoammeter, and were carried out inside a nitrogen glovebox at room temperature.

X-ray Photoelectron Spectroscopy (XPS)

The X-ray photoelectron spectroscopy (XPS) analyses were performed using a ThermoFisher Escalab Xi+ with Al Kα X-ray radiation, in conjunction with an electron flood gun. We quantified the relative atomic percentages from XPS survey spectra through the Avantage software suite, provided by Thermo Fisher Scientific Inc. We specifically focused on integrating and normalizing the C 1s (CPE and BPE), N 1s (BPE and CPE counterion), O 1s (BPE, CPE counterion, and substrate), S 2s (CPE and CPE counterion), and Si 2p (substrate) peaks by their respective photoionization cross sections. The iodine signal, which was at a comparable level to noise in the survey spectra, was omitted from our analysis.

Dynamic Secondary Ion Mass Spectroscopy (DSIMS)

For the DSIMS analysis, films were first coated with a thin layer of Pd/Au to augment conductivity. Examinations were then carried out using a Cmaeca IMS 7f Auto SIMS. Following this, the films were sputtered with reactive O_2^+ ions over an area of 63 × 63 μm^2, while simultaneously monitoring the counts per second of ^{127}I within the central 50 × 50 μm^2 region, against sputtering time. In two distinct regions, a considerable and nearly consistent level of ^{127}I signal was detected throughout the sputtering depth of the sample (refer to **Figure S5.2**). We attribute this to the retention of I- ions within the BPE-rich domains.

5.4 Results and Discussion

This study aims to leverage electrostatic interactions to compatibilize polymers with different functionalities to obtain a polymer complex that is soft (comparable with biological tissues), elastic, and conductive. We chose to form a coacervate from an anionic conjugated polyelectrolyte (CPE) and a cationic bottlebrush polyelectrolyte (BPE) (**Figure 5.1a)**. Subsequent removal of the solvent from this coacervate transformed it into an ionically crosslinked polymer complex, which was the material of interest. Poly(4-methyl caprolactone) (pMCL) was chosen as the BPE side-chain for its low glass-transition temperature ($T_g = -60$ °C),[56] lack of crystallinity as a homopolymer. The hydroxyl chain-ends of the BPE enable post-modification to obtain the pendant ionic group. The degree of polymerization (DP) of the pMCL macromonomer was kept at 17 to stay below the entanglement molecular weight of the linear chain.[56] The macromonomer was then polymerized via ring-opening metathesis polymerization (ROMP) to obtain a bottlebrush polymer with backbone degree of polymerization (N_{BB}) around 100. The resulting bottlebrush polymer was functionalized with

cationic imidazolium chain-ends compensated by iodine counterions. The wide electrochemical stability window of the imidazolium group [57] allows it to remain stable upon electrical doping of the CPE in the resulting complex. Due to the nature of the post-modification reaction on bottlebrush with densely grafted side-chain, we were only able to obtain up to 60% charged repeat unit, as indicated by ^{1}H NMR of the polymer. We note that ionic functionalization did not result in significant increase in the T_g of the BPE (T_g = −55 °C, **Figure S5.1**). This BPE is paired with an anionic CPE, poly[6-(thiophen-3-yl)hexane-1-sulfonate, as thiophene-based polymers have been extensively studied with well documented optoelectronic and transport properties. The fraction of charged repeat units on the CPE was tailored to match the number of charges per macromonomer on the BPE (60%).

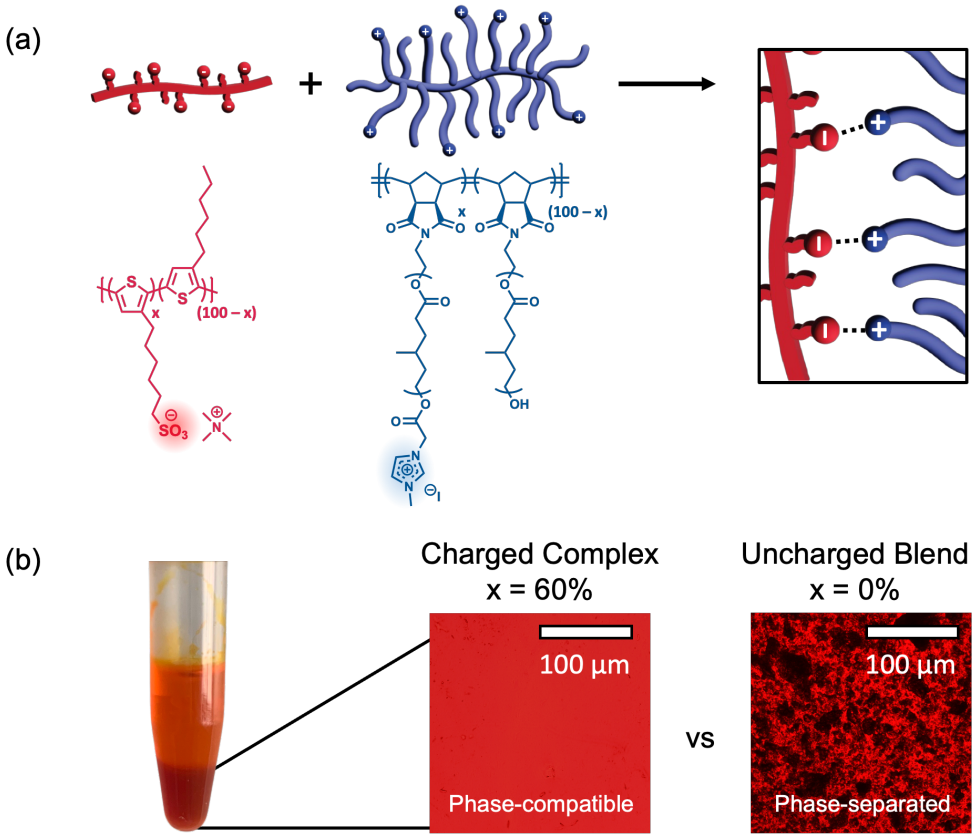

Figure 5.1. (a) Chemical structures of the conjugated polyelectrolyte (CPE – red) and the bottlebrush polyelectrolyte (BPE – blue). **(b)** Associative phase-separation emerged upon mixing CPE and BPE solutions lead to the formation of a concentrated coacervate in coexistent with a polymer-deficient supernatant. Optical microscope images of the CPE – BPE solid-state complex obtained from drying their coacervate. The homogeneous red color indicates homogeneous distribution of the CPE in the blend, confirming phase compatibility between the CPE and the BPE in the complex. In contrast, blend of poly(3-hexylthiophene) (P3HT) with hydroxyl-functionalized PMCL (PMCL-OH) (corresponding to charge fraction x = 0%) shows macroscopic separation between P3HT-rich and PMCL-OH-rich phases due to incompatibility between 2 neutral polymers.

Despite their stark differences in chemistry and architecture, the polymers appear to be effectively compatibilized by the electrostatic interactions. The CPE – BPE coacervate appears to be well-mixed by optical microscopy, as indicated by the homogeneous distribution of the red color (from the CPE) (**Figure 5.1b**). In contrast to the charged complex, a solution blend of uncharged polymers (x = 0%) shows significant phase separation between 2 components and aggregation of the conjugated polymer. These can be seen via the regions of dark-red CPE aggregates heterogeneously distributed in a matrix with lighter color (mainly BPE and low concentration of CPE). While the charge fraction of both polymers is around 60% with respect to the number of monomers, the charge density of the BPE is much lower than that of the CPE due to the macromolecular BPE side-chains. Given that N_{sc} = 17, there is only 1 cation – anion pair to compatibilize 18 repeat units from the BPE with the CPE repeat unit. Our observation agrees with prior mean-field prediction that only a few charges per polymer chain are needed to completely compatibilize most polymer pairs.[45] Lastly, we note that while ionic interactions have been successfully implemented in stabilizing mixtures of 2 linear polymers, little has been investigated for compatibilization of polymers with different architectures. Our observation indicates that electrostatic interactions are a powerful force for

combining very distinct polymers into a stabilized blends for multifunctional polymeric materials.

While the two polymer solutions were mixed in stoichiometric in terms of charge ratio, the resulting solid-state complex obtained from drying the coacervate appears to be non-stoichiometric. In particular, X-ray photoelectron spectroscopy (XPS) suggests that the relative ratio of Nitrogen (only present in the BPE and the CPE counterion) to Sulfur (only present in the CPE) in the complex is N:S ≈ 2:1. For stoichiometric complex, this value would be between 1.4:1 – 1.75:1 depending on the amount of tetramethyl ammonium ions that are still present in the complex. This indicates that the BPE (macromonomer) : CPE (monomer) ratio in the complex is between 1.2 – 1.5. This non-stoichiometry suggests that the BPE preferentially partitions into the complex coacervate phase while the CPE dominates the supernatant phase, a situation that is not unusual in the formation of coacervates of linear polymers with a mismatch in charge density.[58] While the molar ratio of the BPE and the CPE in the complex is still close to 1:1, we note that the material is mainly composed of the BPE due to its much larger size. In particular, the molar mass of the CPE's repeat unit is 213.4 g/mol, while that of the BPE is approximately 12 times larger (2478 g/mol). As a result, approximately 93 – 95 vol% of the complex (95 – 96 wt%) is the BPE, while the conductive CPE is only present as a minor component (details of calculation discussed in the Appendix). These results demonstrate that molecular architecture can have important consequences for the composition of the resulting complex.

While the BPE – CPE complex is homogeneously mixed at mesoscopic scales, hierarchical local structures are present within the material. As shown in **Figure 5.2a**, the small-angle X-ray scattering (SAXS) profile of the complex has a broad peak centered at $q \approx 0.05$ Å^{-1}, corresponding to a correlation length of ≈ 13 nm. As the SAXS profiles of both the CPE and the BPE are featureless, this correlation length indicates formation of structure due to the complexation process. Interestingly, this lengthscale is very close to the size of a BPE – CPE pair stacked in parallel (**Figure 5.2c**, details of calculation included in the Appendix). Since the CPE is only present in minor quantity within the complex (≈ 5 vol% and below stoichiometric molar quantity), we postulate that the complex takes on a morphology as illustrated in **Figure 5.2c**, where the CPE chains adhere onto the surface of the BPE domains and form a percolating CPE network. Charge-mediated complexation should occur at the BPE – CPE interface because the low dielectric constant of the polymers requires close contact between oppositely charged ions. As the BPE are present in excess, the BPE domains can contain more than 1 BPE chain, and the excess ionic groups from the BPE sidechains in these domain are charge-compensated by their counterions (Iodine anions). While XPS detects no Iodine due to its small concentration (i.e. at% I in neat BPE ≈ 0.3%), we were able to confirm its presence in the complex with Dynamic Secondary Ions Mass Spectroscopy (DSIMS) (**Figure S5.2**) thanks to its sensitivity. Due to the mismatch between in charge density of the 2 polymers, it is likely that the more densly charged CPE chain is charge-compensated by multiple BPE chains and act as a crosslinker within the BPE matrix. While there is no direct observation of the real-space morphology of the complex that gives rise to the correlation length observed in SAXS data, our hypothesis on the material's morphology is supported by analysis of the complex's mechanical and charge transport behavior, vida infra.

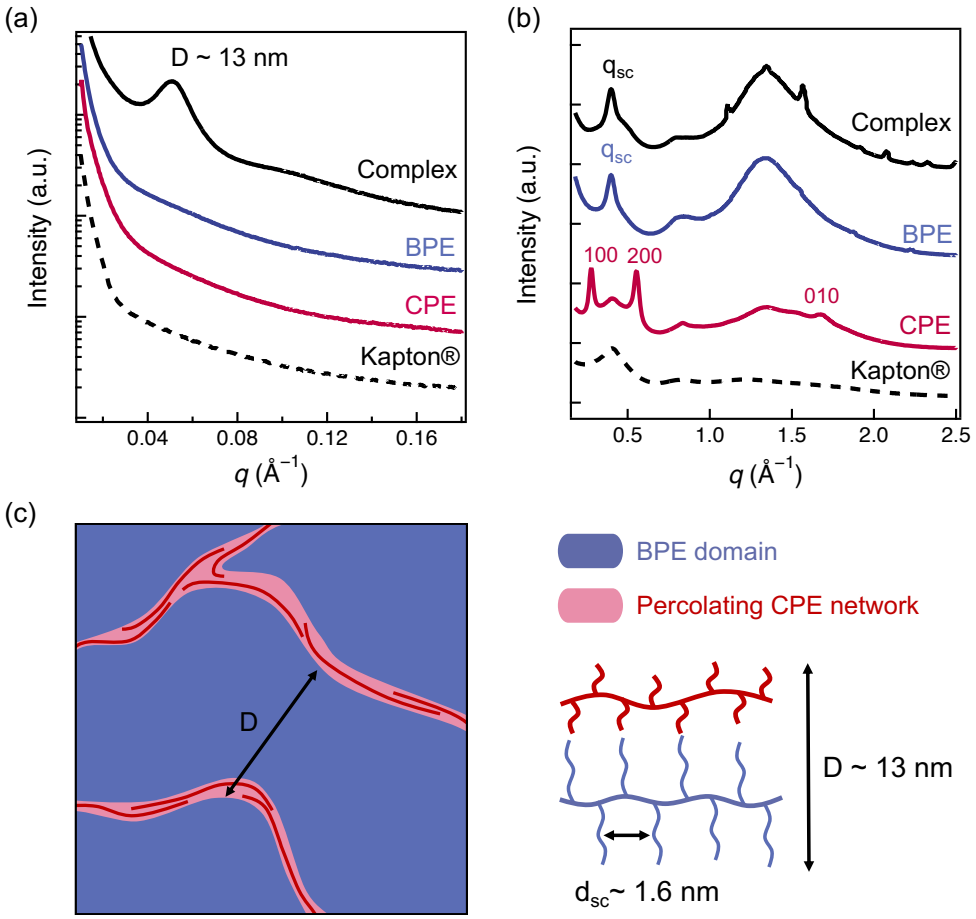

Figure 5.2. (a) SAXS patterns showing formation of nanodomains due to short-range enthalpic repulsion between 2 polymers. **(b)** WAXS data indicating no disturbance of the BPE is observed in the complex. Signals from the stacking of CPE chains (if any) are likely overwhelmed by the scattering from the BPE component. **(c)** Proposed mesoscopic structure of the complex where domains of BPE are separated by thin layers of CPE chains.

Due to the significant dilution of the CPE, no CPE scattering signal is observed in the complex, while the relevant length scales observed in the bulk BPE are unperturbed upon complexation. As shown in **Figure 5.2b**, the peak at $q \approx 0.4$ Å^{-1} (d = 1.6 nm) in the wide-angle X-ray scattering (WAXS) trace of the BPE remain its position and intensity in the complex. This peak likely corresponds to the correlation distance between neighboring segments along the BPE backbone.[59] The neat CPE forms a semicrystalline solid where CPE

chains are stacked both along the backbone and the sidechain directions. Scattering peaks were observed at q ≈ 0.27 $Å^{-1}$, 0.55 $Å^{-1}$, and 1.67 $Å^{-1}$, corresponding to the 100, 200 (alkyl stacking), and 010 (π-stacking) peaks of the CPE crystallite, in agreement with studies of thin films in literature.[60] In our prior work, where a similar CPE with x = 60% was studied, we did not observe crystalline features, which we attribute to the lower MW of that CPE (Mn ≈ 8 kDa) compared to the one employed in this study (Mn ≈ 11kDa and 16 kDa). None of these features show up in the WAXS of the complex, likely due to the absence of CPE crystallites in the complex and the overwhelming scattering signal from the predominantly present BPE component. Lastly, the sharp peaks that are present at high q in the complex WAXS curve, and more weakly in the BPE curve, likely come from residual salts in the BPE synthesis that are difficult to completely remove during the polymer synthesis work-up.

Emission spectroscopy indicates a stronger J-type characteristic of CPE aggregates in the complex compared to its neat form and an improvement in intrachain structural order of the CPE upon complexation. As shown in **Figure 5.3**, the photoluminescence (PL) spectrum of the complex exhibits a higher $I_{0\text{-}0}/I_{0\text{-}1}$ ratio (0.94) compared to neat CPE PL spectrum (0.82). In the limit of pure H-type (inter-chain) aggregates, the 0 – 0 transmission is dipole-forbidden. As a result, the more intense 0 – 0 peak in the complex PL spectrum indicates that electronic coupling of CPE chains in the complex has more J-type character than those in the neat CPE film. As the CPE is dispersed within the BPE matrix at 5 vol%, it is reasonable that the CPE chains are more isolated from each other. Moreover, the complex also has a lower $I_{0\text{-}2}/I_{0\text{-}1}$ ratio (0.37) compared to the neat CPE (0.48). The intensity of the 0 – 2 emission peak has been shown to be an effective measure of intrachain conjugation,[61] with longer intrachain

conjugation length yields weaker 0 – 2 emission. As a result, the smaller $I_{0\text{-}2}/I_{0\text{-}1}$ ratio of the complex suggests that complexation with the BPE enhances the delocalization of exciton along the CPE backbone. This observation is different from what we have previously reported for systems of linear polymers in that the complexation-induced planarization of the CPE is only present in complexes of highly charged polymers.[48] We hypothesize that the cause for this different behavior of the CPE – BPE complex is the asymmetry of this system in both the volume fraction of each polymer and in their relative size.

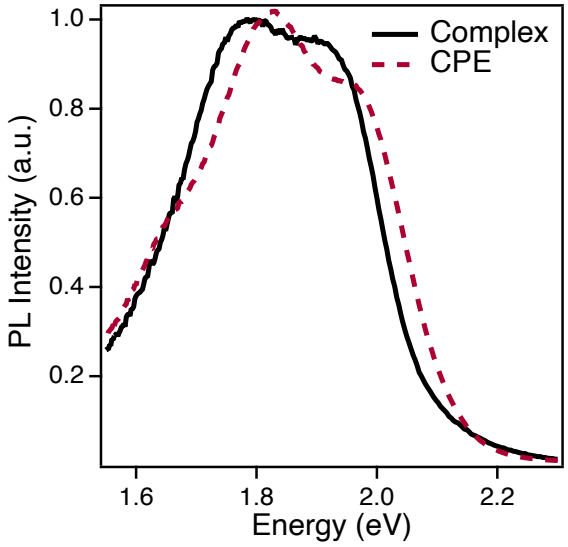

Figure 5.3. Normalized PL emission spectra suggesting predominant J-type aggregate characteristic of CPE in the complex compared to neat CPE film

Doping was carried out to yield electrically conductive films. CPE – BPE complex films were exposed to bistriflimidic acid (HTFSI) vapor at 55°C for 1 hour, followed by a 24-hour heating in an enclosed chamber to ensure sufficient diffusion of dopant molecules into the material. HTFSI was chosen as the dopant as it sublimes at room temperature, so no excessive heating is required to keep minimal disturbance to the complex whose major component is the low-T_g BPE. Moreover, we have shown in our prior works on linear systems that this dopant can

effectively diffuse into the ionically crosslinked polymer complexes and dope the backbone of the CPE component.[46,62] We chose the completion point of the doping process to be the time at which no further increase in the conductivity of the film was observed with longer exposure of the film to the dopant. Effective doping of the polymer complex was confirmed by the bleaching of the neutral CPE backbone absorption and the emergence of the polaronic absorption peak at ~ 1.7 eV and bipolaron absorption at $h\nu \leq 1.5$ eV in the UV-Vis spectrum of the doped film (**Figure S5.3**).

The doped complex is electronically conducting, confirming our prior hypothesis that CPE chains form a macroscopically connected network instead of being confined into droplets, which is a commonly observed morphology for asymmetric polymer blend/block copolymer systems. The conductivity of HTFSI-doped complex can vary significantly from 3×10^{-3} to 3×10^{-1} S/cm; complexes made from higher MW (16 kDa) CPE had higher conductivity (5×10^{-2} to 3×10^{-1} S/cm) than those made from lower MW (11 kDa) CPE (3×10^{-3} to 2×10^{-2} S/cm). These data suggest an influence of the CPE chain length and processing on the resulting electrical conductivity. We attribute this to the variations that can arise during the hot-pressing complex into films and vapor doping processes, which are not well controlled. Despite the variation, the conductivity of complex when normalized by the CPE concentration (14- 20 times dilution) is significantly higher than conductivity of the equivalent neat CPE in thin films (6×10^{-3}S/cm). Neat CPEs of various backbone and side-chain chemistries have been reported to have similarly low electrical conductivity ($\approx 10^{-3}$S/cm), while the conductivity of the most conductive complex sample (3×10^{-1} S/cm) can be normalized by the concentration of CPE to a value of 4 – 6 S/cm, within the range typically

reported for doped P3HT films. This suggests an improvement in charge carrier mobility of the CPE upon complexation with the BPE, which likely is a result of the planarization of the CPE backbone (**Figure 5.3**), leading to more efficient intrachain transport and potentially more interconnectivity between chains resulting from better chain alignment. This hypothesis is further supported when considering the percolation threshold of a conductor – insulator blend. In particular, for various blends of a conductive polymer with an insulating polymer, it is commonly reported that percolation threshold for the insulator – metal transition is 16 vol%.[63,64] This is also the expected threshold for a dispersion of spherical particles in 3-dimension, in both site and continuum percolation.[65] However, the value decreases rapidly as the conducting component forms domains with more elongated and/or lower dimensional shapes (thin rods, or pancake) with improved alignment. For example, it has been shown that the percolation threshold can be as low as 0.05 vol% for pancakes of conducting polymers that are templated onto a mechanically connected gel network.[66] In our system, the complex is conductive with just 5 – 7 vol% of the conducting component, suggesting that the percolation threshold for this electrostatically complexed morphology is below 5 vol%. Our observation supports a previously proposed design rule for lowering the percolation threshold in conductive – insulative polymer blends by dispersing the conductive component at the molecular level instead of forming conducting aggregates inside an insulator matrix.[67]

Despite the lack of chain entanglement in the BPE, the complex is elastic due to the crosslinking nature of ionic complexation. This eliminates the need for subsequent crosslinking that is commonly required in other bottlebrush elastomer composites.[2,34] As shown in **Figure 5.4a**, while the BPE is a viscoelastic liquid ($G'' < G'$), upon its complexation

with the CPE the resulting complex behaves like a viscoelastic solid with a shear storage modulus G′ that is consistently higher than its loss modulus G'' across the broad frequency range studied. While ionic complexation with the CPE significantly stiffens the BPE, the complex's modulus ($G'_{pristine} \approx 0.14$ MPa) is of a similar low value to other bottlebrush elastomer networks [68,69] and is comparable to soft-tissues (**Figure S5.6**).

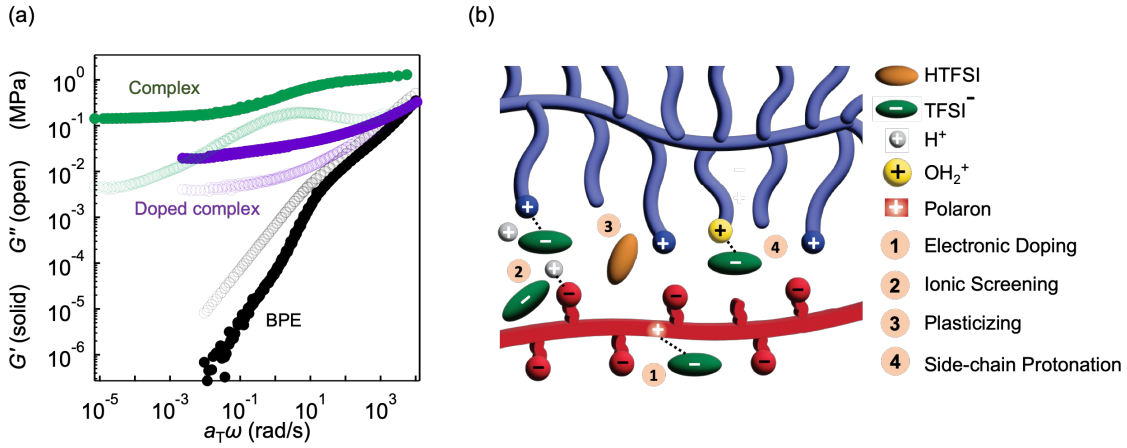

Figure 5.4. (a) Rheological master curves of the BPE, the pristine complex, and the HTFSI-doped complex. The complex (both pristine and doped) are viscoelastic solid, as seen from the shear storage modulus (G′) dominating the loss modulus (G″) across wide range of frequencies at room temperature. (b) Possible impacts of doping on the CPE – BPE network are: (1) electronically dope the CPE backbone, forming a polaron accompanied by an TFSI anion (2) partition into the side-chain ionic crosslink, forming an ionic cluster (3) plasticize the system and (4) Protonating the hydroxyl end of non-ionized BPE repeat units. Objects are not drawn to scale, the ions and HTFSI molecules are enlarged for demonstration purposes.

The introduction of ionic species during vapor doping process complicates the behavior of the charged complex. As shown in **Figure 5.4a**, doping decreases the shear modulus of the complex by approximately 5 folds ($G'_{doped} \approx 0.03$ MPa) but does not significantly disrupt the ionic crosslinks. The storage modulus G′ still dominates the loss modulus G″ in the doped complex across all frequencies below the transition region, confirming that the doped material is a viscoelastic solid at room temperature. As shown in **Figure 5.4b**, the introduction of

HTFSI to the complex, besides electronically doping the CPE backbone (*mechanism 1*), can also: disrupt the ion pairing between the CPE and BPE (*mechanism 2*), plasticize the system if HTFSI is present in unreacted form (*mechanism 3*), and protonate the hydroxyl side-chain ends of the BPE with charge balance by the TFSI counterions (*mechanism 4*). Mechanisms 2 and 4 are driven by the higher pKa of polymeric sulfonic acid and hydroxyl group compared to HTFSI.[70,71] We note that mechanisms 1, 3, and 4 can all introduce the bulky TFSI anion/HTFSI molecule to the system, possibly plasticize the complex.[72] However, if plasticization was the only cause for the softening, the molecular weight between crosslink M_x would have had to increase by 5 folds to result in such change in the modulus, suggesting a 80 wt% uptake of HTFSI. On the other hand, measurement of HTFSI mass uptake of the bulk sample yields only 20% mass gain upon doping, indicating that the significant drop in the material's modulus is likely due to the localization of TFSI anions between crosslinking strands. Indeed, the partitioning of H^+ and $TFSI^-$ into the ionic crosslinks as described in mechanism 2 can screen the ionic interactions within the crosslink and/or increase the length and architecture of the "crosslinker" from a cation-anion pair to an ionic cluster. It is likely that the combination of all these effects and their disruption to the complex's structure ultimately give rise to the changes in the material's mechanical properties.

The use of other dopant molecules might give better controlled on some of these processes, but sublimation temperature needs to be taken into consideration as mentioned above. Lastly, while vapor doping allows minimal disturbance to the polymer complex compared to other methods such as solution (sequential) doping, there are a lot of variables are difficult to control precisely such as the amount of dopant gets absorbed into the material or the rate of dopant

infiltration. Pre-doping the CPE before complexation, or using a self-doped CPE to form charged complex with a BPE, can be promising alternatives to obtain electrically conductive complexes with more controlled doping.

The soft complex is easily stretchable with low tensile modulus as evidenced by the elastic recovery both before and after doping. As shown in **Figure 5.5a**, the pristine complex shows an initial linear elastic region up to 20% strain, with a low tensile modulus E' of ≈ 0.7 MPa, orders of magnitude lower than those of semicrystalline conducting polymers (≈ 10 – 1000 MPa).[7] For the doped complex, the elastic region is extended to nearly 45% strain, while the tensile modulus decreases to ≈ 0.2 MPa. This recovery behavior of the CPE – BPE complex further confirms that ionic bonds can effectively induce elasticity to the system. The wider strain range of elasticity in the doped complex is likely caused by the plasticizing effect and the partitioning of HTFSI into the ionic crosslinks as discussed above. The lower E' of the doped complex is consistent with the softening of the complex upon doping observed from rheology data.

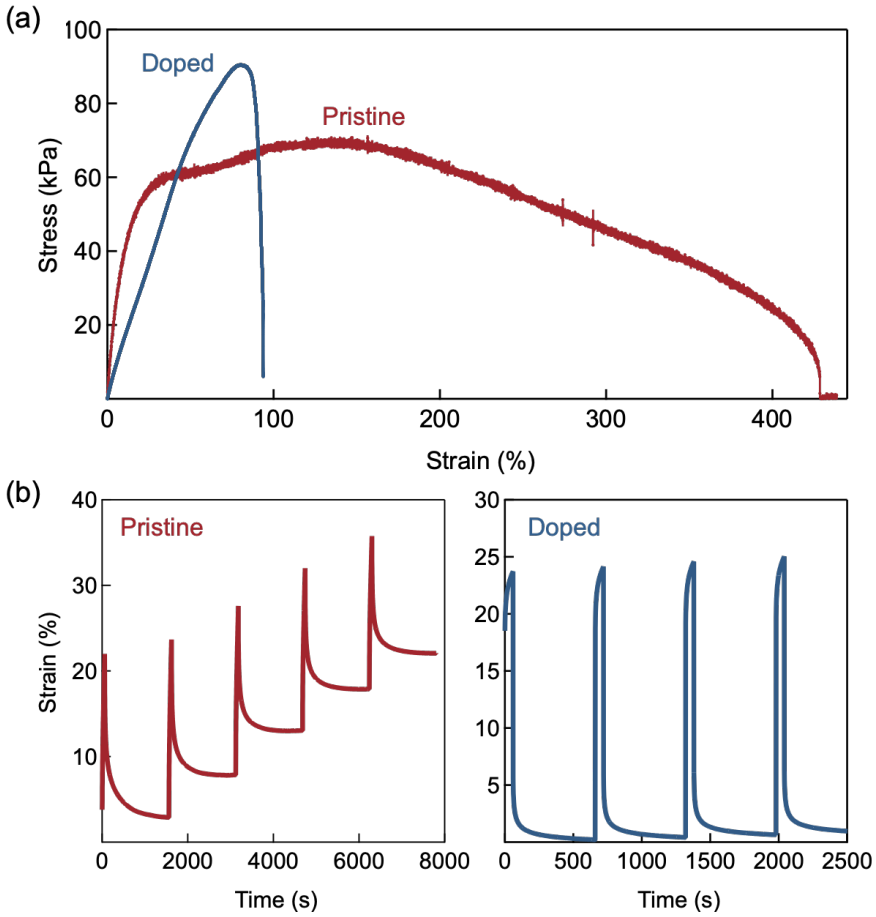

Figure 5.5. (a) Stress-strain curve and **(b)** recovery behavior of the complex before and after doping when subjected to 1 minute of 20% elongation.

The doped complex showed better elastic recovery after deformation compared to the pristine complex when subjected to 20 % strain, suggesting potentials of this material in stretchable – recoverable applications. To probe the recovery behavior of the material, multiple recovery cycles were carried out during which the material was elongated at 20% strain (within the elastic limit of both pristine and doped complex) for 1 min. The strain was then released, and the material was left to relax until no further decrease in strain was observed (**Figure 5.5b**). The pristine complex showed an appreciable recovery of 87% after the first cycle, and its recovery remained consistently >75% on the subsequent cycles. On the other hand, the doped

complex recovered 99% in the first cycle, and the percent recovery stayed consistently around 99% in the 3 subsequent cycles. We postulate that the partition of HTFSI to the ionic crosslinks increases both the crosslink strand size and the chain mobility around these crosslinking points. Both of these impacts can result in the improvement in the recovery of the material when subjected to strain.

Both the pristine and the doped complex can be extended to appreciable elongation before break. As illustrated in **Figure 5.5a**, the pristine complex undergoes plastic deformation after the elastic limit at ≈ 20% strain, reaches an ultimate tensile strength at approximately 70 kPa, and eventually breaks at 450% strain. This stretchability is significantly higher than many previously reported conjugated polymer – linear elastomer composite (typically < 150% strain).[73–75] The doped complex, on the other hand, only has a more narrow region of plastic deformation before breaking, with an ultimate tensile strength of ≈ 90 kPa. We note that the failure mechanism of 2 samples are different: while the pristine complex breaks at the middle of the gauge length region, the doped complex tends to break at the clamped point. This difference makes it difficult to directly compare the failure mechanism and stretchability of the 2 samples. Nonetheless, we found that the complex, both before and after doping, shows good stretchability over a range that is relevant for most applications.

To probe how the electron conduction pathway within the material changes with stretching, we measured the resistance of a sheet of the complex as a function of applied strain. A film of doped complex was formed on a supporting Kraton substrate, so that during the stretching experiment the substrate was clamped instead of the complex (**Figure S5.7a**). This geometry

avoided compression and shearing of the complex that could contribute to the resistance measurement. The change in resistance of the sample upon tensile strain is compared to a model of an ideal elastomeric conductor with an unchanging bulk resistivity, shown in **Figure 5.6** as a blue curve (details of the calculation are in the Appendix).

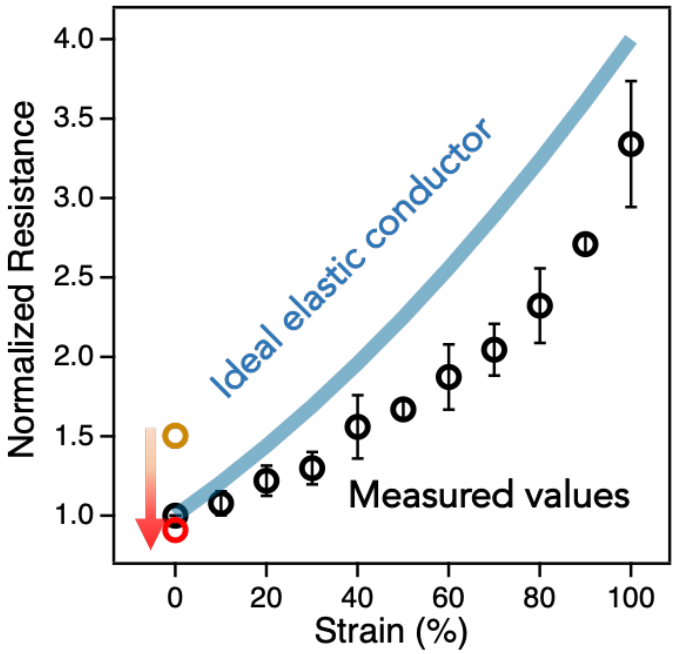

Figure 5.6. Resistance of the doped complex film (normalized to the resistance at 0% strain) as a function of applied strain. Solid line showing predicted behavior of an ideal elastic conductor. The red and orange markers show the normalized resistance of the sample when let relax back to 0% strain that was measured immediately (orange) and after 1 day(red), indicating full recovery of the conductivity.

The increase in the resistance of the complex film when subjected to strain is consistently lower than the behavior expected for an ideal elastomeric conductor, which can be attributed to the non-idealities in the complex. First, it is possible that when the complex is stretched, the CPE chains change their alignment or local interactions, leading to an increase in charge carrier mobility that decreases the resistivity ρ of the complex. Second, the ideal elastomer model assumes the material is isotropic with Poisson's ratio of 0.5 whereas the complex here deviates from this value based on the small strain tensile and shear moduli ($E' = 0.2$MPa and

$G' = 0.03$MPa for doped complex). The strain rate of the electrical measurement was not matched to the rheological data as well. The change in resistance on return to 0% strain after large deformation to 100% and subsequent recovery over 1 day suggests significant relaxation within the sample after deformation. Additionally, measurements of the sample's resistance after cyclic deformation to 20% strain, a comparable strain within the regime of nearly elastic mechanical recovery (**Figure 5.5b**), shows near-complete recovery of the sample resistance after the strain was removed (**Figure S5.7b**). However, detailed origin of such electrical conductivity relaxation requires further investigation. Overall, the mechanical and electrical conductivity relaxation behaviors of the complex show significant promise of this material as stretchable conductors.

5.5 Conclusions

We report here a novel approach to engineer stretchable, elastic, and semiconductive materials by leveraging the charge-induced complexation between two oppositely charged polyelectrolytes. Mixing an anionic semiconducting CPE with a cationic super-soft BPE resulted in a stabilized polymer complex that is mesoscopically homogeneous with some local structures from the BPE component that was preserved upon complexation. The complex has a compatible modulus with that of soft-tissues ($\approx 0.2 - 0.7$ MPa), and possesses an appreciable conductivity up to 3×10^{-1}S/cm when doped with a strong acid. It is important to emphasize that our design strategy requires no addition of crosslinkers or excessive processing to induce elasticity or to homogenize the 2 distinct components. Our study underscores the potentials of ionic compatibilization in engineering multifunctional polymeric materials for soft electronic

applications, with many added processing advantages and potentials for optimizing orthogonal properties.

5.6 Acknowledgement

This work was funded by the Department of Energy Office of Basic Energy Sciences under Grant No. DE-SC0016390. The authors acknowledge the use of shared facilities of the UCSB MRSEC (NSF DMR 1720256), a member of the Materials Research Facilities Network (www.mrfn.org). Tensile testing and X-ray scattering experiments were supported by the BioPACIFIC Materials Innovation Platform of the National Science Foundation under Award No. DMR-1933487. This research used resources of the National Synchrotron Light Source II, a U.S. Department of Energy Office of Science User Facility (DE-SC0012704; beamline 11-BM). We thank our beamline scientist Dr. Ruipeng Li for helping with the collection of X-ray scattering data.

5.7 Appendix

Synthesis of norbornene-poly(4-methylcaprolactone) (pMCL MM)

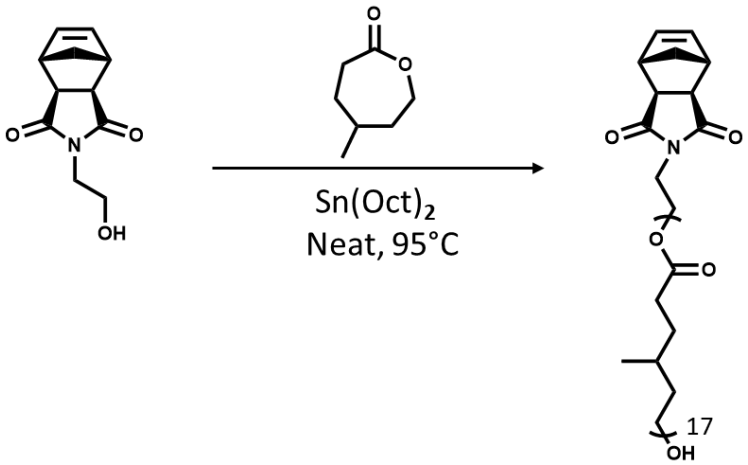

Synthesis of pMCL bottlebrush polymer (pMCL BB)

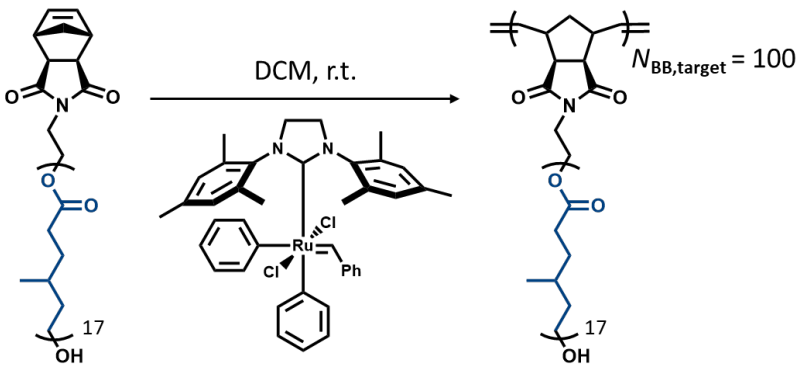

Polymerization of the macromonomers using a Grubbs' third-generation catalyst (G3) was performed in a very dilute solution of the macromonomers. In a nitrogen-filled glovebox, pMCL MM (6.9 g, 3.1mmol, 100 eq) were dissolved in anhydrous DCM (100 mL). In a separate container, G3 (23 mg, 0.0314 mmol, 1 eq) was dissolved in 0.3 mL of anhydrous DCM before rapid injection into a vigorously stirring solution of the macromonomers. After 12 hours, the polymerization was removed from the glovebox and terminated using a large excess ethyl vinyl ether (EVE) (>100 eq) with stirring for 30 minutes. A crude ^{1}H NMR of the freshly quenched reaction was taken. The disappearance of a peak at 6.3 ppm corresponding to unreacted olefin protons was observed suggesting high reaction conversion. The resulting reaction mixture was concentrated *in vacuo* and the polymer precipitated into methanol at 0 °C. After two more precipitations into methanol, the bottlebrush polymer was dried *in vacuo*. The polymer was characterized with ^{1}H NMR. The dispersity of the polymer was determined by SEC in chloroform.

Synthesis of pMCL BB imidazole

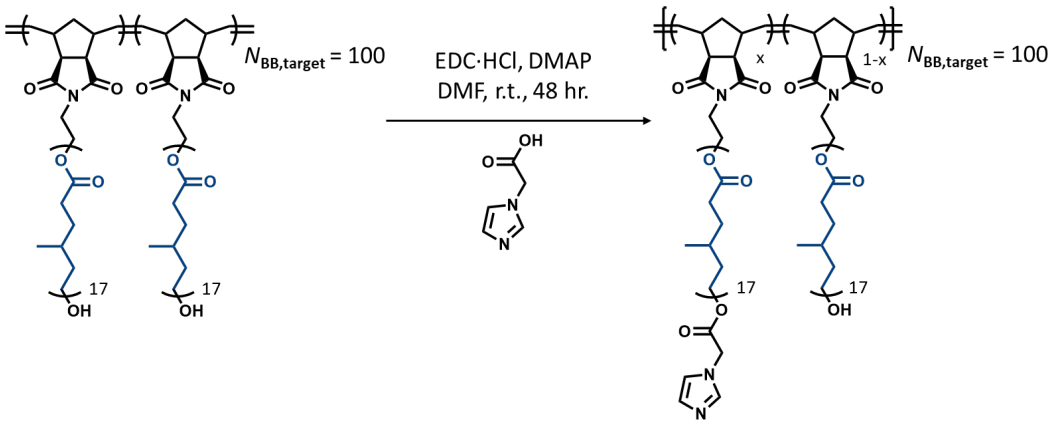

In a round-bottom flask charged with stirbar, EDC·HCl (1.4 g, 400 eq, 7.2 mmol), DMAP (110 mg, 50 eq, 0.9 mmol), imidazole-ylacetic acid (683 mg, 300 eq, 5.42 mmol), and 150 mL of dry DMF are added. The mixture was stirred until EDC·HCl, and DMAP are dissolved. The solution was sonicated for 5 minutes to obtain cloudy solution. In a separate flask, pMCL BB (3.97 g, 1 eq, 0.018 mmol) was dissolved in 50 mL DMF before adding into the reaction mixture. The flask was capped and stir for 48 hours at room temperature. The reaction was condensed in *vacuo*, and 300 mL of DCM was added. The solution was washed repeatedly with diluted HCl (1M, 50 mL), water, and brine. The organic layer was collected and centrifuged (9000 rpm, 5 minutes). A while top-layer emulsion was taken out, and the organic layer was collected. The solution was condensed, and the polymer was precipitated in methanol at 0 °C twice. The polymer was dry in *vacuo*. %Recovery = 68%. The mol% of imidazole was calculated by normalizing the methyl protons of the pMCL sidechain (0.9 ppm) to the amounts observed in the macromonomer, the integration of observed ester peak at 4.9 ppm was, then, calculated to give an approximate mol% imidazole.

Synthesis of the bottlebrush polyelectrolyte (BPE)

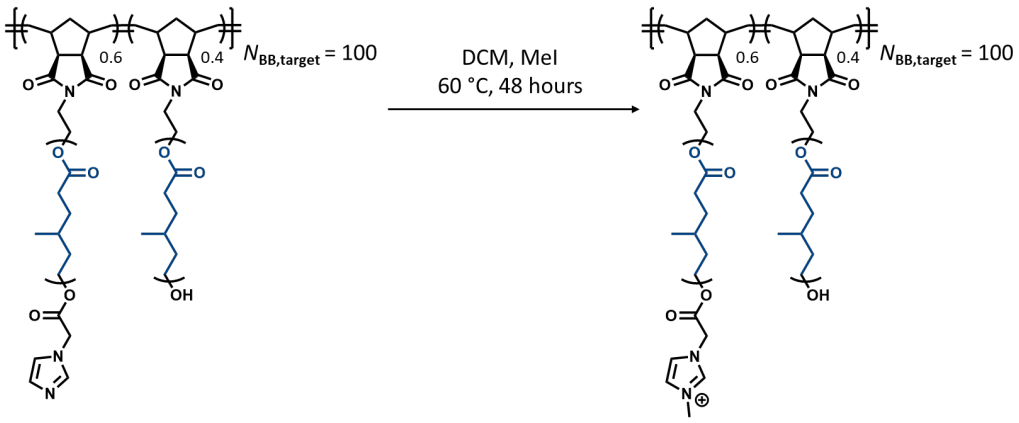

All glassware were oven dried for 24 hours prior to the synthesis. In a thick wall round-bottom pressure flask charged with a stirbar, pMCL BB imidazole (2 g, 1 eq, 0.0083 mmol) was added and dissolved with 70 mL DCM. MeI (809 mg, 650 eq, 5.7 mmol) was added, and the flask was sealed with a bottom-seating PTFE lined cap and a perfluoro O-ring. The reaction flask was heated to 60 °C while stirring for 48 hours. The completion of the reaction was confirmed with the disappearance of the imidazole ester at 4.9 ppm, and the appearance of imidazolium ester at 5.2 ppm. The polymer was dry in a vacuum oven (50 °C, 0.1 mTorr) for 48 hours to evaporate excess MeI.

Synthesis of Poly(3-(6'-bromohexyl)thiophene-co-3-hexylthiophene) (P3BrHT:P3HT)

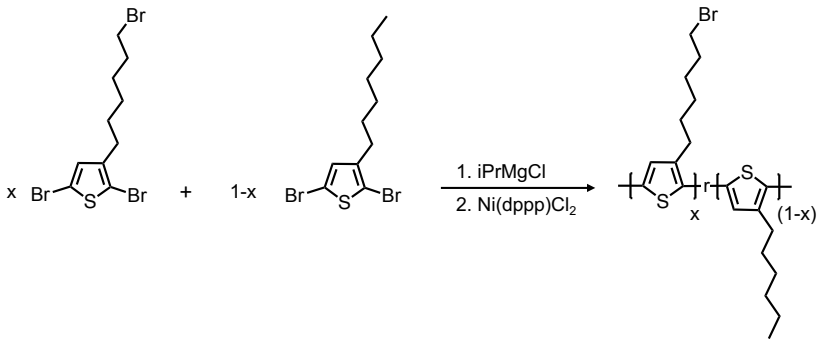

P3BrHT:P3HT random copolymers was synthesized following a previously reported protocol.[76] 2,5-dibromo-3-(6-bromohexyl)thiophene (purchased from eNovation Chemicals LLC) and 2,5-dibromo-3-hexylthiophene monomers were mixed in targeted molar ratios (50:50, 60:40, 75:25, 90:10, and 100:0) in an oven-dried round bottom flask sealed with rubber septa. The mixture was dried under active vacuum overnight, and later dissolved in distilled THF. The solution was purged with dry nitrogen for 20 minutes. Isopropylmagnesium chloride was then added dropwise to the reaction flask under rigorous stirring, and the mixture was let react at ambient temperature for 2 hours. A suspension of $Ni(dppp)Cl_2$ in distilled THF was then added quickly to the reaction, and the mixture turned from pale yellow to vibrant red immediately. The polymerization was run for 12 hours and was then quenched by rapid addition of 1M HCl solution. The mixture was precipitated in cold methanol, and the obtained polymer was purified by washing in a Soxhlet apparatus with methanol, acetone, and ethyl acetate before extraction with THF. The product was concentrated under vacuum, yielding a red-purple solid. The isolated product was then dried overnight under vacuum to remove any remaining solvent.

Synthesis of Poly[6-(thiophen-3-yl)hexane-1-sulfonate-co-3-(hexylthiophene)] (the CPE)

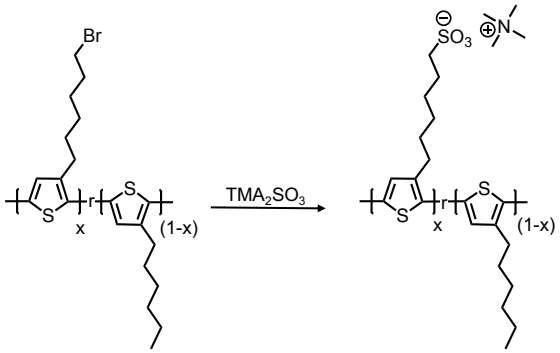

P3BrHT-P3HT was dissolved in THF and the reaction flask was sealed with a rubber septa. The solution was stirred and purged with dry nitrogen for 30 minutes. 1M solution of bis(tetramethylammonium)sulfite (TMA_2SO_3) in methanol was then added in 10-fold excess to the flask, and the mixture was refluxed at 70˚C. Methanol was added to the flask after 1 hour to help dissolve the ionic-functionalized polymer and to drive the reaction to completion. The reaction was let run overnight. The polymer was collected by dialyzing the reaction mixture with methanol for 5 days using 10 kDa cutoff membranes. The dialysate was replaced every 12 h. The CPE was collected in vacuo, and further dried under vacuum at 60˚C, yielding a red-purple solid.

Calculations

- Estimation of CPE vol% and wt%:

CPE repeat unit MW = $0.6 \times 245 + 0.4 \times 166 = 213.4$ g/mol

BPE repeat unit MW = $0.6 \times 2530 + 0.4 \times 2400 = 2478$ g/mol

From XPS data, there is roughly 1.2 – 1.5 moles of BPE for every mole of CPE.

⇨ CPE wt% = $213.4 \div (213.4 + 2478 \times (1.2\ or\ 1.5) \times 100\% \approx 5.4\% - 6.7\ \%$

⇨ BPE wt% = $100\% - 5.4\ \% = 93.3\% - 94.6\%$

Density of BPE = 1.03 g/mL

Density of CPE = 1.33 g/mL

⇨ CPE vol% = $(213.4 \div 1.33) \div (213.4 \div 1.33 + ((1.2\ or\ 1.5) \times 2478 \div 1.03) \times 100\% \approx 4.3\% - 5.3\%$

⇨ BPE vol% = $100\% - 4.3\ \% = 94.7\% - 95.7\%$

- Doped complex theoretical mass uptake

For a complex with BPE : CPE molar ratio = 1.5 : 1, excluding mechanism #3: Assuming HTFSI generate 1 charge carrier per 6 CPE repeat units (mechanism #1) and protonate all OH side-chain ends (mechanism #4), and there are 2 molecules of HTFSI partition into every ionic crosslink, meaning that each ionic sidechain solvates 1 HTFSI molecule (mechanism #2):

Mass of HTFSI = $(\frac{1}{6} + 0.4 \times 1.5 \ + 2 \times 0.6) \times 281.14 = 553$

Mass of pristine complex = $213.4 + 2478 \times 1.5 = 3930$

⇨ wt% mass gain = $553 \div 3930 \times 100\% = 14.1\%$

- Estimation of relevant length scales in the complex

The average length of the side chain of bottlebrush polymers has been shown to follow a scaling law with a power of ≈ 0.41. A linear fit was done for polydimethylsiloxane side chains in a study by Sheiko et al.,[77] yielding:

$$2 < R_{sc} > = 0.5 + 1.2 \times N_{sc}^{0.41}$$

Since a dimethylsiloxane monomer only has 2 atoms along the side-chain projection while the sidechain monomer of our BPE has 7 atoms, we used a rough estimation of an equivalent N_{sc} = $17 \times \ 3.5 \approx 60$. So the diameter of the BPE filament (or 2 times the side-chain size) is:

$$2 < R_{sc} > = 0.5 + 1.2 \times 60^{0.41} = 7\ nm$$

This number is likely close to 8 – 9 nm for the side chains that are functionalized with the methylimidazole acetic group.

Such length scale in the CPE can also be estimated from the 100 peak in Figure 5.2b, which is ≈ 2.3 nm

⇨ The size of a BPE – CPE stack is thus approximately 11 – 12 nm, which is very close to the length scale observed in Figure 5.2a.

- Prediction of the resistance of an ideal elastic conductor when subjected to strain

When the sheet of an elastomer with resistance R and a resistivity of ρ is stretched along the length L with an extension ratio of λ_L (i.e. the new length $L' = L \times \lambda_L$), the width (W) and thickness (t) of the film will decrease by a factor of λ_W and λ_t, respectively. For an ideal elastomer (Poisson's ratio = 0.5, and isotropic):

$$\lambda_L \times \lambda_W \times \lambda_t = 1$$

and

$\lambda_W = \lambda_t$.

Thus, the new dimensions of the stretched film would be $L \times \lambda_L$, $W \times \frac{1}{\sqrt{\lambda_L}}$, and $t \times \frac{1}{\sqrt{\lambda_L}}$. The new resistance of the film is:

$$R' = \rho \frac{L'}{W't'} = \rho \frac{L}{Wt} {\lambda_L}^2 = R \times {\lambda_L}^2$$

meaning that the resistance of the stretched film will increase proportionally to the square of the extension ratio.

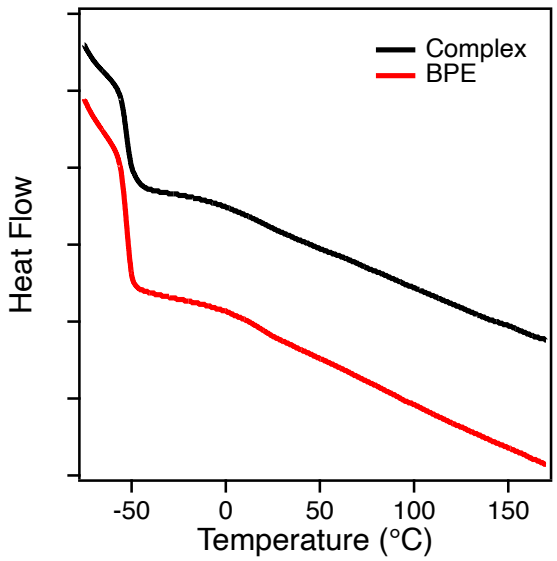

Figure S5.1. DSC shows no change to the Tg of the BPE upon complexation with the CPE

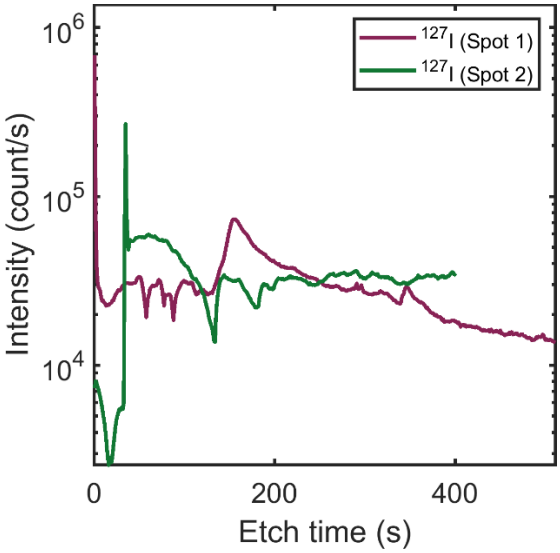

Figure S5.2. DSIMS detects the presence of Iodine in the complex, data shown for 2 different spots in the sample

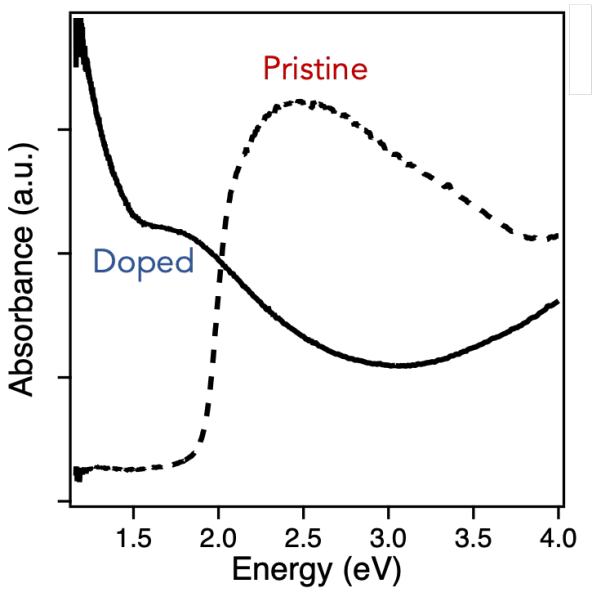

Figure S5.3. Formation of polaron and bipolaron observed upon doping of the complex with HTFSI

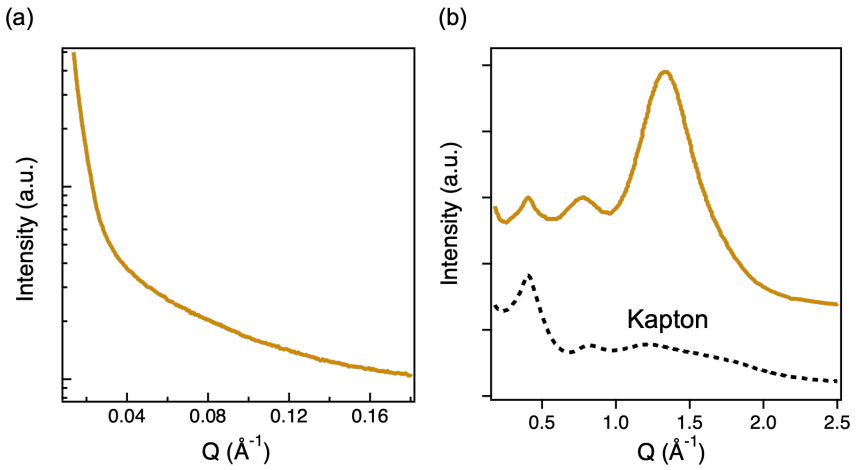

Figure S5.4. (a) SAXS and **(b)** WAXS of the complex after vapor-doped with HTFSI. The introduction of HTFSI into the complex likely swells the CPE- and BPE-domains as well as domain interfaces. Increase concentration of ions in linear charged polymer complex has been shown to shift the correlation peak to higher q and significantly broaden the peak.[47] We postulate that similar effects are seen here for the CPE – BPE complex, however the scattering peak is likely significantly broadened and overwhelmed by the low-q scattering upturn, resulting in a featureless SAXS trace.

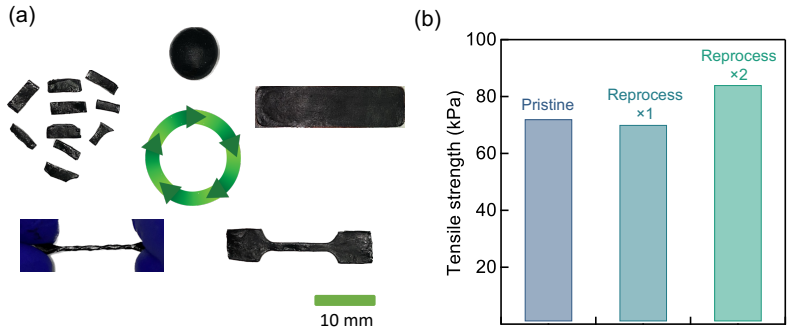

Figure S5.5. (a) Illustration of reprocessing of the complex by simple pressing at room temperature **(b)** Tensile strength of the complex after each reprocessing cycle indicate no loss in mechanical performance.

The complex appears to be dynamic and can be easily reprocessed at room temperature by simple pressing (**Figure S5.5a**), enabling facile processing of this material into different shapes or even μm-scale thin films. Processing conjugated polymers has been a major challenge due to their melt intractability and limited solubility. Our observation suggests that complexation with a super-soft polymer can enable bulk processing of conjugated polymers and open opportunities for the utilization of these materials in applications where bulk/shaped structures are required. We note that reprocessability of the polymer networks can be induced by various types of interaction ranging from van der Waal interaction,[78] hydrogen bonding,[79] metal-ligand interaction,[80] and covalent adaptive network.[81] However, most of these routes require high temperatures to reprocess. Some exceptions such as hydrogen bonding polymer networks can be reprocessed at near room temperature ($\approx$ 40°C) due to the low dissociation energy required.[56] Ionic crosslink polymer networks, on the other hand, usually require $\geq$ 100°C to reprocess.[82,83] Besides dynamic crosslinks, we attribute the room-temperature reprocessability of our complex to the special bottlebrush architecture and the low T_g (−55°C) of the BPE. We note that while the complex contains a high T_g component, CPE, the minor presence of it in the complex likely makes its impact negligible in terms of setting reprocessing

conditions. To demonstrate mechanical strength after reprocessing, uniaxial tensile tests were performed where the blend was pulled at a constant rate of 10 mm/min until break. The material was then recovered, remolded into the original dog bone shape, and the same test was repeated 2 more times on the same sample. As shown in **Figure S5.5b**, the tensile strengths are relatively similar at ≈ 80 kPa in all 3 processing cycles, confirming that there is no loss in the mechanical performance of the complex after reprocessing.

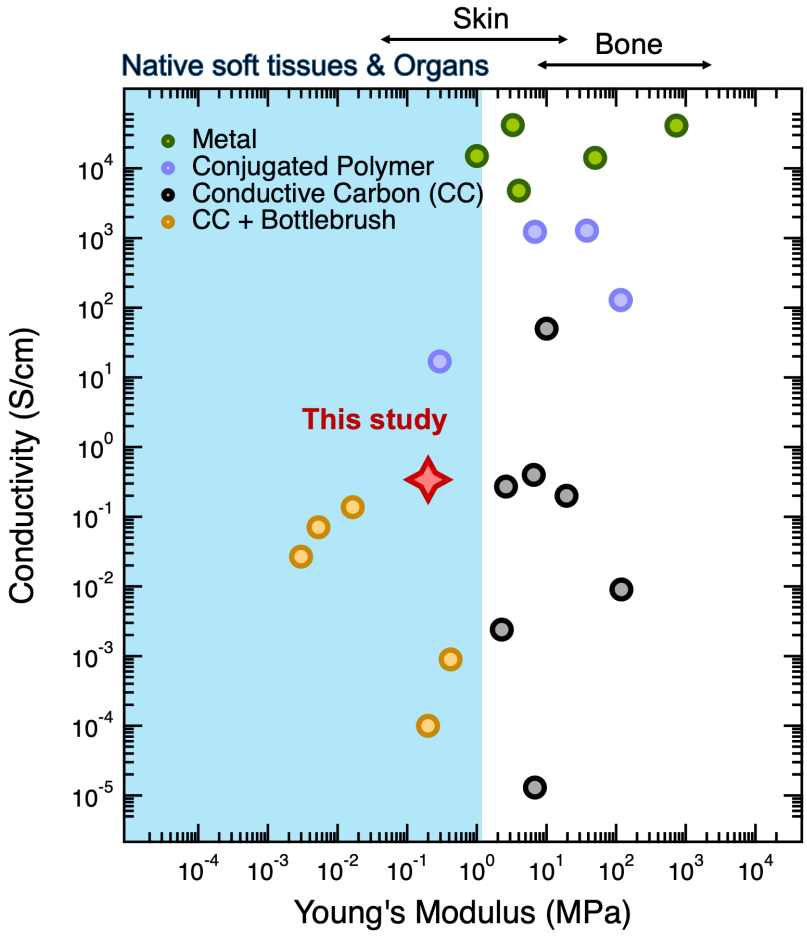

Figure S5.6. Ashby-style plot of conductivity and modulus of different elastomer – conductive material blends. Our material lies well within the modulus range of native soft tissues and organ, and has appreciable conductivity compared to other system of similar modulus range

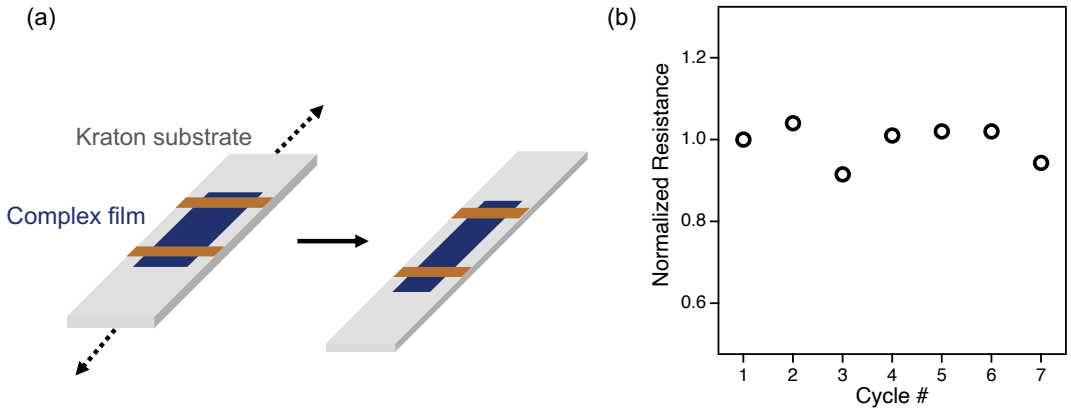

Figure S5.7. (a) Set up for measurement of the complex resistance when subjected to strain. Kraton was chosen as the supporting substrate for the complex film to avoid shearing of the film at the clamped point, which can lead to breaking of the material. Kraton was chosen for the supporting substrate due to its excellent elastic recovery and resistance to acids (in this case, HTFSI from the doped sample). Copper tape was used as the electrodes, and conductive carbon paint was used to ensure good contact between the complex film and the electrodes. **(b)** Full recovery of the doped complex's conductivity when the sample was subjected to 20% strain and let relax for 15 minutes, and the process was repeated for 7 cycles

5.8 References

(1) Rus, D.; Tolley, M. T. Design, Fabrication and Control of Soft Robots. *Nature* **2015**, *521* (7553), 467–475. https://doi.org/10.1038/nature14543.

(2) Xu, P.; Wang, S.; Lin, A.; Min, H. K.; Zhou, Z.; Dou, W.; Sun, Y.; Huang, X.; Tran, H.; Liu, X. Conductive and Elastic Bottlebrush Elastomers for Ultrasoft Electronics. *Nat. Commun.* **2023**, *14* (1), In press. https://doi.org/10.1038/s41467-023-36214-8.

(3) Song, J.; Huang, Y.; Xiao, J.; Wang, S.; Hwang, K. C.; Ko, H. C.; Kim, D. H.; Stoykovich, M. P.; Rogers, J. A. Mechanics of Noncoplanar Mesh Design for Stretchable Electronic Circuits. *J. Appl. Phys.* **2009**, *105* (12), 123516. https://doi.org/10.1063/1.3148245.

(4) Wang, Z.; Zhang, L.; Duan, S.; Jiang, H.; Shen, J.; Li, C. Kirigami-Patterned Highly Stretchable Conductors from Flexible Carbon Nanotube-Embedded Polymer Films. *J. Mater. Chem. C* **2017**, *5* (34), 8714–8722. https://doi.org/10.1039/c7tc01727h.

(5) Khang, D. Y.; Jiang, H.; Huang, Y.; Rogers, J. A. A Stretchable Form of Single-Crystal Silicon for High-Performance Electronics on Rubber Subtrates. *Science (80-.).* **2006**, *311* (5758), 208–212. https://doi.org/10.1126/science.1121401.

(6) Kim, D. H.; Ahn, J. H.; Won, M. C.; Kim, H. S.; Kim, T. H.; Song, J.; Huang, Y. Y.; Liu, Z.; Lu, C.; Rogers, J. A. Stretchable and Foldable Silicon Integrated Circuits. *Science (80-.).* **2008**, *320* (5875), 507–511. https://doi.org/10.1126/science.1154367.

(7) Zokaei, S.; Kim, D.; Järsvall, E.; Fenton, A. M.; Weisen, A. R.; Hultmark, S.; Nguyen, P. H.; Matheson, A. M.; Lund, A.; Kroon, R.; Chabinyc, M. L.; Gomez, E. D.; Zozoulenko, I.; Müller, C. Tuning of the Elastic Modulus of a Soft Polythiophene through Molecular Doping. *Mater. Horizons* **2022**, *9* (1), 433–443.

https://doi.org/10.1039/d1mh01079d.
(8) Moulton, J.; Smith, P. Electrical and Mechanical Properties of Oriented Poly(3-Alkylthiophenes) I. Doping-Enhanced Stiffness of Poly(3-Octylthiophene). *Synth. Met.* **1991**, *40* (1), 13–22. https://doi.org/10.1016/0379-6779(91)91484-R.
(9) Kroon, R.; Hofmann, A. I.; Yu, L.; Lund, A.; Müller, C. Thermally Activated in Situ Doping Enables Solid-State Processing of Conducting Polymers. *Chem. Mater.* **2019**, *31* (8), 2770–2777. https://doi.org/10.1021/acs.chemmater.8b04895.
(10) Hynynen, J.; Järsvall, E.; Kroon, R.; Zhang, Y.; Barlow, S.; Marder, S. R.; Kemerink, M.; Lund, A.; Müller, C. Enhanced Thermoelectric Power Factor of Tensile Drawn Poly(3-Hexylthiophene). *ACS Macro Lett.* **2019**, *8* (1), 70–76. https://doi.org/10.1021/acsmacrolett.8b00820.
(11) Zhao, Y.; Zhao, X.; Zang, Y.; Di, C. A.; Diao, Y.; Mei, J. Conjugation-Break Spacers in Semiconducting Polymers: Impact on Polymer Processability and Charge Transport Properties. *Macromolecules* **2015**, *48* (7). https://doi.org/10.1021/acs.macromol.5b00194.
(12) Wang, G. J. N.; Molina-Lopez, F.; Zhang, H.; Xu, J.; Wu, H. C.; Lopez, J.; Shaw, L.; Mun, J.; Zhang, Q.; Wang, S.; Ehrlich, A.; Bao, Z. Nonhalogenated Solvent Processable and Printable High-Performance Polymer Semiconductor Enabled by Isomeric Nonconjugated Flexible Linkers. *Macromolecules* **2018**, *51* (13). https://doi.org/10.1021/acs.macromol.8b00971.
(13) Schroeder, B. C.; Chiu, Y. C.; Gu, X.; Zhou, Y.; Xu, J.; Lopez, J.; Lu, C.; Toney, M. F.; Bao, Z. Non-Conjugated Flexible Linkers in Semiconducting Polymers: A Pathway to Improved Processability without Compromising Device Performance. *Adv. Electron. Mater.* **2016**, *2* (7). https://doi.org/10.1002/aelm.201600104.
(14) Xiao, W. J.; Wang, J.; Li, H. J.; Liang, L.; Xiang, X.; Chen, X. Q.; Li, J.; Lu, Z.; Li, W. S. Interconnecting Semiconducting Molecules with Non-Conjugated Soft Linkers: A Way to Improve Film Formation Quality without Sacrifice in Charge Mobility. *RSC Adv.* **2018**, *8* (42). https://doi.org/10.1039/c8ra04405h.
(15) Savagatrup, S.; Zhao, X.; Chan, E.; Mei, J.; Lipomi, D. J. Effect of Broken Conjugation on the Stretchability of Semiconducting Polymers. *Macromol. Rapid Commun.* **2016**, *37* (19). https://doi.org/10.1002/marc.201600377.
(16) Song, E.; Kang, B.; Choi, H. H.; Sin, D. H.; Lee, H.; Lee, W. H.; Cho, K. Stretchable and Transparent Organic Semiconducting Thin Film with Conjugated Polymer Nanowires Embedded in an Elastomeric Matrix. *Adv. Electron. Mater.* **2016**, *2* (1), 1500250. https://doi.org/10.1002/aelm.201500250.
(17) Shin, M.; Oh, J. Y.; Byun, K. E.; Lee, Y. J.; Kim, B.; Baik, H. K.; Park, J. J.; Jeong, U. Polythiophene Nanofibril Bundles Surface-Embedded in Elastomer: A Route to a Highly Stretchable Active Channel Layer. *Adv. Mater.* **2015**, *27* (7), 1255–1261. https://doi.org/10.1002/adma.201404602.
(18) Xu, J.; Wang, S.; Wang, G. J. N.; Zhu, C.; Luo, S.; Jin, L.; Gu, X.; Chen, S.; Feig, V. R.; To, J. W. F.; Rondeau-Gagné, S.; Park, J.; Schroeder, B. C.; Lu, C.; Oh, J. Y.; Wang, Y.; Kim, Y. H.; Yan, H.; Sinclair, R.; Zhou, D.; Xue, G.; Murmann, B.; Linder, C.; Cai, W.; Tok, J. B. H.; Chung, J. W.; Bao, Z. Highly Stretchable Polymer Semiconductor Films through the Nanoconfinement Effect. *Science (80-.).* **2017**, *355* (6320). https://doi.org/10.1126/science.aah4496.
(19) Liu, K.; Wei, S.; Song, L.; Liu, H.; Wang, T. Conductive Hydrogels - A Novel Material:

Recent Advances and Future Perspectives. *J. Agric. Food Chem.* **2020**, *68* (28), 7269–7280. https://doi.org/10.1021/acs.jafc.0c00642.
(20) Yuk, H.; Lu, B.; Zhao, X. Hydrogel Bioelectronics. *Chem. Soc. Rev.* **2019**, *48* (6), 1642–1667. https://doi.org/10.1039/c8cs00595h.
(21) Danielsen, S. P. O.; Sanoja, G. E.; McCuskey, S. R.; Hammouda, B.; Bazan, G. C.; Fredrickson, G. H.; Segalman, R. A. Mixed Conductive Soft Solids by Electrostatically Driven Network Formation of a Conjugated Polyelectrolyte. *Chem. Mater.* **2018**, *30* (4), 1417–1426. https://doi.org/10.1021/acs.chemmater.7b05303.
(22) Shin, M. K.; Oh, J.; Lima, M.; Kozlov, M. E.; Kim, S. J.; Baughman, R. H. Elastomeric Conductive Composites Based on Carbon Nanotube Forests. *Adv. Mater.* **2010**, *22* (24), 2663–2667. https://doi.org/10.1002/adma.200904270.
(23) Hu, N.; Karube, Y.; Arai, M.; Watanabe, T.; Yan, C.; Li, Y.; Liu, Y.; Fukunaga, H. Investigation on Sensitivity of a Polymer/Carbon Nanotube Composite Strain Sensor. *Carbon N. Y.* **2010**, *48* (3), 680–687. https://doi.org/10.1016/j.carbon.2009.10.012.
(24) Ma, R.; Kang, B.; Cho, S.; Choi, M.; Baik, S. Extraordinarily High Conductivity of Stretchable Fibers of Polyurethane and Silver Nanoflowers. *ACS Nano* **2015**, *9* (11), 10876–10886. https://doi.org/10.1021/acsnano.5b03864.
(25) Li, Z.; Le, T.; Wu, Z.; Yao, Y.; Li, L.; Tentzeris, M.; Moon, K. S.; Wong, C. P. Rational Design of a Printable, Highly Conductive Silicone-Based Electrically Conductive Adhesive for Stretchable Radio-Frequency Antennas. *Adv. Funct. Mater.* **2015**, *25* (3), 464–470. https://doi.org/10.1002/adfm.201403275.
(26) Fan, Y. J.; Yu, P. T.; Liang, F.; Li, X.; Li, H. Y.; Liu, L.; Cao, J. W.; Zhao, X. J.; Wang, Z. L.; Zhu, G. Highly Conductive, Stretchable, and Breathable Epidermal Electrode Based on Hierarchically Interactive Nano-Network. *Nanoscale* **2020**, *12* (30), 16053–16062. https://doi.org/10.1039/d0nr03189e.
(27) Choi, S.; Han, S. I.; Jung, D.; Hwang, H. J.; Lim, C.; Bae, S.; Park, O. K.; Tschabrunn, C. M.; Lee, M.; Bae, S. Y.; Yu, J. W.; Ryu, J. H.; Lee, S. W.; Park, K.; Kang, P. M.; Lee, W. B.; Nezafat, R.; Hyeon, T.; Kim, D. H. Highly Conductive, Stretchable and Biocompatible Ag–Au Core–Sheath Nanowire Composite for Wearable and Implantable Bioelectronics. *Nat. Nanotechnol.* **2018**, *13* (11), 1048–1056. https://doi.org/10.1038/s41565-018-0226-8.
(28) Dauzon, E.; Lin, Y.; Faber, H.; Yengel, E.; Sallenave, X.; Plesse, C.; Goubard, F.; Amassian, A.; Anthopoulos, T. D. Stretchable and Transparent Conductive PEDOT:PSS-Based Electrodes for Organic Photovoltaics and Strain Sensors Applications. *Adv. Funct. Mater.* **2020**, *30* (28), 2001251. https://doi.org/10.1002/adfm.202001251.
(29) Lee, J. H.; Jeong, Y. R.; Lee, G.; Jin, S. W.; Lee, Y. H.; Hong, S. Y.; Park, H.; Kim, J. W.; Lee, S. S.; Ha, J. S. Highly Conductive, Stretchable, and Transparent PEDOT:PSS Electrodes Fabricated with Triblock Copolymer Additives and Acid Treatment. *ACS Appl. Mater. Interfaces* **2018**, *10* (33), 28027–28035. https://doi.org/10.1021/acsami.8b07287.
(30) Guo, L.; Ma, M.; Zhang, N.; Langer, R.; Anderson, D. G. Stretchable Polymeric Multielectrode Array for Conformal Neural Interfacing. *Adv. Mater.* **2014**, *26* (9), 1427–1433. https://doi.org/10.1002/adma.201304140.
(31) Moniruzzaman, M.; Winey, K. I. Polymer Nanocomposites Containing Carbon Nanotubes. *Macromolecules* **2006**, *39* (16), 5194–5205.

https://doi.org/10.1021/ma060733p.
(32) Kim, J. H.; Hwang, J. Y.; Hwang, H. R.; Kim, H. S.; Lee, J. H.; Seo, J. W.; Shin, U. S.; Lee, S. H. Simple and Cost-Effective Method of Highly Conductive and Elastic Carbon Nanotube/Polydimethylsiloxane Composite for Wearable Electronics. *Sci. Rep.* **2018**, *8* (1), 1–11. https://doi.org/10.1038/s41598-017-18209-w.
(33) Yu, Z.; Niu, X.; Liu, Z.; Pei, Q. Intrinsically Stretchable Polymer Light-Emitting Devices Using Carbon Nanotube-Polymer Composite Electrodes. *Adv. Mater.* **2011**, *23* (34), 3989–3994. https://doi.org/10.1002/adma.201101986.
(34) Self, J. L.; Reynolds, V. G.; Blankenship, J.; Mee, E.; Guo, J.; Albanese, K.; Xie, R.; Hawker, C. J.; de Alaniz, J. R.; Chabinyc, M. L.; Bates, C. M. Carbon Nanotube Composites with Bottlebrush Elastomers for Compliant Electrodes. *ACS Polym. Au* **2022**, *2* (1), 27–34. https://doi.org/10.1021/acspolymersau.1c00034.
(35) Wang, M.; Baek, P.; Akbarinejad, A.; Barker, D.; Travas-Sejdic, J. Conjugated Polymers and Composites for Stretchable Organic Electronics. *J. Mater. Chem. C* **2019**, *7* (19), 5534–5552. https://doi.org/10.1039/c9tc00709a.
(36) Natansohn, A.; Murali, R.; Eisenberg, A. Miscibility Enhancement in Polymers via Ionic Interactions: Dynamic Mechanical and NMR Studies. *Makromol. Chemie. Macromol. Symp.* **1988**, *16* (1), 175–193. https://doi.org/10.1002/masy.19880160113.
(37) Tannenbaum, R.; Rutkowska, M.; Eisenberg, A. Ionomeric Blends. V. FTIR Studies of Ionic Interactions in Polyurethane-styrene Blends. *J. Polym. Sci. Part B Polym. Phys.* **1987**, *25* (3), 663–671. https://doi.org/10.1002/polb.1987.090250316.
(38) Natansohn, A.; Rutkowska, M.; Eisenberg, A. Nuclear Magnetic Resonance Studies of Ionomers: 2. Proton Transfer in Polyurethane-Poly(Styrene-Co-Styrene Sulphonic Acid) Mixtures in Solution. *Polymer (Guildf).* **1987**, *28* (6), 885–888. https://doi.org/10.1016/0032-3861(87)90158-3.
(39) Rutkowska, M.; Eisenberg, A. Ionomeric Blends. 3. Miscibility Enhancement via Ionic Interactions in Polyurethane-Styrene Blends. *Macromolecules* **1984**, *17* (4), 821–824. https://doi.org/10.1021/ma00134a050.
(40) Natansohn, A.; Eisenberg, A. Nuclear Magnetic Resonance Studies of Ionomers. 1. Interactions between Poly(Methyl Methacrylate-Co-4-Vinylpyridine) and Poly(Styrene-Co-Styrenesulfonic Acid) in Dimethyl Sulfoxide Solution. *Macromolecules* **1987**, *20* (2), 323–329. https://doi.org/10.1021/ma00168a015.
(41) Zhang, X.; Natansohn, A.; Eisenberg, A. Intermolecular Cross-Polarization Studies of The Miscibility Enhancement of PS/PMMA Blends Through Ionic Interactions. *Macromolecules* **1990**, *23* (2), 412–416. https://doi.org/10.1021/ma00204a010.
(42) Noro, A.; Ishihara, K.; Matsushita, Y. Nanophase-Separated Supramolecular Assemblies of Two Functionalized Polymers via Acid-Base Complexation. *Macromolecules* **2011**, *44* (16), 6241–6244. https://doi.org/10.1021/ma201440v.
(43) Russell, T. P.; Jérôme, R.; Charlier, P.; Foucart, M. The Microstructure of Block Copolymers Formed via Ionic Interaction. *Macromolecules* **1988**, *21* (6), 1709–1717. https://doi.org/10.1021/ma00184a030.
(44) Grzetic, D. J.; Delaney, K. T.; Fredrickson, G. H. Electrostatic Manipulation of Phase Behavior in Immiscible Charged Polymer Blends. *Macromolecules* **2021**, *54* (6), 2604–2616. https://doi.org/10.1021/acs.macromol.1c00095.
(45) Fredrickson, G. H.; Xie, S.; Edmund, J.; Le, M. L.; Sun, D.; Grzetic, D. J.; Vigil, D. L.; Delaney, K. T.; Chabinyc, M. L.; Segalman, R. A. Ionic Compatibilization of Polymers.

ACS Polym. Au **2022**, *2* (5), 299–312. https://doi.org/10.1021/acspolymersau.2c00026.
(46) Le, M. L.; Rawlings, D.; Danielsen, S. P. O.; Kennard, R. M.; Chabinyc, M. L.; Segalman, R. A. Aqueous Formulation of Concentrated Semiconductive Fluid Using Polyelectrolyte Coacervation. *ACS Macro Lett.* **2021**, *10* (8), 1008–1014. https://doi.org/10.1021/acsmacrolett.1c00354.
(47) Le, M. L.; Grzetic, D. J.; Delaney, K. T.; Yang, K. C.; Xie, S.; Fredrickson, G. H.; Chabinyc, M. L.; Segalman, R. A. Electrostatic Interactions Control the Nanostructure of Conjugated Polyelectrolyte-Polymeric Ionic Liquid Blends. *Macromolecules* **2022**, *55* (18), 8321–8331. https://doi.org/10.1021/acs.macromol.2c01142.
(48) Le, M. L.; Warner, C.; Segalman, R. A.; Chabinyc, M. L. The Role of Segregation-Induced Nanostructure on the Optoelectronic Properties of Conjugated Polyelectrolyte – Polymeric Ionic Liquid Blends. *Macromolecules* **2023**, *submitted*.
(49) Abbasi, M.; Faust, L.; Wilhelm, M. Comb and Bottlebrush Polymers with Superior Rheological and Mechanical Properties. *Adv. Mater.* **2019**, *31* (26), 1806484. https://doi.org/10.1002/adma.201806484.
(50) Self, J. L.; Sample, C. S.; Levi, A. E.; Li, K.; Xie, R.; De Alaniz, J. R.; Bates, C. M. Dynamic Bottlebrush Polymer Networks: Self-Healing in Super-Soft Materials. *J. Am. Chem. Soc.* **2020**, *142* (16), 7567–7573. https://doi.org/10.1021/jacs.0c01467.
(51) Daniel, W. F. M.; Burdyńska, J.; Vatankhah-Varnoosfaderani, M.; Matyjaszewski, K.; Paturej, J.; Rubinstein, M.; Dobrynin, A. V.; Sheiko, S. S. Solvent-Free, Supersoft and Superelastic Bottlebrush Melts and Networks. *Nat. Mater.* **2016**, *15* (2), 183–189. https://doi.org/10.1038/nmat4508.
(52) Matson, J. B.; Grubbs, R. H. Synthesis of Fluorine-18 Functionalized Nanoparticles for Use as in Vivo Molecular Imaging Agents. *J. Am. Chem. Soc.* **2008**, *130* (21), 6731–6733. https://doi.org/10.1021/ja802010d.
(53) Atzrodt, J.; Derdau, V.; Kerr, W.; Reid, M. Applications of Hydrogen Isotopes in the Life Sciences. *Angew. Chemie Int. Ed.* **2017**, 1–26. https://doi.org/10.1002/(ISSN)1521-3773.
(54) Levi, A. E.; Lequieu, J.; Horne, J. D.; Bates, M. W.; Ren, J. M.; Delaney, K. T.; Fredrickson, G. H.; Bates, C. M. Miktoarm Stars via Grafting-Through Copolymerization: Self-Assembly and the Star-to-Bottlebrush Transition. *Macromolecules* **2019**, *52* (4), 1794–1802. https://doi.org/10.1021/acs.macromol.8b02321.
(55) Levi, A. E.; Fu, L.; Lequieu, J.; Horne, J. D.; Blankenship, J.; Mukherjee, S.; Zhang, T.; Fredrickson, G. H.; Gutekunst, W. R.; Bates, C. M. Efficient Synthesis of Asymmetric Miktoarm Star Polymers. *Macromolecules* **2020**, *53* (2), 702–710. https://doi.org/10.1021/acs.macromol.9b02380.
(56) Xie, R.; Lapkriengkri, I.; Pramanik, N. B.; Mukherjee, S.; Blankenship, J. R.; Albanese, K.; Wang, H.; Chabinyc, M. L.; Bates, C. M. Hydrogen-Bonding Bottlebrush Networks: Self-Healing Materials from Super-Soft to Stiff. *Macromolecules* **2022**, *55* (23), 10513–10521. https://doi.org/10.1021/acs.macromol.2c01886.
(57) Kazemiabnavi, S.; Zhang, Z.; Thornton, K.; Banerjee, S. Electrochemical Stability Window of Imidazolium-Based Ionic Liquids as Electrolytes for Lithium Batteries. *J. Phys. Chem. B* **2016**, *120* (25), 5691–5702. https://doi.org/10.1021/acs.jpcb.6b03433.
(58) Rubinstein, M.; Liao, Q.; Panyukov, S. Structure of Liquid Coacervates Formed by Oppositely Charged Polyelectrolytes. *Macromolecules* **2018**, *51* (23), 9572–9588.

https://doi.org/10.1021/acs.macromol.8b02059.
(59) Chremos, A.; Douglas, J. F. A Comparative Study of Thermodynamic, Conformational, and Structural Properties of Bottlebrush with Star and Ring Polymer Melts. *J. Chem. Phys.* **2018**, *149* (4). https://doi.org/10.1063/1.5034794.
(60) Schmode, P.; Ohayon, D.; Reichstein, P. M.; Savva, A.; Inal, S.; Thelakkat, M. High-Performance Organic Electrochemical Transistors Based on Conjugated Polyelectrolyte Copolymers. *Chem. Mater.* **2019**, *31* (14), 5286–5295. https://doi.org/10.1021/acs.chemmater.9b01722.
(61) Paquin, F.; Yamagata, H.; Hestand, N. J.; Sakowicz, M.; Bérubé, N.; Côté, M.; Reynolds, L. X.; Haque, S. A.; Stingelin, N.; Spano, F. C.; Silva, C. Two-Dimensional Spatial Coherence of Excitons in Semicrystalline Polymeric Semiconductors: Effect of Molecular Weight. *Phys. Rev. B - Condens. Matter Mater. Phys.* **2013**, *88* (15), 155202. https://doi.org/10.1103/PhysRevB.88.155202.
(62) Le, M. L.; Warner, C.; Segalman, R.; Chabinyc, M. Role of Complexation Strength on the Photophysical and Transport Properties of Semiconducting Charged Polymer Complexes. *Chem. Mater.* **2023**.
(63) De Jesus, M. C.; Fu, Y.; Weiss, R. A. Conductive Polymer Blends Prepared by in Situ Polymerization of Pyrrole: A Review. *Polym. Eng. Sci.* **1997**, *37* (12), 1936–1943. https://doi.org/10.1002/pen.11844.
(64) Njuguna, J.; Pielichowski, K. Recent Developments in Polyurethane-Based Conducting Composites. *J. Mater. Sci.* **2004**, *39* (13), 4081–4094. https://doi.org/10.1023/B:JMSC.0000033387.51728.de.
(65) Zallen, R. The Physics of Amorphous Solids. *Phys. Amorph. Solids* **2007**, 1–304. https://doi.org/10.1002/9783527617968.
(66) Suzuki, Y. Y.; Heeger, A. J.; Pincus, P. Percolation of Conducting Polymers on a Gel. *Macromolecules* **1990**, *23* (21), 4730. https://doi.org/10.1021/ma00223a037.
(67) Hotta, S.; Rughooputh, S. D. D. V.; Heeger, A. J. Conducting Polymer Composites of Soluble Polythiophenes in Polystyrene. *Synth. Met.* **1987**, *22* (1), 79–87. https://doi.org/10.1016/0379-6779(87)90573-X.
(68) Reynolds, V. G.; Mukherjee, S.; Xie, R.; Levi, A. E.; Atassi, A.; Uchiyama, T.; Wang, H.; Chabinyc, M. L.; Bates, C. M. Super-Soft Solvent-Free Bottlebrush Elastomers for Touch Sensing. *Mater. Horizons* **2020**, *7* (1), 181–187. https://doi.org/10.1039/c9mh00951e.
(69) Vatankhah-Varnoosfaderani, M.; Daniel, W. F. M.; Zhushma, A. P.; Li, Q.; Morgan, B. J.; Matyjaszewski, K.; Armstrong, D. P.; Spontak, R. J.; Dobrynin, A. V.; Sheiko, S. S. Bottlebrush Elastomers: A New Platform for Freestanding Electroactuation. *Adv. Mater.* **2017**, *29* (2), 1604209. https://doi.org/10.1002/adma.201604209.
(70) Dong, H.; Du, H.; Wickramasinghe, S. R.; Qian, X. The Effects of Chemical Substitution and Polymerization on the PK a Values of Sulfonic Acids. *J. Phys. Chem. B* **2009**, *113* (43), 14094–14101. https://doi.org/10.1021/jp906087c.
(71) Self, J. L.; Dolinski, N. D.; Zayas, M. S.; Read De Alaniz, J.; Bates, C. M. Brønsted-Acid-Catalyzed Exchange in Polyester Dynamic Covalent Networks. *ACS Macro Lett.* **2018**, *7* (7). https://doi.org/10.1021/acsmacrolett.8b00370.
(72) Boschin, A.; Johansson, P. Characterization of NaX (X: TFSI, FSI) - PEO Based Solid Polymer Electrolytes for Sodium Batteries. *Electrochim. Acta* **2015**, *175*. https://doi.org/10.1016/j.electacta.2015.03.228.

(73) Li, P.; Sun, K.; Ouyang, J. Stretchable and Conductive Polymer Films Prepared by Solution Blending. *ACS Appl. Mater. Interfaces* **2015**, *7* (33), 18415–18423. https://doi.org/10.1021/acsami.5b04492.
(74) Choi, D.; Kim, H.; Persson, N.; Chu, P. H.; Chang, M.; Kang, J. H.; Graham, S.; Reichmanis, E. Elastomer-Polymer Semiconductor Blends for High-Performance Stretchable Charge Transport Networks. *Chem. Mater.* **2016**, *28* (4), 1196–1204. https://doi.org/10.1021/acs.chemmater.5b04804.
(75) Song, E.; Kang, B.; Choi, H. H.; Sin, D. H.; Lee, H.; Lee, W. H.; Cho, K. Stretchable and Transparent Organic Semiconducting Thin Film with Conjugated Polymer Nanowires Embedded in an Elastomeric Matrix. *Adv. Electron. Mater.* **2016**, *2* (1), 1500250. https://doi.org/10.1002/aelm.201500250.
(76) Danielsen, S. P. O.; Davidson, E. C.; Fredrickson, G. H.; Segalman, R. A. Absence of Electrostatic Rigidity in Conjugated Polyelectrolytes with Pendant Charges. *ACS Macro Lett.* **2019**, *8* (9), 1147–1152. https://doi.org/10.1021/acsmacrolett.9b00551.
(77) Keith, A. N.; Clair, C.; Lallam, A.; Bersenev, E. A.; Ivanov, D. A.; Tian, Y.; Dobrynin, A. V.; Sheiko, S. S. Independently Tuning Elastomer Softness and Firmness by Incorporating Side Chain Mixtures into Bottlebrush Network Strands. *Macromolecules* **2020**, *53* (21). https://doi.org/10.1021/acs.macromol.0c01725.
(78) Watts, A.; Kurokawa, N.; Hillmyer, M. A. Strong, Resilient, and Sustainable Aliphatic Polyester Thermoplastic Elastomers. *Biomacromolecules* **2017**, *18* (6), 1845–1854. https://doi.org/10.1021/acs.biomac.7b00283.
(79) Bosman, A. W.; Sijbesma, R. P.; Meijer, E. W. Supramolecular Polymers at Work. *Mater. Today* **2004**, *7* (4), 34–39. https://doi.org/10.1016/S1369-7021(04)00187-7.
(80) Mozhdehi, D.; Ayala, S.; Cromwell, O. R.; Guan, Z. Self-Healing Multiphase Polymers via Dynamic Metal-Ligand Interactions. *J. Am. Chem. Soc.* **2014**, *136* (46), 16128–16131. https://doi.org/10.1021/ja5097094.
(81) Robinson, L. L.; Self, J. L.; Fusi, A. D.; Bates, M. W.; Read De Alaniz, J.; Hawker, C. J.; Bates, C. M.; Sample, C. S. Chemical and Mechanical Tunability of 3D-Printed Dynamic Covalent Networks Based on Boronate Esters. *ACS Macro Lett.* **2021**, *10*, 857–863. https://doi.org/10.1021/acsmacrolett.1c00257.
(82) Raidt, T.; Hoeher, R.; Meuris, M.; Katzenberg, F.; Tiller, J. C. Ionically Cross-Linked Shape Memory Polypropylene. *Macromolecules* **2016**, *49* (18), 6918–6927. https://doi.org/10.1021/acs.macromol.6b01387.
(83) Xu, C.; Huang, X.; Li, C.; Chen, Y.; Lin, B.; Liang, X. Design of "Zn2+ Salt-Bondings" Cross-Linked Carboxylated Styrene Butadiene Rubber with Reprocessing and Recycling Ability via Rearrangements of Ionic Cross-Linkings. *ACS Sustain. Chem. Eng.* **2016**, *4* (12), 6981–6990. https://doi.org/10.1021/acssuschemeng.6b01897.

Chapter 6

Conclusions

This chapter is reproduced in part with permission from:

Fredrickson, G. H., Xie, S., Edmund, J., **Le, M. L.**, Sun, D., Grzetic, D. J., Vigil, D. L., Delaney, K. T., Chabinyc, M. L., Segalman, R. A. Ionic Compatibilization of Polymers. *ACS Polym. Au* **2022***,* 2, 299−312. DOI: 10.1021/acspolymersau.2c00026

In summary, this Dissertation highlights the potentials of electrostatic interactions in designing advanced semiconducting polymers. We have shown that polyelectrolyte complexation can be leveraged to process conjugated polymers at high loading (Chapter 2), to control the structure (Chapter 3) and optoelectronic properties (Chapter 4) of the resulting polymer complexes, and to introduce new functionalities to the material besides electronic conductivity (Chapter 5). We believe that our findings suggest not only an additional handle for optimizing the processability and the performance of conjugated polymers, but also exciting opportunities to further study these materials in applications where they have not been widely utilized.

The conformation of the polymer backbone and how chains pack are critical in applications that utilize conjugated polymers, as they play direct roles in determining the material's electronic structure and transport properties. While we have gained initial insights on the arrangement of CPE chains within a complex, mainly by exploiting the strong coupling between the conformation of a conjugated polymer and its optical properties, the nature of chain conformations in conjugated complexes and how factors such as charge density, rigidity

mismatch, and molecular structure of individual components influence chain packing and conformation remain elusive. Moreover, experimental investigations of conjugated polymer complexes to date have not employed CPEs with highly rigid backbones, which are subjected to specific and directional interactions such as π–π stacking. Clearly, more theoretical and experimental attention is required, but the universality of complexation-induced conformation changes in such systems may be limited. Other experimental techniques are needed to complement spectroscopic measurements to reveal the chain conformation and structure of the individual components. For example, neutron scattering could be conducted on complexes with one of the chains deuterated to probe the structure of an individual component.

We only focused on complexes of CPE with an insulating polyelectrolyte in this Dissertation. Studies on charged complexes in which both polymers are conjugated, on the other hand, have shown some intriguing complexation physics. CPE–CPE complexes in solid-state precipitate form [1] and in dilute aqueous solution [2] were reported to show a qualitative difference in complexation thermodynamics compared to conventional (nonconjugated) polyelectrolytes. At least in the particular systems studied, CPE–CPE complexation appears to have an enthalpic contribution that changes sign with temperature. In particular, at room temperature, complexation is driven mainly by counterion entropy and electrostatic correlations, yet at elevated temperatures, a significant negative enthalpic contribution was measured. This exothermic process was attributed to the extension of the more flexible CPE chains at elevated temperature within the dilute aqueous solution CPE complex, resulting in more delocalization of the π-electron wave function and thus a reduction in chain energy. It is important to note that fluid or gel coacervate phases were not observed in these systems at higher concentration

but, rather, solid precipitates were. Such precipitates cannot be easily processed into uniform thick films, although the introduction of an appropriate cosolvent could potentially mitigate this problem.[3] Together, these observations suggest that charged polymer blend systems with conjugated components have rich complexation behavior that can differ from conventional complex coacervation. The presence of the conjugated backbones in the complex introduces additional intermolecular interactions to the system such as π–π stacking, hydrophobic interactions, hydrogen bonding, and cation−π interactions. A fundamental understanding of how the interplay among such complex interactions determines the phase behavior, structure, and rheology of conjugated charged polymer blends in (lean) mixed solvent conditions is still lacking, and further investigation is needed.

Ultimately, the knowledge of how complexation controls chain conformation and interchain packing of one or more conjugated components will enable electrostatic manipulation of optoelectronic and transport properties for a range of applications. There are also opportunities in optimizing and engineering the existing properties of the conjugated polymers. In particular, electrostatic blends of two CPEs with different backbones could be utilized to continuously tune (with composition and charge density) bandgap and electronic structure for active layers in light-emitting/light-harvesting devices. Currently, electronic structure manipulation of conjugated polymers is limited to the synthesis of new monomers (e.g., donor–acceptor monomers), copolymerization, or post-polymerization functionalization, all of which are laborious, or to doping/additive strategies, which can be unpredictable.[4]

6.1 References

(1) Hollingsworth, W. R.; Segura, C.; Balderrama, J.; Lopez, N.; Schleissner, P.; Ayzner, A. L. Exciton Transfer and Emergent Excitonic States in Oppositely-Charged Conjugated Polyelectrolyte Complexes. J. Phys. Chem. B 2016, 120 (31), 7767–7774. https://doi.org/10.1021/acs.jpcb.6b06533.

(2) Hollingsworth, W. R.; Williams, V.; Ayzner, A. L. Semiconducting Eggs and Ladders: Understanding Exciton Landscape Formation in Aqueous π-Conjugated Inter-Polyelectrolyte Complexes. Macromolecules 2020, 53 (7), 2724–2734. https://doi.org/10.1021/acs.macromol.0c00029.

(3) Danielsen, S. P. O.; Nguyen, T. Q.; Fredrickson, G. H.; Segalman, R. A. Complexation of a Conjugated Polyelectrolyte and Impact on Optoelectronic Properties. ACS Macro Lett. 2019, 8 (1), 88–94. https://doi.org/10.1021/acsmacrolett.8b00924.

(4) Müllen, K.; Pisula, W. Donor–Acceptor Polymers. J. Am. Chem. Soc. 2015, 137 (30), 9503–9505. https://doi.org/10.1021/JACS.5B07015.